UNIVERSITY
OF TRENTO - Italy
DEPARTMENT OF INDUSTRIAL ENGINEERING

XXVII cycle

Doctoral School in Materials Science and Engineering

Understanding the effect of nanofillers on the properties of polypropylene and glass fiber/polypropylene multiscale composites

Diego Pedrazzoli

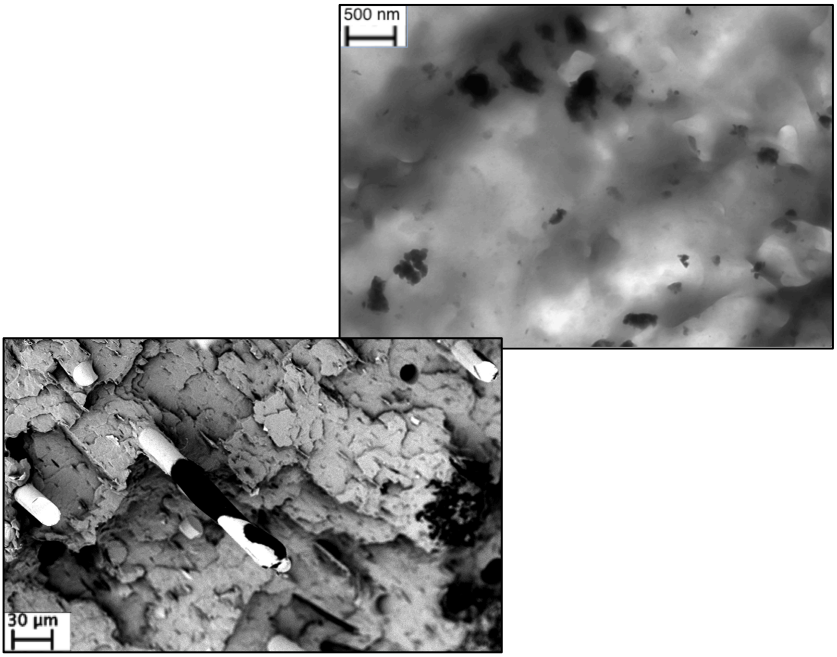

October 2014

UNDERSTANDING THE EFFECT OF NANOFILLERS ON THE PROPERTIES OF POLYPROPYLENE AND GLASS FIBER/POLYPROPYLENE MULTISCALE COMPOSITES

Diego Pedrazzoli

E-mail: pedrazzoli.diego@gmail.com

Approved by:

Prof. Alessandro Pegoretti, Advisor
Department of Industrial Engineering
University of Trento*, Italy.*

Ph.D. Commission:

Prof. F. Deflorian,
Department of Industrial Engineering
University of Trento, *Italy.*

Prof. P. Leisner,
School of Engineering
Jönköping University, Sweden.

Dr. S. Pandini,
Department of Mech. & Ind. Engineering
University of Brescia*, Italy.*

University of Trento, Italy

Department of Industrial Engineering

October 2014

University of Trento - Department of Industrial Engineering

Doctoral Thesis

Diego Pedrazzoli – 2014
Published in Trento (Italy) – by University of Trento

ISBN: ----------

To my Family

Abstract

In this study, polypropylene (PP) based nanocomposites were prepared by incorporating different kinds and amounts of silica nanoparticles and graphite nanoplatelets (GNP). The role of various percentages of compatibilizer polypropylene grafted with maleic anhydride (PPgMA) into PP nanocomposites was also investigated. In order to analyze the effect of the manufacturing process on the material's properties, the samples were produced by (i) melt compounding and compression molding and (ii) extrusion and injection molding. It was found that injection molding provides significantly greater stiffness and strength compared to compression molding for all types of PP nanocomposites. Several characterization techniques were used in order to correlate the microstructure to the physical and mechanical properties of the materials.

Both silica and GNP were found to be effective nucleating agents, significantly increasing the crystallization rate during isothermal crystallization and favoring the nucleation of the the β-phase, which manifests superior impact strength and toughness compared to the most common α-form crystals. Graphite nanoplatelets were found more efficient in inducing polymorphism and favoring the formation of a transcrystalline phase on the filler surface.

A significant correlation between the tensile modulus, glass transition temperature and the amount of constrained phase, as assessed through tensile and DMA analyses, revealed the presence of a secondary reinforcing mechanisms, which, concurrently to the primary stiffening effect of the high modulus filler, contributes to the enhancement of the bulk properties. A complex constrained phase, responsible for providing a secondary reinforcing mechanism, was modeled as immobilized amorphous and transcrystalline regions located at the filler surface.

The non-linear viscoelastic creep of the composites, successfully studied by the application of the time strain superposition principle (TSSP), showed a considerable enhancement of the creep stability in nanocomposites with respect to unfilled PP, especially for higher creep stresses. The study of creep dependance on the temperature showed that the stabilizing effect provided by the nanoparticles was more effective at high temperatures and, considering the time temperature superposition principle (TTSP), at long loading times. The equivalence between the time strain- and time temperature- superposition principle was substantiated by comparing the correspondent superimposed master curves.

The nanofilled PP matrices have also been used for the preparation of microcomposites reinforced with short glass fibers (GF). Interfacial shear strength (ISS) was measured by means of the single fiber fragmentation test on various PP/GF microcomposites. Results show that the strength at the fiber/matrix interface can be remarkably increased when using nanocomposite systems, especially in the case of dimethyldichlorosilane-functionalized silica nanoparticles and GNP platelets, and that the improvement is further increased when the nanoparticles are used in combination with PPgMA. The thermodynamic fiber/matrix work of adhesion, estimated by contact angle measurements, showed a good correlation with the ISS values.

Hybrid composites reinforced with short glass fibers and nanofillers were produced and characterized in order to investigate how the morphology and the mechanical properties of the composites were affected by the combined effect of two fillers of rather different size scales (i.e. micro- and nano- scale). The stronger fiber/matrix adhesion combined with the enhancement of the matrix properties resulted in superior tensile properties and impact resistance and improved viscoelastic behavior. As means of comparison, thermosetting hybrid composites based on epoxy resin were also produced by incorporation of GNP and short GF.

TABLE OF CONTENTS

LIST OF FIGURES

LIST OF TABLES

LIST OF ABBREVATIONS AND ACRONYMS

ABS	Acrylonitrile Butadiene Styrene
AFM	Atomic Force Microscopy
ANOVA	Analysis of Variance
ASTM	American Society for Testing and Materials
BA	Boehmite Alumina
BET	Brunauer-Emett-Teller
BHJ	Barrett-Joiner-Holenda
BN	Boron Nanotubes
CB	Carbon Black
CNF	Carbon Nanofibers
CNT	Carbon Nanotubes
COC	Cyclic Olefin Copolymer
CTE	Coefficient of Thermal Expansion
CVD	Chemical Vapor Deposition
DENT	Double Edge Notched Tension
DMA	Dynamic Mechanical Analysis
DMTA	Dynamic Mechanical Thermal Analysis
DSC	Differential Scanning Calorimetry
EBM	Equivalent Box Model
EPDM	Ethylene Propylene Diene Monomer
EPR	Ethylene Propylene Rubber
ESEM	Environmental Scanning Electron Microscopy
EWF	Essential Work of Fracture
FRPC	Fiber-Reinforced Polymer Composites
FTIR-ATR	Fourier Transform Infrared-Attenuated Total Reflectance
FWHM	Full Width Half Maximum
GF	Glass Fiber
GNP	Graphite Nanoplatelets
HDPE	High Density Polyethylene
IR	Infrared Spectroscopy
ISO	International Organization for Standardization
ISS	Interfacial Shear Strength
LCP	Liquid Crystalline Polymer
LDPE	Low Density Polyethylene
LLDPE	Linear Low Density Polyethylene
MDSC	Modulated Differential Scanning Calorimetry
MFI	Melt Flow Index
MMT	Montmorillonite
MWCNT	Multi-Walled Carbon Nanotubes
NMR	Nuclear Magnetic Resonance
OAN	Oil Adsorption Number
OMMT	Organomodified Montmorillonite

PA	Polyamide
PAN	Poly-Acrylo Nitrile
PC	Polycarbonate
PE	Polyethylene
PEEK	Polyether-Ether Ketone
PET	Polyethyleneterephtalate
PMMA	Polymethyl-methacrylate
POSS	Polyhedral Oligomeric Silsequioxanes
PP	Polypropylene
PVA	Polyvinyl Alcohol
PVC	Polyvinylchloride
PVDF	Polyvinylidene Fluoride
SAN	Styrene Acrylonitrile resin
SAXS	Small-Angle X-ray Scattering
SEBS-g-MA	Maleated-Styrene Ethylene Butylenes Styrene
SEM	Scanning Electron Microscopy
SFFT	Single-Fiber Fragmentation Test
SFRC	Short-Fiber Reinforced Composites
SSA	Specific Surface Area
SWCNT	Single-Walled Carbon Nanotubes
TEB	Tensile Energy at Break
TEM	Transmission Electron Microscopy
TGA	Thermogravimetric Analysis
TMS	Trimethyl-Silane
TTSP	Time-Temperature Superposition Principle
TTSSP	Time-Temperature-Strain Superposition Principle
UCT	Cryo-Ultramicrotome
UTS	Ultimate Tensile Strength
UV	Ultraviolet
VCT-MAS	Variable Contact Time Magic Angle Spinning
VIECA	Vibrated Induced Equilibrium Contact Angle
WAXD	Wide-Angle X-ray Diffraction
WLF	William-Landel-Ferry
xGnP	Expanded Graphite Nanoplatelets
XPS	X-Ray Photoelectron Spectroscopy
XRD	X-Ray Diffraction analysis

Chapter I

Introduction

Polymer nanocomposites are polymer matrix composites in which the fillers are less than 100 nm in at least one dimension. In contrast to traditional polymer composites with high loadings of microsized fillers (up to 60 vol%), polymer nanocomposites typically incorporate very low amounts (less than 5 vol%) of well dispersed nanometric filler particles. While nanomodification of elastomers with spherical nanofillers has been used for several decades, novel nanofillers exhibiting superior physical properties have emerged in the last 15 years, leading the development of advanced multifunctional nanocomposites [1].

Nanometric sized fillers are being intensively investigated for several reasons: (i) the properties of such nanofillers are different from the bulk properties of the same material (for example carbon nanotubes are much stronger and stiffer than the micrometric carbon fibers), (ii) nanofillers represent very small defects when considered incorporated in a polymeric matrix, with size smaller than the critical crack size thus preventing early failure and (iii) the extremely large volume of interfacial matrix material exhibits properties different from the bulk matrix, leading to dramatic changes in physical properties of the overall composite.

Multifunctional nanocomposites have exhibited extraordinarily interesting properties. The incorporation of small quantities of nanostructured materials in polymeric matrices can dramatically enhance the physical, mechanical, thermal and functional properties (e.g. electrical and thermal conductivity, wear resistance, flame retardant properties, surface finish and biological interactions) of the resultant composite, providing the opportunity to be used in different fields such as automotive, electronic packaging, aerospace, energy storage, etc.

Although polymer nanocomposites exhibit improved thermal and mechanical properties at very low filler contents, loadings of more than 10 wt% usually lead to poor dispersion and processing characteristics [2]. Moreover, polymer nanocomposites are much less resistant to mechanical load and fatigue damage than the traditional fiber reinforced composites, greatly limiting their use in structural applications. Increasing interest is therefore growing in the development of hybrid composites, in which a nanosized reinforcement is utilized alongside traditional microscale reinforcing fibers in order to obtain high-performance multifunctional nanocomposites.

Traditional, continuous fiber-reinforced polymer composites (FRPC) have made a huge impact over the past decades, particularly in the aerospace and oil/gas

industries. Their superior mechanical properties and low weight, combined with their chemical and environmental resistance, make them the ideal material for many structural applications, including automotive, civil and marine structures and sport equipment [3]. In most cases, high fiber loadings are required to achieve the desired performances, leading to an undesirable increase in specific gravity, decreased melt flow, and increased brittleness [4]. Moreover, although excellent in-plane tensile properties can be achieved using continuous FRPC, the relatively weak compression and interlaminar properties of such composites remain major issues. On the other hand, short-fiber reinforced composites (SFRC) have been recently applied in a growing number of applications in engineering and consumer products in order to improve or tailor certain thermo-mechanical properties of the matrix for specific applications or to reduce the cost of the article. In general, SFRC are less resistant to mechanical load than the continuous FRPC, mainly because the weak matrix has to sustain a greater proportion of the load. Therefore, the incorporation of nanofillers in SFRC might alleviate the existing limitations associated with the matrix-dominated properties or to improve the stress transfer mechanism between fiber and matrix.

Starting from these considerations, both thermoplastic nanocomposites and hybrid composites reinforced with short fibers were produced and characterized. Special focus was given to the study of the matrix/filler interactions in nanocomposites and fiber reinforced composites and their impact on the properties of the resultant composite. Specifically, polypropylene (PP) nanocomposites based on different nanofillers (either silica nanoparticles or expanded graphite nanoplatelets (xGnP)) were produced by melt compounding and injection molding. Moreover, composites reinforced with short glass fibers (GF) and nanofillers were also produced. The main aims of this work was to :

- Explore how the presence of nanofillers with different physical and chemical characteristics (i.e. silica and xGnP) alters the crystallization behavior and polymorphism in PP and the correspondent impact on the mechanical properties.
- Understand the interfacial interactions occurring between filler and PP and their influence on the physical and macroscopic properties of the PP nanocomposites.
- Investigate the effect of matrix nanomodification (and/or nanofiller coating onto the fibers) on the fiber/matrix adhesion properties in PP/GF composites.
- Explore whether combining two fillers of rather different size scales (i.e. micro- and nano- scale) in PP matrix would give the desired physical and mechanical performance at low to intermediate filler loadings.

Several tools and characterization techniques were used in order to correlate the microstructure to the physical and mechanical properties of the materials :

- The isothermal and non-isothermal crystallization behavior of the nanocomposites was studied through in-situ crystallization studies using optical microscopy, modulated differential scanning calorimetry (DSC) and x-ray diffraction analyses.
- The mechanical properties (including tensile elastic modulus and strength) and thermo-mechanical properties such as glass transition temperature, storage and loss modulus, were investigated as a function of the filler type and content in order to study the interfacial interactions occurring between filler and matrix. In addition, scanning electron microscopy and atomic force microscopy were carried out to characterize the morphology and properties of the filler/matrix interphase.
- The viscoelastic behavior of the prepared nanocomposites was investigated adopting different techniques. In particular, rheological analyses enabled the characterization of the viscoelastic properties in the melt state (i.e. particle-particle and polymer-particle interactions) under different shearing conditions. Viscoelastic behavior in the solid state was also studied by quasi-static tensile tests, creep tests and dynamic mechanical tensile analyses. Special attention was placed on the effect of temperature and stress on the creep behavior.
- The fiber/matrix interfacial shear strength was evaluated by the single-fiber fragmentation tests on PP–GF microcomposites filled with various types and amounts of nanofillers. Contact angle measurements were performed in different liquids in order to determine the work of adhesion of PP with respect to glass.
- Morphological observations and various mechanical tests (including tensile tests, DMA analyses and Izod impact tests) were carried out in order to investigate how the morphology and the physical and mechanical properties of the composites were affected by the combined effect of two fillers in GF reinforced PP nanocomposites.
- A two-population model, based on the Halpin-Tsai and Tsai-Pagano composite theories, and accounting for changes in aspect ratio and orientation of the micro- and nano- filler was used to predict the elastic modulus of the hybrid composites.

Chapter II

Background

2.1 Polymer nanocomposites

Composite materials can be defined as materials containing at least two constituents that can be physically or visibly distinguished. In particular, engineering composite materials represent a special class of composites that meet the three following criteria: (i) they contain two or more distinct constituents, (ii) they are synthesized in a way that the form, distribution and amount of constituents are controlled in a predetermined way and (iii) they have unique, useful and superior performances that can be predicted from the properties, amounts and arrangements of constituents using principles of mechanics [5]. Compared to conventional engineering materials, composites can be designed to exhibit exceptional high strength and stiffness with respect to their density (Figure II-1).

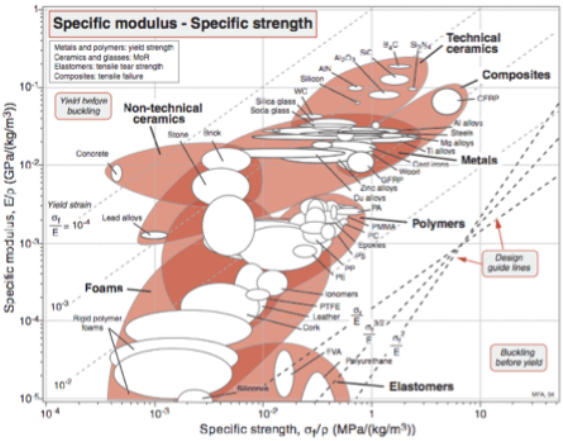

Figure II-1. Specific elastic modulus E/ρ plotted against specific strength σ_f/ρ (on log scales) [5].

The matrix is the continuous phase of the composite that holds the reinforcement in place. Polymeric matrices are among the most common matrices

used for the production of composites and are further subdivided in thermosets and thermoplastics. Both thermoplastics and thermosettings are particularly useful because they are relatively cheap and can be easily processed.

The reinforcement is a dimensionally controlled constituent with fixed geometry, that can either be in form of particles, fiber or flakes (or platelets) [6]. In many cases the reinforcements have unique properties that contribute significantly to the properties of the composite. Figure II-2 describes the effect of reinforcement shape and size on composite strengthening.

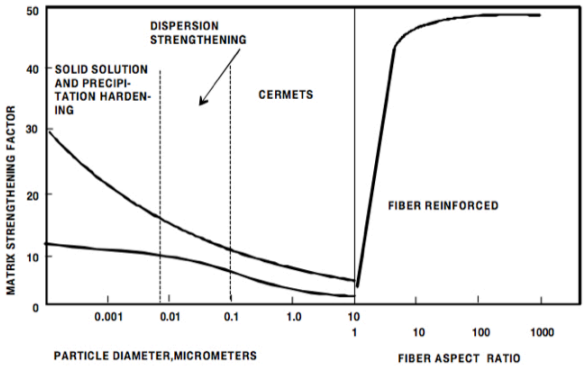

Figure II-2. The effect of reinforcement size and shape on strength [6].

The most common forms of reinforcement for polymer composites are fibers, as they can carry the majority of the load and contribute to most of the stiffness in polymer composites (since the matrix stiffness is usually only a very small fraction, i.e. 1/10 to 1/100 of the reinforcement stiffness). In particular, glass fibers (GF) are most extensively used as reinforcements for polymer matrix composites due to their combination of low cost, high strength and relatively low density.

When taking into account *fiber-reinforced composites*, polymeric matrices generally contribute very little to strength and stiffness. The main functions of the matrix include: holding the fibers in place, protecting the fibers by reaction with the environment, transmitting loads to fibers and protecting the fibers from mechanical abrasion.

On the other hand, in the recent years, scientific and technological progress led to the development of two different types of *particulate polymer composites*, distinguished by the characteristic size and shape of the filler particles:

- traditional *micro-composites* that contain micrometer-scale fillers (carbon black, kaolin and clay, metal oxides microparticles, etc.)
- *nanocomposites* that contain nanometer-scale fillers, i.e. fillers that have at least a characteristic dimension under 100 nm

Thanks to their extremely high aspect ratio, tensile strength and potential functional properties, nanofillers may be preferred over traditional microfillers for the production of polymer composites. In particular, the current literature shows evidence that the addition of small amounts of nanofiller (up to 5 wt%) to polymers can improve their mechanical behavior, thermal degradation, gas and solvents barrier properties and chemical resistance, avoiding drawbacks such as embrittlement and loss of transparency usually occurring in traditional microcomposites [7].

2.1.1 Micro- and nano- fillers

In general, for particles and fibers the surface area per unit volume is inversely proportional to the material's diameter. Common particle geometries and their respective surface area-to-volume ratios are shown in Figure II-3. For the fibers and the layered materials the ratio surface area/volume is dominated by the first term in the equation because the second term (that depends on the length) has a very small influence compared to the first one. Therefore a change in particle diameter, fibrous diameter or layer thickness from the micro to the nanometer range, will bias the surface area to volume by three orders of magnitude.

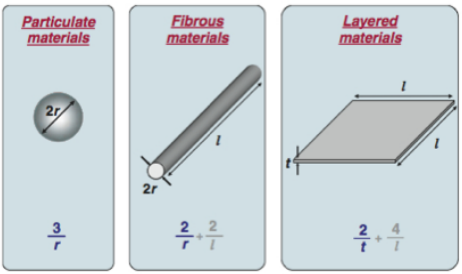

Figure II-3. Common particle geometries and their respective surface area-to-volume ratios [8].

Although nanofillers are used at significantly lower volume fractions, the total surface present in a composite is still much higher than that of most conventional fillers. For instance, the silica nanofiller added at 5 wt% would contribute about 1250 m^2 of surface to 100 g of composite, compared to about 200 mm^2 for fine $CaCO_3$ microparticles used at 40 wt%.

The nanofillers are generally classified depending on the number of dimensions in the nanometer size (Figure II-4):

- one nanodimensional fillers (1-D), i.e. *plate-like materials* such as layered silicates and graphite nanoplatelets

- two nanodimensional fillers (2-D), i.e. *nanotubes* or *nanofibers* such as carbon nanotubes, carbon nanofibers, halloysite nanotubes, nanotubes of several oxides and organic nanotubes

- three nanodimensional fillers (3-D), i.e. *particulate like-spherical materials* such as metal oxides (ZnO, Al_2O_3, $CaCO_3$, TiO_2, etc.), fumed metal oxides (SiO_2, TiO_2, etc.), silicon carbide (SiC), polyhedral oligomeric silsesquioxanes (POSS) and carbon black (CB)

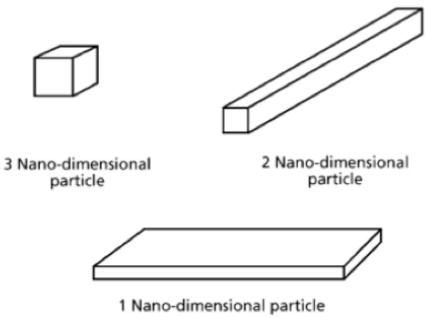

Figure II-4. Three basic geometries of nanofillers [9].

The filler dispersion and its adhesion at the matrix play a dominant role in determining the mechanical properties of nanocomposites. In fact, an homogeneous dispersion of the nanofiller can assure improved mechanical properties over those of the conventional composite, while a bad dispersion can even degrade these properties (Table II-1).

Table II-1. Effect of nanoparticles introduction in polymeric matrices [9].

Improved properties	Disadvantages
■ Mechanical properties (tensile strength, stiffness, toughness)	■ Viscosity increase (limits processability)
■ Gas barrier	■ Dispersion difficulties
■ Synergistic flame retardant additive	■ Optical issues
■ Dimensional stability	■ Sedimentation
■ Thermal expansion	■ Black color when different carbon containing nanoparticles are used
■ Thermal conductivity	
■ Ablation resistance	
■ Chemical resistance	
■ Reinforcement	

In particular, the extremely small size of nanometric fillers leads to a dramatic increase in interfacial area as compared to traditional composites. This interfacial area creates a significant volume fraction of polymer at the interface with properties different from the bulk polymer even at low loadings [1]. Interfacial properties can play a significant role on the properties of the overall composite.

By taking advantage of this large interfacial area and interfacial volume (Figure II-5), unique combinations of properties have been achieved, such as thermal and electrical conductivity [10, 11].

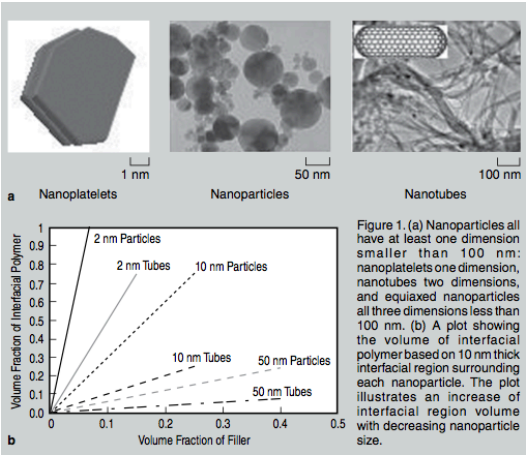

Figure II-5. Volume of interface in polymer nanocomposites as a function of the filler size [1].

On the other hand, since the properties and structure of this interfacial region are not yet known quantitatively, the control and prediction of properties of polymer

nanocomposites remains a challenge. In order to exploit all the advantages offered from polymer nanocomposites, the key factor is controlling the nanoparticles dispersion degree, in such a way that the nanofiller results homogeneously distributed and dispersed within the polymeric matrix. Figure II-6 shows examples of the different dispersion and distribution conditions that can be eventually reached [9]. For instance, the optimum mechanical properties of the resulting nanocomposite are obtained when a layered silicate is fully exfoliated, with polymer intercalated into the silicate galleries.

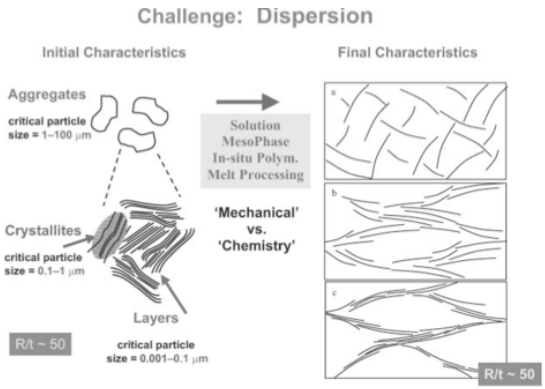

Figure II-6. Dispersion of layered silicates using different processing methods [9].

In order to obtain a high dispersion degree and good interfacial interaction, different techniques can be used to prepared polymer nanocomposites [9]:

- *Solution process*: the nanofiller is firstly dispersed using a solvent in which the polymer is soluble. After obtaining a homogeneous solution of well dispersed nanoparticles, the solvent is removed through evaporation. For instance, it is well known that layered silicates, due to the weak forces that stack the layers together, can be easily dispersed in an adequate solvent. The polymer then absorbs onto the delaminated sheets, and when evaporated, the sheet reassembles, sandwiching the polymer to form an ordered, multilayered structure

- *Melt compounding*: the filler is mixed with the solid polymer matrix in the molten state. Under these conditions, and if the filler surfaces are sufficiently compatible with the selected polymer, the polymer can be pinned onto the filler surface, or be inserted into the interlayer space in

case of layered fillers. Traditional techniques, such as melt mixing using a twin-screw extruder or injection molding, can be employed in this case. No solvent is required

- *In-situ polymerization*: The nanofiller is firstly dispersed in the monomer and the polymerization of the matrix is activated and completed by adding a crosslinking agent and heating the reactive system

- *Shear mixing*: Low-shear mixing or high-shear mixing can be used for incorporating solid nanoparticles into a liquid polymer. Under these conditions and if the nanoparticles are compatible with the selected polymer, the mixing will disrupt the nanoparticle aggregates and disperse the polymer matrix into the nanoparticle layers or onto the nanoparticle surfaces.

The dispersion degree of the nanofiller can be generally improved by (i) using surface-treated filler to reduce aggregation phenomena and (ii) incorporating a compatibilizer within the polymer matrix (such as maleic anhydride grafted polypropylene) in order to improve filler dispersion and enhance the filler/matrix interaction. The main advantages given when using nanocomposites are related to a significant improvement of the thermo-mechanical properties, to an increase of the dimensional stability and better thermal degradation resistance, without compromising optical clarity and density with respect to the pristine matrix [8].

On the other hand, one of the major problems with nanoparticles reinforcement is that it might cause severe material embitterment when incorporating a nanofiller loading needed to get optimum stiffness and strength properties. Blending the thermoplastic with elastomeric modifiers has been found to be a successful way to overcome this problem and to improve the toughness characteristics [12]. In additional, few research studies addressed the property improvements of polymers by adding carbon nanofibers (CNFs) and nanotubes (CNTs), showing improvements in strength and stiffness with loss of elongation at break [13]. However, there have been a number of experimental studies reported in the literature about the influence of CNT/CNF on the toughness enhancements of various types of polymers [14]. The increased ductility in thermoplastics such as PE was attributed to the chain mobility enhancement, in particular due to the secondary crystal formation promoted the presence of MWCNT.

Recent studies have shown that the addition of nanoparticles can improve the fatigue behavior of polymer composites, without sacrificing the stiffness [15]. It is believed that the mechanisms involved in the enhanced fatigue resistance in

nanocomposites include cracking pinning, crack tip deflection, crack bridging and particle debonding.

Since the interfacial region in nanocomposites is extremely large, the interaction of the polymer with the nanoparticles gives significant opportunity for changing the polymer mobility and relaxation dynamics. Dynamic mechanical analyses (DMA) tests performed over a wide temperature range are very sensitive to the physical and chemical structure of polymers and composites. They allow the study of glass transitions or secondary transitions and yield information about the morphology of polymers. Some studies showed how the incorporation of rigid micro- and nano-fillers in thermoplastics results in a remarkable increase in the storage and loss modulus. Moreover, at elevated temperatures, in the rubbery plateau well above the glass transition temperature (T_g), the nanocomposites retain higher modulus and damping than the neat polymer, which probably indicates a decreased chain mobility due to nanomodification [16]. The current literature widely reports that with rising filler content, the T_g of nanocomposites increases, while the damping peak decreases. The increase in T_g may be attributed to a loss in the flexibility of the polymeric chains resulting from the nanoparticle/matrix interfacial interactions. Impeded chain flexibility is possible if the nanoparticles are well dispersed in the matrix. Therefore, strong adhesion between nanoparticles and surrounding polymer matrix additionally enhances the dynamic modulus and T_g, by further reducing molecular flexibility.

Incorporation of nanofillers in thermoplastics is generally associated to a marked increase in the melt viscosity, at least in the range of low frequencies. Furthermore, a significant enhancement in the dynamic shear storage modulus *(G')*, ascribed to a pseudo solid-like transition caused by the dispersed nanoparticles, is generally observed [17]. However, a decrease in both viscosity and *G'* was found for some thermoplastic nanocomposites such as linear low-density polyethylene (LLDPE) modified with boehmite alumina (BA). This decrease was attributed to the beneficial effect of BA particles that fill in the spaces between chain branches, favor their disentanglement and enable an easier and more uniformly flow [18].

Nanofillers are frequently added to polymers in order to achieve functional properties not possessed by the matrix polymer itself. The most relevant of such additives are flame retardants and conductive fillers [19]. These modifiers are added in order to achieve the desired goal (i.e. to prepare composites with a given functional property), and maintaining acceptable mechanical and aesthetic characteristics at the same time. For instance, it has been reported that by adding inorganic fillers [20], may increase the thermal stability of thermoplastics. In particular, both onset and maximum degradation temperature remarkably increased when inorganic particles were incorporated in LLDPE, PE and PA [21-23], showing a significant retardation of the thermal degradation. Two factors are considered

responsible for improving the thermal stability in thermoplastic nanocomposites with respect to the neat matrix: (i) the chemical structure of the nanocomposites is different from that of the pristine polymer; (ii) the thermal motion of the polymer molecules is restricted by the filler nanoparticles.

Another interesting feature offered by polymer nanocomposites is the improvement of the dimension stability, which is critical in many applications. Nanocomposites provide methods for improving both thermal and environmental dimensional stability. The composite coefficient of thermal stability (CTE) decreases due to the presence of the nanofiller [24]. Moreover, when considering nanocomposites, the lowering of CTE is not generally approaching linearity, as it occurs for traditional low-filled microcomposites. The deviation from linearity is mainly attributed to the dominant role played by the wide interfacial region.

Other interesting functional properties can be exploited in polymer matrices thanks to the unique physical properties, such as high thermal or electrical conductivity, of the constituents. Electrically conductive polymer composites, for example, are used in anti-static packaging applications, as well as in specialized components in the electronics, automotive, and aerospace sector. Common conductive fillers are metallic or graphitic particles in any shape and size. The use of CNTs and xGnP as an electrically and thermally conductive filler in thermoplastics is one of the biggest current application, and is widespread across the automotive and electronic sectors [25, 26].

A limitation in the development of transparent nanocomposites with improved mechanical or electrical performance is the light scattering due to the presence of the particles. In general, to minimize scattering, the particles must be as small as possible with an index of refraction as close as possible to that of the matrix material. Relatively good optical clarity has been obtained in many nanocomposites, particularly at low volume fractions. For example, PMMA modified with bentonite up to 10 wt% shown to maintain relatively good optical clarity. Furthermore, nanomodification of polymeric matrices can also alter the original refractive index of the material [27].

The extraordinary barrier properties of some polymer nanocomposites, such ad layered silicate nanocomposites, open new frontiers for their application as surface protective layers. In particular, the recent development of organic coatings, with a surface resistance better than standard coatings, promoted the research for improving the water, solvent and corrosion resistance of polymer by incorporating nanofillers, without significant changes of their optical properties and processability. Improved barrier properties were observed in thermoplastics incorporating clay [8], xGnP [2] and halloysite nanotubes [28].

The incorporation of nanofillers may also induce significant improvements in abrasion resistance. As an example, incorporation of only 3 wt% of $CaCO_3$ in PMMA led to a significant improvement of the abrasion resistance of the material [29]. Moreover, nanoparticles can simultaneously improve wear resistance and decrease the coefficient of friction [30].

Modification of thermoplastic polymers can significantly affect many other chemical and physical properties. These modifications might result in a potential use of the material in several technological applications.

2.1.2 Types of nanofillers

2.1.2.1 Layered nanofillers

Layered crystals nanomaterials are characterized by only one dimension in the nanometer range. The typical structure of layered nanofillers is represented by sheets of few nanometers thick and hundred to thousand nanometers long. Polymer nanocomposites are obtained by exfoliation of the layered nanofillers and concurrent intercalation of the polymeric chains within the crystal galleries.

Although many crystalline fillers are commercially available and are able to be dispersed, exfoliated and host the polymer in the crystalline galleries during production, two main types of nanoplatelet particle fillers have been widely investigated: silicate clay minerals and graphite.

The clay mineral is usually of a layered type and a fraction of hydrous, magnesium, or aluminum silicates. Every clay mineral contains two types of sheets, tetrahedral *(T)* and octahedral *(O)* [31], as schematically represented in Figure II-7. The most commonly used layered silicates for the preparation of nanocomposites are hectorite, saponite, and montmorillonite (MMT). In particular, MMT is the widest used in polymer because of their high surface area, and surface reactivity [8]. The aspect ratio is in the range 10–1000, while the surface area is around 750 m^2/g. However, the aspect ratio of 1000 is only achievable when a clay platelet is well dispersed into the polymeric matrix without breaking, but practically, the breaking up of clay platelets during mixing process at high shear rates results in an aspect ratio of 30–300.

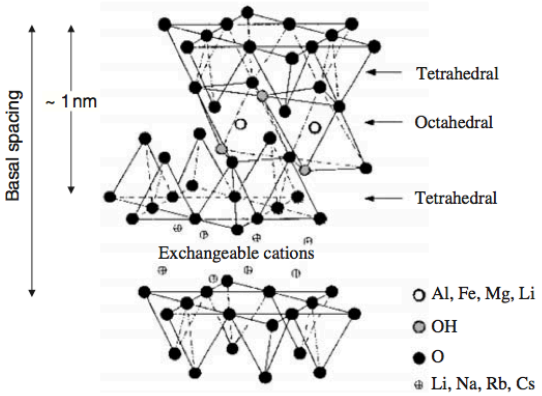

Figure II-7. Typical structures of 2 : 1 clay minerals [8].

Depending on the nature of the layered silicate and the polymer matrix, three main types of composites may be obtained, as represented in Figure II-8. In particular, when the silicate layers are well exfoliated and uniformly dispersed in a continuous polymer matrix, an *exfoliated* or *delaminated* structure can be obtained. However, due to difficulties in the processing of the materials, the most commonly observed microstructures are the *intercalated* and the *phase-separated*. While the *intercalated* structure is characterized by very few extended polymer chains intercalated between the layers resulting in a quite ordered and homogeneous morphology, the *phase-separated* microstructure is obtained when diffuse between the silicate layers.

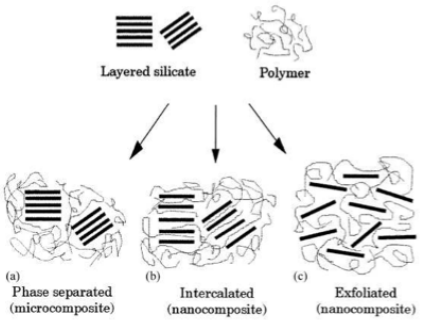

Figure II-8. Different microstructures obtained in layered silicate nanocompsites.

Nanoclay has been used as filler in polymeric systems since the early 1990s, when Toyota researchers reported that the mechanical properties of PA showed significant improvement at a loading of only 4.2 wt% clay, the modulus doubled, and the increase in strength was more than 50%. In recent years, organoclay has been used in various polymer systems including epoxy, polyurethanes, vinyl ester, etc. [32-34], in order to investigate not only the thermo-mechanical properties, but also the ballistic and fire-retardant performances for aerospace and automotive structures. Moreover, nanoclay was used in fiber reinforced polymer composites in order to further enhance the mechanical, interfacial and interlaminar properties. Roy and Hussain [35] manufactured PP clay nanocomposites reinforced with E-glass fibers using prepreg tape. They achieved significant improvements in compressive strength and modulus.

Graphite shows a similar geometry with nanoclay (i.e. layered structure). Natural graphite flakes (NGF) are commonly intercalated with chemical compounds and exfoliation is achieved by applying rapid heating up to 950-1200 °C. The original graphite flakes with a thickness of 0.4–60 μm may expand up to 2–20,000 μm in length [36]. These layers get separated down to 1 nm thickness, forming a high aspect ratio (200–1500) graphite nanosheets with high modulus (~ 1 TPa). Graphite nanosheets, when properly dispersed in a polymeric matrix, result in a dramatic improvement of both the physical and mechanical properties of the resultant nanocomposite. Moreover, one of the advantages given from the use of expanded graphite flakes is that electrical and thermal conductivity can be induced in the final material, which are absent in nanoclay materials [26]. Noteworthy, incorporation of a very small amount of exfoliated graphite (typically < 5 wt%) can produce a sharp transition of the polymer (either thermoplastic or thermosetting) from an electrical insulator to a non-perfectly conductive material. Fukushima and Drzal [37] observed better flexural and tensile properties of epoxy matrices and PP when chemically functionalized graphite nanoplatelets were added to the matrix. In addition, lower CTE and electrical resistivity were achieved compared to other carbon fillers such as carbon black and carbon nanofibers. The functional properties induced by graphite nanoplatelets, combined with the low cost, make it a very promising filler in the field of thermal conductors, super capacitors and electromagnetic interference shields.

Investigation of polymers modified with layered nanofillers is usually carried out by two complementary techniques: x-ray diffraction (XRD) is employed to identify intercalated structures, while transmission electronic spectroscopy (TEM) is used to characterize the nanocomposite morphology. The XRD diffractograms and corresponding TEM micrographs are reported in Figure II-9 for nanocomposites

presenting different microstructure. Since the multilayer structure is maintained in the composite, the interlayer spacing can be determined, allowing for the determination of the degree of exfoliation or intercalation. Intercalation results in increased interlayer spacing, leading towards lower 2θ angles.

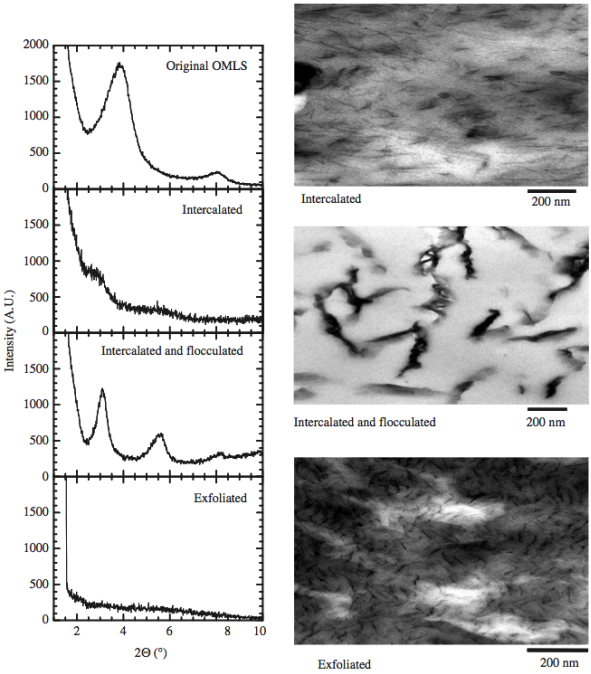

Figure II-9. WAXD patterns and TEM images of three different types of nanocomposites [8].

2.1.2.2 Nanotubes and nanofiber fillers

When taking into account 2-D nanomaterials, carbon nanotubes (CNTs) and carbon nanofibers (CNFs) represent the most relevant fillers. In particular, since their first discovery in 1991 by Iijima [38], CNTs have been widely investigated as potential filers for polymeric materials, because of their peculiar physical, mechanical and electrical properties. However, other kinds of nanotubes, such as halloysite nanotubes and hexagonal boron/nitrogen nanotubes are becoming progressively object of research in the filed of polymer nanocomposites.

CNTs have typical diameters in the range of ~1–50 nm and lengths of many microns. They typically consist of one or more concentric graphitic cylinders (i.e. single-wall and multi-wall CNTs). On the other hand, much larger dimensions are shown by commercial carbon fibers (PAN are typically in the 7–20 μm diameter range, while vapor-grown carbon fibers (VGCFs) have intermediate diameters ranging from a few hundred nanometers up to around a millimeter), as represented in Figure II-10.

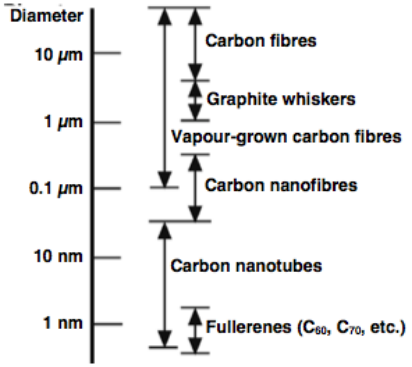

Figure II-10. Comparison of diameters of various fibrous carbon-based materials [39].

Carbon nanofibers (CNFs) differ from nanotubes by the orientation of the graphene planes: while the graphitic layers are parallel to the axis in nanotubes, nanofibers can manifest a wide range of orientations of the graphitic layers, such as stacked graphitic discs or (truncated) cones. However, CNFs can be in the form of hollow tubes with an outer diameter ranging from 5 to 100 nm. Representative TEM micrographs of commercially available nanofibers showing an outer diameter of around 150 nm are represented in Figure II-11.

A variety of methods are currently available to synthesize CNTs and CNFs, providing different diameter, aspect ratio, crystallinity, crystalline orientation, purity, and surface chemistry. However, it is not yet clear which type of nanotube material is most suitable for polymer composite applications, and the selection depends on the matrix type, processing technology, and the property enhancement required. In particular, both MWCNTs and SWCNTs can be produced by two main processing techniques: high-temperature evaporation using arc-discharge or laser ablation [40], and various chemical vapor deposition (CVD) or catalytic growth processes [41].

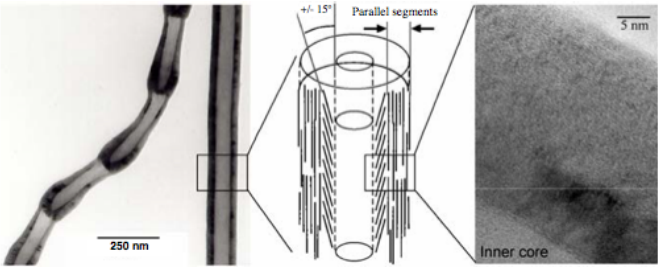

Figure II-11. Representative TEM micrographs of commercial carbon nanofibers, highlighting structural variations both in overall morphology and in the orientation of the graphitic planes [39].

While in the high-temperature methods MWCNTs can be obtained from the evaporation of pure carbon, the synthesis of SWCNTs requires the presence of a catalyst. On the other hand, the CVD method requires a catalyst for obtaining CNTs and also allows the production of CNFs.

Polymer composites based on CNTs or CNFs are usually produced following three general processing techniques: (i) mixing in the liquid/molten state, (ii) solution-mediated processes and (iii) in-situ polymerization techniques. The direct melt-blending method is more commercially used than the latter two methods, as both solvent processing and in-situ polymerization are less versatile and more environmentally invasive. Approaches to the manufacture of CNTs/CNFs thermoplastic composites are typically represented by extrusion and injection-molding because of economical reasons, but are often inapplicable due to limited filler loading. For instance, the extensional rheology of PEEK/CNF blends have been measured as a function of filler amount, showing a stabilization or even reduced viscosity at high shear rates that allows an easier production of PEEK blends (Figure II-12).

Current scientific research is still widely investigating polymer composites modified with CNTs and CNFs, in particular their structure (i.e. on filler dispersion, distribution, alignment and interface with the polymer matrix) and the impact of nanomodification on their mechanical and physical properties (i.e. stiffness, strength, toughness, etc.). Incorporation of both fillers generally leads a significant increase in stiffness with the filler content, while the enhancements of the other mechanical properties, such as yield stress, strength, and toughness, generally appear more difficult to achieve. For example, the impact properties of PC/CNFs composites were significantly decreased, even at low filler amounts, probably due to chemical stress cracking of the polycarbonate activated by the aromatic hydrocarbons present on the nanofiber surface [42].

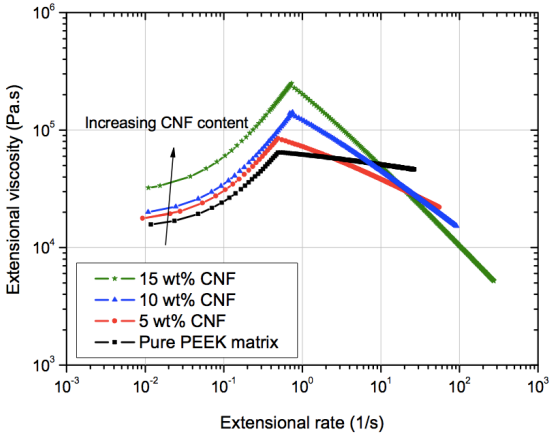

Figure II-12. Elongational viscosity of a PEEK/CNFs composites at 360 °C as a function of the strain rate, with increasing CNFs content [39].

Several studies have shown a significant influence of CNTs and CNFs on the resulting morphology of a semicrystalline matrix. Specifically, degree of crystallinity, crystalline forms and crystal orientation of a semicrystalline polymer are dependent not only on the manufacturing process employed and thermal history, but also on the presence of possible nucleation sites, which can be greatly promoted by nanomodification [43]. Both MWCNTs and SWCNTs were found to change the crystallization rate and the resulting crystal structure in different semicrystalline polymers [44, 45].

Considerable research efforts have been done for the investigation on the functional properties exhibited by nanocomposites based on CNTs and CNFs, such as electrical and thermal conductivity. Several applications in the field of electronics, automotive, as well as aerospace sector, require electrically conductive polymer composites. Although the most common conductive fillers are metallic or graphitic particles because of their relatively low price, the incorporation of CNTs allows for a generally lower percolation threshold (Figure II-13) and good mechanical properties. Such combination of mechanical and functional properties is difficultly achievable when using any other filler. The electrical percolation threshold of polyvinyl alcohol (PVA) and polymethyl-methacrylate (PMMA) modified with MWCNTs has been reported as low as 0.06 wt% and 0.5 wt%, respectively [46, 47].

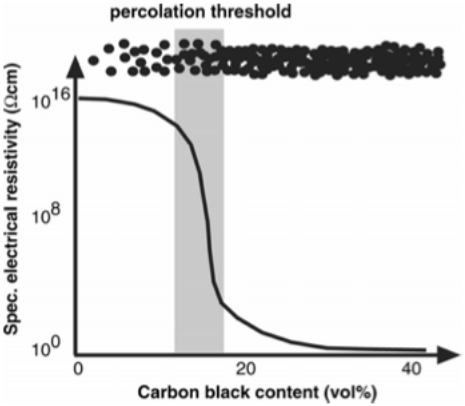

Figure II-13. Trend of the electrical resistivity in a polymer composite modified with carbon black, as a function of the filler loading [39].

CNTs and CNFs can also be successfully used as additives for tribological applications. In particular, they can significantly reduce the wear rate of polymers [48].

Although less common as nanofillers in polymer nanocomposites, other types of nanotubes are commercially available. In particular, many layered materials such as dichalcogenides (MoS_2, WS_2, etc.) and organic materials can be fabricated into nanotubes, but very little research has been carried out for the improvement of techniques to obtain them. Therefore, few studies report the investigation of the mechanical and functional properties in composites containing these nanotubes.

On the other hand, hexagonal boron/nitrogen (BN) nanotubes and halloysite nanotubes (HNTs) are progressively becoming subject of new research. In particular, BN nanotubes exhibit modulus and strength comparable to those of CNTs, but they show lower electrical conductivity and better oxidation resistance [49].

Moreover, various features of HNTs like rigidity, high aspect ratio and low density of surface hydroxyl groups compared with other silicates, make it a promising reinforcing filler for polymer materials [50]. Its abundant availability, biocompatibility and low price promoted HNTs as subject of recent research.

2.1.2.3 Equiaxic nanoparticles

Although nanoparticles have been commercially available for more than a century, only in the last decades many research efforts have been done towards

significant developments in this field. The main research focuses are (i) the production of nanoparticles with controlled size, structure and degree of aggregation and (ii) study of surface functionalization in order to improve the particles dispersion and adhesion with the matrix. The most common equiaxic nanofillers are carbon blacks (CB) and fumed metal oxides nanoparticles (silicon dioxide, nanosilica, nanoaluminum oxide, nanotitanium oxide). Equiaxic nanoparticles are typically obtained by pyrolysis, gas condensation or by grinding performed in a ball mill or a planetary ball mill.

2.1.2.3.1 Carbon black (CB) nanoparticles

CB is virtually a pure elemental carbon in the form of colloidal particles that are produced by incomplete combustion or thermal decomposition of gaseous or liquid hydrocarbons under controlled conditions. The primary particles of CB are arranged in blocks of graphene layers with reduced dimensions and organized with a turbostratic structure in order to form spherical particles with diameter from 10 to 100 nm. Primary particles usually fuse into aggregates during the production process and can form bigger structures called agglomerates (i.e. complex of aggregates stuck together by strong Van der Waals forces), as schematically represented in Figure II-14.

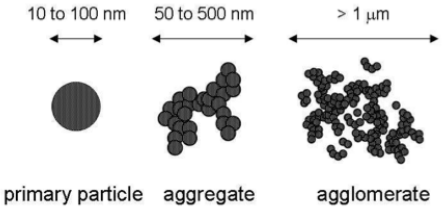

Figure II-14. Primary particles of CB bonded together to from aggregates and agglomerates.

Significant effects of the different grades of CB result from variations in the specific surface and/or structure of the primary aggregates. The specific surface depends mainly on the size of the primary particles (ranging from 10 m^2/g to more than 1500 m^2/g), while the structure of the primary aggregates is related to the amount of void volume (from 30 $cm^3/100g$ to 330 $cm^3/100g$). The characteristic shape of carbon black aggregates is illustrated in Figure II-15.

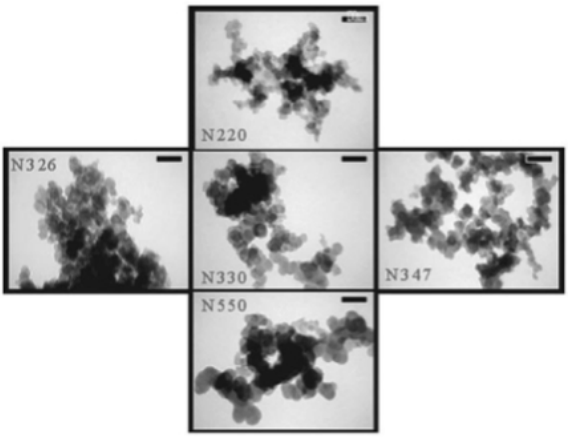

Figure II-15. TEM images of five different grades of CB. The specific surface increases from top to bottom, while the structure increases from left to right (bar length: 100 nm) [51].

The particle size can be measured by transmission electron microscope (TEM) measurements, while the specific surface area (SSA) can be determined by nitrogen adsorption measurements using the Brunauer-Emmet-Teller procedure (ASTM D 6556). Moreover, the structure of CB is typically evaluated by oil adsorption number (OAN) technique, which indicates the amount of oil that can be absorbed onto the CB surfaces in order to reach a critical viscosity (ASTM D 2414). Therefore, the higher the OAN, the higher the structure. Other characteristics of CBs are commonly represented by the porosity and the functional groups present on the surfaces (such as carbon-oxygen, carbon-hydrogen surface groups, carbon-nitrogen moieties, and carbon-halogen surface compounds). On the other hand, the characterization of the physical properties is very complicated for this type of nanoparticle. Since none dimension is prevalent, the measurement operations are often impossible to carry out with sufficient reliability. Thus the values of stiffness, tensile strength, electrical resistivity, thermal conductivity and coefficient of thermal expansion are still unknown.

More than 90% of the carbon black produced is used as a filler [52]. In elastomers (including tires), CB is added at relatively high filler loadings in order to improve many properties of the composite, especially stiffness, tensile strength, tear strength, abrasion resistance and dynamic properties. CB is also widely used in thermoplastics and thermosettings, at low to intermediate amounts, to enhance the

thermo-mechanical properties and/or induce electrical conductivity [53, 54]. Other commonly applications of CB are printing inks and coatings.

2.1.2.3.2 Fumed metal oxides nanoparticles

Metal oxides nanoparticles are commonly obtained by condensation from a gas phase using aerosol processes such as hydrolysis [12]. During the process, a vapor precursor (such as silicon tetrachloride when silica is produced) reacts with hydrogen and oxygen mixture at high temperatures in order to produce the metal oxide (Figure II-16).

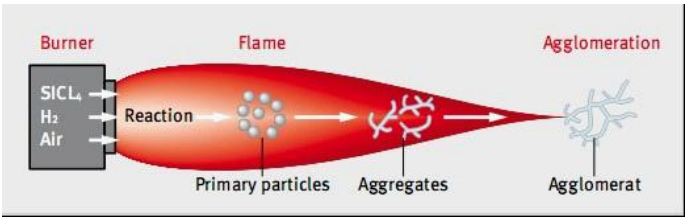

Figure II-16. Schematic of the production process of fumed silica.

The structure of the particles (i.e. primary particles size and the structure degree) is controlled by the time and temperature of the reaction. In general, the lower the temperature, the higher the surface area of the particles because coalescence is slow compared to the collision dynamics of the particles and structure with higher degrees are generated [55]. Metal oxides such as silica, alumina, titania and zirconia are all produced by aerosol. In particular, silica primary particles with dimensions ranging from 7 to 27 nm and surface area from 100 to 380 m^2/g can be produced in commercial quantities. Figure II-17 shows a representative example of fumed silica nanoparticles with surface area of 124 m^2/g.

Nananoparticles can be surface treated with chemical compounds in order to attach specific functionalities that can alter the properties of the nanofiller. For instance, fumed silica nanoparticles are commonly surface treated using small ions in simple salts or silanol groups which improve the rheological and thixotropic behavior of coatings and paints. One of the most common applications of surface

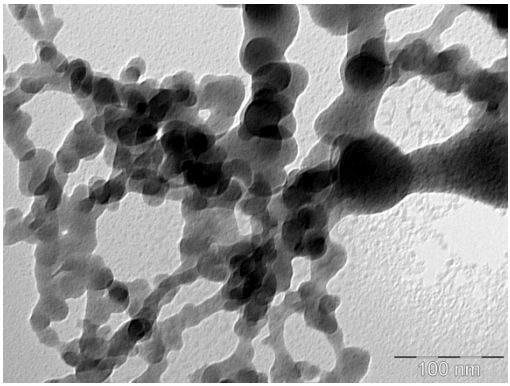

Figure II-17. Structure of fumes silica Aerosil® R974 (surface area of 124 m^2/g) as represented by TEM.

functionalization applied on silica particles is to decrease the surface forces which arise among nanoparticles. These interactions are mainly responsible for promoting the formation of aggregates and agglomerates, resulting in higher viscosity of the coating or paint. Therefore, hydrophilic (untreated) nanoparticles tend to aggregate and agglomerate due to the hydrogen bonds established between silanol groups of adjacent particles. On the other hand, hydrophobic particles (surface-treated) manifest not only hydrogen bonds, but also hydrophobic interactions due to the present of additional functional groups (Figure II-18).

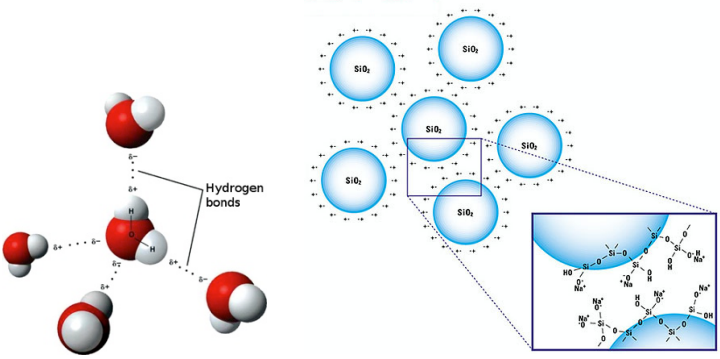

Figure II-18. (a) Interactions among untreated silica nanoparticles due to hydrogen bonds and (b) stabilization of silica particles through cations such as Na^+, K^+, NH_4^+.

In other cases, the chemical modification of nanoparticles creates an organic coating layer onto the particle surface which increases the interphase thickness when the particle is incorporated within a polymeric matrix. For instance, the hydrophilic–hydrophobic repulsive interactions existing between PP and untreated SiO_2 nanoparticles result in the formation of an interphase (Figure II-19). However, after a surface modification of silica particles with alkyl chains, the interactions are stretched far away from the particle surface, resulting in a thicker interphase. Some studies on the particle-matrix interphase behavior suggest that thicker interphase can lead to increased tensile yield strength and strain compared to using untreated particles [56].

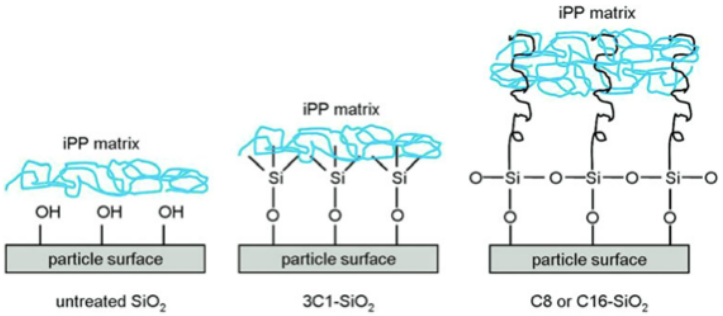

Figure II-19. Schematic representation of the interphase in PP / SiO_2 composites [56].

Fumed metal oxides are commonly incorporated in elastomers at medium and high loadings to enhance elasticity and mechanical properties such as stiffness, strength and toughness. Moreover, nanomodification of thermoplastics using metal oxides nanoparticles has been widely investigated, showing considerable improvements in the physical and mechanical properties at low filler contents. Moreover, the reinforcing effect has been observed to depend on the specific surface area of the nanoparticles [57, 58]. In particular, the higher the surface area, the greater the number of interactions with the polymeric chains, resulting in a stronger reinforcing effect. Tensile properties at yield and at break were found to increase with the surface area of fumed silica used to nanomodify LLDPE. Moreover, the presence of organosilane on the surface of the nanoparticles was also observed to be beneficial to the tensile, viscoelastic and toughness properties of the resultant composites.

2.1.2.3.3 Other types of equiaxic nanoparticles

There have been a recent development of newer techniques for the production of equiaxic nanoparticles and several alternatives to the aerosol process are currently available. In particular, gas condensation method performed in an oxygen atmosphere or inert gas and laser ablation, where nanoparticles are formed by supplying an inert or reactive gas to the reactive target material. Other methods are includes chemical vapor condensation, spray pyrolysis, electrospray, and plasma spray.

Among the most commonly used equiaxic nanoparticles, aluminum Oxide C, titanium dioxide and zirconium oxide represent very promising alternatives, showing relatively large surface area but higher density when compared to silica AEROSIL® 200 (Figure II-20). In particular, aluminum Oxide C has proven to be effective in controlling the rheological and thixotropic behavior of polar liquids and has been widely applied in applications including ink-jet papers, cable insulation, high voltage insulators and transparent coatings.

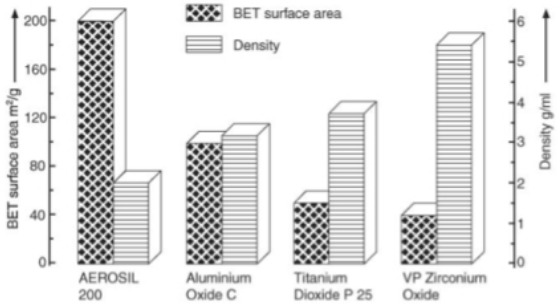

Figure II-20. Comparison of BET surface areas and densities of silica AEROSIL® 200, Al_2O_3 C, TiO_2 P25 and ZrO VP [9].

2.1.2.4 Polyhedral oligomeric silsesquioxanes (POSS)

A departure from the use of natural occurring clays and the synthesized carbon fillers is the employment of inorganic-organic nanostructured materials. The basic approach to developing better materials is to create inorganic-organic composite materials, in which inorganic building blocks are incorporated into organic polymers. In this context, polyhedral oligomeric silsesquioxane (POSS) nanostructured

materials represent a very recent and promising family of fillers. Owing to their peculiar chemical and physical nature, POSS can be used as multifunctional additives for polymer, acting as molecular level reinforcements, processing aids, and flame retardants [59].

POSS were firstly synthesized in 1946 [60] by condensation of different organosilicon monomers such as $RSiCl_3$, $RSi(OMe)_3$. POSS are typically characterized by a Si – O cage-structure and different organic functional groups can be attached to the Si atoms (Figure II-21), enabling the possibility to be linked to a wide variety of polymeric matrices.

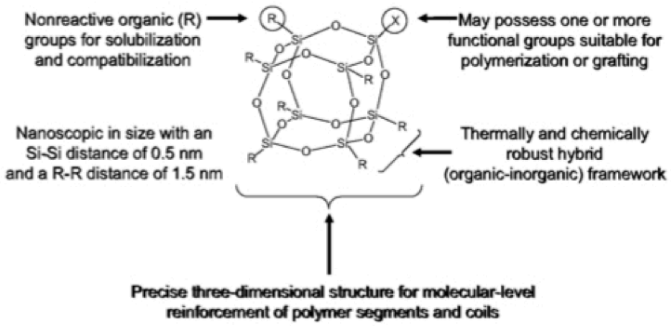

Figure II-21. Characteristic structure of the basic POSS molecule.

One of the peculiarities of POSS molecules, when compared to other nanofillers, is their significantly smaller size, which makes them equivalent to the typical size of most polymer segments and coils (Figure II-22).

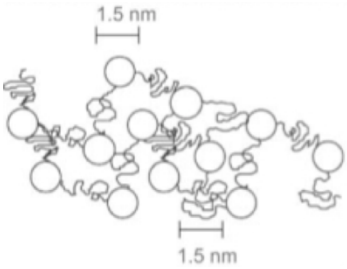

Figure II-22. Characteristic dimensions of the POSS molecules as compared to polymeric segments.

POSS molecules are not only smaller then silica primary particles, but they also exhibit reactive functionalities which are able, under appropriate conditions, to promote the polymerization or grafting of POSS monomers to polymeric chains. Therefore, a very broad choice of POSS monomers and polymers is currently available.

The key purpose of POSS technology is to create hybrid materials that are tough, light-weight, and as easy to process as polymers, yet with the characteristics of high temperature and oxidation resistance, like ceramics. In fact, POSS molecules are thermally and chemically more robust than silicones, and their nanostructured shape and size provide unique properties by controlling polymer chain motion at the molecular level. Likewise other technological nanofillers, POSS incorporation led to an improvement in stiffness and hardness in many polymer matrices, while maintaining values of toughness and strain at break comparable to those of unfilled resin [61]. Owing to their ability to control and limit the chain motion in most polymers, nanomodification via POSS has been shown to increase the glass transition temperature by more than 100 °C in some thermoplastics. Moreover, nanocomposites added with POSS (either thermoplastics and thermosettings) have shown noticeable improvements also in the fire resistance behavior, manifesting delayed combustion and reduced heat evolution. Additional features of this novel nanofiller family are mainly represented by the possibility of improving processability of materials and even changing the properties of existing patented compounds, enabling the patentability of the resultant materials. A general list of property enhancements via POSS incorporation is represented in Figure II-23.

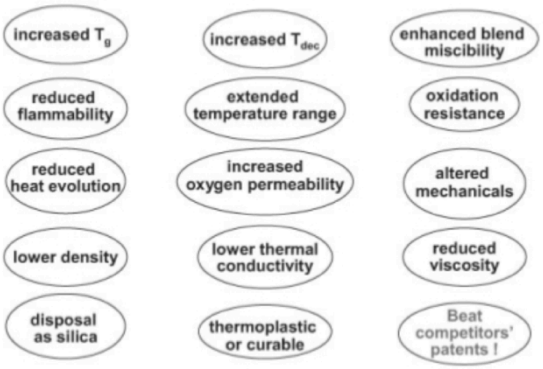

Figure II-23. Property enhancements of polymers by POSS incorporation [9].

2.2 Properties of polymer nanocomposites

2.2.1 Crystallization behavior

2.2.1.1 Polymorphism in semicrystalline polymers

One of the peculiarities of nanocomposites, when compared to micro-filled composites, is that by taking advantage of the large interfacial area and interfacial volume, unique combinations of properties can be achieved. In particular, not only the physical and mechanical properties of common polymer matrices can be dramatically enhanced with the incorporation of small amounts of nanofillers, but also functional properties (such as electrical and thermal conductivity) can be induced. Several examples reported in the current literature show that the structure and properties of the interfacial region are not only different from the bulk, but are also critical to controlling properties of the overall nanocomposite [1]. In thermoplastics the *interfacial polymer* can exhibit changes in crystallinity, mobility chain conformation, molecular weight, chain entanglement density and even charge distribution [62, 63].

For instance, the nanomodification of semicrystalline polymers can produce significant changes in the degree of crystallinity, crystal phases, lamellar thickness and organization and even the spherulite structure (Figure II-24).

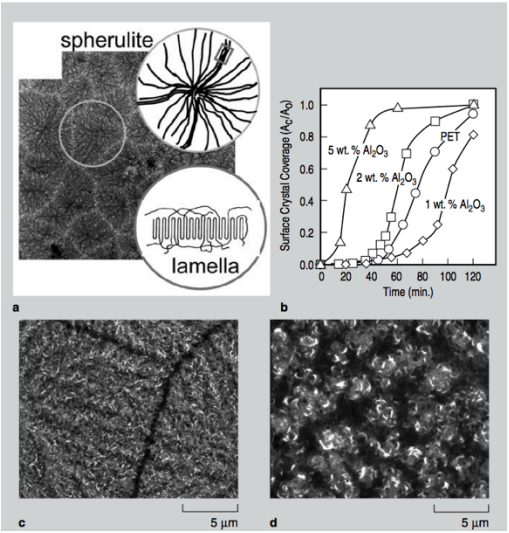

Figure II-24. Crystallization study on PET nanomodified with γ-phase alumina [1].

Moreover, this change is particularly important in polymer where the crystalline phase and spherulite structure significantly impact the physical, mechanical and tribological properties. Figure II-24 shows the main results of a study on the PET modified with γ-phase alumina, evidencing that filler loadings a slow as 1 wt% can influence the crystallization behavior, inhibiting nucleation and growth compared to the unfilled PET. However, when higher filler contents are added and agglomeration occurred, the filler acted as heterogeneous nucleating agent, increasing the nucleation and growth rates. Figures II-24 *c* and *d* show the tapping AFM performed on the unfilled and nanomodified PET (1 wt%), respectively, indicating that nanomodification led to the formation of smaller spherulites. Furthermore, the higher crystallization temperature achieved with filler incorporation (increase of 6 °C at 1 wt% filler) might dramatically decrease the tendency of PET fibers to fibrillate and fail in wear applications.

Other semicrystalline polymers such as PA 6, poly (vinylidene fluoride) (PVDF) and PP typically exhibit different crystalline phases. In particular, there are three crystalline phases of PA 6 (α, β and γ), five phases of PVDF (α, β, γ, δ and ε) and four polymorphs for isotactic PP including α (monoclinic), β (hexagonal), γ (triclinic) and δ (smectic) [64, 65]. The crystalline phases generally coexist in the semicrystalline polymer, and their amounts generally depend on the processing conditions [66].

2.2.1.2 Polymorphism in isotactic PP and relative nanocomposites

A particularly interesting case is represented by isotactic PP, widely investigated in the past and also more recently with the emergence of nanocomposites. Commercial isotactic PP crystallize predominantly into the α phase, with sporadic occurrence of the β phase at high undercooling (Figure II-25).

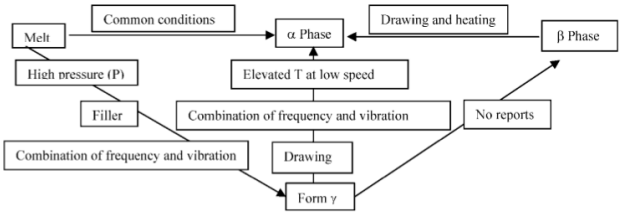

Figure II-25. Transitions among different crystalline phases in isotactic PP [66].

However, crystallization under the influence of temperature gradient, sheared or strained melt condition might favor the development of the β phase in commercial PP. It is also known that the γ phase of crystalline PP can be obtained in low molecular weight PP by slow cooling and from conventional PP by crystallization under high pressure. The γ phase crystalline PP is most thermodynamically stable, while the β phase is the least stable and tends to recrystallize to the α phase under proper conditions. In particular, when being subjected to external conditions such as heat or force.

Although the most significant and widely occurring crystal form in PP is the α-form, intensive investigation has been recently focused on the β-form because of its interesting physical and mechanical properties [67] including the higher impact strength and toughness of the β-form when compared to the α-form, attributed to the different lamellar morphology of β-PP [68]. On the other hand, the Young's modulus and yield strength of isotactic PP, as measured in quasi-static tensile tests, slightly decrease with the β-phase content [69]. The presence of a foreign material (e.g. polymeric compatibilizer, micro- or nano- filler) can affect the crystallization behavior of semicrystalline polymers including PP [67, 70]. However, only few studies addressed the effect of foreign materials on the polymorphism of such polymers and the formation of the less common crystalline structure forms [71-73]. For instance, it has been shown that the introduction of only 0.5 wt% of N, N′-dicyclohexylo-2,6-naphthaleno dicarboxy amide (common β-phase nucleating agent) can lead to the formation of almost 100% β-crystalline phase in isotactic PP, with a significant changes of the structure, morphology and properties [74]. Moreover, it has been reported that a β nucleating agent, namely pimelic acid, can be supported on nano-$CaCO_3$ with high specific surface area and significantly increase the efficiency of the β-phase nucleation [75].

Interestingly, the nanofiller itself, in absence of a special nucleating agent, can also promote nucleation of the less common crystalline forms in semicrystalline polymers. For example, as reported [76], clays can promote nucleation of polyamide crystals and induce the formation of the less common β- and γ- form crystals. Other studies investigated the mechanisms responsible for the presence of polymorphism in PP/clay nanocomposites [64, 68, 77]. In particular, the introduction of clay increases the crystallization rate and the crystallization peak temperature, inducing an orientation of the crystals and promoting the formation of the less common β- and γ - phase with a significant enhancement of the impact strength and toughness. In addition to clays, carbon nanotubes [78, 79], and graphite nanoplatelets [43], even at low concentration, can also act as nucleating agents for PP. Therefore, the advantage of using nanofillers, especially carbon based ones, over the traditional β

nucleating agents is that, in addition to the nucleation of the less common β-phase that exhibits greater toughness and impact strength, there is a dramatic improvement of the mechanical, thermal and electrical properties achieved at filler content of less than 5 wt% due to the reinforcing effect provided by the rigid inclusions (i.e. higher elastic modulus and yield strength) [2, 26, 54, 80-82]. Noteworthy, the current research is also focused on the investigation of the dominant structure/properties relationships in order to determine the impact of the changes in crystallinity features in the physical and mechanical properties.

2.2.1.3 Crystalline morphology

The crystalline morphology of polymorphism polymer is rather complicated and is currently a major focus in polymer physics. Crystalline structure characteristics (i.e. lamellae structure, thickness of the individual lamellae and amorphous phase) are typically investigated by various techniques, including polarized optical and electron microscopy, X-ray diffraction analysis (XRD) and small angle X-ray scattering (SAXS), differential scanning calorimetry (DSC) and modulated DSC.

The main processing parameters affecting crystalline morphology are crystallization temperature, pressure and cooling rate, while the presence of a foreign filler may also alter the crystalline structure. Moreover, crystallization can be effectively used to control the extent of the intercalation or exfoliation of polymer chains into the silicate layers and the final properties of resultant nanocomposites.

For instance, the spherulitic structure of PP–clay nanocomposites, as investigated by polarized light microscopy, shows smaller and more numerous spherulites compared to unfilled PP (Figure II-26).

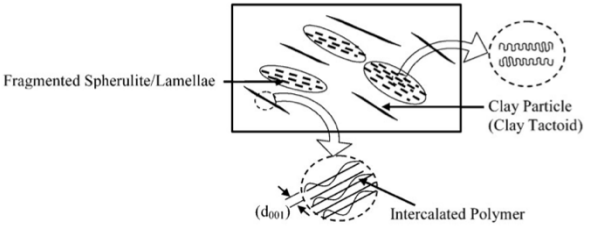

Figure II-26. Proposed schematic of the crystalline structure of PP-clay nanocomposite, characterized by a fibrillar morphology [66].

Moreover, the lamellae thickness increased from 1.77 to 2.07 nm when the clay content increased from 0 to 8 wt% [83]. In addition, when the crystallization occurs at higher temperatures, the morphology of PP–clay nanocomposites may change from

spherulites to fibrillar morphology. The structural change was attributed to the rigid clay platelets which can fragment the lamellae structure, resulting in a new structure characterized by dispersed clay particles surrounded by fragmented spherulite/lamellae.

Recent studies indicated that a decrease in spherulite size and crystallinity decreases the modulus of PP. Moreover, semicrystalline polymers with small spherulites tend to be tougher than that with coarse spherulites because large spherulites have weak boundaries. For instance, in HDPE/$CaCO_3$ composites, the decrease in spherulite size from 90 mm in neat HDPE to 35 mm (filler content of 20 wt%), was accompanied by a significant the increase in toughness over neat HDPE [66].

2.2.2 Interfacial properties

With the incorporation of nanoparticles, new interfaces are generated during crystallization. By taking advantage of the large interfacial area and volume at the filler/matrix interface, unique properties can be achieved in nanocomposites.

Therefore, multiscale interfaces regions have to be considered in a semicrystalline nanocomposite: (i) crystal–crystal interface, (ii) crystal–amorphous interface, (iii) particle–matrix interface and (iv) particle–particle interface [66]. Since the size of crystal particles is different, distinct characterization techniques need to be used for a proper characterization of each interface. Noteworthy, the size of crystals is in the order of micrometers, while the lamellar thickness is typically several nanometers and the size of particles is around nanometers. The investigation of the interfacial properties is important for the understanding of the structure/properties relationships governing the physical and mechanical properties of polymer nanocomposites.

2.2.2.1 Crystal–crystal and crystal–amorphous interfaces

The morphology of crystal–crystal and crystal– amorphous interfaces is an important factor in the control of physical and mechanical properties of polymer nanocomposites. However, the question of the structure of the interface between the amorphous and crystalline regions in semicrystalline polymers is not yet fully solved. Flory has estimated that at most one-half of the chains emanating from the crystal can proceed into the amorphous region, while the other half turns back or fold [84]. Moreover, interfaces of non-crystalline phase-separated systems also appear to be narrow (around 15-20 Å for interface thickness of diblocks both of whose

components are amorphous). Both conventional optical microscopy and confocal microscopy offer the possibility to investigate the interfaces morphology.

2.2.2.2 Matrix-particles interactions

A polymer nanocomposite can be modeled as a three-phase material including matrix, matrix–filler interface and reinforcement filler. There are very few reports in the literature about changes in the conformation of long chain molecules (i.e. primary bond spatial arrangement) in the vicinity of the fillers surfaces. Jancar et al. [85] suggested that chains are less densely packed at interface, i.e. they exist as expanded coils. Quite on the contrary, Vollenberg et al. [86] attributed the effect of particle size on the elastic modulus in both amorphous and semicrystalline polymers in terms of an interface of increased density compared to the bulk matrix.

During solidification from the melt, gradients of mass transport occur near the filler surface, resulting in an alteration of both the supermolecular structure and the chain mobility of PP in the thin layer near the filler surface. The thickness of this layer ranges from 10 to several hundred nanometers and has more or less an amorphous character. However, recent studies on the crystallization behavior of PA modified with xGnP suggested the presence of amorphous and crystalline at the interface [62, 87], as schematically presented in Figure II-27.

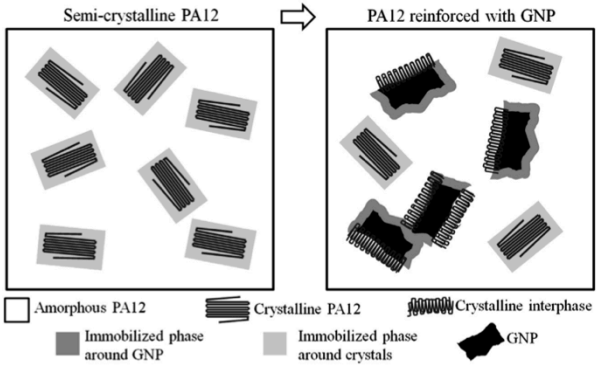

Figure II-27. Proposed model describing the formation of a complex constrained phase [62].

The properties change at the interface, when compared to the bulk, is proportional to the surface activity of the filler and the topology of the surface. In particular, surface affinity (i.e. the ratio between adhesive and cohesive energies of the filler and matrix) gives a quantitative estimation of the compatibility between

matrix and reinforcement. In general, surface-active fillers produce greater changes in polymer morphology [66].

The structure and properties of the matrix/particle interfacial regions are expected not only to be different from the bulk material, but are also critical to controlling the bulk properties of the nanocomposite. For instance, in thermoplastics the interfacial region can exhibit changes in crystallinity, mobility, chain conformation, molecular weight, chain entanglement density and even charge distribution [1]. These changes can have a significant impact on the physical properties and mechanical behavior. Indeed, the deformation of polymer nanocomposites strongly depends not only on the modulus and strength of filler and matrix, but also on the strength of the matrix–filler interface. Moreover, when considering nanocomposites incorporating functional nanofillers (such as CNTs, CB, xGnP, etc.) the interfacial properties become also important in controlling the functional properties of the bulk nanocomposite (e.g. electrically or thermal conductivity, storage media, low dielectric materials, tribological surface coatings of storage media).

Most classical mechanical models proposed for nanocomposites implies that strong filler–matrix interfaces lead to greater stiffness and strength of the composite, but also to low toughness due to the brittleness of the particle and the absence of crack deflection at the interface [88]. However, when the interface is strong enough, the high stiffness and strength in composites is also associated to a greater toughness. Recent studies based on calorimetry and characterization of the viscoelastic properties, have provided clear evidence on how the presence of a constrained amorphous phase located not only at the crystal surface but also at the filler surface can induce secondary reinforcing mechanisms which, in addition to the primary stiffening effect due to the high modulus of the filler particles, can significantly contribute to the enhancement of the bulk properties of semicrystalline polymers [62, 87].

Nevertheless, the current experimental techniques able to evaluate the interfacial strength and adhesion at the filler/matrix interface are slowly developing. Noteworthy, the investigation of the properties at the filler/matrix interface represent an important development (both experimental and theoretical) for the understanding of the relationships between bulk properties and interfacial properties. As representative example of the development of nano-mechanical testing, current research conducted by Barber et al. focuses on the probing of single CNT pullout from a polymer matrix (Figure II-28).

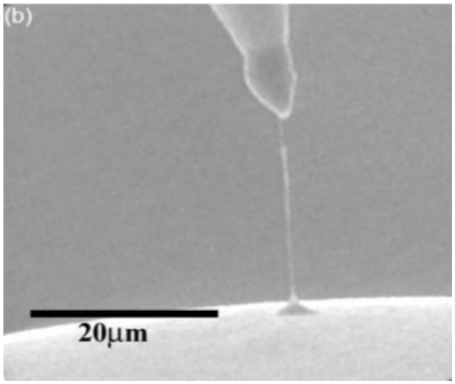

Figure II-28. Pull-out testing of single CNT from a polymer droplet [89].

Moreover, very few studies have been dedicated to the modeling of the relationships between the macroscopic mechanical properties of nanocomposites and their interfacial strengths. Pukanszky developed a model to predict the variation of the composite's yield stress with the filler content, introducing a parameter that accounts for the interfacial interaction [90, 91]. Sumita et al. utilized the information obtained from dynamic mechanical analysis (DMA) measurements to estimate the effective volume fraction of the dispersed phase. Also in this case, a parameter is introduced to describe the interfacial interaction [92]. Shang et al. proposed another model by correlating the work of adhesion, which is related to the interfacial interactions, with the elastic modulus and the tensile strength in silica-filled polymer composites [93].

2.2.3 Viscoelastic behavior in the molten state: rheological behavior

2.2.3.1 Overview

While it is clear that the interfacial region has a significant impact on the properties of nanocomposites, quantitative understanding of the structure and morphology of the polymer matrix interacting with nanoparticles is slowly developing. Indeed, direct measurements of the properties of the interfacial region are extremely difficult. Therefore, other measurement techniques which are more feasible and reliable, can be used to probe the properties of the interfacial region more specifically. In particular, different techniques have been recently adopted to characterize the interfacial properties, including:

- Differential scanning calorimetry (DSC) and modulated DSC analysis
- Rheological measurements
- Dynamic mechanical analysis (DMA)
- Methods to measure differences in surface energy (wettability, gas chromatography, etc.)

For instance, when considering amorphous polymers, it is assumed that an attractive interface will decrease the mobility of the polymer chains and a repulsive interface will increase the mobility [94]. One method for probing this change in mobility of the polymer chains in the interfacial region is to measure the glass transition temperature (T_g), using DSC, rheological measurements and DMA. Recent studies using these methods have shown that the T_g of a polymer nanocomposite can be increased or lowered with the incorporation of nanoparticles which manifest attractive and repulsive interaction with the matrix, respectively [95].

In particular, rheological analyses can be effectively used in nanocomposites to probe the extent, structure, and properties of the interfacial region, which depend on the filler/matrix interaction. For instance, the loss modulus is sensitive to the distribution of relaxation times of the polymer matrix. When the nanofiller is added, if the mobility of the polymer chains is altered, the relaxation spectra can either shift (if the interface causes global changes in the polymer relaxation behavior) or broaden (if the interface creates only local changes in polymer relaxation) [96].

2.2.3.2 General definitions

The flow behavior of a melt polymer under different conditions is of great importance in polymer manufacturing. Therefore, the investigation of flow phenomena by rheological analyses is highly desirable in order to predict the deformational behavior under different loading conditions and polymer composition. Indeed, the rheological behavior of polymers is strongly affected by the presence of filler particles and different variables (including filler concentration, chemistry and surface morphology) play a key role in governing the rheological properties.

In principle, every material will behave in a different way under different stresses and all materials present a viscoelastic response at an imposed load. However, when taking into account a polymeric matrix, the viscoelastic behavior is predominant above the glass transition temperature (T_g), while the linear elastic response is prevalent in the glassy state (i.e. below T_g). Based on the viscoelasticity theory, two ideal models can be taken into account: the elastic solid and the viscous liquid. While the perfect solid deforms itself elastically under a stress (i.e. deformational energy accumulated as elastic potential energy and can released

when the load is removed), the ideal fluids deform irreversibly (i.e. the deformational energy is dissipated and not recoverable). The behavior of the perfectly elastic body and ideally viscous fluids can be described by Hooke law (Eq. II-1) and Newton law (Eq. II-2), respectively [97]:

$$\tau = G\,\gamma \qquad (II-1)$$

$$\tau = \eta\,\dot{\gamma} \qquad (II-2)$$

where τ is the applied shear stress, G is the shear modulus, η is the viscosity and γ is the shear strain. According to the above models, the stress exhibited in an elastic material is proportional to the deformation and does not depend on the deformation rate, while the stress is proportional to the deformation rate and independent from the deformation in pure viscous fluids. In particular, the viscosity is a property of the fluid that describes the resistance of the fluid to the irreversible deformation. In general, viscosity is defined in a different way for *Hookean* (i.e. elastic) and *Newtonian* (i.e. viscous) behavior (Figure II-29).

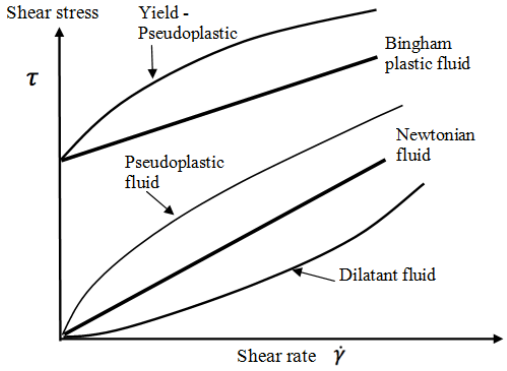

Figure II-29. Divergence from Newtonian behavior: dilatant and pseudoplastic fluids.

Many rheological models rely on the definition of the shear stress in a solid (or viscosity in a liquid) as a function of the shear rate:

$$\tau = K\,(\dot{\gamma})^{n} \qquad (II-3)$$

$$\eta = K\,(\dot{\gamma})^{n-1} \qquad (II-4)$$

where *n* is a parameters that controls the rheological behavior of the materials (called as fluid in this specific context), being *n > 1* for dilatant fluids, *n < 1* for pseudoplastic fluids and *n = 1* for Newtonian fluids.

Most polymeric materials behave as a pseudoplastic material. The typical rheological behavior followed by a thermoplastic polymer is described in Figure II-30. Interestingly, while the Newtonian behavior is well followed at low shear rates, a decrease in apparent viscosity can be observed for non-Newtonian fluids.

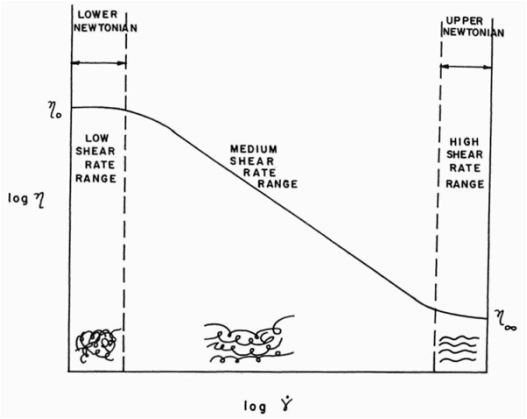

Figure II-30. Rheological behavior of Newtonian and non-Newtonian fluids as a function of the shear rate.

Therefore, different technological processes are adopted depending on the shear rate range: low shear rate range (e.g. roto-molding, compression molding), medium shear rate range (e.g. blow molding and thermoforming, pipe extrusion, film extrusion and injection molding) and high shear rate range (e.g. fiber spinning and coating).

2.2.3.3 Dynamic rheological behavior

The modeling of the rheological behavior of various materials has been widely investigated and different functions (both theoretical and empirical) have been proposed [98]. Moreover, the investigation of the rheological properties of polymers has been more intensively studied by dynamic rheological analyses. By adopting dynamic methods, the characteristic curve of a material can be extended over a wider frequency range (10^{-9} to 10^{9} Hz) while maintaining short testing times. In the case of a linear viscoelastic material, when a sinusoidal shear strain $(\gamma(t))$ is applied

with a certain frequency *(ω)*, the correspondent shear stress *(τ(t))* will present a phase shifted by an angle δ.

$$\gamma(t) = \gamma_0 \, sin(\omega t) \qquad (II-5) \qquad\qquad \dot{\gamma}(t) = \omega \, \gamma_0 \, cos(\omega t) \quad (II-6)$$

$$\tau(t) = \tau_0 \, sin(\omega t + \delta) = \tau_0 \, cos(\delta) sin(\omega t) + \tau_0 \, sin(\delta) cos(\omega t) \qquad (II-7)$$

where $\dot{\gamma}(t)$ is defined as the strain rate. By realaborating Eq. (II-7):

$$\tau(t) = \tau_0 \, G' sin(\omega t) + \tau_0 \, G'' cos(\omega t) \qquad (II-8)$$

$$G' = {}^{\tau_0}/_{\gamma_0} \; cos(\delta) \qquad\qquad G'' = {}^{\tau_0}/_{\gamma_0} \; sin(\delta)$$

where *G'* and *G"* are defined as storage and loss modulus, respectively. Another typical notation used in rheological studies is the complex notation:

$$\gamma^*(\omega) = \gamma_0 \, e^{i\omega t} \quad (II-9) \qquad\qquad \tau^*(\omega) = \tau_0 \, e^{(i\omega t + \delta)} \quad (II-10)$$

$$\frac{\tau^*(\omega)}{\gamma^*(\omega)} = G'(\omega) + i \, G''(\omega) \qquad (II-11) \qquad\qquad \tan(\delta) = {}^{G'(\omega)}\Big/_{G''(\omega)} \quad (II-12)$$

where *G'(ω)* and *G"(ω)* describes the ability of the materials to store or dissipate the input energy, respectively. The complex viscosity *(η*(ω))* is defined as:

$$\eta^*(\omega) = \frac{\tau^*(\omega)}{\dot{\gamma}^*(\omega)} = \eta'^{(\omega)} + i \, \eta''(\omega) \qquad (II-13)$$

where η' (i.e. dynamic viscosity) describes the dissipative phenomena and tends to the steady flow viscosity at frequencies approaching zero.

The rheological behavior has been widely studied in microfilled and nanoreinforced composites [99, 100]. In particular, when taking into account thermoplastic nanocomposites, the melt rheology, as evaluated under controlled strain conditions and at constant temperature, can describe the dependence of the dynamic shear storage modulus (*G'*) and complex viscosity *(|η*|)* on the shear rate.

A representative example regarding LLDPE and relative nanocomposites filled with various types contents of boehmite alumina (BA) is depicted in Figure II-31. In particular, LLDPE were prepared with two different grades of untreated BA (D40 and D80, with crystallite size of 40 and 74 nm, respectively) and a silane surface-treated BA with crystallite size of around 40 nm (D40 OS) [18].

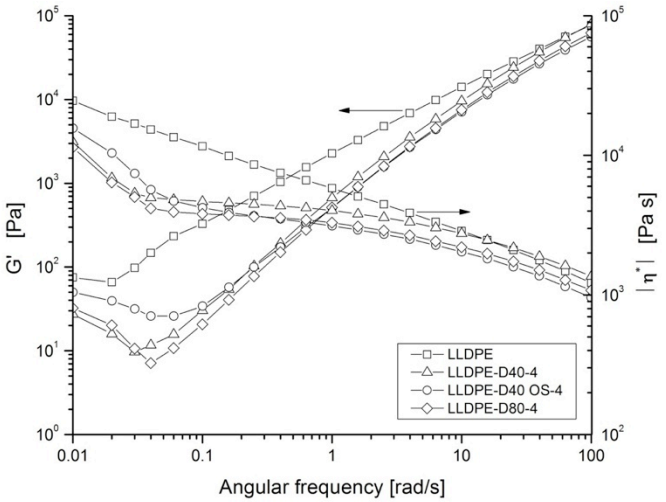

Figure II-31. Complex viscosity $|\eta^*|$ and storage modulus (G') with respect to angular frequency (ω) for LLDPE and relative nanocomposites filled with 4 wt% BA [18].

A general decrease in both G' and $|\eta^*|$ can be detected for all LLDPE-BA nanocomposites over the whole frequency range. Noteworthy, the lowering in viscosity is very beneficial for the material processing.

Incorporation of nanofillers in thermoplastics is generally associated to a marked increase in the melt viscosity, at least in the range of low frequencies (as presented in the examples above). Furthermore, a significant enhancement in G' is generally observed. These changes are usually ascribed to a pseudo solid-like transition caused by the dispersed nanoparticles [101-107]. Nevertheless, the lowering of both $|\eta^*|$ and G' by BA addition to LLDPE contradicts such general trend. It is interesting to observe that Khumalo et al. reported the same rheological behavior for polyethylene/synthetic boehmite alumina nanocomposites [108]. In particular, a decrease in both G' and $|\eta^*|$ was recorded for LDPE-BA and HDPE-BA nanocomposites with respect to the neat matrices. Also Blaszczak et al. studied the rheological behavior of LDPE-BA nanocomposite and found that the addition of BA produces a decrease in $|\eta^*|$ compared to that of unfilled LDPE [109]. A possible explanation is based on the fact that, as a result of good adhesion between the polymer matrix and the mineral filler, the polymer melt with filler flows more uniformly, thus at a lower viscosity despite adding solid filler [109]. Moreover, since LLDPE is a highly branched polymer whose chains would tend to get entangled,

apparently even poorly bonded plain BA particles fill in the spaces between chain branches and enable an easier flow.

2.2.3.4 Modeling of rheological properties

The composition dependence of rheological properties is modeled only in few cases which have been derived from Einstein's equation (i.e. prediction of the viscosity dependence on the composition in suspensions containing spherical particles). While the original equation is valid only at infinite dilution (< 1–2%), additional parameters have to be taken into account when modeling real composites [19].

Other studies tried to address the dependence of the rheological behavior of nanofilled systems on the characteristics of the filler (including particle size and shape, surface treatment) and of the melt polymer matrix. Moreover, the characteristics of the interphase generated due to matrix/filler interactions have to be taken into account. In particular, the model proposed by Mooney, which contains adjustable parameters in order to account for both the effect of interactions and particle anisotropy [110]:

$$ln\left(\eta/\eta_0\right) = \frac{k_E\ \varphi_f}{1 - \varphi_f/\varphi_f^{max}} \qquad (II-14)$$

where η and η_0 are the viscosity of the composite and the matrix, respectively, k_E is an adjustable parameter related to the shape of the particles and $\varphi_{f\ max}$ is the maximum amount of filler which can be introduced into the composite (i.e. maximum packing fraction). The study of the rheological behavior of PP/$CaCO_3$ nanocomposites showed that filler/matrix interfacial interactions lead to the formation of a stiff interface that significantly influences the viscosity and the maximum amount of filler which can be incorporated into the polymer decreases with the specific surface area of the filler. Moreover, when large filler amounts are added, particles interact with each other, resulting in the formation of a high-order structure and a yield stress appears during flow.

Particular attention has been also paid to the investigation of aggregation phenomena, including detection of aggregation by Casson or modified Casson plots [111]. Other structure related phenomena in melt flow are the orientation of anisotropic particles and segregation. Both were observed in particulate filled composites, but no model equation or theoretical treatment was developed to describe such behavior.

2.2.4 Viscoelastic behavior in the solid state: creep behavior

2.2.4.1 Creep behavior and linear superposition principle

Creep is the time-dependent change in the dimensions of a generic polymeric part when it is subjected to a constant stress. Creep and other creep-related properties are among the most important mechanical characteristics of polymers. Polymers that have significant time sensitivity at the temperature of use will have limited value for structural applications or applications demanding dimensional stability. In particular, while the modulus can be considered constant in metals (except at high temperatures), this is not the case for polymers. Provided its variation is known, the creep behavior of the polymer can be compensated by using well-established design procedures or by modification of the polymer's composition with reinforcing fillers [112].

In a creep experiment a constant stress σ_0 is applied to a sample and the strain ε is measured as a function of time *t*. The creep compliance *D(t)* is the ratio of the strain to the stress and is generally a function of time.

$$D(t) = \frac{\varepsilon(t)}{\sigma_0} \qquad (II-15)$$

The creep behavior is typically divided into three different stages: *primary stage* (i.e. when the stress is applied there is a correspondent strain in the elastic region), *steady state* (i.e. when the material strains at a constant strain rate) and *tertiary creep* (i.e. deformation occurring at an increasing strain rate). When the amount of strain is high, creep fracture or other failure mechanisms will occur (Figure II-32). The total strain $\varepsilon(t)$ can be represented as the sum of the instantaneous elastic strain ε_E (i.e. instant strain obtained upon application of the stress) and the viscoelastic strain ε_V. In the same way, the compliance can be divided into elastic and viscous components.

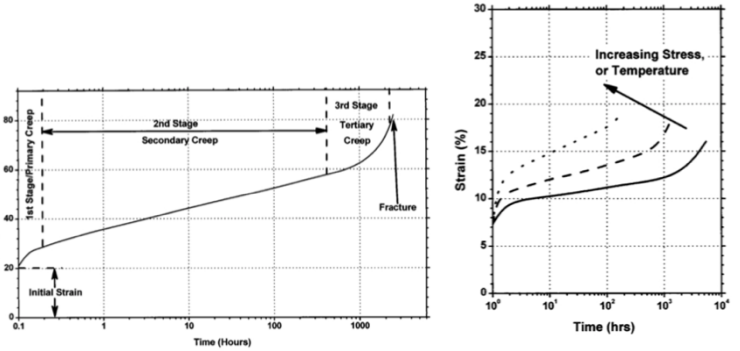

(a) (b)

Figure II-32. (a) Strain versus time curve and (b) effect of stress and temperature on the strain of a polymeric material [112].

When the deformation of the material can be described by a linear viscoelastic behavior, the *linear superposition principle* can be applied. In particular, the deformation can be modelled as arrangements of springs (i.e. Hookean deformation, typical of an elastic solid), dashpots (i.e. Newtonian flow, characteristic of a viscous liquid) and friction elements (in order to describe yielding properties). The basic configurations are typically considered the *Kelvin-Voig*t model and the *Maxwell* model, described in Figure II-33.

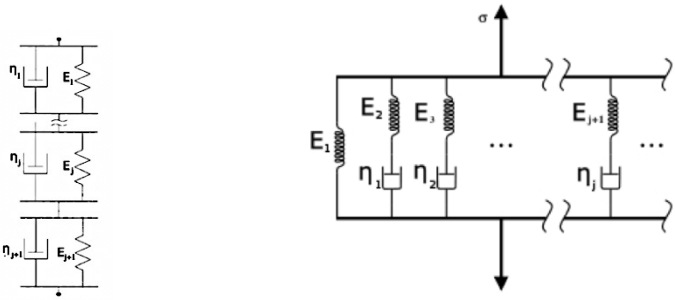

(a) (b)

Figure II-33. (a) Generalized Kelvin-Voigt model and (b) Maxwell model.

While the Kelvin-Voigt model is represented by a parallel combination of spring and a dashpot (Eq. (II-16)), the Maxwell model can be described as a series connection of a spring and a dashpot (Eq. (II-17)). The viscoelastic behavior of the material is

described in both systems through a characteristic time τ, which is the ratio of the viscosity η with respect to the stiffness *E*. Note that the equations presented below refer to the simplest model, characterized by a single parallel and a single series for the Kelvin-Voigt and Maxwell model, respectively.

$$D(t) = \frac{1}{E}\left(1 - e^{-t/\tau}\right) \qquad (II-16)$$ where τ is called *retardation time*

$$D(t) = \frac{1}{E}\left(1 + t/\tau\right) \qquad (II-17)$$ where τ is called *relaxation time*

Moreover, more complicated behaviors can also be described by a proper combination of the basic elements as connected in series or in parallel. In particular, the *Burgers model*, as derived from a combination of a Maxwell and a Kelvin-Voigt model in series, has been successfully applied to describe the viscoelastic behavior in a number of polymer, polymer blends and relative composites (Figure II-34).

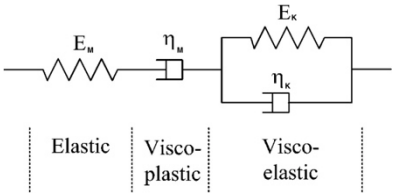

Figure II-34. Burgers model for the modeling of viscoelastic behavior in more complicated polymeric systems.

The creep compliance, as described according the Burgers model, is given in Eq (II-18):

$$D(t) = \frac{1}{E_M} + \frac{t}{\eta_M} + \frac{1}{E_K}\left(1 - e^{E_K t/\eta_K}\right) \qquad (II-18)$$

Another examples of more accurate models to describe the viscoelastic behavior of polymers are represented by the *Jeffrey model* and *Zener model* [113].

2.2.4.2 Time-temperature superposition principle

Creep behavior in polymers and polymer composites has been observed to depend on several factors, in particular the applied constant stress, temperature and moisture absorption. A comprehensive work on the effect of temperature and stress intensity on the creep of unidirectional and multidirectional composites can be found in the works of Brinson et al. [113], Yeow et al. [114], Gramoll et al. [115] and Dillard

et al. [116]. It was observed that an increase in temperature results in acceleration of the creep rupture time. Similar to the temperature effect, increase in stress causes an increase in the creep compliance of the composite material. These researchers have also shown that the combined effect of temperature and stress causes a further increase in the creep compliance and correspondent decrease in rupture time. Moisture absorption also accelerates the time dependent response of the polymer composites mainly due to plasticization of the matrix (i.e. presence of moisture in polymer lowers the glass transition temperature, causing a reduction in modulus).

With the purpose of developing accelerated procedures able to fully characterize the viscoelastic behavior in a polymeric system, both experimental and theoretical investigations have been focused on the effect of temperature and stress on the creep behavior of polymers in the linear viscoelastic region. Three widely accepted methods are the *Time Temperature Superposition Principle* (TTSP), *Time Stress Superposition Principle* (TSSP) and *Time Temperature Stress Superposition Principle* (TTSSP) [113].

According to the TTSP, for many polymer systems, the effect of temperature *(T)* on the linearly viscoelastic creep *(D(T,t))* can be combined into a single curve, following the below relation :

$$D(T,t) = D\left(T_0, {}^{t}/_{a_{T_0}}\right) \qquad (II-19)$$

where $\left({}^{t}/_{a_{T_0}}\right)$ is the reduced time *t**, which is related to the real time *t* by the temperature shift factor $a_{T_0}(T)$, being T_0 the reference temperature. Therefore, the effect of temperature on the creep behavior is considered equivalent to dilating (or contracting) the real time for temperatures above (or below) the reference temperature. Once the temperature-dependence of the shift factors $a_{T_0}(T)$ is determined, the superposition principle enables the construction of master curves. Most polymeric materials show a creep behavior that depends on temperature following the Arrhenius relation at temperature below T_g, or the Williams, Landel and Ferry (WLF) equation when the temperatures above T_g.

$$\ln a_{T_0}(T) = \frac{\Delta H}{R}\left(\frac{1}{T} - \frac{1}{T_0}\right) \qquad (Arrhenius\ equation) \quad (II-20)$$

$$\log a_{T_0}(T) = -\frac{C_1\,(T - T_0)}{C_2 + (T - T_0)} \qquad (WLF\ equation) \qquad (II-21)$$

Where ΔH is an activation energy, R is the constant of an ideal gas, while C_1 and C_2 are characteristic constants of the material. A common practice for building the

master curves is to reduce creep data to the temperature T_g. In this case the constants in the WLF equation are independent on the material characteristics (C_1=17.44 and C_2=51.6 K). A representative example of the construction of creep master curve is depicted in Figure II-35.

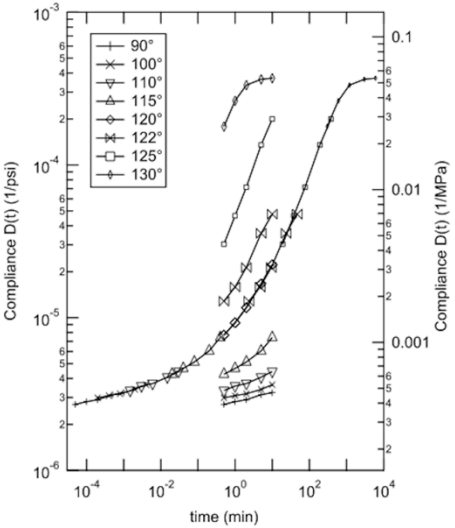

Figure II-35. Example of creep compliance master curve constructed applying the TTSP (T_0=120 °C) [113].

2.2.4.3 Time-temperature-strain superposition principle

Recent studies have demonstrated that that TTSP is valid in the linear viscoelastic region also for polymer composites [114]. However, existing literature points to the fact that TTSP is not valid within the non-linear viscoelastic region, mainly because of the change in shape of the creep curve with stress levels. On the other hand, the TTSSP is based on the fact that creep deformation curves for different thermo-mechanical conditions are of the same shape. Therefore, by collecting short- time creep deformation data at elevated temperatures (or stresses), long-time creep behavior at lower temperatures (or stresses) can be predicted. Figure II-36 schematically illustrates the TTSSP technique: the master curves are reduced to T_1 (reference temperature) and σ_1 (reference stress). The resultant master curve is valid through all the temperatures and stress levels within the data range.

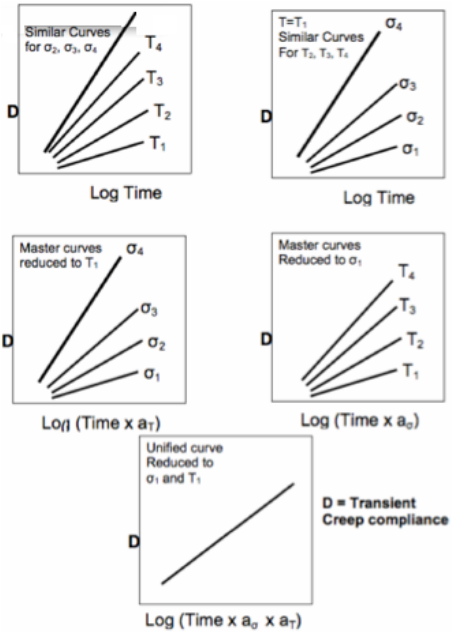

Figure II-36. Schematic illustration of TTSSP technique [117].

For a given specific thermo-mechanical condition, the Findley equation can be rewritten as:

$$\varepsilon(t,T,\sigma) = \varepsilon_0(\sigma,T) + m(\sigma,T)t^n \qquad (II-22)$$

where *n* is a coefficient independent on the stress and temperature. Based on the concept of TTSSP, Eq. (II-22) can be expressed in terms of the creep response of a given reference condition (σ_0, T_0) :

$$\varepsilon(t,T,\sigma) = a_V[\varepsilon_0(\sigma_0,T_0) + m(\sigma_0,T_0)(t/a_H)^n] \qquad (II-23)$$

where :

$a_V = \varepsilon_0(\sigma,T) \,/\, \varepsilon_0(\sigma_0,T_0)$

$a_H = \{[\varepsilon_0(\sigma_0,T_0)\, m(\sigma,T)] \,/\, [\varepsilon_0(\sigma,T)\, m(\sigma_0,T_0)]\}^{-1/n}$

2.2.4.4 Non-linear tensile creep behavior

Another interesting approach has been recently proposed by Kolarik et al. [118] in order to address the non-linearity of the tensile creep by considering the strain induced increment of the free volume. With the introduction of a new variable, namely the *internal time*, the non-linear creep data can be reduced in order to construct a generalized compliance curve, which corresponds to a pseudo iso-free volume state. This approach, which is presented in details in *Appendix A*, enables the prediction of the real time-dependent compliance for any applied stress within the range of reversible strains.

2.2.5 Viscoelastic behavior in the solid state: dynamic mechanical behavior

2.2.5.1 Dynamic mechanical analysis (DMA)

DMA experiments are designed to excite the tested material with a sinusoidal strain at a certain amplitude and frequency (ω). The monitored response of the material is usually considered as the stress $\sigma(t)$, which also follows a sinusoidal function with a phase shift δ. However, in dynamic mechanic experiments performed within the linear viscoelastic region, the output data are reduced to functions that depend on the temperature (T) or the frequency (Figure II-37) :

- $E'(\omega) = (\sigma_0 / \varepsilon_0) \cos(\delta)$
- $E''(\omega) = (\sigma_0 / \varepsilon_0) \sin(\delta)$
- $\tan \delta = E''(\omega) / E'(\omega)$

Where $E'(\omega)$ is the *storage modulus* (i.e. related to the stress components in-phase with the strain), $E''(\omega)$ is the *loss modulus* (i.e. related to the stress components out-of-phase with the strain) and $\tan \delta$ is *the loss factor* (i.e. gives an indication on the out-of-phase components with respect to the in-phase components).

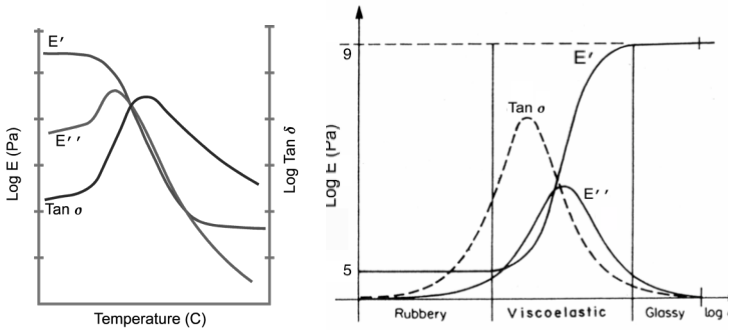

Figure II-37. Representative example of *E', E''* and *tanδ* trends as a function of (a) temperature and (b) frequency.

E' gives an indication on the elastic behavior of the material, while *E''* is related to the viscous behavior (i.e. the energy lost to friction and internal motions). Moreover, *tanδ* is a property called *damping*, and is an indicator of how efficiently the material loses energy to molecular rearrangements and internal friction. Noteworthy, being the ratio of the two moduli, this property is independent of geometry effects and can be used as a check on the possibility of measurement errors in a test.

2.2.5.2 Time-temperature superposition principle (TTSP)

As already observed in the case of creep experiments, the TTSP can be applied in dynamic mechanical measurements. TTSP is based on the observation that the curves representing the viscoelastic properties of a material, determined at different temperatures, are similar in shape when plotted against ($log\ \omega$). Therefore, the master curves can be constructed over any broad range of frequency by taking data at several temperatures over a more limited range of or frequency and shifting the curves horizontally on the ($log\ \omega$) axis until they fit together and exactly align in a single continuous curve [119]. Therefore, the resultant master curve refers to the reduced frequency ω^*.

The experiment is typically carried out by performing DMA experiments at different frequencies (at least 5-6) while scanning the temperature. The data are then reduced in order to obtain the spectrum of modulus as a function of the frequency at different temperatures. The master curve is finally constructed by applying the TTSP [113]. A representative example of the application of TTSP in the case of poly(ethylene terephalate) is depicted in Figure II-38.

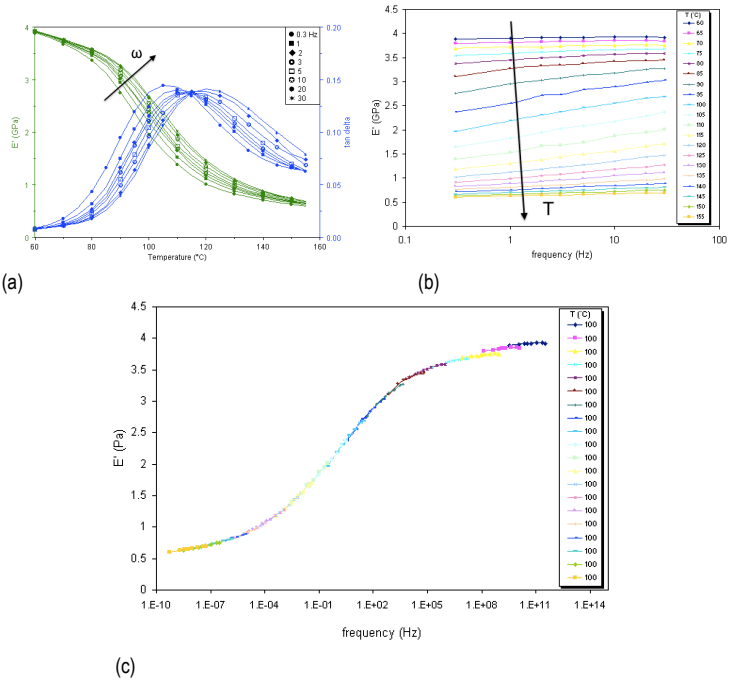

Figure II-38. Example of the application of TTSP for the construction of the master curve of E' : (a) E' as function of temperature, (b) spectrum of E' and (c) master curve.

2.2.6 Fracture behavior

2.2.6.1 Quasi-static tensile test

The mechanical behavior of a material describes the response the material to the external loads. This behavior defines the usefulness of the material in a variety of applications, from automotive to civil structures, as well as common products [120]. Moreover, knowledge of the mechanical behavior of materials is also necessary during manufacturing processes (e.g. forming and shaping of components). In particular, the result obtained from a tensile test is a so-called stress/strain curve $(\sigma - \varepsilon)$, and is basic for the determination of the suitability of a material for a particular load-bearing application. The characteristic $\sigma - \varepsilon$ curve can be obtained

through different loading conditions (tension, compression, flexure, etc.) by using a universal mechanical testing machine. Electro-mechanical machines typically have a load capacity up to some hundreds KN and the mechanical testing is performed controlling the displacement. Typical cross-head speeds range from 0.001 to several hundreds mm/min (Figure II-39). On the other hand, servo-hydraulic machines enable the carry out the test under load or displacement controlled conditions. By using a hydraulic actuator, loads as high as 5000 KN can be achieved. Tensile testing can be carried out at different temperatures, loading rates, and environmental conditions.

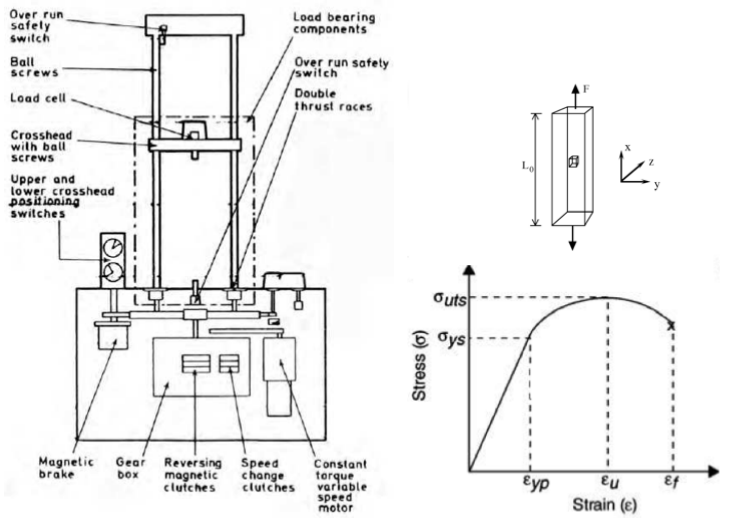

(a) (b)

Figure II-39. (a) Schematic of an electromechanical tensile testing machine and (b) characteristic $\sigma - \varepsilon$ curve typical of many polymers.

When performing a tensile test on a given material, a uniaxial tensile stress σ can be imagined as applied on a small portion of the material and a correspondent deformation ε is observed in the same direction of stress application (Eq. II-24 and Eq. II-25).

$$\sigma_x = {}^{F_x}/_{A} \quad (II-24)$$

$$\varepsilon_x = {}^{\Delta L_x}/_{L_0} \quad (II-25)$$

where A is the cross-section area of the specimen, as considered perpendicular to the applied load, while ΔL_x is the uniaxial elongation and L_0 is the gaga length.

If the material exhibits a linear elastic behavior, the elastic modulus (typically called Young's modulus) can be estimated from the slope of the linear, reversible portion of the $\sigma - \varepsilon$ curve. Typical engineering materials show linear elastic behavior only at small deformations (ε < 1 % in case of polymers). When performing uniaxial tensile testing on polymeric materials, the most common specimen types are dogbones (ASTM D638) and dumbbell (ISO 527).

Plastic properties are those that describe the relationships between stress and strains when the deformation is large enough to be irreversible. Typical plastic properties are the yield stress (the stress at which deformation become permanent, denoted by the symbol σ_{ys}), the maximum in the stress/strain plot (the ultimate tensile strength, indicated as σ_{uts}), the maximum deformation. Toughness is the ability of a material to absorb energy while deforming and brought to fracture [120]. This property is related to the area under the curve $\sigma - \varepsilon$.

Different deformation mechanisms are usually involved in the yielding and fracture of polymers. In particular, yielding is typically characterized by shear-yielding of crystallites (i.e. the flow of polymeric chains occurs without loss of molecular cohesion or volumetric changes) and crazing (i.e. microscopically localized phenomenon that bring the formation of fibrilis and can support the crack, delaying failure), as represented in Figure II-40 and Figure II-41.

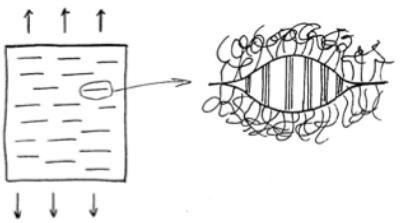

Figure II-40. Dynamics of crazing occurring in polymers.

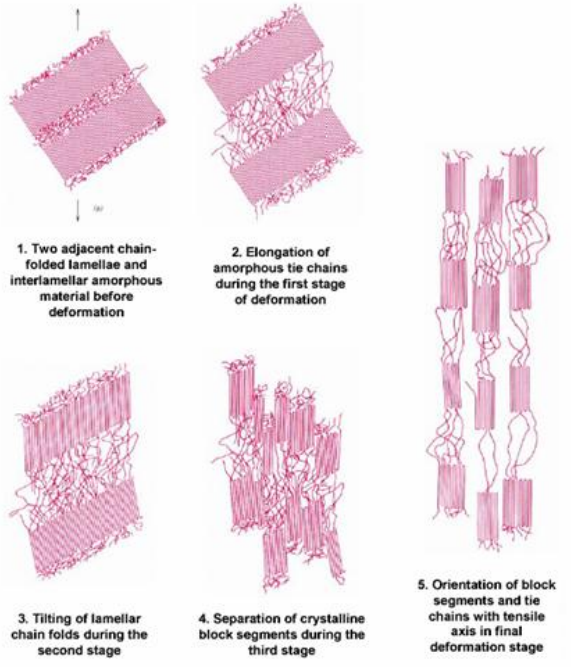

Figure II-41. Different deformation mechanisms in semicrystalline polymers.

2.2.6.3 Impact test

Nowadays, many applications employing polymeric parts require the materials to stand deformations at high strain rates and impacts. The evaluation of the material's fracture behavior under such conditions can be achieved through impact testing. Different configurations can be used (Figure II-42), in particular:

- Charpy impact test (ASTM D6110 or ISO 179)
- Izod impact test (ASTM D256)
- Tensile impact test (ASTM D1822)
- Falling weight normal impact test (ISO 8256)

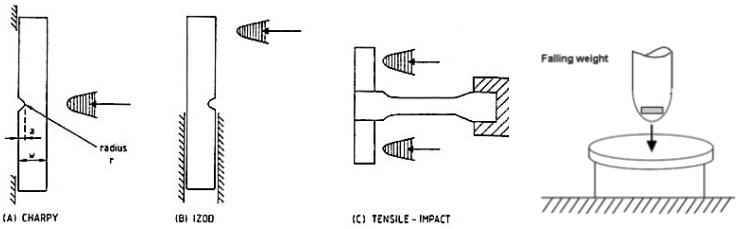

Figure II-42. Different configurations of impact testing.

Mechanical energy is required both to create a crack (initiation energy) and to allow its propagation through the material. If the available energy in the system undergoing impact exceeds the crack initiation energy, the crack will continue to propagate. In this case, complete failure will occur if the system has sufficient energy to also exceed the crack propagation energy.

Different factors can affect the impact strength in a material, specifically:

- *Rate of loading*: because plastic materials are viscoelastic, the speed at which the test piece or part is struck has a significant effect on the behavior of the polymer under impact loading. At low rates of impact, relatively stiff materials can still have good impact strength, but at high enough rates of impact, even rubbery materials will exhibit brittle failure. All polymer materials seem to have a critical velocity above which they behave as glassy, brittle materials. This has important consequences for designing with plastics, and both Charpy and Falling Weight tests may be used to screen potential candidate materials.
- *Temperature*: the viscoelastic nature of plastics makes the effect of temperature much more significant than it is for ceramics and metals. Decreasing the temperature tends to promote the onset of brittle failure, while increasing temperature has the opposite effect of increasing speed and so there is not a single temperature at which brittleness occurs, but a locus of temperature/speed values where the transition from ductile to brittle behavior takes place
- *Notch sensitivity*: A notch in a test specimen can dramatically lower the impact strength of the material, due to local stress concentration. All plastics are notch-sensitive, but the notch sensitivity varies with the type of plastic being considered. Both notch depth and notch radius have an effect on the impact behavior of materials

- *Fillers*: The peculiar impact properties of a polymer can be modified by filler incorporation. Modifiers might be added to act as barriers or crack blunting regions to the advancing crack front. Low molecular weight plasticizers are typically added to PVC to improve the impact behavior. Another way to improve the impact strength is the use fibrous fillers that act as stress transfer agents. Good coupling between the fiber and the polymer matrix is required to obtain significant improvements. Moreover, many micro- and nano- fillers have been observed to improve the impact toughness when added in a certain amount range or when surface treated.
- *Molecular weight, degree of crystallinity and orientation*: In general, a reduction in the average molecular weight reduces the impact strength and vice versa. On the other hand, increasing the percentage crystallinity decreases the impact resistance and increases the probability of brittle failure, so the thermal history of the product will influence the outcome of an impact event.
- *Processing conditions*: Processing conditions also play a key role in determining the impact behavior of a material. For instance, high processing temperatures may cause thermal degradation and, therefore, reduce the impact strength; inadequate drying of plastics that have a tendency to absorb moisture can have a dramatic effect in reducing the resulting impact strength. Moreover, molecular orientation is deliberately introduced by drawing films and fibers, for example, to give extra strength and toughness along the stretch direction compared to the isotropic material.

Impact testing methods usually yield data related to the toughness of a material, but they do not provide an actual toughness value. The energy absorbed during fracture is measured and such tests may be used for screening and comparing materials based on toughness.

2.2.6.4 Essential work of fracture (EWF)

Fracture toughness is a measure of resistance to cracking in notched specimens. In general, during fracture toughness testing, the load-versus-displacement behavior of a pre-cracked specimen is recorded [120]. In practice, the goal of fracture toughness testing is to measure a single parameter that is a material property and can be directly used in design.

The essential work of fracture method (EWF) is a relatively recent approach to experimentally characterize the plain stress fracture toughness of polymers and relative composites [14, 121]. According to this approach, [122], the total fracture energy (W_f) spent to bring a pre-cracked body to complete failure can be partitioned into an essential work (W_e) required in the fracture zone to create new fracture surfaces and a non-essential work (W_p) dissipated in the outer plastic zone related to yield the material (Figure II-43). It can be easily derived that the essential work of fracture should be proportional to the ligament length (L), whereas the non-essential work of should be proportional to L^2:

$$W_f = W_e + W_p = w_f\, L\, B = w_e\, L\, B + w_p\, \beta\, L^2\, B \qquad (II-26)$$

which can be rewritten as

$$w_f = w_e + \beta\, w_p L \qquad (II-27)$$

where B is the specimen thickness, β is a shape factor, w_e is the specific essential work of fracture, w_p is the specific non-essential work of fracture.

The quantities w_e and βw_p are determined by a linear interpolation of a series of experimental data of w_f obtained by testing specimens having different ligament lengths. The quantity w_p can be explicitly deduced for some shapes of the outer plastic zone with known β e.g., for circular, elliptical and diamond-type zones β is given by $\pi/4$, $\pi h/4L$, and $h/2L$, respectively, where h is the height of the corresponding zone [121].

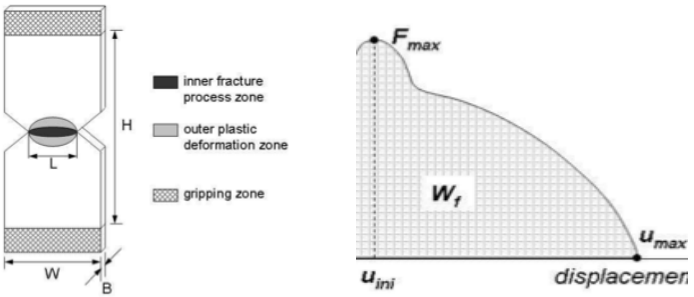

(a) (b)

Figure II-43. (a) DENT specimen and (b) characteristic load-displacement curve for DENT specimens of a relatively ductile polymer such as LLDPE.

Notched specimens such as the double edge notched tension (DENT) are commonly used for EWF testing. This specimen is characterized by a rectangular shape with a width *W*, length *H*. In order to prevent edge effects occurring in correspondence of the plastic and to ensure complete yielding of the ligament region before the crack starts to propagate, the maximum ligament length *L* should be lower than one third of the specimen width *W* or less than the plastic zone size. Moreover, the ligament length *L* should be greater than three to five times the specimen thickness *B* in order to favor a state of pure plane-stress [123]. Two sharp edge notches should be performed on each specimen, with direction opposite one another, by using razor pushing, razor sliding and razor tapping.

The fracture tests are conducted in tensile mode on DENT specimens that have the ligament lengths spanning the allowable rang, while a minimum of 25 specimens is usually required. Moreover, in order to verify that the tests were performed under plane-stress conditions, the obtained should be checked applying the Hill's criterion [124]. The procedure proposed by Hill consists in plotting the σ_{max} (i.e. ratio between the maximum load and the net-section *LB*) with respect to ligament length for each group of specimens. If the σ_{max} values are around 1.15 σ_y, the validity criterion is satisfied. A more useful method to check the validity was proposed by Williams and Rink through the standardization of the EWF test [122]. In this case, the σ_{max} values can be assumed valid if they fall within the range of 0.9 – 1.1 σ_{max} (Figure II-44).

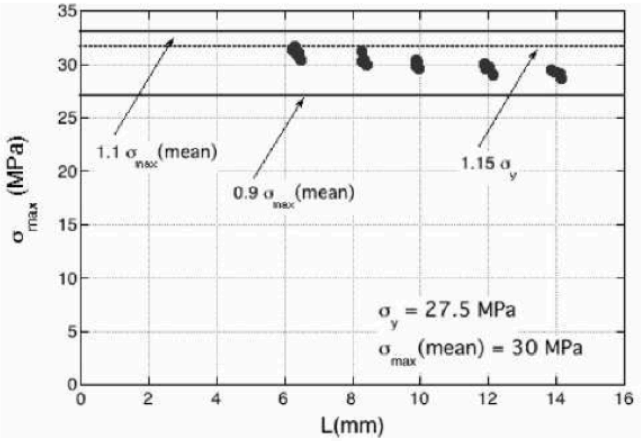

Figure II-44. Method proposed by William and Rink to verify the validity of the data obtained through the EWF test [122].

A more detailed analysis of the fracture energy assumes that the specific total work of fracture (w_f) can be divided into a specific work of fracture for yielding (w_y) and a specific work of necking (w_n) [121]:

$$w_f = w_y + w_n = \left(w_{e,y} + \beta' w_{p,y} L\right) + \left(w_{e,n} + \beta'' w_{p,n} L\right) \qquad (II-28)$$

where w_y and w_n are the yielding and the necking components of the specific essential work of fracture, respectively, while $(\beta' w_{p,y} L)$ and $(\beta'' w_{p,n} L)$ are the fracture components of the specific non-essential work of fracture.

2.3 Fiber reinforced polymer composites

2.3.1 General features

Composite materials are multiphase materials obtained by the combination of different materials, in order to attain properties that the individual components cannot attain by themselves. These materials can generally be tailored for various properties by choosing their components, proportions, distributions, morphologies, as well as the structure and composition of the interface between components. Owing to their strong tailorability, composite materials can be properly designed to satisfy the needs of many engineering and technological applications in the field of aerospace, automobile, electronics, construction, energy, biomedical and other industries [13].

Among the most advanced composites, fiber reinforced polymer composites (FRPC), generally consists of a polymer matrix (e.g., thermoplastic or thermosetting) reinforced by thin diameter fibers (e.g. glass, carbon, graphite, aramids, boron, etc.). The fibers provide most of the strength and stiffness while the polymer serves as the binder. The reasons why they are among the most common composites include their high specific strength and stiffness, low cost and relatively simple manufacturing principles. On the other hand, the main drawbacks of FRPC include low operating temperatures, high coefficients of thermal and moisture expansion and anisotropic properties in certain composites [125]. Applications of FRPC range from sport goods, to automotive components, to the space shuttle.

A FRPC component used for lightweight structural applications typically show several attractive properties such as:

- High specific stiffness and strength (compared to steel and aluminum)
- Good fatigue and creep resistance
- Toughness and damage tolerance

- Vibration damping ability
- Low friction coefficient and good wear resistance
- Chemical and corrosion resistance (generally controlled by the matrix)
- Dimensional stability
- Low electrical resistivity, high electromagnetic interference shielding
- High thermal conductivity

FRPC can be classified according to (i) fiber architecture, (ii) the matrix material and (iii) the type of the reinforcing fiber. Some representative schematics of the possible structures and morphologies typically found in FRPC is depicted in Figure II-45.

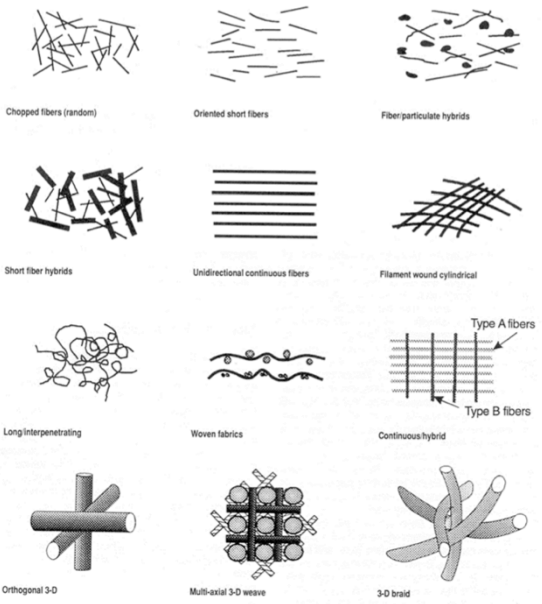

Figure II-45. Different fiber architectures and distributions in FRPC.

2.3.1.1 Fiber architecture

The properties of many composites are strongly dependent on the arrangement and distribution the fibers. Moreover, other parameters such as fiber diameter and aspect ratio, volume fraction of the fiber, their alignment and packing arrangement

have a direct impact on the mechanical properties of the composite. In special cases, the chemical, thermal and electrical properties may also be altered by the choice of reinforcing material.

- *Glass composition*: the chemical composition of the glass can have a direct effect on the fiber properties which can impact the composite performances
- *Filament diameter* : in general, finer filaments gives the composites higher flexural and tensile strengths and modulus. On the other hand, coarser filaments gives composites improved compressive strengths
- *Glass to resin ratio*: in general, the physical properties for GF reinforced composites follow the *rule of mixtures*, thus the composite's strength increases as matrix content is reduced
- *Fiber distribution*: reinforced composites that have the glass strands aligned parallel to each other have the maximum strength and stiffness in the direction of the alignment. However, when the alignment is random within the matrix, the mechanical strength is fairly uniform in all directions but in this case the physical properties are relatively low

Depending on the above considerations, fibers can be organized in laminae (sheets containing aligned long fibers), in short or continuous form. High-performance polymer components usually consist of layers or laminate joined in a predetermined arrangement. The fibers in the laminae may be continuous or in short lengths and can be aligned in one or more directions or randomly distributed in two or three dimensions (Figure II-46).

Another typical architecture of FRPC is represented by short-fiber composites (SFC), which has been recently used for the realization of many components because of several advantages, such as the easier and more versatile fabrication method compared to continuous fiber composites (Figure II-47). In particular, processing of continuous fiber composites tends to be more problematic due to the difficult impregnation of long fibers (or fabric wovens). Quite on the contrary, many manufacturing techniques typical of the thermoplastics (e.g. injection molding, extrusion, etc.) can be used for the fabrication of short-fiber polymer composites.

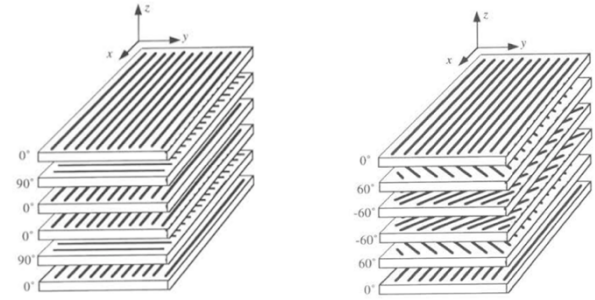

(a) (b)

Figure II-46. Arrangement of plies in (a) a cross-ply laminate and (b) angle-ply laminate sandwiched between 0 plies [126].

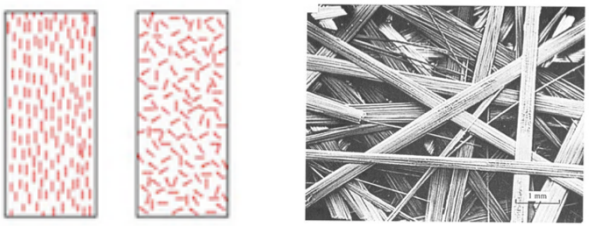

(a) (b)

Figure II-47. (a) Typical fiber dispersion and distributions in short-fiber composites and (b) SEM micrograph of chopped fiber strands before incorporation with the polymer matrix [126].

2.3.1.2 Reinforcing fibers

Glass is the most common fiber used in FRPC. Its advantages include its high strength, low cost, high chemical resistance and good insulating properties (Table II-2).

Table II-2. Typical mechanical properties of fibers used in FRPC [125].

Property	Units	Graphite	Aramid	Glass	Steel	Aluminum
Specific gravity	—	1.8	1.4	2.5	7.8	2.6
Young's modulus	GPa	230	124	85	206.8	68.95
Ultimate tensile strength	MPa	2067	1379	1550	648.1	275.8
Axial coefficient of thermal expansion	μm/m/°C	–1.3	–5	5	11.7	23

The drawbacks include low elastic modulus, poor adhesion to some polymers, high specific gravity, sensitivity to abrasion (which might reduce the tensile strength), and low fatigue strength.

The main types of GF are *E-glass* and *S-glass*. While *E-GF* is commonly used for a broad variety of applications including structural and decorations, *S-GF* show higher performances because it can retain its great strength at high temperatures compared to E-GF and has higher fatigue strength. It is used mainly for aerospace applications. Other types of commercially available fibers are *C-GF* used in chemical environments, such as storage tanks. Additionally, *R-GF* are used in structural applications such as construction, while *D-GF* are commonly employed for applications requiring low dielectric constants, such as radomes. Finally *A-GF* are typically used to improve surface appearance.

Glass fibers are generally produced by drawing from a melt which is formed in a refractory furnace at about 1400 °C. The melt mixture generally includes sand, limestone, and alumina (Figure II-48).

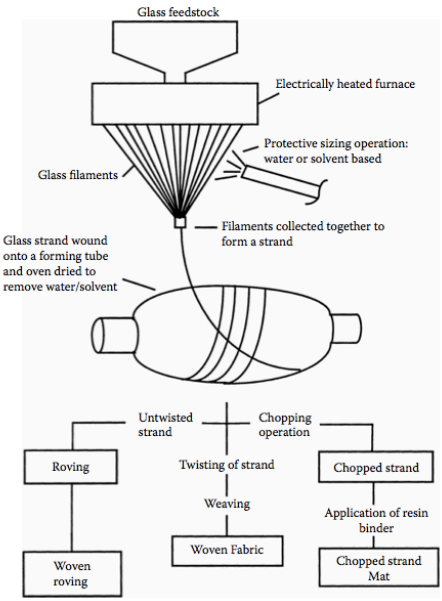

Figure II-48. Schematic of manufacturing process of GF [125].

The melt is stirred, while maintained at a constant temperature, and it passes through many (up to 250) heated nozzles of about 10 μm diameter, where it is drawn into filaments of specific size. The fibers are finally sprayed with an organic sizing solution before they are drawn. The sizing is typically a mixture of binders, lubricants, and coupling and antistatic agents. While binders allow filaments to be packed in strands, lubricants prevent abrasion of filaments, and coupling agents can give better adhesion between the inorganic GF and the organic matrix. Fibers are finally drawn into strands (i.e. groups of more than 204 filaments) and wound (i.e. array of strands).

Graphite fibers and carbon fibers are commonly used in high-modulus and high-strength applications such as aircraft components and sport equipment components. The advantages of graphite fibers include high specific strength and modulus, low coefficient of thermal expansion and high fatigue strength. On the other hand, the high cost, low impact resistance, and high electrical conductivity might represent considerable drawbacks. Graphite fibers are generally manufactured from three precursor materials: rayon, polyacrylonitrile (PAN), and pitch. PAN is the most popular precursor and the process to manufacture graphite fibers from it is given next (Figure II-49).

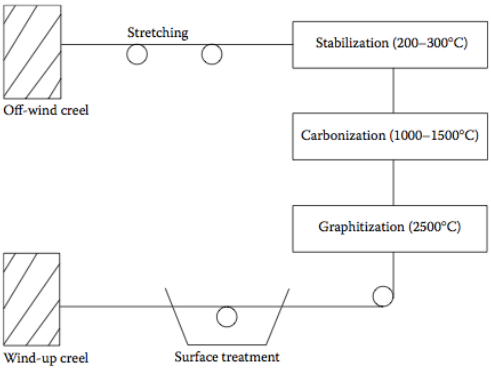

Figure II-49. Stages of manufacturing of carbon fibers obtained from PAN precursor [125].

PAN fibers are first stretched five to ten times their length in order to improve their mechanical properties and then passed through three heating processes, including stabilization (carried out between 200 and 300°C), carbonization (i.e pyrolysis in an inert atmosphere of nitrogen or argon between 1000 and 1500°C) and graphitization (i.e. heating above 2500°C to impart a more graphitic microstructure).

At the end of the heat treatment process, the fibers are surface treated (to enhance the fiber adhesion when they are used in composite structures) and finally collected on a spool.

Carbon fibers differ from graphite fibers for their content of carbon (~ 93 to 95 %), while graphite has more than 99% carbon content. In addition, carbon fibers are produced at around 1320 °C and graphite fibers are typically manufactures above 1900 °C.

Aramid fibers are based on an aromatic organic compound made of carbon, hydrogen, oxygen and nitrogen. Its advantages are low density, high tensile strength, low cost and high impact resistance. Its drawbacks include low compressive properties and degradation when exposed to sunlight. Commercially available aramid fibers include *Kevlar 29®* and *Kevlar 49®*, which present similar specific strengths, but Kevlar 49 has a higher specific stiffness and Kevlar 29 is mainly used in bulletproof, vests, ropes, and cables. Aramid fibers are widely applied in high-performance applications in the aircraft industry.

Aramid fibers are produced from a solution of proprietary polymers and strong acids such as sulfuric acid. The solution is extruded into hot cylinders at 200°C, washed and dried on spools. The fibers are finally stretched and drawn to increase their strength and stiffness.

While carbon, graphite and aramidic fibers are mainly combined to thermosetting matrices (e.g. epoxies, phenolics and polyesters) in order to manufacture advanced polymer composites, GF have been widely applied in fiber reinforced thermoplastic composites.

2.3.1.3 Polymeric matrix typology

The most commonly used *thermosetting resins* are epoxy, phenolic and vinyl ester. In thermosetting polymers, the liquid resin is converted into a hard rigid matrix by cross-linking, which leads to the formation of a three-dimensional network [126]. The mechanical properties depend on the network molecular units and on the density of the cross-links. Curing can be achieved at room temperature, but it is usually carried out by a multistep heat treatment, with final post-cure at high temperature to minimize any further cure and change in properties during service. Thermosets have rather different properties from thermoplastics, in particular much lower strains to failure (Table II-3). Thermosets are essentially brittle materials, while thermoplastics can undergo high plastic deformation. Moreover, there are also significant differences between different types of thermoset. In general, epoxies are tougher than unsaturated polyesters or vinyl esters, can have good resistance to

heat distortion and shrink less during curing. Epoxies are thus usually preferred also because of their cheap cost.

Table II-3. Physical and mechanical properties of polymer matrices [126].

Matrix	Density ρ (Mg m^{-3})	Young's modulus E (GPa)	Poisson's ratio ν	Tensile strength σ_r (GPa)	Failure strain ϵ_r (%)	Thermal expansivity α (10^{-6} K^{-1})	Thermal conductivity K (W m^{-1} K^{-1})
Thermosets							
epoxy resins	1.1–1.4	3–6	0.38–0.40	0.035–0.1	1–6	60	0.1
polyesters	1.2–1.5	2.0–4.5	0.37–0.39	0.04–0.09	2	100–200	0.2
Thermoplastics							
Nylon 6.6	1.14	1.4–2.8	0.3	0.06–0.07	40–80	90	0.2
polypropylene	0.90	1.0–1.4	0.3	0.02–0.04	300	110	0.2
PEEK	1.26–1.32	3.6	0.3	0.17	50	47	0.2

Thermoplastic polymers have become progressively more important because of their higher ductility and processing speed compared to thermosettings. Thermoplastic matrices are not cross-linked by they derive their strength and stiffness from the intrinsic properties of the monomer units and the very high molecular weight. In addition to their high failure strains, they generally exhibit good resistance to attack by chemicals and good thermal stability (in particular polyether ether ketone (PEEK)). Most thermoplastics exhibit good resistance to water absorption of water, while this is not true of the polyamides. Unlike thermosettings, all thermoplastics yield and undergo large deformations before fracture and their mechanical properties strongly depend on the temperature and applied strain rate. This means that the matrix may allow a redistribution of the loads during deformation and in-service loading conditions. When manufacturing FRPC, processing of thermoplastics tends to be more difficult than with thermosets, mainly due to the high viscosity of the melt polymer which makes the impregnation of fibers (or fabric wovens) much more difficult. Once fibers and matrix have been combined, various shaping operations typical of the thermoplastics (e.g. injection molding, extrusion, calendering and thermoforming) can be carried out.

Typical applications of advanced polymer composites include:

- *Aircraft and marine components* for weight reduction, performances enhancement and improved resistance in high temperature and moisture conditions, corrosive environments
- *Sporting goods and medical devices* (such as prosthesis) because of high stiffness, light weight, and transparency to radiation
- *Automotive components (*including bumpers, body panels, and doors) for improved specific mechanical properties, fatigue life and resistance to harsh conditions

- *Commercial commodities* such as handles and decoration components, which can be made lighter than traditional metal tools and thus are suitable for children and people with physically challenged hands

By utilizing both the high strength and the excellent insulating electrical properties of GF, the aircraft industry has found this fiber type as an excellent reinforcement for several applications. The printed circuit board industry has used the combination of electric properties and superior dimensional stability of GF to manufacture circuit boards that can be used under the various environmental conditions. Thanks to the advent of nanocomposite materials, the polymeric matrix can be electrically conductive due to the nanofillers present within it. This property allows the monitoring of the matrix without changing dramatically the mechanical properties of either matrix and composite [53]. Finally, in numerous applications glass reinforcement is chosen because it allows composites to retain maximum properties in high moisture environments. Thus the water resistance helps maintain the physical characteristics of the composite over prolonged time exposure to aqueous atmospheres [127].

2.3.1.4 Hybrid short-fiber composites

The properties of a polymer composite are strongly dependent on their microstructure. For example, the tensile modulus of a polymeric matrix can be remarkably increased by the incorporation of short fibers, especially when a sufficient fibers alignment have been obtained during processing (such as injection molding). However, the properties are hardly changed in the transverse direction. Moreover, the mechanical properties of the short-fiber reinforced composites are also strongly dependent on the effectiveness of the stress transfer from the matrix to the fibrous filler. In order to optimize the mechanical properties of the resultant composites, two basic conditions are strongly required: (i) sufficient contact area and (ii) strong interfacial bonding between the matrix and fiber. The increase of the aspect ratio (length/diameter) in continuous-fiber composites leads to have the advantage to make full use of the reinforcement, but more complicated and problematic fabrication techniques are required. Therefore, the best option would be to have an effectively continuous reinforcement while still adopting the fabrication techniques commonly used for the production of short-fiber reinforced composites [128].

The addition of a small amount of a second filler phase (sufficiently miscible with the matrix) might potentially result in an effectively continuous reinforcing network of

fibers, improving the properties of the final material in all three directions (Figure II-50).

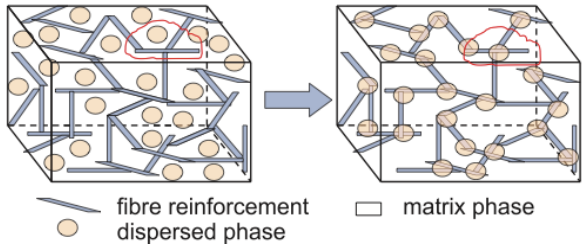

Figure II-50. Incorporation of a small amount of a second reinforcing filler can potentially result in a continuous fiber network, producing a significant enhancement in the composite mechanical properties [128].

In particular, the length scales of microcomposites (such as glass and carbon fiber composites) and nanocomposites are so different that the two can be combined. For instance, the thickness of an exfoliated silicate sheet is 10,000 times smaller that the diameter of an average glass fiber. The nanoparticles dispersed within the matrix are only supposed to improve the matrix-dominated properties of the composite. The modulus and strength of the composite is mainly determined by the fibers, and therefore the increased modulus of the matrix is not expected to provide any significant increase in the modulus of the bulk composite. On the other hand, since the compressive strength and flexural strength of a fiber composite depend on the modulus of the matrix, the matrix nanomodification might provide a further reinforcing mechanism.

Recent studies on short GF reinforced nanocomposites reported that when the filler is also present at the fiber/matrix interface, a higher adhesion might result from the improved interactions, leading to a stronger interface and better stress transfer between the reinforcing fibers and the matrix [129]. Hybrid composites that combine the advantages of nano-materials and micro-size reinforcements showed a concurrent enhancement of the viscoelastic behavior and impact toughness. Therefore, matrix nanomodification offer the possibility to produce lighter and stronger composites, as part of the higher density GF can be replaced with a small amount of the nano-materials. In addition to decreasing the weight of the composite, the processability is significantly improved, as confirmed by rheological measurements, because the increase in polymer viscosity reduces with decreasing the GF content. Moreover, other physical properties of the composites (such as

electrical and thermal conductivity) might be enhanced when dispersing a conductive nanofiller in the matrix.

2.3.3 Mechanical and functional properties of short-fiber reinforced polymer composites (SFPC)

2.3.3.1 Physical and mechanical properties

The mechanical and physical properties of SFPC strongly depend on different factors, in particular: (i) type and amount of the reinforcing fibers, (ii) fibers morphology (i.e. orientation, aspect ratio) and (iii) interfacial bonding between fibers and matrix. All these variables have a direct impact on the final properties exhibited by the resultant composites [130]. The incorporation of short fibers to thermoplastics generally leads to significant improvements in mechanical properties (such as strength and elastic stiffness) (Table II-4).

Table II-4. Strength (σ) and elastic modulus (E) of some SFPC (C) and relative matrices (M) [130].

Materials	Fibre content (%)	σ_M^u (MPa)	σ_c^u (MPa)	E_m (GPa)	E_c (GPa)
ABS/SGF	15 vol.	42.8	68.0	2.39	8.33
ABS/SGF	30 wt.	43.4	68.0–84.0	2.24	5.12–6.47
ABS/ PA6(70:30)/ SGF	30 wt.	43.4	93.0	2.24	8.82
PA 6,6/ SEBS-g-MA(80:20)/ SGF	30 wt.	39.0	65.0	0.83	4.07
PA6,6/SGF	50 wt.	~78.0	~250.0	—	—
PEEK/SGF	10 wt.	91.4	108.9	3.10	4.70
PEEK/SCF	10 wt.	91.4	135.6	3.10	6.37
PP/SCF	25 vol.	31.6	60.1	1.30	14.9
PP/SGF	25 vol.	31.6	51.5	1.30	8.75
PC/SGF	30 wt.	40.3	67.2	1.33	8.74

Note: volume fraction (vol.); weight fraction (wt.); short glass fiber (SGF); acrylonitrile-butadiene- styrene (ABS); polypropylene (PP); polycarbonate (PC); polyamide 6,6 (PA6,6); polyamide 6 (PA6); maleated styrene-ethylene butylenes-styrene (SEBS-g-MA).

Moreover, for relatively brittle polymer matrices, incorporation of short fibers may increase the fracture toughness.
Quite on the contrary, fracture toughness may be reduced in certain systems, in particular when considering polycarbonate and polyamide matrices. More specifically, the mechanical and physical properties of SFPC have been shown to depend mainly on the following factors [130] :

- Properties of components
- Fiber volume fraction
- Fiber orientation distribution
- Fiber aspect ratio distribution
- Fiber-matrix interface shear strength (ISS)

Theoretical predictions of strength, stiffness and fracture toughness of SFPC are usually based on models that accounts for the above variables. Likewise continuous fiber reinforced composites, the mechanical properties of SFPC strongly depend on the efficiency of stress transfer from the matrix to the fibers. Different theories and models have been formulated to predict the stress transfer in SFPC [127, 131, 132]. However, because the stress transfer takes place between the only fiber and surrounding matrix, these models do not account for the neighboring fibers on the stress transfer. In real SFPC, the neighboring fibers affect the stress transfer between matrix and fibers. However, increasing research on nanocomposites led to some clear indications that the matrix nanomodification can significantly enhance the ISS in fiber reinforced composites, allowing the optimization of the stress transfer also in SFRC.

Different examples are reported in the recent literature about the beneficial effect of introducing a nanofiller in SFPC, in order to create hybrid composites that combine the advantages of nano-materials and micro-size reinforcements (Figure II-51).

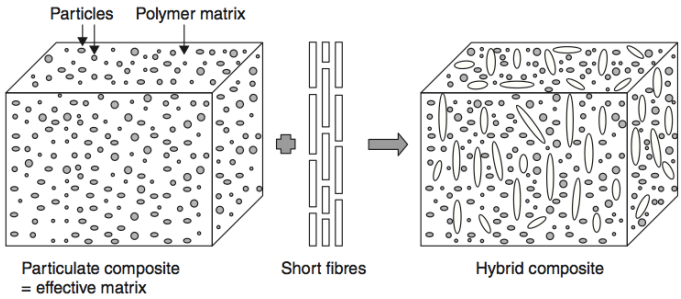

Figure II-51. Incorporation of micro- or nano- fillers in SFRP to create hybrid composites.

For instance, when short fibers were combined with exfoliated layered silicate in polyamide matrix, a significant enhancement of the elastic modulus was observed. Moreover, layered silicate in concentration of 4 wt% can add around 2 GPa to a composite based on PA matrix and short GF [133]. The layered silicate can therefore reduce the loading of GF (or replace larger amounts of low aspect ratio fillers), reducing the density and viscosity of the compound. Moreover, Akkapeddi [134] reported that the nature of the increase in properties of PA 6 composites reinforced by MMT and short GF is not completely additive, but there is clearly an increase over single filler based composites. The synergistic role of the multi-scale reinforcements can be explained by a positive change in the stress distribution near the fiber surface and the plastic zone ahead of the crack tip.

Yoo et al. studied the morphology and mechanical properties of Nylon 6 hybrid composites containing both an organoclay and GF, observing an orientation of both fillers due to extrusion processing (Figure II-52). Moreover, the elastic modulus was predicted by applying a two-particle population model based on the Mori-Tanaka composite theory and accounting for changes in particle aspect ratios.

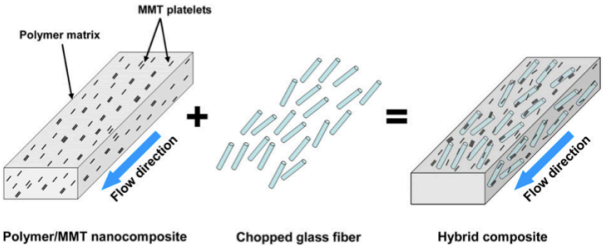

Figure II-52. Incorporation of MMT nanoplatelets and chopped glass fibers to create hybrid fiber reinforced composites [135].

Another major advantage of clay nanocomposites for fabricating fiber composites is its superior barrier characteristics to moisture and gases. The enhanced gas barrier properties of hybrid composites are finding applications in packaging material, flame retardant, polymer coatings under the UV environment and concrete materials. For instance, modification of fiber composites employing clay as a barrier significantly improved the alkali corrosion toward the fiber surface in an alkaline environment due to the barrier resistance of clay nanocomposites [136]. Isitman et al. [20] observed a synergistic effect on the flame retardancy of organoclays and GF in nylon 6 matrix.

Nevertheless, other important mechanical properties, such as the viscoelastic behavior (including creep and dynamic mechanical behavior), fracture toughness

and impact toughness in thermoplastic hybrid composites have not been investigated sufficiently and are yet to be exploited. Moreover, little research about the synergistic effects of glass fibers and the nanofiller on other governing physical properties of composites has been carried out. For instance, one of major issues for composites is to reduce the thermal expansion coefficient (CTE), in order to obtain higher dimension stability. It is known that adding glass fiber to a polymeric matrix can reduce its CTE, while nanofiller incorporation also leads to a lowering in CTE of the matrix. Nevertheless, very few studies have been addressed to the investigation of the dimension stability in hybrid composites.

2.3.3.2 Fiber-matrix interfacial adhesion

The mechanical properties of SFPC strongly depend on the efficiency of stress transfer from the matrix to the fibers. Nevertheless, because of the complicated morphology of short fibers dispersed in a polymer matrix, the stress-transfer models studied for continuous fiber reinforced composites cannot be directly applied in the composites based on short fibers. Moreover, the interfacial adhesion in hybrid composites is further complicated by possible synergistic effects due to the presence of fillers. However, increasing research on nanocomposites led to some clear indications that the matrix nanomodification can significantly enhance the interfacial shear strength (ISS) in fiber reinforced composites, allowing the optimization of the stress transfer also in SFP.

An interesting examples is provided with PP/GF composites, where interfacial adhesion is a critical issue due to the non-polar nature of the matrix [137]. Over the years, two main strategies have been proposed to improve the fiber/matrix adhesion in PP/glass composites: i) the development of specific fiber sizings/coatings [138-145] and/or ii) the addition of coupling agents to the PP matrix [140, 141]. Thomason and Schoolenberg [143] observed that the use of silane coupling agents have little effect on the level of PP/GF interfacial shear strength. At the same time, they experimentally observed that full commercial coating formulation applied to glass fibers is very important for the interface strength: variations of one order of magnitude in PP/GF adhesion were observed depending on the nature of the glass fiber coating (Figure II-53a). As reported by Barber et al. [146], SWCNTs can be used as strain sensors to evaluate different levels of interfacial adhesion between sized E-glass fibers and PP matrix (Figure II-53b)

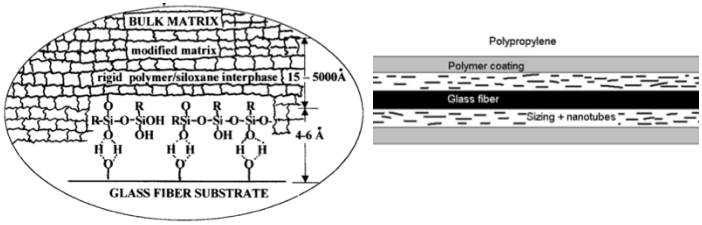

(a) (b)

Figure II-53. (a) Concept of a polymer/siloxane/glass interphase [147] and (b) Schematic representation of a sized and coated E-glass fiber incorporated in PP micro-composite [146].

On the other hand, Mader and Freitag [140] evidenced how the bond strength in the PP/GF system can be remarkably enhanced by modifications of the PP matrix, such as the addition of polypropylene grafted with acrylic acid or irradiation with electron beams. More recently, some indications emerged on the fact that nanoparticles homogeneously dispersed in a polymer matrix [32, 148, 149] or localized at the interfacial region [150-152] could play a beneficial role on the fiber/matrix interfacial adhesion in several types of structural composites. For instance, in a recent work of our group, it was shown how the incorporation of both non-functionalized and dimethyldichlorosilane-functionalized silica nanoparticles led to a remarkable increase of the interfacial strength in PP/GF systems [129] (up to a factor of about 5 for a 7 wt% content of surface treated nanoparticles) with respect to the case of neat matrix. Moreover, in another recent research, we reported that the adhesion measured during SFFT for PP/GF systems modified with the addition of xGnP was found to significantly increase (up to a factor of about 6 for a 7 wt% content of xGnP) with respect to the case of neat PP. The experimental results were explained by considering that xGnP increases the work of adhesion of the matrix with respect to the glass fibers, as proven by wettability measurements in different liquids [153].

Interestingly, recent research on the improvement of ISS in nanocomposites/GF systems emphasized that the addition of nanoparticles can also result in a simultaneous enhancement of the mechanical properties of the polymer matrix [32] or induce specific functional properties [154].

2.3.3.3 Functional properties

One of the most recent trend in the application of advanced polymers and composites is their use in electronic packaging (Figure II-54a), where highly thermally and electrically conductive materials are required.

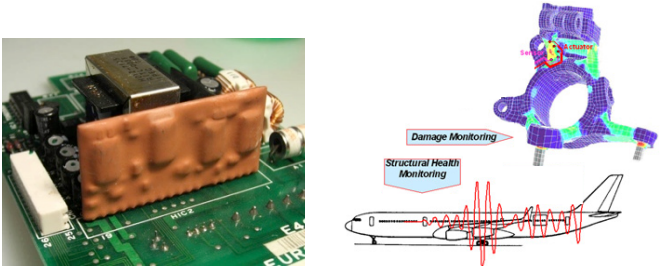

(a) (b)

Figure II-54. (a) Use of conductive polymer parts in electronic packaging and (b) examples of health monitoring applications by use of conductive composites.

These polymers are often incorporated with micro- or nano- fillers (such as short carbon fibers, CB, xGnP, etc.) with a high conductivity to fabricate the composites to meet the high conductivity criterion.

Another typical application of electrically conductive nanocomposites or composites is their use in monitoring purposes (Figure II-54b). This methodology implies the measurement of the electrical resistance of the components, without any additional sensors. For instance, the usage of an electrically conductive polymer matrix can provide some insight on matrix-related failure mechanisms, enabling the approach also for structural composites reinforced with non conductive fibers, such as glass, basalt or organic fibers [53, 54].

Shape-memory polymers (SMPs) and their composites is a special family of smart materials that have the ability to return to their original (permanent) shape from a deformed state (temporary shape) through the application of an external stimulus (trigger), such as temperature change [155]. In addition to thermal actuation, SMPs composites filled with functional fillers can also be actuated by other external stimuli, such as electrical-resistive heating and the magnetic field [155]. Therefore, SMPs can be not only electrically and thermally conductive materials, but also can display the capability of shape-memory effect and respond in various ways to stimuli. These novel actuation approaches play a key role in the development of important applications in the field of aerospace, automobile, textiles and medical science.

Chapter III

Experimental

3.1 Materials

3.1.1 Polypropylene

The matrix of the nanocomposites used in this work was an isotactic homopolymer polypropylene (MFI at 190 °C and 2.16 kg = 6.9 g/10min, density = 0.904 g/cm^3) produced by Polychim Industrie S.A.S. (LOON-PLAGE, France) and provided by Lati Industria Termoplastici S.p.A (Varese, Italy) with the commercial code PPH-B-10-FB.

Isotactic polypropylene (iPP), in which all the methyl groups are positioned on the same side of the zigzag plane, results from polymerization of only one isomeric configuration form of propylene monomer (Figure III-1).

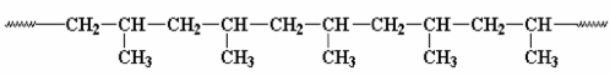

Figure III-1. Chemical representation of isotactic polypropylene macromolecule.

In order to select one isomeric configuration during polymerization, the use of catalysts is necessary. The most common commercially used catalysts used for preparation of iPP are Ziegler-Natta catalysts, such as titanium trichloride ($TiCl_3$), combined with an organometallic compound (typically aluminum triethyl or aluminum tributyl as cocatalyst) to initiate the polymerization. Since Zeigler-Natta catalysts are multi-sited catalysts, the resultant polypropylene (PP) can include polymer molecules with a broad range of molecular weights, which induce different properties. The principal properties of the iPP used in this research, according to the producer datasheet, are listed in Table III-1.

Polypropylene is one of the most commercially used thermoplastic polymer [67]. In particular, iPP is a semi-crystalline polymer, which is employed in a wide variety of industrial applications because of its ease of processing, low density, remarkable stiffness and relatively low cost (Figure III-2). Nevertheless, its use has been limited by its brittleness at low temperatures. In order to enhance PP impact properties, several kinds of impact modifiers (including EPR, EPDM and various POEs) have

been successfully used, proving superior low temperature performances which are especially required in the automotive field [156]. Moreover, to provide PP an optimal balance of stiffness and toughness, elastomers such as EPR, EPDM and POEs have been added, together with inorganic micro- or nano- sized fillers including $CaCO_3$, SiO_2, talc and $BaSO_4$ [8].

Figure III-2. Typical applications of PP: fiber spinning, production of commodity items and packaging.

Table III-1. Technical datasheet of the isotactic PP (PPH-B-10-FB).

Sample	Test method	Value
MFI (g/10min)	ASTM D1238 (190 °C and 2.16 kg)	12 ± 2
Molecular weight distribution		broad
Density (g/cm^3)	ASTM 1505	0.904
Atacticity	Xylene solubles	5 % max
Vicat softening point (°C)	ASTM D1525-A (9,81 N)	154
Heat deflection temperature	ASTM D648 (455 kPa)	82
Tensile strength at yield (MPa)	D638 (50 mm/min)	35
Elongation at yield (MPa)	D638 (50 mm/min)	14
Flexural modulus (MPa)	ASTM D790 (1.3 mm/min, 1% secant)	1650 max
Rockwell hardness (R scale)	ASTM D785	111

FUSABOND® P M-613-05 maleic anhydride modified polypropylene (PPgMA) (MFI at 190 °C and 2.16 kg = 106.8 g/10min, density = 0.903 g/cm^3, maleic anhydride content = 0.35 - 0.70 wt%), was supplied by DuPont™ de Nemours (Geneva, Switzerland).

PPgMA is commonly incorporated in PP composites and nanocomposites as a compatibilizer (Figure III-3). The general principle of compatibilization is to reduce the interfacial energy between the polymer and the filler in order to increase adhesion. Thus, the resulting composite exhibits enhanced properties (i.e. interfacial and mechanical properties) which are appropriate for most end uses. Generally, adding compatibilizers results in improved adhesion of the polymer with the reinforcing fibers and/or finer dispersion of the micro- or nano- filler, as well as more regular and stable morphology.

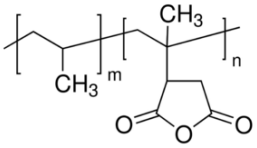

Figure III-3. Chemical representation of maleic anydride grafted polypropylene.

3.1.2 Glass fibers

E-glass fibers, designed as RO99 P319, were supplied by Saint-GobainVetrotex (Chambèry Cedex, France) and were used as-received. These glass fibers (GF) are indicated as treated with a silane-based coupling agent specifically designed for polypropylene matrices (Figure III-4). Chopped strand glass fibers (single fiber diameter of 15.3 ± 1.5 μm, and average length of 6.50 ± 0.44 mm) were obtained by chopping long glass fibers using a chopper gun CDA-08 provided by GlasCraft (Graco®, Bury, England).

Glass fibers coated with expanded graphite nanoplatelets (xGnP) were prepared by sonication of xGnP-M5 in isopropanol with a filler concentration of 5 mg/ml. Sonication was carried out using a Misonix S-4000-010 (Farmingdale, NY) for 1 h (30% amplitude, 8 W power) equipped with a probe of 12.5 mm diameter. After adding the glass fibers to the solution, a second sonication was performed for ½ h. Coated glass fibers were finally rinsed in isopropanol and left under hood overnight to let the solvent completely evaporate. The xGnP content added onto the fibers' surfaces through sonication was measured around 0.10-0.15 wt% as considered with

respect to the composite weight. An optical micrograph of pristine GF and xGnP-coated glass fibers is represented in Figure III-5.

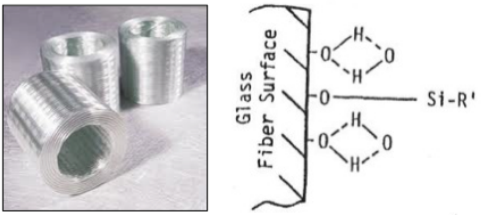

(a) (b)

Figure III-4. (a) Representative image of GF bobbin and (b) schematic of the surface functionalization using silane-based coupling agents.

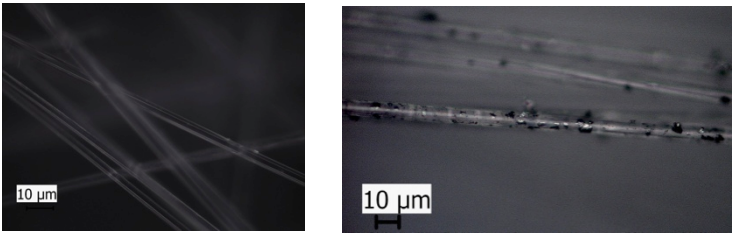

(a) (b)

Figure III-5. Optical micropicture of the GF as received (a) and the xGnP-coated GF (b).

Glass fibers are typically combined to thermoplastic or thermosetting polymer matrices in order to produce reinforced composite materials, whose mechanical properties are greatly enhanced and can be applied in structural applications. Moreover, composite materials represent a very attractive family of materials because their properties can be tailored to meet the specific needs of a variety of applications. The mechanical and thermal properties of a composite generally follow the rule of mixtures. As the glass fiber loading can reach 70–75% by weight (50–60% by volume), a proper selection of the correct glass product is critical [157].

Glass fiber reinforcement is typically available in many forms, including continuous strands, chopped fibers, fabrics, and nonwoven mats. In addition to form, selection of a reinforcement product involves choosing a glass type, chemistry on the glass (sizing) filament diameter and tex. The glass type governs mechanical, thermal, and corrosion properties, while the sizing protects the glass during handling

and provides better compatibility with the polymeric system. Filament diameter and strand tex are usually chosen in order to balance physical properties and manufacturing efficiency.

3.1.3 Fumed silica nanoparticles

Both untreated and surface treated fumed silica nanoparticles were supplied by Evonik Industries AG (Hanau, Germany). Untreated nanoparticles (Aerosil® A380) had an average primary particle size of 7 nm and a specific surface area of 321±3 m^2/g, as determined by BET analysis [158].

In order to study the effect of silica surface nature on the properties of the nanocomposite systems, dimethyldichlorosilane functionalized silica nanoparticles (Aerosil® R974) were characterized by an average primary particle size of 12 nm and a BET specific surface area of 124±1 m^2/g.

The main features of the fumed silica used in this work are reported in Table III-2.

Table III-2. Data from technical datasheet and experimental measurements on Degussa Aerosil® fumed silica nanoparticles.

Sample	Aerosil R974	Aerosil A380
BET surface area [(a)] (m^2/g)	124 ± 1	321 ± 3
Primary particle diameter (nm)	12	7
Density [(b)] (g/cm^3)	2.298 ± 0.017	2.356 ± 0.017
Moisture content (wt%) (2h @ 105 °C)	≤ 0.5	≤ 2.5
SiO_2 content (wt%)	≥ 99.8	≥ 99.8

[(a)] : Determined by porosimetry technique.
[(b)] : Measured by helium pycnometry at 23 °C, using a testing chamber of 3.5 cm^3.

Aerosil® hydrophilic fumed silica nanoparticles (such as A380) are commonly used in paints and coatings, and also added in cable resin compounds and unsaturated polyester resins, in adhesives, sealants and printing inks. These nanoparticles are used to control rheology and thixotropy of liquids, binders, polymers. On the other hand, Aerosil® hydrophobic fumed silica nanoparticles (such as Aerosil R974) are employed in silicone rubber adhesives and sealants, defoamers, and toners. These nanoparticles can provide a low thickening effect and good processability, enabling high filler loadings in polymer nanocomposites, while maintaining good transparency.

Figure III-6 reports a representative TEM image of silica R974 nanoparticles, characterized by primary particles with size of 12 nm, organized in aggregates and agglomerates.

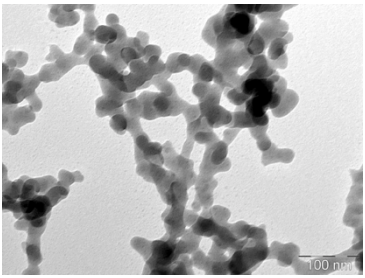

Figure III-6. Transmission electron microscopy of silica R974.

3.1.4 Expanded graphite nanoplatelets (xGnP)

Expanded graphite nanoplatelets xGnP® - M5 have been supplied from XG Sciences® (East Lansing, USA). This filler is characterized by platelets with an average diameter of ~5 μm (Figure III-7a-b), thickness in the range of 10~20 nm and a specific surface area of around 150 m^2/g. Details on the exfoliation process as well as on the morphology of xGnP can be found elsewhere [159].

In order to investigate the effect of graphite platelet size on the properties of the nanocomposites, xGnP-C750, supplied from XG Sciences®, were also used to prepare the materials. This filler is represented by platelets with an average diameter of 0.7-0.8 μm and a specific surface area of around 750 m^2/g. The principal physical characteristics of xGnP-M5 and xGnP-C750 are reported in Table III-3.

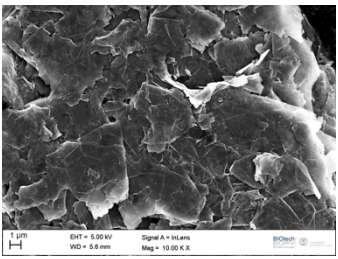

(a)

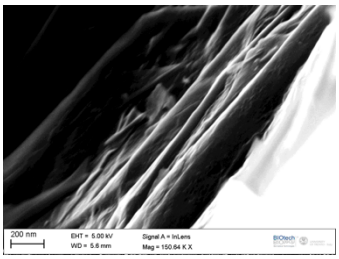

(b)

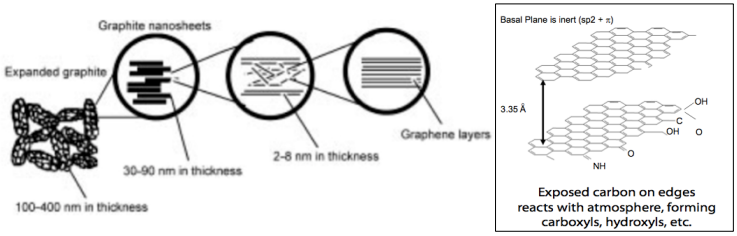

(c)

Figure III-7. ESEM images of (a) graphite nanoplatelets xGnP®-M5 and (b) package at higher magnification showing layered structure. (c) Model of the expanded graphite consisting of graphite nanosheets and graphene layers [160].

Table III-3. Data from technical datasheet of expanded graphite nanoplatelets (Properties evaluated parallel to the surface).

Property	**xGnP**
Density (g/cm^3)	2.2
Carbon content (%)	≥ 99.5
Thermal conductivity (W/mK)	3,000
Coefficient of thermal expansion (m / (m/K))	4-6 x 10 $^{-6}$
Tensile modulus (GPa)	1,000
Tensile strength (GPa)	5
Electrical conductivity (S/m)	10^7

Expanded graphite nanoplatelets are obtained from natural graphite flakes, which is quite abundant in nature, through a process of intercalation with acid compounds and following expansion upon abrupt heating up to 800 – 950 °C [7]. In order to obtain nanographene platelets (Figure III-7c), the expanded graphite worms are broken up by high-energy sonication or ball milling.

Graphene nanoplatelets represent a relatively new class of carbon nanoparticles with multifunctional properties. xGnP® brand graphene nanoplatelets have a 'platelet' morphology, meaning they have a very thin but wide aspect ratio. This unique platelet morphology makes these particles especially effective at providing barrier

properties, while their pure graphitic composition makes them excellent electrical and thermal conductors [161]. Incorporation of small amounts (i.e. < 7-10 wt%) of xGnP in polymer matrices can significantly improve the mechanical properties of the matrix material, such as stiffness, strength and surface hardness. xGnP nanoplatelets are compatible with almost all polymers, and can be an active ingredient in inks or coatings. The unique manufacturing processes adopted by XG Sciences are non-oxidizing, in such a way that the material maintains a pristine graphitic surface of sp^2 carbon molecules that makes it especially suitable for applications requiring high electrical or thermal conductivity. Promising applications include: additive for light-weighting composites, barrier material for packaging, conductive additive for battery electrodes, thermally-conductive films and coatings, electrically-conductive inks, etc.

3.2 Methods

3.2.1 Composites preparation

3.2.1.1 Melt compounding and compression molding

Composite samples were prepared by melt mixing and compression molding. Binary nanocomposites containing a certain quantity of nanoparticles were prepared by melt mixing in a Thermo Haake® internal mixer (T=190 °C, n=50 rpm, t=10 min) followed by hot pressing using a Carver® hot press (T=190 °C, p=0.76 MPa, t=10 min), in order to get plane sheets with thickness of around 0.7 mm. Ternary nanocomposites were also prepared by adding both PPgMA as compatibilizer and the nanofiller. Prior to the melt processing, silica nanoparticles were dried for 24 h at 100 °C.

The internal mixer and the hot press are depicted in Figure III-8.

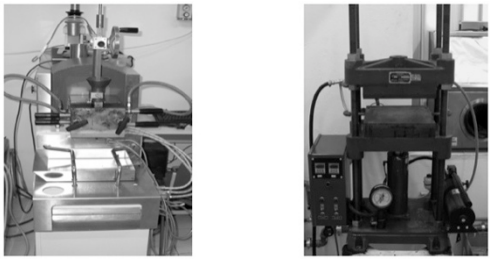

(a) (b)

Figure III-8. (a) Haake® internal mixer and (b) Carver® hot plates press.

In order to investigate the effect of the melt mixing on the material, the torque applied by the melt mixer was monitored with respect to the time of process. As it can be observed in Figure III-9, the torque increases when the polymer chips are introduced in the mixer chamber, following a progressive decrease due to melting of the polymer. A final plateau is reached when the material is completely melt.

In particular, no thermo-oxidative degradation phenomena can be noticed by the analysis of the torque. When considering filled samples, a lower torque is registered because of the smaller amount of polymer added, while a slight instantaneous increase in torque can be noticed with the incorporation of nanofiller (t ~ 2 min). Moreover, the plateau value of the torque recorded for filled samples was similar to that of PP.

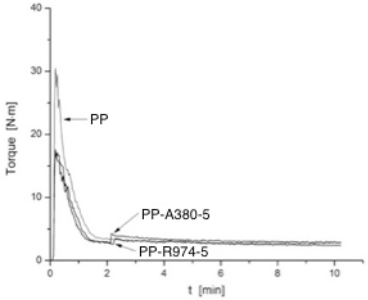

Figure III-9. Torque recorded during compounding for neat PP and relative composites.

3.2.1.2 Melt compounding and injection molding

Composite samples were also produced by melt mixing and injection molding. A vertical, co-rotating, bench-top twin-screw micro-extruder (DSM Micro 15 cm^3 Compounder) connected to a micro-injection molding unit (DSM) were used to obtain dogbone specimens. The compound was mixed for 3 min, at 190 °C and a screw speed of 250 rpm. The temperature of the mold was 80 °C, while the injection molding pressure was about 800 KPa. The twin-screw micro-extruder and the micro-injection molding unit are represented in Figure III-10.

(a) (b)

Figure III-10. (a) DSM twin-screw micro-extruder and (b) DSM micro-injection molding unit.

Fiber reinforced composites were also prepared by melt compounding and compression molding (or injection molding). After the polymer compound had melted and homogenized, short GF strands were added to the melt and further mixing and final compression (or injection) molding were carried out.

3.2.1.3 Samples designation

Nanocomposites were designated indicating the matrix, the compatibilizer (if any) with its content, the kind of filler and its amount. For instance, a sample filled with 5 wt% of PPgMA and 5 wt% of xGnP-M5 was indicated as PP-PPgMA-5-xGnP-5.

Glass fiber reinforced composites were designated by indicating the nanocomposite matrix, the glass fiber type and its loading. Coated glass fibers were indicated as GFc. For instance, the sample based on unfilled matrix loaded with 10 wt% GF was denoted as PP/GF-10. On the other hand, a sample filled with 5 wt% of PPgMA, 5 wt% of xGnP-C750 and 10 wt% coated GF was indicated as PP-PPgMA-5-xGnP_C-5/GFc-10.

3.2.2 Testing procedures

3.2.2.1 Glass fiber strength and elastic modulus evaluation

Tensile tests on single GF filaments were carried out according to ASTM C 1557-03 standard. Single fibers of three different gauge lengths (5, 15 and 30 mm) were fixed on paper tab frames and tested with an Instron (Norwood, USA) model 4502 tensile machine equipped with a 2.5 N load cell, at a strain rate of 0.2/min (Figure III-11). Prior testing, fiber diameter was measured on three locations on each specimens by an optical microscope (Leitz Ortholux II POL-BK) through a video-camera (PIKE F032C).

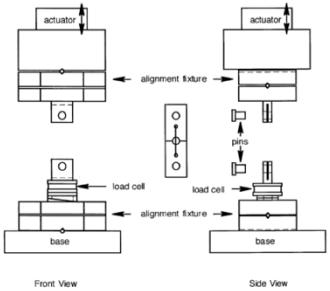

Figure III-11. Tensile testing on single GF filaments supported on paper frames.

3.2.2.2 Microstructural characterization of the nanofillers

Density measurements were carried out through helium pycnometry technique (Micromeritics® Accupyc 1330 helium pycnometer, Norcross USA), at a temperature of 23 °C, using a testing chamber of 3.5 cm^3.

In order to evaluate the surface morphology of the fillers, BET (Brunauer, Emmett, Teller) surface area and porosity measurements were performed on the fillers silica Aerosil® R974 and xGnP-M5, while these characterizations had been already performed on the silica Aerosil® A380 [57]. An ASAP® 2010 Accelerated Surface Area and Porosimetry machine (Norcross, USA) was utilized referring to the nitrogen gas physisorption process, setting a saturation pressure of 738.57 mmHg and a bath temperature of 77.35 K.

The morphology of silica nanoparticles was observed by transmission electron microscopy (TEM), using a Philips® EM 400 T (Amsterdam, Netherlands) transmission electronic microscope at an acceleration voltage of 120 kV. Samples were prepared by sonicating for 5 min a suspension of silica particles in acetone (concentration = 0.5 mg/ml), in order to break down the filler aggregates, and observing a droplet of the suspension on a 600-mesh copper grid.

The morphology of expanded graphite platelets xGnP-M5 was observed at various magnifications by using a Zeiss Supra 40 (Berlin, Germany) field emission scanning electron microscope (FESEM), at an acceleration voltage of 5 kV.

3.2.2.3 Morphological characterization on the PP nanocomposites

Fracture surfaces of PP nanocomposite samples were observed at various magnifications by using a Phenom G2 Pro (Phenom-World BV., Eindhoven, The Netherlands) bench-top scanning electron microscope (SEM), at an acceleration voltage of 5 kV. Prior to the SEM observations, a thin gold coating was applied onto the surface by plasma sputtering in order to minimize the charging effects.

TEM technique was adopted to analyze cryocut surfaces of PP nanocomposites. A Philips® EM 400 T (Amsterdam, Netherlands) transmission electronic microscope, was utilized at an acceleration voltage of 120 kV. Samples were prepared by cutting 70 nm-thin sections by a cryo-ultramicrotome UCT (Leica, Vienna, Austria) operating at -100 °C. Sections were collected on a 600-mesh copper grid.

The characteristics of the filler/matrix interphase were investigated by atomic force microscopy (AFM). A schematic of the AFM principle and of the measurement settings are represented in Figure III-12.

In particular, the width and stiffness of the interphase were determined using a Veeco AFM (Plainview, NY, USA), supported by Nanoscope V controller, operating in tapping mode using an aluminum coated cantilever (length of 225 mm, spring constant of 45 N/m, resonance frequency of 190 KHz), with silicon tip of 2 nm radius provided by Nanoscience Instruments (Inc. Phoenix, AZ, USA). In order to avoid interactions among fillers because of the interphase of adjacent fillers can overlap and significantly impair the measurements [162], AFM was operated on composites with 0.01 wt% filler.

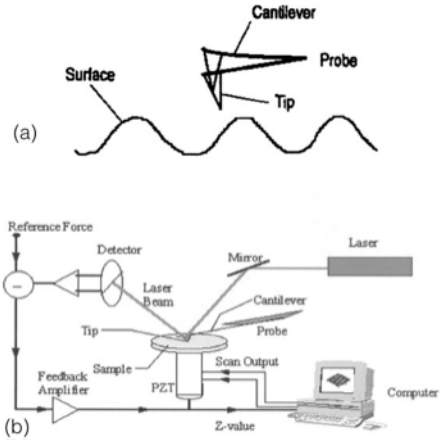

Figure III-12. (a) Basic principle of AFM and (b) schematic of the measurement settings and signal processing for AFM spectroscopy.

3.2.2.4 Morphological characterization on the PP/GF composites

Fracture surfaces PP/GF composites samples were observed at various magnifications by using a Phenom G2 Pro bench-top SEM, at an acceleration voltage of 5 kV. Prior to the SEM observations, a thin gold coating was applied onto the surface by plasma sputtering in order to minimize the charging effects.

Thin (70-80 μm) films required for the analysis of the glass fiber length distribution were obtained by hot pressing stage (temperature=200 °C, pressure=4

MPa, time=10 min). Each film specimen was observed by an optical microscope Leica DMRM (Leica Microsystems Inc., Buffalo Grove, USA) through a video-camera DFC 420 (Leica Microsystems Inc.). At least 200 measurements of glass fiber length were acquired in order to estimate the average fiber length.

In-plane observations of dogbone specimens were carried out by SEM on chemically-etched surfaces, in correspondence of the dogbone central section. The etching was performed in a solution of CrO_3 with a concentration of 60g CrO_3 / 100ml H_2O, maintaining a constant temperature of 70 °C for 24 h.

3.2.2.5 Spectroscopy analyses on the PP nanocomposites

X-ray diffraction (XRD) analysis was performed by a Rigaku® 3D Max X-Ray diffractometer operating at the Cu Kα wavelength (1.54056 Å), scanning the samples in a 2θ range between 3° and 67° at a 2θ step of 0.05°.

Solid-state ^{13}C NMR experiments were carried out through a Bruker 300 WB instrument (Bruker Biospin, Italy) operating at a proton frequency of 300.13 MHz. Solid-state NMR spectroscopy is a kind of nuclear magnetic resonance spectroscopy, characterized by the presence of anisotropic (directionally dependent) interactions. This technique is commonly employed as an analysis tool in organic and inorganic chemistry, in particular to investigate local dynamics, kinetics, and thermodynamics of a variety of systems (Figure III-13).

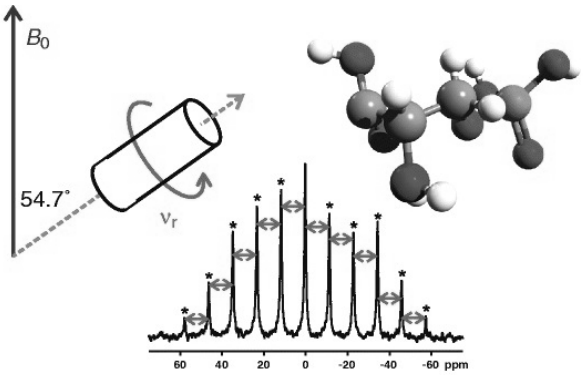

Figure III-13. Schematic of solid-state NMR technique, showing the spinning angle and the spectrum obtained analyzing the chemical compound depicted on the right.

High resolution experiments, characterized by cross polarization with magic angle spinning and variable contact time technique (VCT-MAS), were performed operating at a ^{13}C resonance frequency of 75.48 MHz. The spectra were acquired with a 5 s recycle delay, decoupling length 6.2 μs and 200 scans. The samples were packed in 4 mm zirconia rotors, which were spun at 6.5 kHz under air flow. Adamantane was used as external secondary reference. The relaxation times T_{CH} (cross-polarization rate constant) and $T^{H}_{1\rho}$ (^{13}C spin–lattice relaxation time) were determined indirectly by the profile decay of all resolved carbon nuclei with the increase of contact-time, which was established in a range varying from 200 to 9000 ms. In particular, intensity signal profiles M(t) were fitted to a one-component equation, assuming that all carbons were in similar motional domains, in according to Eq (III-1).

$$M(t) = M_0 \cdot \exp(-t / T^{H}_{1\rho}) \cdot (1 - \exp(-t / T_{CH})) \qquad \text{(III-1)}$$

Where M_0 is a normalization factor. The two relaxation times obtained from NMR experiments can be directly related to the mobility of the carbons being observed. Low mobility (higher heterogeneity) generally results in shorter T_{CH} and longer $T^{H}_{1\rho}$ values, while a mobility increases (e.g. with increasing amorphous phase or homogeneous character of the material) leads to larger T_{CH} and smaller $T^{H}_{1\rho}$ values. However, since the fitting was not satisfactory in the case of some samples, the decay curve was fitted by a double-exponential function, in according to Eq (III-2).

$$M(t) = M_0 \cdot \left[\exp(-t / T^{H}_{1\rho}) + \exp(-t / T^{H}_{2\rho})\right] \cdot (1 - \exp(-t / T_{CH})) \qquad \text{(III-2)}$$

Where $T^{H}_{1\rho}$ and $T^{H}_{2\rho}$ represent the long and short spin–lattice relaxation times, respectively [163]. The latter equation is usually used to describe relaxation phenomena in materials showing highly heterogeneous distribution of the filler within the matrix or phase separation.

Infrared (IR) spectroscopy was carried out by using a Perkin Elmer Spectrum One FT-IR-ATR analyzer on 80 μm thick films, previously cleaned in acetone and dried using a nitrogen flow. The analyses was performed within a scanning interval between 650 and 4000 cm^{-1}, setting a resolution of 2 cm^{-1}, for a total number of co-added scans of 64.

3.2.2.6 Rheological behavior in the molten state

Melt rheology of neat PP and of PP composites was analyzed by an ARES-G2 rheometer (TA Instruments, New Castle, Delaware, USA) under controlled strain conditions. The test geometry was plate-plate with a diameter of the plates of 25 mm. Injection molded disks of around 1.5 mm thickness were placed between the plates at 180 °C. The gap width was set to 1.35 mm by squeezing the PP disk. Isothermal frequency sweep tests were carried out at 180°C. During the measurement a small amplitude (10%) oscillatory shear was applied to the samples. The low strain was verified to be within the linear viscoelastic range. The storage and loss shear moduli (*G*' and *G*'', respectively) and the dynamic viscosity $|\eta^*|$ were measured as a function of the angular frequency (ω) in the range 0.1–200 rad/s. At least three specimens were tested in order to verify the measurement repeatability.

3.2.2.7 Characterization of the melting and non-isothermal crystallization behavior

Standard and modulated differential scanning calorimetry (MDSC) tests were carried out by a DSC Q2000 (TA Instruments, New Castle, Delaware, USA) under a constant nitrogen flow of 50 ml/min on specimens of about 5-8 mg. Isothermal crystallization experiments were performed by standard DSC, heating the sample to 200 °C at a rate of 30 °C/min and maintaining isothermal conditions for 10 min in order to erase any previous thermal history followed by cooling to 145 °C the crystallization behavior was investigated. Every date point is an average of at least three measurements.

The data regarding melting and crystallization behavior was collected by MDSC, heating the samples from the equilibrated temperature of 0 °C to 200 °C at a rate of 5 °C/min, with subsequent cooling to 0 °C, at a rate of 5 °C/min. During heating and cooling a modulation of ± 1 °C every 60 s was set in order to decompose the total heat flow signal into reversing (describing heat capacity events including the glass transition and melting) and non-reversing information (related to kinetic events such as crystallization and crystal perfection/recrystallization). An illustrative example of heat flow decomposition is schematically illustrated in Figure III-14 for polyethylene terephthalate.

In particular, the reversing heat flow curves during heating were used to investigate the melting behavior of the nanocomposites. No annealing or thermal history removal was performed in order to compare the effects of manufacturing process on the investigated properties.

The melting enthalpy (ΔH_m) and melting temperature (T_m) were determined during the heating cycle, whereas crystallization enthalpy (ΔH_c) and crystallization peak temperature (T_c) were determined during the following cooling cycle. In particular, the degree of crystallinity was calculated by taking the weight fraction of PP in the composite into account, according to the following equation :

$$\chi_{\%} = \frac{\Delta H_c}{\Delta H_f^* \left(1 - {wt_{\%}}/{100}\right)} 100 \qquad (III-3)$$

where ΔH_c is the crystallization enthalpy, ΔH_f^* corresponds to the theoretical crystallization enthalpy of 100% crystalline isotactic PP equal to 209 J/g [156], whereas wt% is the filler weight content.

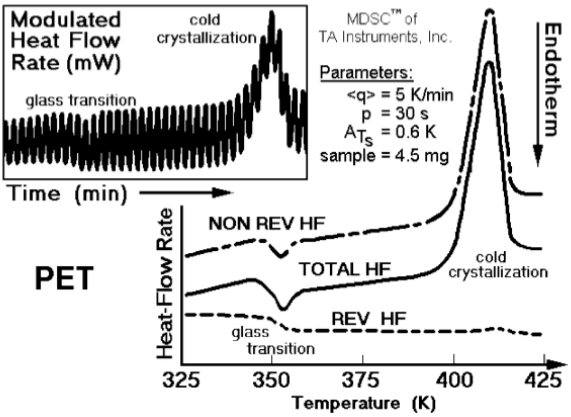

Figure III-14. Total, reversing and non-reversing heat flow rates of polyethylene terephthalate (PET) using sinusoidal temperature modulation [164].

3.2.2.8 Characterization of the isothermal crystallization behavior

Isothermal crystallization behavior was also investigated by adopting the following experimental conditions. A hot stage (Instep HCS302, Boulder, CO, USA) was used to heat the samples above their melting temperature and erase any thermal history due to previous processing. Samples were heated to 200 °C at a rate

of around 30 °C/min and held isothermally for 10 min. Isothermal crystallization experiments were carried out by cooling to 145 °C and holding the temperature in time while at the same time observing the sample microstructure by an optical microscope (Leica DMRM, Buffalo Grove, IL, USA).

Figure III-15. Hot-stage Instec HCS302 used for isothermal crystallization experiments.

3.2.2.9 Characterization of thermal degradation behavior

Thermogravimetric analysis (TGA) was carried out through a Q5000 IR thermogravimetric analyzer (TA Instruments-Waters LLC, New Castle, USA) imposing a temperature ramp between 40 and 700 °C at a heating rate of 10 °C/min under a constant nitrogen flow of 25 ml/min. The onset of degradation temperature *($T_{d,onset}$)* was determined by the point of intersection of tangents to two branches of the thermogravimetric curve, while the maximum rate of degradation temperature *($T_{d,max}$)* was determined from the peak maxima in the first derivative of weight loss curve. The two reference temperatures are schematically indicated in Figure III-16,

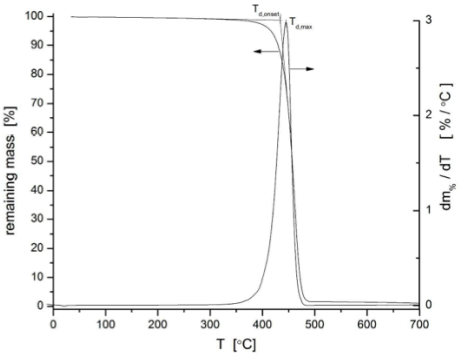

Figure III-16. Representative thermograph of PP, showing the thermogravimetric curve (left y-axis) and the first derivative of weight loss curve (right y-axis) [165].

3.2.2.10 Mechanical testing

3.2.2.10.1 Single fiber fragmentation test (SFFT)

The effect of nanomodification on the adhesion between matrix and GF was investigated through SFFT performed on composite models characterized by a single fiber filament sandwiched between two polymer films.

Microcomposites were prepared according to a procedure well assessed for thermoplastic matrices [138, 166, 167]. About ten fibers were aligned between two thin polymer films, sandwiched between two Mylar® foils and two aluminium plates. This assembly was placed in a vacuum oven at a temperature of 165 °C under a pressure of 10 kPa for 20 min and then cooled in air. The specimens were obtained by cutting strips (0.18x5x25 mm^3) containing one single fiber longitudinally aligned in the centre line (Figure III-17).

Fragmentation tests were performed at room temperature by a tensile tester (Minimat, by Polymer Laboratories, Loughborough, UK) located under a polarized optical stereo-microscope (Wild M3Z by Leica). At least five specimens for each sample were tested at a strain rate of 0.05/mm up to a strain of 10%, necessary to assure the saturation of the fragmentation process (Figure III-17 and III-18).

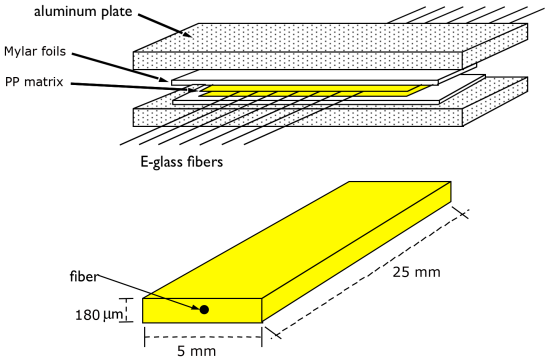

Figure III-17. Preparation of the microcomposites for the fragmentation test.

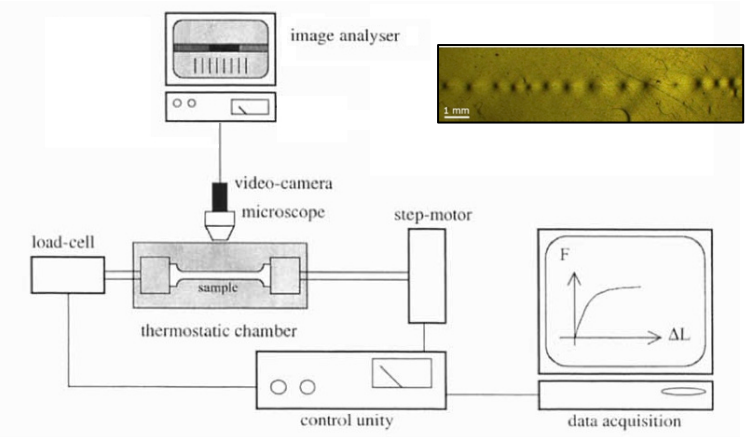

Figure III-18. Test apparatus for the fragmentation test (adapted from [138]) and representative example of a sample tested until saturation (PP-PPgMA-5-R974-5).

The mean fiber length, L_s, was evaluated by an image analysis software (Image J). The fiber critical length, L_c, was taken as 4/3 L_s [132]. Interfacial shear strength (ISS) values were derived according to the simplified micromechanical models proposed by Kelly-Tyson [168] and by Cox [131].

According to the Kelly–Tyson approach (Eq. III-4) an average value of ISS is the result of the static equilibrium between the tensile force acting on a fiber and the shear force transferred through the fiber–matrix interface:

$$ISS = \frac{\sigma_{fb(Lc)} d}{2 L_c} \qquad \text{(III-4)}$$

where d is the fiber diameter and $\sigma_{fb(Lc)}$ is the tensile strength of a fiber with a critical length L_c, which was computed on the basis of Eq. III-5.

$$\sigma_{fb(Lc)} = \sigma_0 \left(\frac{L}{L_0} \right)^{-\frac{1}{m}} \Gamma\left(1 + \frac{1}{m} \right) \qquad \text{(III-5)}$$

where Γ is the Gamma function, while σ_0 and m are the scale and shape parameters of the Weibull distribution, respectively, which were estimated from

strength data determined at one single gauge length by fitting the distribution of failure probability.

On the other hand, the traditional shear – lag model assumes a number of hypotheses, such as: perfectly elastic and isotropic matrix and fiber properties, proportionality between interfacial shear force and the difference between the displacement in the matrix and the displacement that would exist if the fiber were absent, perfect bonding between matrix and fiber, same lateral stiffness of fiber and matrix, no residual stresses Furthermore, the stress is taken as uniform through a radial section of fiber, and the stress is entirely transferred from matrix to fiber by shear at the interface. The axial stress s_f in the fiber can thus be written as:

$$\sigma_f = E_f\ \varepsilon_f\ \left(1 - \frac{\cosh(\beta\ z)}{\cosh(\beta\ t)}\right) \qquad (III - 6)$$

Where ε_f is the far-field applied strain, E_f is the elastic modulus of the fiber, z is the axial coordinate, t is the fiber half-length, while β (shear – lag parameter) is defined as:

$$\beta = \left[\frac{H}{\pi\ R_f^2\ E_f}\right]^{1/2} \qquad (III - 7)$$

with

$$H = \frac{\pi\ E_m}{(1 + \nu_m)\ ln\left(R_m\ /\ R_f\right)} \qquad (III - 8)$$

where E_m and ν_m are the matrix elastic modulus and Poisson's ratio, while R_m and R_f are te matrix and fiber radii, respectively. The interfacial shear stress profile $\tau(z)$ can be calculated:

$$\tau = \frac{E_f\ R_f\ \varepsilon_f\ \beta}{2}\left(\frac{\sinh(\beta\ z)}{\sinh(\beta\ t)}\right) \qquad (III - 9)$$

Further considerations regarding the shear-lag theory as alternative to the Kelly-Tyson model are reported in *Appendix B*.

3.2.2.10.2 Single fiber microdebonding test

The effect of the filler incorporation on the fiber-matrix adhesion was also studied through microdebonding tests performed on specimens characterized by a PP microdrop solidified onto a single fiber filament supported on a paper tab. Single filaments were randomly extracted from an E-glass fiber woven. In order to avoid the formation of asymmetric droplets with respect to the filament, a PP fiber was tied around the filament prior to heating [169]. PP microdrops were distributed symmetrically around the filament during melting occurred in a hot-stage equipment (Instec HCS302, Boulder, CO, USA) while observing under an optical microscope Leica DMRM (Leica Microsystems Inc., Buffalo Grove, USA). Prior to testing the microbond samples were examined using the optical microscope in order to determine the fiber diameter (*d*), embedded fiber length (*L*), and the maximum droplet diameter (*D*), as indicated in Figure III-19.

Microdebonding tests were conducted at a crosshead speed of 1 mm/min by an Instron 33R 4466 (Norwood, USA) tensile tester equipped with a 500 N load cell. During testing the paper tab attached to one end of the glass fiber was slowly pulled up, while the droplet was constrained by a shearing plate, which was fixed on a stationary support (Figure III-19b). A nominal interfacial shear stress (τ) was computed by using the following expression:

$$\tau = \frac{F}{\pi d L} \qquad (III-10)$$

where *F* is the applied load recorded during the test. When a critical load is reached, the fiber-matrix interface fails and the load dramatically decreases. The interfacial shear strength (*ISS*) can be estimated by substituting the maximum applied load in Eq. III-10. In order to investigate the failure mode occurring upon debonding, the single fiber specimens were observed before and after the microdebonding test through a Phenom G2 Pro (Phenom-World BV., Eindhoven, The Netherlands) bench-top SEM at an acceleration voltage of 5 kV.

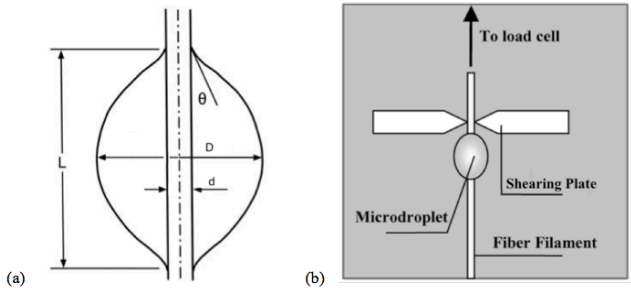

Figure III-19. (a) Schematic representation of a matrix drop deposited onto a rigid fiber and (b) schematic of the microdebonding test (right).

3.2.2.10.3 Quasi-static tensile tests

Uniaxial tensile tests were performed with an Instron® 4502 (Norwood, USA) tensile machine on compression moded samples of at least five ISO 527 type 1BA specimens. The tests were carried out at a crosshead speed of 0.25 mm/min up to a maximum axial deformation of 1%. The strain was recorded by using a resistance extensometer Instron® model 2620-601 with a gage length of 12.5 mm. The elastic modulus was measured as secant modulus between deformation levels of 0.05 % and 0.25 % in according to ISO 527 standard.

Uniaxial tensile properties, such as stress at yield (σ_y), stress at break (σ_b) and strain at break (ε_b) were determined at an higher crosshead speed (5 mm/min) without extensometer.

In the same way, tensile tests were also performed on injection molded samples with an Instron model 33R 4466 (Norwood, USA) tensile tester equipped with a 500 N load cell, on samples consisting of at least five dogbone specimens. The strain was recorded by using a resistance extensometer Instron® model 2630-101 with a gauge length of 10 mm.

3.2.2.10.4 Izod impact testing

In order to study the fracture behavior of the material at high strain rate levels, tensile impact tests (Izod type) were performed according to the ASTM D256 standard test method, using a mechanical pendulum provided by Custum Scientific Intruments, Inc. (Whippany, NJ). The dimension of the notched Izod impact specimens was 63.5 x 12.7 x 3.2 mm^3, and a notch of 2.55 mm depth and 0.25 mm radius was cut along the thickness direction.

3.2.2.10.5 Creep and dynamic mechanical analysis (DMA) tests

Creep tests were performed utilizing a dynamic mechanical analyzer DMA Q800 (TA Instruments®-Waters LLC, New Castle, USA) applying a constant stress *(σ_0)* of 3 MPa (i.e 10% of the stress at yield of unfilled PP) for 3600 s at 30 °C. Rectangular samples 25 mm long, 5 mm wide and 0.20 mm thick were used, adopting a gage length of 11.5 mm. The creep compliance *D(t)*, computed as the ratio between the strain and the creep stress, was plotted against the time for the different samples. Since the samples PP-PPgMA-5-A380-5, PP-PPgMA-5-R974-5 and PP-PPgMA-5-xGnP_M5-5 showed the best creep stability, different creep tests were performed at 30 °C for 3600 s by ranging σ_0 between 10% and 50% of the stress at yield. Master curves were constructed by applying the time-strain superposition principle (TSSP) [170] *(Appendix A)*.

Other creep tests were carried out imposing a constant stress of 3 MPa for 1200 s and ranging the temperature between 30 and 70 °C, in 10 °C steps. The temperature range was properly chosen in order to remain within the linear viscoelastic region. Master creep curves were constructed by applying the time-temperature superposition principle (TTSP) in according to the model proposed by Williams, Landel and Ferry (WLF equation) setting the reference temperature T_0 to 30 °C.

In particular, many materials exhibit a viscoelastic behavior that follows the Arrhenius relation (Eq. III-11) for temperature lower than the glass temperature and the relation proposed by Williams, Landel and Ferry (Eq. III-12) for higher temperatures.

$$\ln a_{T_0}(T) = \frac{\Delta H}{R}\left(\frac{1}{T} - \frac{1}{T_0}\right) \qquad (III-11)$$

$$\log a_{T_0}(T) = -\frac{C_1(T - T_0)}{C_2 + (T - T_0)} \qquad (III-12)$$

Where ΔH is an activation energy, R the ideal gas constant, and C_1 and C_2 are empirical constants that depend on the material.

DMA were carried out at the DMA Q800 testing machine on film specimens 25 mm long, 5 mm wide and 0.2 mm thick. Firstly, some selected samples were analyzed over a temperature range between -20 °C and 160 °C, imposing a heating rate of 3 °C/min and a frequency of 1 Hz. A preload of 0.2 MPa and a maximum strain of 0.05 % were set for each test. The most important viscoelastic functions *(E', E'', tanδ)* were recorded at different temperatures. Multi-frequency DMA tests

were carried out on PP, PP-PPgMA-5-A380-5, PP-PPgMA-5-R974-5 and PP-PPgMA-5-xGnP_M5-5 samples, imposing a temperature increment of 10 °C from -20 °C to 140 °C and setting the following test frequencies: 0.1, 0.32, 1, 3.2, 10, 31.6 and 100 Hz. Master curves were obtained according to the frequency-temperature superposition principle and setting the reference temperature to 30 °C.

3.2.2.11 Surfaces energetics and roughness

The contact angle is the angle, conventionally measured through the liquid, at which a liquid/vapor interface meets a solid surface. It quantifies the wettability of the solid surface by the liquid. Contact angle measurements were performed on both matrix and GF in order to correlate the interfacial shear strength *(ISS)* values to a measurable surface property such as the contact angle. In general, the higher the wettability of the matrix material, the higher its compatibility with the fiber, the greater the interfacial strength.

The contact angle generally depends not only on the chemistry of the surface being tested, but also on the surface roughness. For the latter reason, roughness measurements were also carried out on matrix specimens in order to check if all specimens presented comparable roughness.

The wettability of some selected matrix compositions and the glass fiber was measured by contact angle measurements with two different liquids: water as a polar liquid (milli-Q grade, surface tension γ_1 =72.8 mN/m, polar component of surface tension γ_1^p =50.7 mN/m, dispersive component of surface tension γ_1^d =22.1 mN/m, polarity $\chi_1^p = \gamma_1^p/\gamma_1$=0.7), and ethylene glycol as a non-polar liquid (surface tension γ_2 =48.0 mN/m, polar component of surface tension γ_2^p =19.0 mN/m, dispersive component of surface tension γ_2^d =29.0 mN/m, polarity $\chi_2^p = \gamma_2^p/\gamma_2$=0.4) [171].
The total surface tension (γ^{tot}) can be factorized by considering two additive terms: the dispersive surface tension (γ^d) and the polar surface tension (γ^p).

$$\gamma^{tot} = \gamma^d + \gamma^p \qquad (III-13)$$

The polar component of the surface energy characterizes polar interactions between the surface of polymer and the test liquid (within the context of a contact angle measured by static or dynamic (i.e. Wilhelmy) technique). In particular, this component is determined by the presence of polar groups, electric charges and free radicals on the polymer surface. In contrast, the dispersive component represents the dispersive interactions taking place between polymer and test liquid and is determined by surface roughness, unevenness and blanching level of the polymer surface [172].

The estimation of the surface tension components of matrix with various compositions was done on the basis of the equilibrium contact angle measured in both test liquids by a modified Wilhelmy technique, based on the vibration induced equilibrium contact angle (VIECA) method [173] and adopting the geometric mean [171]. A representative experiment of the Wilhelmy force loop pf the sample PP-R974-5 is represented in Figure III-20. Surface tension components of glass fiber were calculated referring to the advancing contact angle measured by Wilhelmy technique and applying the geometric mean.

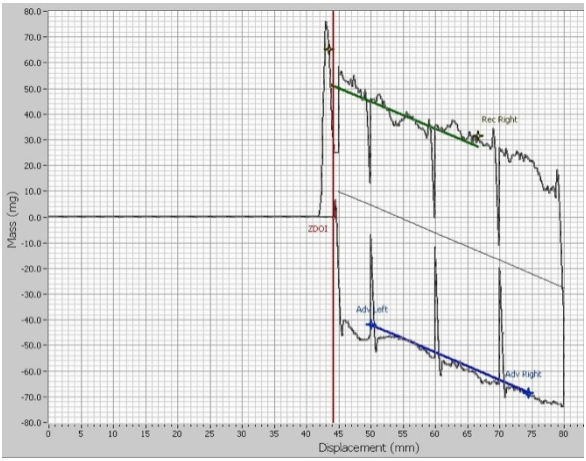

Figure III-20. Representative vibrated Wilhelmy force loop of the sample PP-R974-5; the force loop is composed of one cycle consisting of one immersion (advancing) and one emersion (receding) process.

Knowing the surface tension components of the adherents, the work of adhesion was evaluated using the harmonic mean ($W_a{}^h$) equation, applicable to predict interactions between low-energy materials [171]:

$$W_a^h = 4\left(\frac{\gamma_l^d\ \gamma_s^d}{\gamma_l^d + \gamma_s^d} + \frac{\gamma_l^p\ \gamma_s^p}{\gamma_l^p + \gamma_s^p}\right) \qquad (III-14)$$

and the geometric mean ($W_a{}^g$) equation, more suitable to describe interactions between low-energy and high-energy materials:

$$W_a^g = 2\left(\sqrt{\gamma_l^d\ \gamma_s^d} + \sqrt{\gamma_l^p\ \gamma_s^p}\right) \qquad (III-15)$$

where the superscripts *d* and *p* refer to the dispersive and polar components, respectively. Further details on the theory about dynamic contact angle measurement through Wilhelmy technique are reported in *Appendix C*.

The roughness of the samples was determined by a Wave System rugosimeter (Hommelwerke Waveline GmbH, Villingen-Schwenningen, Germany) scanning a 15 mm line at a speed of 0.50 mm/min. At least three measurements were performed per each sample on the same specimens previously adopted for the estimation of the contact angle. The ANOVA analysis was carried out on the means of R_a and R_{max} at a significance level of 5 %.

3.2.2.12 Appendix A: nonlinear tensile creep of thermoplastics and their blends

3.2.2.12.1 Tensile creep as a non-iso-free volume process

The free volume approach to the nonlinear tensile creep is based on the assumption that the strain-induced volume increment of a polymer matrix depends on the increment in the free volume, in particular, increasing the strain during tensile creep produces an increase in the molecular mobility and a significant shortening of retardation times. The free volume theory of the viscoelastic creep was for the first time successfully applied to construct generalized curves of silica modified - linear low density polyethylene (LLDPE) nanocomposites by Dorigato et al. [174]. In particular, the authors found that the superposition procedure was viable for both unfilled LLDPE and nanocomposites with different nanosilica types. On the basis of these findings, the superposition principle was applied in this research to carry out a quantitative analysis of the nonlinear creep. While the theoretical background is fully described in [174], only the most important equation are written in this appendix.

The strain in tensile creep, $\varepsilon(t, \sigma, T)$, generally depends on time t, stress σ, and temperature T, and can be expressed as the sum of the elastic (reversible, instantaneous) $\varepsilon_e(\sigma, T)$, viscoelastic (reversible, time-dependent) $\varepsilon_v\ (t, \sigma, T)$ and plastic $\varepsilon_p\ (t, \sigma, T)$ parts:

$$\varepsilon(t,\sigma,T) = \varepsilon_e(\sigma,T) + \varepsilon_v(t,\sigma,T) + \varepsilon_p(t,\sigma,T) \qquad (III-16)$$

The tensile compliance $D(t,\sigma) = \varepsilon(t, \sigma)/\sigma$ considered during isothermal nonlinear creep with no plastic deformation, can be written as follow:

$$D(t,\sigma) = D_e(\sigma) + D_V(t,\sigma) \qquad (III-17)$$

Despite various empirical equations were proposed to fit $D(t, \sigma)$ or $D_v(t, \sigma)$, a simple equation based on the retardation time approach was found suitable for describing isothermal creep of polypropylene and of its blends [118, 175-177] :

$$logD(t,\sigma) = \log W(\sigma) + n\, log\left(\frac{t}{\tau_{rm}}\right) \qquad (III-18)$$

where $W(\sigma)$ is a function of stress, τ_{rm} is the mean retardation time and $0 \leq n \leq 1$ is the shape parameter indicating the distribution of retardation times.

The time-strain shift factor, log $a_\varepsilon(t)$, defined as the ratio of the mean retardation time $t_{rm}\,[\varepsilon(t), T_c]$ at a strain $\varepsilon(t)$ and $\tau_{rmi}\,[\varepsilon_i = 0, T_c]$ for initial time $t_i = 0$ (at a constant temperature T_c) can be obtained as [174] :

$$\log a_\varepsilon(t) = -\left(\frac{B}{2.303}\right)\frac{\left[\frac{(1-2\nu)M\varepsilon(t)}{f_g+\Delta f_{T_c}}\right]}{\left[(1-2\nu)M\varepsilon(t) + \left(f_g + \Delta f_{T_c}\right)\right]} \qquad (III-19)$$

Where B is a numerical factor related to the ratio of the volume of a jumping segment to the volume of the critical vacancy necessary for the implementation of a segment jump, ν is the Poisson's ratio, M is the ratio of the average strain of the creeping phase in the multiphase test specimen and the measured strain. The fractional free volume of the glassy state is defined as f_g and for most polymers the glassy state is considered as iso-free-volume state with f_g =0.025. If only the effects of temperature T and of strain $\varepsilon(t)$ are considered, the fractional free volume can be expressed as:

$$f\big(t,\varepsilon(t)\big) = f_g + \alpha_{fv}\big(T - T_g\big) + (1-2\nu)\varepsilon(t) = f_g + \Delta f_T + \Delta f_\varepsilon \qquad (III-20)$$

Where α_{fv} is the expansion coefficient of the free volume at $T > T_g$, ν is Poisson's ratio and $[(1 - 2n)\ \varepsilon(t)]$ is the strain-induced dilatation for an isotropic material.

The compliance can be expressed in logarithmic form as:

$$\begin{aligned} logD(t,\sigma) &= [\log W(\sigma) - n\, log\tau_{rmi}] + n\,[log(t) - \log a_\varepsilon(t)] \\ &= \log C^* + n^* \log(t^*) \end{aligned} \qquad (III-21)$$

Where the parameters C^* and n^* refers to the internal time t^*, defined as:

$$\log(t^*) = \log(t) + \log a_\varepsilon(t) = \log(t) + \left(\frac{B}{2.303}\right)\frac{\left[(1-2\nu)M\varepsilon(t)/(f_g + \Delta f_{T_c})\right]}{\left[(1-2\nu)M\varepsilon(t) + (f_g + \Delta f_{T_c})\right]} \qquad (III-22)$$

3.2.2.12.2 Strain magnification factor for the amorphous phase in crystalline polymers

In semicrystalline polymers the crystalline phase has significantly lower compliance than the amorphous phase at $T > T_g$, thus the viscoelastic creep processes in semicrystalline polymers at $T > T_g$ mainly occur within the amorphous phase [175]. Semicrystalline polymer structure can be modeled by a two-parameter equivalent box model (EBM) (Figure III-21), which takes into account differing strains of amorphous (subscript 1) and crystalline (subscript 2) phases, by means of the strain-magnifying factor *M*.

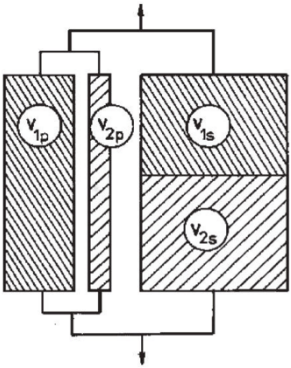

Figure III-21. Schematic of the Equivalent Box Model (EBM) for a two-component system.

It was shown that the mean value of *M* for the amorphous phase is :

$$M = 1 + \left(\frac{v_{2s}}{v_1}\right) \qquad (III - 23)$$

The volume fractions of the EBM were determined on the basis of a universal formula proposed by the percolation theory in heterogeneous binary systems:

$$v_{1p} = \left[\frac{v_1 - v_{1cr}}{1 - v_{1cr}}\right]^q \qquad (III - 24)$$

$$v_{2p} = \left[\frac{v_2 - v_{2cr}}{1 - v_{2cr}}\right]^q \qquad (III - 25)$$

Where v_{1cr} (or v_{2cr}) is the critical volume fraction (regarding the percolation threshold) at which the phase 1 or 2 becomes partially continuous and q is the critical exponent. For three-dimensional cubic lattice, the percolation threshold v_{cr} = *0.156* was calculated [178, 179]. The volume fractions v_{1s} and v_{2s} are calculated as:

$$v_{1s} = v_1 - v_{1p} \quad (III-26)$$
$$v_{1s} = v_1 - v_{1p} \quad (III-27)$$

Since the most common values of q were reported in the interval *1.6 – 2.0*, a value of q = 1.8 can be be considered typical.

3.2.2.12.3 Choice of the model parameters and qualitative considerations

The superposition of the nonlinear creep data necessitates the application of the outlined approach based on the fractional free volume rising with the creep strain. For this end, the inputs B, ν, M, f_g, and α_{fv} occurring in Eq. III-21 and Eq. III-22 are required. As no reliable data for PP can be found in existing literature, these parameters can only be estimated.

The value of B is supposed to be a constant close to 1 [174]. The Poisson's ratio of thermoplastics usually depends on strain and/or time following a quite complex dependance. Furthermore, very few data can be found in the existing literature. In the specific case of isotactic PP, only a constant value of ν was used to characterize a polymer, ν = 0.46, which was experimentally measured on ISO 527 1B specimens of the same material produced by injection moulding. The value of M = *1.59* was computed considering v_{1cr} = v_{2cr} = *0.156* and q = *1.8* in Eq. III-23. Regarding the fractional free volume in the glassy state and its expansion coefficient, values which are considered as universal constants, i.e. f_g = *0.025* and α_{fv} = *0.00048 K^{-1}* were used as first tentative [174].

When trying to adopt these values, with T_g = *-16.40 °C* measured by DSC analysis on unfilled PP, the superposition was not achievable. The superposition became feasible for α_{fv} = *0.00033 K^{-1}*. Dorigato et al also found good superposition of creep compliance curves when using lower values of both f_g and α_{fv}, attributing the discrepancies to relatively high crystallinity and to the fact that amorphous parts are mainly formed loops at the surface of lamellae [174]. The parameters used to carry out the superposition of the nonlinear creep data are all reported in Table III-4.

Table III-4. Parameter used for the evaluation of the non-linear creep behavior of PP nanocomposites.

Parameter	Value
f_g	0.025
T_g [°C]	-16.40
T [°C]	30.00
α_{fv} [K^{-1}]	0.000330
Δf_{Tc}	0.0153
x_c	0.488
v_2	0.488
v_{2cr}	0.156
q	1.800
M	1.589
ν	0.460
B	1.000

The generalized *log D(t*) vs. log t** dependence can be utilized for constructing the real *log D(t) vs. log t* curves by employing the experimentally found constants *log C** and *n**. To this end, the ''real'' time *t* can be obtained by modifying Eq. III-28 and introducing $\varepsilon(t) = D(t)\,\sigma$:

$$\log a_\varepsilon\,(t) = -\left(\frac{B}{2.303}\right)\frac{\left[\frac{(1-2\nu)MD(t)\sigma}{f_g+\Delta f_{T_c}}\right]}{\left[(1-2\nu)MD(t)\sigma+\left(f_g+\Delta f_{T_c}\right)\right]} \qquad (III-28)$$

$$\log(t) = \log(t^*) - \log a_\varepsilon\,(t) \qquad (III-29)$$

3.2.2.13 Appendix B: Shear-lag Cox model to study the fiber/matrix interfacial shear strength

The shear-lag theory for the study of the fiber-matrix adhesion properties was firstly proposed by Cox [131] in 1952. The elastic solution to the stress field in the reinforcing phase and at the interface found significant success for studies of single fiber composites. This approach was limited by the one-dimensional analysis where the radial and hoop stresses were not determined, and the stress state was not entirely known. Moreover, it was necessary to determine an interfacial shear parameter *H*, for which Cox proposed a solution in the limit of high fiber volume fractions; this solution includes an effective matrix radius. However, single fiber

composites have inherently low fiber volume fractions and the Cox approach may describe their stress field poorly.

One complete analytical derivation of shear lag analysis was given in the work of Piggot [127], with an estimate for the interface parameter *H* for the case of hexagonal and square fiber packing. Cox analysis has been shown to be robust where R_m / R_f is far from 1 and ∞, where R_m and R_f denote the effective matrix radius and fiber radius, respectively. The traditional shear – lag analysis assumes:

- Perfectly elastic and isotropic matrix and fiber properties
- Proportionality between interfacial shear force and the difference between the displacement in the matrix and the displacement that would exist if the fiber were absent
- Perfect bonding between matrix and fiber
- Same lateral stiffness of fiber and matrix
- No residual stresses

Furthermore, the stress is taken as uniform through a radial section of fiber, and the stress is entirely transferred from matrix to fiber by shear at the interface.

The axial stress σ_f in the fiber can thus be written as:

$$\sigma_f = E_f \, \varepsilon_f \left(1 - \frac{\cosh(\beta \, z)}{\cosh(\beta \, t)}\right) \qquad (III - 30)$$

Where ε_f is the far-field applied strain, E_f is the elastic modulus of the fiber, *z* is the axial coordinate, *t* is the fiber half-length, while β (shear – lag parameter) is defined as:

$$\beta = \left[\frac{H}{\pi \, R_f^2 \, E_f}\right]^{1/2} \qquad (III - 31)$$

with

$$H = \frac{\pi \; E_m}{(1 + \nu_m) \; ln\left(R_m / R_f\right)} \qquad (III - 32)$$

where E_m and ν_m are the matrix elastic modulus and Poisson's ratio, while R_m and R_f are te matrix and fiber radii, respectively.

The interfacial shear stress profile $\tau(z)$ can be calculated:

$$\tau = \frac{E_f \, R_f \, \varepsilon_f \, \beta}{2} \left(\frac{\sinh(\beta \, z)}{\sinh(\beta \, t)} \right) \qquad (III - 33)$$

The correlation between experimental data and Cox based models was generally good, but use was limited by the introduction of the effective radius of matrix R_m whose physical existence has not been defined clearly in the case of single fiber composites. As a consequence, these models are often used for comparative rather than predictive purposes [180]. Typical profiles of axial stress in fiber and shear stress at the interface are represented schematically in Figure III-22.

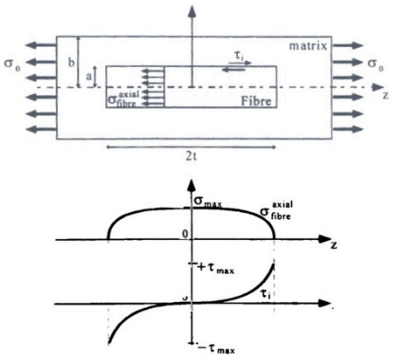

Figure III-22. Schematic fiber axial stress and interfacial shear stress as determined by Cox model [131].

Most methods currently used to interpret the results of interface tests in terms of interface parameters (such as the Kelly-Tyson model and the shear-lag model) are based on simplistic stress analysis models that can at best lead only to nominal values for the interface properties. Such interface data should not be expected to show consistency when comparing results from different types of test, when non-consistent models are used. In addition such data should not be reliable when attempting to predict the behavior of the fiber/matrix interfaces within a typical composite material.

The fragmentation test is the only interfacial test technique that involves fiber fracture. The energy released during such fracture processes is such that dynamic effects may be important where stress waves may initiate more than one fracture at a given load, and lead to stick-slip processes within the interface debonding zone.
Interface performance can also be characterized by the consideration of interfacial fracture energies rather than interfacial strength, i.e. using fracture mechanics

principles rather than a strength of materials approach. The analysis of the energy release rate of a debonding interface was introduced recently by Nairn and Wagner [181, 182]. This energy-based approach is strongly dependent on the stress analysis, and has consequently been upgraded several times, as the modelling effort constantly increased in the field. Some energy methods are applicable in the small strain regime, without the necessity to reach saturation of the fragmentation test.

The shear-lag model proposed by Cox was applied to the study of the fiber-matrix interfacial properties as an alternative approach with respect to the empirical model proposed by Kelly-Tyson [183]. Since the basic assumption of perfectly elastic matrix was assumed, the the far-field applied strain (ε_f) was considered correspondent to the strain value reached when the maximum applied load was achieved, before the plastic deformation region. This is an approximation because, as confirmed by experimental observation, the fragmentation process occurring in model composite samples begins before reaching the maximum load and terminates within a deformation slightly greater than that correspondent to the maximum load. The dynamic of the fragmentation process was studied for many composites in the past, also applying acoustic emission techniques. One example is shown in Figure III-23, where a the load-displacement curve and the associated chart of acoustic emission events are represented for a fiber fragmentation test performed on an AS4 carbon fiber PEEK matrix composite [132].

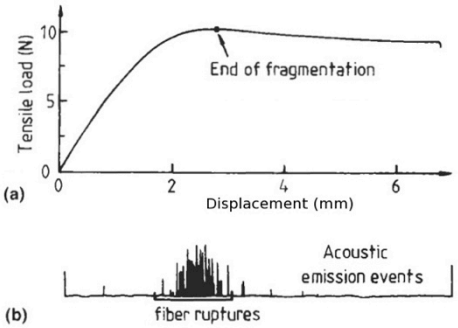

Figure III-23. (a) Typical load-displacement curve and (b) acoustic emission events for a fiber fragmentation test performed on an AS4 carbon fiber PEEK matrix composite [132].

In the basic shear-lag type model, both the fiber and the matrix are treated as linear elastic bodies and it is assumed that the interfacial shear stress is constant. However, to discuss the damage progress behavior in a composite in detail, it is necessary to consider more realistic stress transfer models. On the basis of this point of view, Okabe and Takeda [184] suggested an elastoplastic shear-lag analysis that

assumed that the matrix is an elastoplastic body and can consider the effect of strain hardening of the matrix material. Furthermore, Ogihara and Nakatani conducted an elastoplastic shear-lag analysis that considers plastic deformation in the matrix material [185]. In the one-dimensional shear-lag analysis that considers the fiber, the matrix, and the interfacial shear layer, it is assumed that the fiber is a linear elastic body, and the matrix and the interfacial shear layer are elastoplastic bodies.

3.2.2.14 Appendix C: Contact angle measurements and determination of the work of adhesion

The contact angle value, where the system entails its absolute minimum of surface free energy, assumes the name of equilibrium contact angle, while the other possible contact angles correspond to different metastable equilibrium states depending on the surface and on the different initial conditions. The highest of these values is commonly referred as advancing contact angle (θ_A), while the lowest one is defined as receding contact angle (θ_R). Moreover, other two characteristic angles are usually defined: Young's angle considered as the equilibrium angle on an ideal surface and the static normal equilibrium angle. Noteworthy, the equilibrium contact angle does not correspond to the Young's angle as it refers to a non-ideal surface. Advancing and receding contact angles can be measured on a flat specimen using the *static sessile drop method* or the *dynamic Wilhelmy method*. In this research work only the second method was adopted.

The Wilhelmy balance apparatus is composed of an electronic balance interfaced with a PC computer. The tensiometer measures the force exerted by a partially immersed thin-sample plate in water. A beaker containing water is moved up (increasing the immersion) and down (emerging the sample) by a constant speed, and the corresponding force change is recorded. The total force exerted to the microbalance may be given by the following force balance equation:

$$F = Mg - \rho gtHd + L\,\gamma_L cos\theta \qquad (III-34)$$

Where F is the total exerted force on the balance, M is the mass of the plate, g is the gravitational acceleration, r is the liquid water density, t is the thickness of the plate, H is the width of the plate, d is the immersion/emersion depth, L is the plate perimeter [L= 2 x (thickness x width)], γ_L is the liquid water surface tension, and θ is the contact angle at the liquid/solid/air contact line [186]. Moreover, an additional contribution of the measured force is represented by the so-called viscous term. This contribution is usually negligible when the ratio between viscous forces and

superficial forces is low (i.e. in the order of 10^{-2}). On the other hand, the viscous term should be taken into account at higher immersion/emersion speed (i.e. in the order of 200 mm/s) also in milliQ water and not particularly viscous liquids.

Lowering and raising a platform, where a beaker with water rests, performs partial immersion and partial emersion of a plate in water. The force is usually measured during a series of a certain number of consecutive wetting cycles. The entire process is called 'force loop' (Figure III-24).

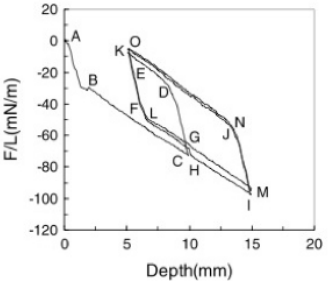

Figure III-24. A typical Wilhelmy force loop of a relatively hydrophobic surface. The sample plate is polycarbonate (PC) modified with TMS plasma [186].

Wilhelmy balance force measurements are obtained while the three-phase contact line is moving with respect to the polymer surface. This dynamic method requires the immersion and withdrawal of a sample of specific geometry through liquid water. Both advancing and receding contact angles are calculated from the force balance data; therefore, values of contact angle hysteresis can be obtained even for very fast changes in surface configuration. The Wilhelmy balance method is a more versatile and sensitive tool for monitoring the surface dynamics of polymeric surfaces than the sessile droplet method. Dynamic advancing and receding contact angles can be calculated by extrapolating corresponding immersion and emersion *F/L* lines to zero immersion depth.

A common phenomenon observed in measurements of contact angle of water on a polymer surface is the discrepancy found between advancing and receding contact angles. This discrepancy is referred to as *contact angle hysteresis*. Many factors are known to influence contact angle hysteresis, such as surface configuration change, swelling, crystallinity, surface roughness, adsorption/desorption, and the energy level of surface electrons. For low surface energy polymers, contact angle hysteresis is mostly due to surface configuration change [187]. Contact angle hysteresis can be represented numerically as the difference between the receding and advancing contact angles, $\Delta\theta = \theta_R - \theta_A$.

Contact angle hysteresis, in the context of dynamic wetting by the Wilhelmy balance method, is due to a combination of three main factors: (1) changing meniscus shape, (2) sample geometry, and (3) surface state change due to surface configuration change.

The contact angle measurement is performed in conditions not corresponding to true equilibrium states and gives non-equilibrium values (i.e. advancing and receding contact angles). To solve this problem, a 'vibrated Wilhelmy experiment' can be performed in order to transfer mechanical energy to the system in such a new stable minimum of the surface free energy can be obtained. This minimum state is independent on the initial conditions and corresponds to a value of the contact angle intermediate between the advancing and receding ones [188].

Under ideal conditions the adhesion energy is a well-defined thermodynamic quantity. It is denoted by *W* (work of adhesion) and gives the reversible work done on bringing two surfaces together or the work needed to separate two surfaces from contact [129, 189]. Under ideal, equilibrium conditions these two quantities are the same, but under more realistic conditions they are not: the work needed to separate two surfaces is always greater than that originally gained by bringing them together. Adhesion hysteresis may be due to mechanical effects such as instabilities, or chemical effects such as interdiffusion, interdigitation, molecular reorientations and exchange processes occurring at an interface after contact. Such processes induce roughness and chemical heterogeneity even though initially both surfaces are perfectly smooth and chemically homogeneous. The adhesion hysteresis may be expressed as:

$$\Delta W = (W_R - W_A) > 0 \qquad (III - 35)$$

where W_R and W_A are the adhesion for receding (separating) and advancing (approaching) two solid surfaces, respectively. Hysteresis effects are also commonly observed in wetting/dewetting phenomena. For example, when a liquid spreads and then retracts from a surface the advancing contact angle θ_A is generally larger than the receding angle θ_R. Since the contact angle is related to the solid–liquid adhesion energy (*W)* by the Dupré equation, wetting hysteresis or contact angle hysteresis actually implies adhesion hysteresis.

Solids surfaces can be characterized for their interaction with liquids by the thermodynamic parameter known as the work of adhesion (W_a) [187]:

$$W_a = \gamma_{SV} + \gamma_{LV} - \gamma_{SL} \qquad (III - 36)$$

where the terms γ_{SV}, γ_{LV} and γ_{SL} represent the interfacial energies, respectively, at the solid-vapor, liquid-vapor, and solid-liquid interfaces. By combining Eq. (III-36) with Dupre-Young's balance of force equation ($\gamma_{LV} \cdot cos\,\theta = \gamma_{SV} - \gamma_{SL}$), we can obtain the following relation for the work of adhesion:

$$W_a = \gamma_{LV}(1 + cos\,\theta) \qquad (III - 37)$$

Where θ is the contact angle at the interface between the liquid and the solid. Both contact angle and work of adhesion can give an estimation of the surface energy or wettability and can be taken into account for a comparison of different materials.
When both θ_A and θ_R are measured (for example by the sessile drop technique or Wilhelmy technique), one can calculate from Eq (III-37) the work of adhesion for both advancing and receding modes, respectively:

$$W_a^A = \gamma_{LV}(1 + cos\,\theta_A) \qquad (III - 38.1)$$
$$W_a^R = \gamma_{LV}(1 + cos\,\theta_R) \qquad (III - 38.2)$$

Noteworthy, the latter equations describe typical approaches followed when measuring the work of adhesion through contact angle measurement. Therefore, it should be necessary to underline the empirical and simplified character of these approaches.

When taking into account only bulk phases, the work of adhesion is a thermodynamic parameter that refers to equilibrium energies associated with the reversible process of separation of the interface between the two bulk phases *F* and *M* (which could be considered as pairs Filler – Matrix or Fiber – Matrix) [190]. In general the W_a should correlate with the strength of the adhesive joint as long as the system satisfies the conditions dictated by the thermodynamic relations of Eqs [190].

$$\frac{W_a}{A_{FM}} = \gamma_F + \gamma_M - \gamma_{FM} \qquad (III - 39)$$

where A_{FM} is the interfacial area of the joint, while the terms γ_F, γ_M and γ_{PM} represent the interfacial energies, respectively, of the *F* phase, *M* phase, and *F-M* phase. After a substitution of Young's equation into Eq (III-39), we can obtain the following relation for the work of adhesion:

$$\frac{W_a}{A_{FM}} = \gamma_M(1 + cos\,\theta) \qquad (III - 40)$$

Where γ_M and θ can be experimentally determined. In particular, Eq. (III-40) holds for liquids with $\theta > 0$. It is important to recognize that the concept of work of adhesion is applicable only to systems with secondary force interactions (no chemical bonds across the interface) and with no mechanical interlocking (i.e. electronic repulsion between the two surfaces in contact).

Several different mechanisms of adhesion between phases have been proposed in the literature. The mechanism of adsorption (including interfacial chemical reactions) seems to be the main mechanism responsible for intrinsic adhesion between the two phases. However, in many systems, two or more mechanisms can be involved in one joint [191]. It is not always correctly recognized that thermodynamic relations describing three-phase systems are applicable to systems with secondary force interactions. For example, the thermodynamic work of adhesion may correlate with the strength of the adhesive joint if there are no chemical bonds across the interface and no mechanical interlocking occurs.

An alternative method, of empirical nature, in order to compare different surfaces is the computation of the total solid surface free energy, γ_S (Eq. III-41)

$$\gamma_S = \gamma_{LV}(cos\ \theta_R - cos\ \theta_A)\ \frac{(1 + cos\ \theta_A)^2}{(1 + cos\ \theta_R)^2 - (1 + cos\ \theta_A)^2} \qquad (III - 41)$$

If this model works, the total surface free energy of a solid can be evaluated from three measurable parameters, i.e. the probe liquid surface tension and its advancing and receding contact angles measured on the solid surface [190]. Note that if the surface energy of the solid is greater than the interface energy of the solid-liquid, the liquid on the surface of the solid will be spread in a continuous layer.

Chapter IV

Results and discussion

4.1 Understanding the effect of nanofillers on the crystallization behavior of PP

Part of this chapter has been published in:

Pedrazzoli D, Kalaitzidou K, Pegoretti A,

"*Understanding the effect of silica nanoparticles and expanded graphite nanoplatelets on the crystallization behavior of polypropylene*",
Polymer Engineering and Science, (2014), In press.

Isotactic PP can crystallize in various forms or phases. In particular, depending on the crystallization conditions and molecular characteristics, different packing structures of the PP helices lead to the formation of the four well-known crystal forms: monoclinic (α), trigonal (β), triclinic (γ), and smectic (δ) structure [64, 65]. Although the most significant and widely occurring crystal form is the α-form structure, intensive investigation has been also focused on the β-form because of its interesting physical and mechanical properties [67] including the higher impact strength and toughness of the β-form when compared to the α-form, attributed to the different lamellar morphology of β-PP [68]. As reported in the literature [67, 70], the presence of a foreign material (e.g. polymeric compatibilizer, micro- or nano- filler) can affect the crystallization behavior of semicrystalline polymers including PP. In particular, the nanofiller itself, in absence of a special nucleating agent, can promote nucleation of the less common crystalline forms in semicrystalline polymers. For instance, some studies investigated the mechanisms responsible for the presence of polymorphism in PP / clay nanocomposites [64, 68, 77], showing that the introduction of clay increases the crystallization rate and the crystallization peak temperature, inducing an orientation of the crystals and promoting the formation of the less common β- and γ- phase with a significant enhancement of the impact strength and toughness. Moreover, the advantage of using nanofillers over the traditional β nucleating agents is that, in addition to the nucleation of the less common β-phase that exhibits greater toughness and impact strength, there is a dramatic improvement of the mechanical, thermal and possibly functional properties

achieved at filler content lower than 5 wt% due to the reinforcing effect provided by the rigid inclusions [2, 26, 54, 80-82].

Therefore, the aim of this study is to explore how the presence of nanofillers with different structural and chemical characteristics, specifically silica nanoparticles and exfoliated graphite nanoplatelets, alters the crystallization behavior and polymorphism of a semicrystalline polymer, such as PP as prepared by extrusion and injection molding.

4.1.1 Isothermal crystallization behavior

Representative optical micrographs of the isothermal crystallization experiments are represented in Figure IV-1.1. Using the hot stage under the microscope, the temperature was decreased from the melting temperature to 145 ^{o}C, (time is set to 0) and then it was kept constant until the crystallization was completed. In case of neat PP at t = 0 s, some pre-existing small nuclei can be noticed, probably due to impurities and catalyst residues (Figure IV-1.1-left). Crystallization occurs through the formation and growth of spherulites around the pre-existing nuclei, while no recrystallization or secondary crystallization can be observed.

On the other hand, PP nanomodified with 0.01 wt% silica R974 (Figure IV-1.1-central) or 0.01 wt% xGnP-C750 (Figure IV-1.1-right) exhibits a much faster crystallization, evidencing the formation of smaller and more numerous spherulites of quite irregular shape. The faster crystallization dynamics observed in nanofilled PP indicated the nucleation ability of the silica particles and xGnP, which provide larger surface area available for nucleation and growing of the polymer crystals. Interestingly, when taking into account the system modified with xGnP, it can be noticed that the nucleation takes place around the graphite nanoplatelets (Figure IV-1.1-right, t=1'), forming a transcrystalline zone.

In order to estimate the crystallization kinetics, the rate of crystallization occurred at 145 °C was quantified by i) standard DSC experiments and ii) *in situ* experiments with observation through optical microscope (Table IV.1-1). In particular, in case of the *in-situ* study, the crystallization rate is computed as the inverse of the time required for the spherulites to completely cover the observed micrograph area. Crystallization rate results clearly show that the incorporation of nanomaterial, even at a content as low as 0.01 wt%, can remarkably affect the crystallization characteristics of PP, resulting in a dramatic increase of the crystallization rate.

Table IV.1-1. Crystallization rate during isothermal crystallization at 145 °C based on DSC and in-situ hot stage/microscopy studies.

Sample	Based on DSC (min^{-1})	Based on *in situ* hot stage/microscopy (min^{-1})
PP	0.069 ± 0.002	0.05
PP-R974-0.01	0.209 ± 0.012	0.20
PP-xGnP_C750-0.01	0.331 ± 0.015	0.25

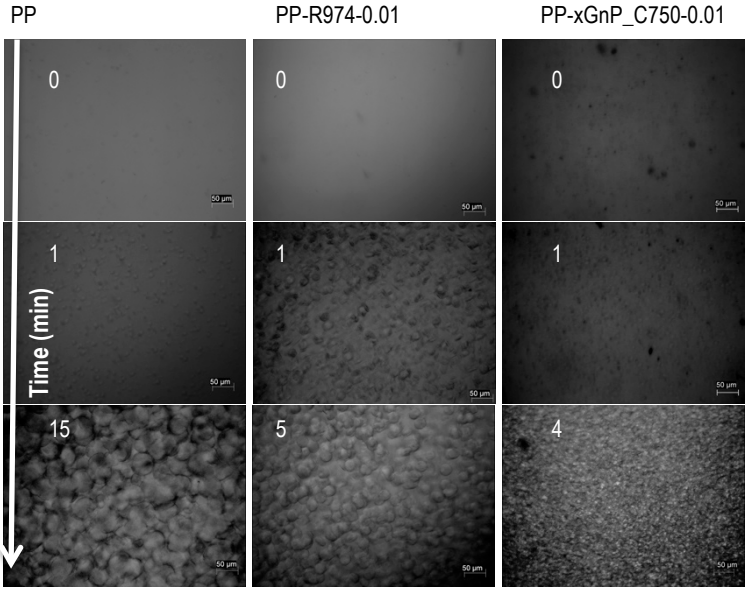

Figure IV-1.1. Isothermal crystallization at 145 °C of PP (left column), PP-R974-0.01 (central column) and PP-xGnP_C750-0.01 (right column) as a function of time.

4.1.2 Non-isothermal crystallization behavior

The degree of crystallinity ($\chi_{\%}$), as determined by MDSC during non-isothermal crystallization experiments, decreases with the filler content (Table IV.1-2). Moreover, the increase in crystallization temperature (T_c) evidences the nucleation effect of the nanomaterials, noticing a greater effect obtained with xGnP compared to that of silica.

Table IV.1-2. Crystallization and melting parameters obtained by MDSC.

Sample	T_c [°C]	$\chi_{\%}$ [%]	Induction time [min]	T_{m1} [°C]	T_{m2} [°C]	Enthalpy of recrystallization [J/g]
PP	126.2 ± 0.2	51.1 ± 0.3	3.7 ± 0.1	154.6 ± 0.1	166.3 ± 0.2	~ 0
PP- R974- 0.5	126.9 ± 0.2	50.6 ± 0.4	3.7 ± 0.1	154.7 ± 0.2	167.6 ± 0.4	~ 0
PP- R974- 1	127.2 ± 0.2	49.8 ± 0.4	3.8 ± 0.0	154.9 ± 0.2	168.0 ± 0.2	~ 0
PP- R974- 3	127.5 ± 0.1	49.7 ± 0.4	4.0 ± 0.1	154.4 ± 0.1	168.6 ± 0.3	~ 0
PP- R974- 5	127.6 ± 0.2	48.3 ± 0.4	4.1 ± 0.1	156.5 ± 0.3	167.1 ± 0.2	2.1 ± 0.2
PP- R974- 7	127.7 ± 0.1	47.1 ± 0.3	4.2 ± 0.1	158.6 ± 0.2	167.0 ± 0.4	15.9 ± 0.6
PP- xGnP_C750- 0.5	130.8 ± 0.2	49.8 ± 0.5	4.2 ± 0.0	/	160.2 ± 0.2	~ 0
PP- xGnP_C750- 1	133.2 ± 0.2	48.6 ± 0.4	4.7 ± 0.2	/	160.3 ± 0.3	2.5 ± 0.2
PP- xGnP_C750- 3	137.2 ± 0.2	48.7 ± 0.5	5.0 ± 0.1	/	161.3 ± 0.2	30.9 ± 0.4
PP- xGnP_C750- 5	138.8 ± 0.2	47.4 ± 0.4	5.2 ± 0.1	/	162.1 ± 0.3	23.5 ± 0.6
PP- xGnP_C750- 7	139.3 ± 0.3	46.7 ± 0.4	5.5 ± 0.2	/	161.7 ± 0.2	12.2 ± 0.4

This difference might be also attributed to the higher surface area of xGnP, which is 750 and 124 m^2/g for xGnP and silica respectively, according to the suppliers.

The crystallization induction time, defined as the time difference between onset and endset of non-isothermal crystallization, gives an estimation of the crystallization rate during both nucleation and growth. In particular, this characteristic time is increased with the filler amount, indicating that the polymer chains have more time to re-arrange, forming more perfect and / or thicker crystals [192].

4.1.3 Polymorphism and crystal thickness

The effect of filler type and amount on the PP polymorphism and lamella thickness was studied by both XRD and MDSC on PP nanocomposites prepared by extrusion and injection molding (section 3.2.1.2).

Isotactic PP can exhibit four crystal structures: monoclinic (α), trigonal (β), triclinic (χ), and smectic (δ), whose formation depends on processing conditions (i.e melting history, crystallization temperature, pressure and cooling rate) and the presence of nucleating agents or fillers [65, 193].

In particular, while the α-form is the most common crystalline phase, the β-form can occur under particular conditions (i.e. temperature gradients, presence of shearing forces or nucleating agents). Moreover, the least common γ-form is more likely to be observed in low molecular weight PP [194].

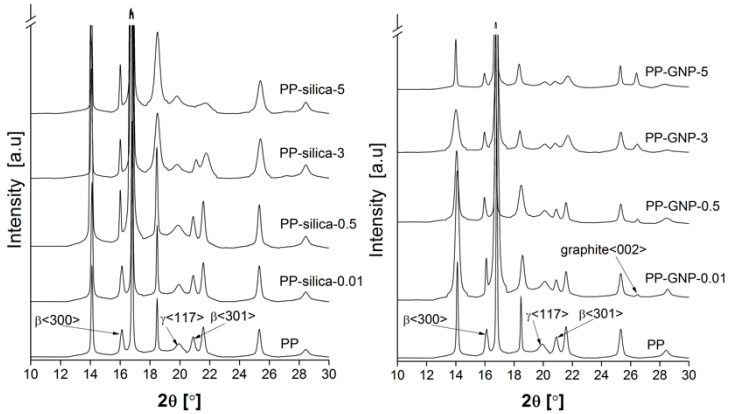

Figure IV.1-2. X-ray diffractograms of (a) PP-R974 and (b) PP-xGnP_C750 nanocomposites as a function of the nanomaterial content.

The diffractograms of PP-R974 and PP-xGnP_C750 nanocomposites are presented in Figure IV-1.2a and Figure IV-1.2b, respectively. The characteristic six reflections of the α-form (2θ=14.08° <110>, 2θ=16.95° <040>, 2θ=18.50° <130>, 2θ=21.85° <041>, 2θ=25.00° <060> and 2θ=28.00° <220>) [194-196], two reflections of the β-form (2θ=16.00° <300>, 2θ=21.00° <301>) [195] and one reflection associated to the γ-form (2θ=20.07° <117>) [194] can be identified on the diffractogram of neat PP (Figure IV.1-2a).

Incorporation of silica results in an increase of the first three reflections of the α-form, noticing the reflection at 2θ=16.95° dominating, while the reflection at 2θ=21.85° decreases in intensity with the filler amount. Quite different trend is followed by the β-form reflections, as they increase up to a filler content of 0.5 wt% and diminish at higher filler content, while the γ reflection (recognizable at 2θ=20.07°) becomes slightly broader with the filler content. Noteworthy, the addition of only 0.01 wt% silica is shown to promote the formation of the β-phase crystals. As confirmed by XRD analyses, given the amorphous nature of the silica nanoparticles, no peak can be attribute to the silica filler itself.

The β-phase content, typically indicated as *k* value, was estimated adopting the formula proposed by Turner-Jones et al., specifically derived for isotactic PP [197] :

$$k = \frac{I_\beta}{I_{\alpha 1} + I_{\alpha 2} + I_{\alpha 3} + I_\beta} \times 100 \quad [\%] \qquad (IV-1)$$

where I_β is the intensity of the β-phase reflection corresponding to the <300> plane, while I_{a1}, I_{a2} and I_{a3} are the intensities of the α-phase reflections corresponding to the <110>, <040> and <130> plane, respectively. Incorporation of silica results in an increase (in the order of ~13%) in the *k* value with silica content up to 0.5 wt%, followed by a slow decrease at larger filler contents (Figure IV-3a). The non-monotonic trend of *k* as a function of the silica content indicates that silica is able to promote the formation of the less common β-phase up to an optimal filler content. In fact, further addition of silica strongly limits the available surface of silica nanoparticles, due to aggregation and agglomeration, and increases the crystallization rate, hindering the formation of β-phase in favor of the α-phase. As indicated by the estimation of the lamella thickness shown below, the higher crystallization rate results in less time for the β-nuclei to form and insufficient space that the nuclei have to grow due to the faster nucleation and growing of the α-nuclei.
The lamella thickness of the crystals (L_t), which is a measure of the crystal size, was computed using the full width at half maximum (*FWHM*) of the predominant XRD reflections according to the Debye-Scherrer formula [198], presented in Eq (IV-2):

$$L_t = \frac{K \cdot \lambda}{FWHM \cdot \cos(\theta)} \qquad (IV-2)$$

where K is the crystal shape factor assumed as 0.9, while λ is the X-ray source wavelength.

The thickness of the dominant α-form crystal of PP-silica composites, corresponding to the reflection at 2θ=16.95°, is observed to significantly increase with the silica content (Figure IV.1-3a). Since the α-form is the predominant crystalline morphology in PP, the higher crystal thickness is in agreement with the increase of induction time as measured during non-isothermal crystallization experiments (Table IV.1-2). Quite different behavior is represented by the β-phase crystals (2θ=16.10°), whose thickness increases for addition of silica up to 1 wt% and slowly decreases at higher contents, concurrently with the reduction in β-phase content.

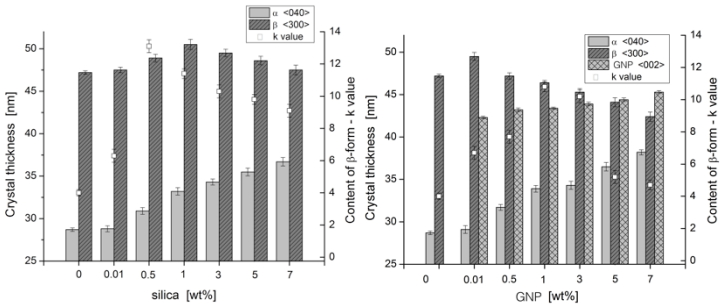

(a) (b)

Figure IV.1-3. (a) Crystal thickness of the α-form evaluated at 2θ=16.95° (<040> plane) and β-form evaluated at 2θ=16.10° (<300> plane) for PP-silica composites and (b) crystal thickness of the α-form, β-form and of the graphite's <002> plane at 2θ=26.45°.

Addition of xGnP into PP results in an increase of the reflections of the α-form crystals with the filler content but a slight increase of the reflections associated to the β-form crystals at low GNP content of 0.01 wt% (Figure IV.1-2b). Moreover, the reflection at 2θ=26.45°can be attributed to the presence of the nanofiller, corresponding to the graphite's <002> plane [199], whose intensity increases with the filler loading. Noteworthy, the fact that the graphite reflection observed for PP-xGnP composites does not shift towards smaller values of theta, compared to the peak of neat xGnP, indicates that the polymer chains cannot enter the xGnP narrow galleries due to high viscosity [200-202]. However, the crystal size associated to the graphite's <002> plane increases with the filler loading (Figure IV.1-3b), evidencing

the presence of large agglomerates formed and possibly oriented during processing along the injection molding direction [203].

As indicated by the *k* value, the β-phase content increases up to a graphite content of 1 wt% (~ 11%). Nevertheless, a decrease in content and lamellar thickness of the β-phase observed at greater filler amount might be attributed to the higher crystallization rate which may might favor the formation of the α-phase over the β-phase.

4.1.4 Melting behavior

The analysis of the structural morphology obtained by XRD are in general agreement with the melting behavior as determined using MDSC. In particular, the reversing heat flow measured through MDSC is strongly associated to reversible transformations, including melting related phenomena. Interestingly, PP-silica composites show two distinct peaks on the thermograms, a minor peak T_{m1} at lower temperature and the main peak T_{m2} at higher temperature (Figure IV.1-4a). As already reported in the literature, the double melting peak might be associated with the recrystallization of the monoclinic α_1 into the more ordered α_2 phase [204]. However, as observed in the XRD diffractograms, PP-silica nanocomposites present a significant β phase content, whose melting properties differ from those of the α phase. In fact, the β phase of isotactic PP manifests a melting peak at lower temperature (i.e between 153 and 159 °C) compared to the α phase [74, 205]. Therefore, the two melting peaks T_{m1} and T_{m2} are attributed to the β and α crystal form, respectively. Moreover, the characteristic splitting of the low temperature peak T_{m1} is not observed, indicating the absence of a β – β' recrystallization (usually attributed to crystal perfection phenomena of the β phase), as it might take place in some cases under different cooling condition [206, 207]. Furthermore, the melting peak T_{m1} shifts towards higher temperatures and decreases in intensity at higher silica content, probably because of the β phase attenuation.

Noteworthy, the reversing heat flow excludes all phenomena related to recrystallization and crystal perfection, possibly occurring upon heating. Therefore, in order to further investigate the melting behavior, the thermogram of the non-reversing heat flow was analyzed (Figure IV.1-4b) as a function of the filler content.

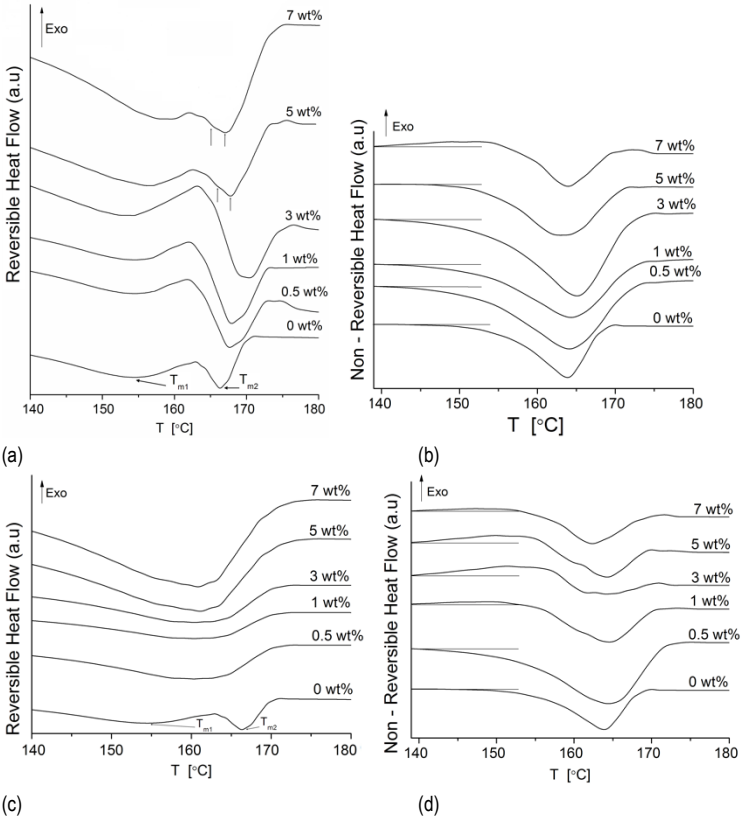

Figure IV.1-4. Reversible and non-reversible heat flow describing the melting behavior of (a-b) PP-R974 and (c-d) PP-xGnP_C750 nanocomposites during MDSC analyses.

Limited recrystallization occurs only at 7 wt% silica, probably because of a crystals perfection phenomena or because the imperfect β crystals that undergo recrystallization, recrystallize in the α-form and/or at the transcrystalline regime [208-210]. Table IV.1-2 reports the recrystallization enthalpy determined as the area under the exothermic transformation of the $\beta - \alpha$ transition. As reported by Marco et al., PP exhibiting recrystallization may also show evidence of a slight but significant splitting of the endotherm peak associated with the α_1 and α_2 phases at 165 and 168°C, respectively, which is also observed on the reversible thermograms (Figure IV.1-4a) of PP-silica 7 wt% [205]. Specifically, the new monoclinic crystals that form

during the $\beta - \alpha$ transition are α_2 and melt at a higher temperature than the α_1 crystals, formed during cooling from the melt.

The PP-xGnP nanocomposites show a rather different melting behavior. In particular, the melting peak T_{m1} progressively disappears upon addition of xGnP, because the β-phase is hindered (Figure IV.1-4c). Note that since the two melting peaks T_{m1} and T_{m2} were rather difficult to distinguish on the thermogram, only one representative melting temperature was reported in Table IV.1-2. Recrystallization occurs at filler loadings between 1 and 5 wt%, possibly indicating crystal perfection phenomena or recrystallization of the β-form in the α-form and/or at the transcrystalline zone (Figure IV.1-4d). As confirmed by XRD analysis, the β-form crystals become fewer and thinner with xGnP loading larger than 1 wt%, when recrystallization begins to occur.

When considering an overall analysis, taking into account the crystallization induction time based on DSC, the vanishing of the β-phase and the recrystallization enthalpy according to MDSC; and the increased lamella thickness of the α -phase calculated based on XRD, the overall effect of xGnP on the crystallization of PP is to promote the formation of more perfect α-crystals and of transcrystalline region at the crystal boundaries.

4.1.5 Tensile and impact mechanical properties

Previous studies on the crystallization of isotactic PP demonstrated that a higher amount of the β-form results in higher impact strength and toughness compared to the α-form [43], accompanied with a slight decrease in elastic modulus and yield stress [69]. Based on these considerations, both quasi-static and impact tests were performed on some selected samples.

The elastic modulus of the PP-silica and PP-xGnP composites increases non-monotonically with addition of fillers, as shown in Figure IV.1-5a and IV.1-5b, respectively. This trend indicates the presence of two competing mechanisms, specifically the stiffening effect given by high modulus filler particles (E ~ 70 GPa for both silica and xGnP) and the formation of aggregates due to the relatively poor dispersion within the matrix.

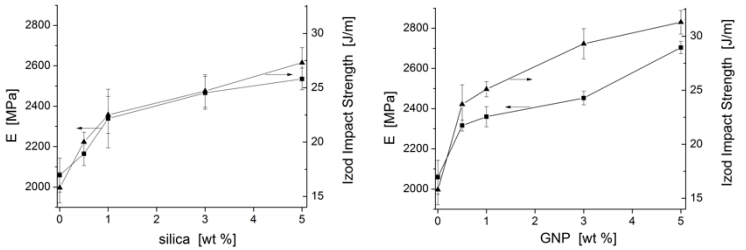

Figure IV.1-5. Elastic modulus and Izod impact strength of (a) PP-R974 and (b) PP-xGnP_C750 nanocomposites.

Moreover, taking into account the impact of the α and β-forms on the elastic modulus described above, the non-monotonic trend followed by the elastic modulus might also be attributed to the polymorphism behavior. However, other effects should be accounted for, especially the dependence of morphology and filler interfacial interactions upon the filler content.

The impact strength shown in Figure IV.1-5a-b significantly increases with the filler content, noticing a greater enhancement in the case of xGnP composites. Noteworthy, the increase in toughness obtained in PP composites at low and intermediate filler content can be attributed to (i) changes in the energy absorbing mechanisms (i.e. higher plastic deformation of the matrix along the filler/matrix interface, crack branching due to hindrance by reinforcements, bridging of the crack, creation of voids etc.) and (ii) different crystalline morphology occurring upon nanomodification. In particular, as already shown in the isothermal crystallization experiments, the presence of the filler may change the spherulite size. Moreover, the filler type and content can, as shown earlier, affect the polymorphism and lamella thickness. Both spherulite size and polymorphism play a key-role in determining the impact strength of PP [65]. Some studies reported how an increase in β-phase content results in a significant enhancement in impact strength and toughness in semicrystalline polymers [64, 77]. Since the investigated nanocomposites show a higher β-phase content at filler contents between 0.5 and 5 wt%, this might be one of the reasons explaining the higher impact strength observed with respect to unfilled PP, whose amount of β-phase is significantly lower.

4.1.6 Morphological analyses

Fracture surfaces of PP nanocomposites were analyzed by SEM and compared to that of neat PP (Figure IV.1-6a) in order to study the filler dispersion and distribution.

Although uniform distribution of relatively small silica aggregates is shown in PP-R974-1 samples (Figure IV.1-6b), non-homogeneous agglomeration is observable when considering PP filled with 7 wt% silica (Figure IV.1-6c). Similar consideration can be reported for xGnP, which appear rather well distributed at a content of 1 wt%, with very few distinguishable platelets with dimension of around 1 μm (Figure IV.1-6d). On the other hand, larger aggregates can be noticed in case of the PP-xGnP_C750-7 composites (Figure IV.1-6e). Noteworthy, the presence of aggregates strongly limit the xGnP surface area available for nucleation of the PP crystals.

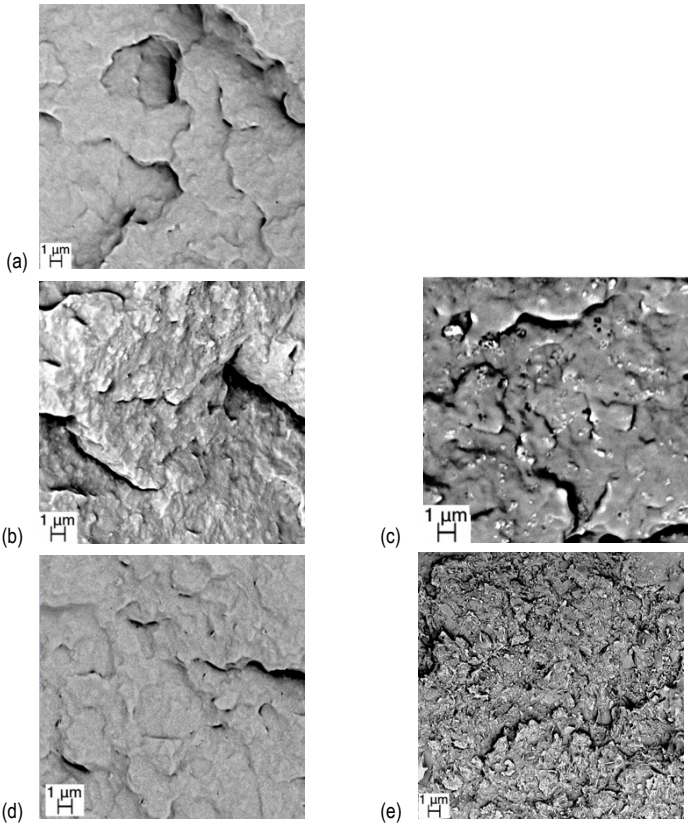

Figure IV.1-6. SEM micropictures of neat PP (a), PP composites filled with 1 and 7 wt% of silica R974 (b-c) and xGnP_C750 (d-e).

In this study, it was shown that both silica and graphite act as effective nucleating agents, even at loadings as low as 0.01 wt%, significantly increasing the crystallization rate during isothermal crystallization, with greater changes observed in case of xGnP composites. The nucleation of the β-phase, which exhibits superior impact strength and toughness compared to the most common α-form, was observed in both silica and graphite composites even at low filler concentration.

Because of the overall changes were found generally greater for xGnP with respect to silica, the xGnP is significantly more efficient in inducing polymorphism and favoring the formation of a transcrystalline phase on the filler surface.

4.2 Understanding the interfacial interactions in PP nanocomposites and their impact on the mechanical properties

Part of this chapter has been published in:

Pedrazzoli D, *Kalaitzidou K*, Pegoretti A,

"*Understanding the interfacial interactions in silica reinforced polypropylene nanocomposites and their impact on the mechanical properties.*",
Polymer Composites. (2014) Under review.

Although the interface interactions can be disregarded in micro-reinforced composites, they need to be considered in case of polymer nanocomposites, because the interfacial effects have a predominant influence on the dispersion and agglomeration of the filler within the matrix and the stress transfer, which dictates the physical properties of the polymer matrix and consequently the macroscopic characteristics of the polymer nanocomposite [56, 200, 211, 212]. The recent literature emphasizes the need of considering various experimentally observed filler characteristics such as aspect ratio [213-215], agglomerate size and presence and properties of interphase [216-219] in order to develop better design tools to fabricate multifunctional polymer composites [212]. In particular, it is of great interest to understand how nano-scale interfacial interactions affect the macro-scale properties in polymer nanocomposites [62, 87, 220-223]. Recent studies based on calorimetry and characterization of the viscoelastic properties, have shown clear evidence on how the presence of a constrained amorphous phase located not only at the crystal surface but also at the filler surface can induce secondary reinforcing mechanisms which, in addition to the primary stiffening effect due to the high modulus of the filler particles, can significantly contribute to the enhancement of the bulk properties of semicrystalline polymers [62, 87]. *Therefore, the aim of this study is to provide better understanding on the impact of interfacial interactions on the physical characteristics of the PP matrix and in turn on the macroscopic mechanical performance of silica reinforced PP nanocomposites, as prepared by extrusion and injection molding.*

4.2.1 Tensile mechanical properties and viscoelastic properties

The tensile elastic modulus and the glass transition temperature *(T_g)*, evaluated by DMA analysis as the temperature correspondent to the tanδ peak, were observed to follow a similar trend when considered as a function of the filler content

(Figure IV.2-1(a-b)). In particular, modulus and T_g of the composites based on silica A380 increase with filler content up to ~1 wt%, reaching a plateau at filler loadings between 1 and 3 and continue increasing at higher filler amounts. This non-monotonic trend evidences the presence of two competing effects, specifically the stiffening effect given by high modulus silica particles (E ~ 70 GPa) and the formation of silica aggregated because of poor dispersion within the matrix. On the other hand, PP-R974 composites manifested a monotonic trend characterized by a greater increase of the quantities at low filler content, reaching almost a plateau at higher filler amounts. Noteworthy, the higher efficiency of the surface treated silica (i.e. R974) in reinforcing the polymeric matrix might indicate a better dispersion of the filler.

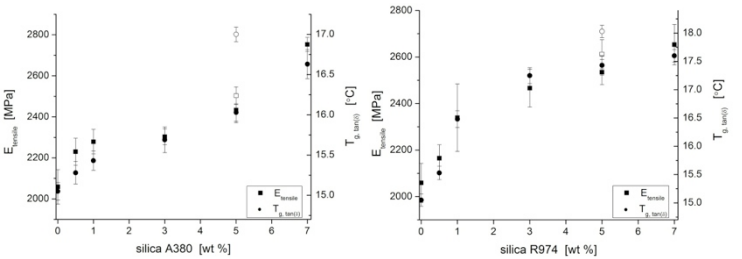

(a) (b)

Figure IV.2-1. Tensile elastic modulus and T_g obtained from DMA of (a) PP-A380 and (b) PP-R974 composites as a function of the filler content. The compatibilized samples (i.e. PP-PPgMA-5-A380-5 and PP-PPgMA-5-R974-5) are represented by open point in their correspondent plots.

The correlation between tensile modulus and glass transition temperature can help understanding the reinforcing mechanisms which contribute to the enhancement of the tensile and visco-elastic properties. Specifically, the increase of both the modulus and T_g occurs primarily due to the reinforcing effect of the high modulus silica filler [56, 224-226]. Moreover, since changes in T_g are related to the primary relaxation of polymer chains and the extent of the immobilized chains, the alteration of polymer chain mobility upon nanofiller addition might significantly contribute [227-230]. Other secondary effects, such as the change in polymer's crystallinity and crystal structural forms, might play a significant role in the reinforcing effect [64, 69, 71, 77]. The strong correlation between the tensile modulus and T_g, which is related to the immobilized fraction of the polymer chains in the amorphous region, motivated further investigation of the tensile and viscoelastic properties as a function of the polymer/filler interfacial interaction.

4.2.2 Characterization of the interfacial interactions

4.2.2.1 Relationships between interfacial interactions and the tensile and visco-elastic properties

In order to explore the role of interfacial interactions in enhancing the mechanical performances of nanocomposites, the relationships between interfacial interactions and the tensile and visco-elastic properties of silica nanocomposites were investigated using the models mentioned below. Unlike fiber-reinforced composites, the interfacial interactions in particulate-filled composites is hard to measure directly. In order to overcome this technical issue, Pukanszky [91] developed a model expressing the ratio of the yield stress of the nanocomposites to that of the neat polymer ($\sigma_{y,c}/\sigma_{y,m}$) as a function of the filler volume fraction ϕ :

$$\frac{\sigma_{y,c}}{\sigma_{y,m}} = \frac{1-\phi}{1+2.5\phi}\exp(B_P\phi) \qquad (IV-3)$$

where the fraction $[(1-\phi)/(1+2.5\phi)]$ takes into consideration the decrease of the effective load-bearing cross-section, while the exponential represents all other effects resulting in an increase of the yield stress [90]. Specifically, the parameter B_P accounts for the interface and interphase properties and larger B_P values correspond to higher interfacial adhesion [231]:

$$B_P = \left(1+\tau\,\rho_f\,S_f\right)\ln\left({}^{\sigma_{y,i}}/_{\sigma_{y,m}}\right) \qquad (IV-4)$$

where τ is the thickness of the interphase, while the quantities ρ_f, S_f and $\sigma_{y,i}$ represent the density of the filler, the specific surface area of the filler and the yield stress of the interphase, respectively. Because of obvious technical difficulties in providing reliable values of the thickness and yield stress of the interphase, the parameter B_P can be extrapolated from the experimental data according to Eq. (IV-3):

$$B_P = \frac{1}{\phi}\,ln\left(\frac{\sigma_{y,c}}{\sigma_{y,m}}\,\frac{1+2.5\phi}{1-\phi}\right) \qquad (IV-5)$$

On the other hand, Sumita et al [92] proposed a model to express the ratio of the loss modulus of the nanocomposites to that of the neat polymer (E_c''/E_m'') as a function of the effective volume fraction of the dispersed phase (ϕ_e), which is represented by the volume of filler (ϕ) plus that of the 'constrained matrix' associated with the interface :

$$\frac{E_c''}{E_m''} = (1-\phi_e)^{-1} = (1-\phi\, B_s)^{-1} \qquad (IV-6)$$

where the parameter B_S describes the relative value of the effective volume per single particle.

In order to investigate the relationships between interfacial interactions and the tensile and visco-elastic properties, the parameters B_P and B_S are plotted as a function of the filler volume fraction ϕ for PP-A380 and PP-R974 samples in Figure IV.2-2(a-b). For both samples, B_P and B_S increase up to a threshold value ~0.005-0.010 vol% (correspondent to ~1-3 wt%) and decrease at higher volume fractions.

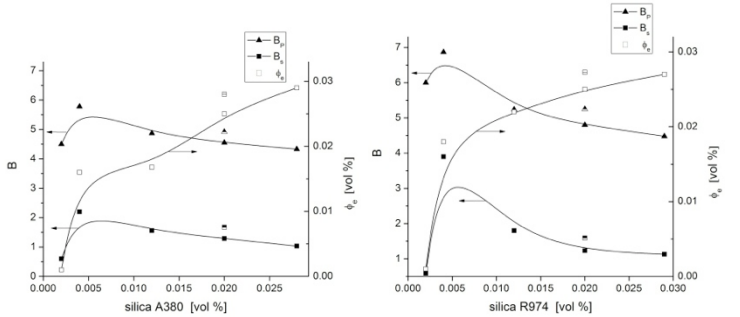

Figure IV.2-2. Plot of the *B* parameters and of the effective volume fraction of the dispersed phase *(ϕ_e)* as a function of the filler volume content for (a) PP-A380 and (b) PP-R974 composites. Half full points denote data related to the PP-PPgMA-5-silica-5 samples.

This trend indicates that the polymer/filler interfacial adhesion is enhanced up to the threshold value, while the higher concentration of aggregates at greater filler contents leads to a significant decrease in the average specific surface area of silica particles, resulting in a decrease of the *B* parameters [90]. Specifically, when passing the threshold filler value, the value of ϕ_e increases less rapidly with further addition of particles, indicating that the thickness of the physically absorbed PP layer on the surface of the silica particles is limited due to the agglomeration [231]. Moreover, the effective volume per single particle (*B* parameter) continuously decreases, evidencing that the extent of the particle agglomeration also increases with filler content. The fact that generally higher *B* values are obtained for PP-R974 than for PP-A380 samples, can be explained by the better dispersion of R974 silica. Moreover, the existence of silica aggregates in both samples at higher filler fractions explains why differences between *B* values of the two samples, at a given volume

fraction above 0.020 vol%, disappear. Samples added with compatibilizer (i.e. PP-PPgMA-5-A380-5 and PP-PPgMA-5-R974-5) show higher values in B values and ϕ_e , indicating a better filler dispersion and / or an increase in interphase thickness.

When considering the quantities involved in the Pukansky and Sumita models, the similar trend followed by B_P and B_S parameters evidences a correlation between the tensile macroscopic properties and visco-elastic properties. In addition, a similar trend can also be recognized between elastic modulus, T_g and ϕ_e , providing further evidence of the presence of secondary reinforcing mechanisms in silica nanocomposites.

4.2.2.2 Complex constrained phase at the filler surface

The recent literature reports evidence of the formation of a complex polymer phase constrained on the filler surface. In particular, the model proposed by Karevan and Kalaitzidou for particle-filled semicrystalline polymers considers as constrained phase (*C*) the crystalline phase (χ) and part of the amorphous phase that is immobilized not only at the crystal surface but also on the filler surface [62]. The rest of the amorphous phase is considered as the mobile phase. The *tan* δ and degree of crystallinity *c* used to apply the model were determined using DMA and MDSC, respectively (Table IV.2-1). In particular, the degree of crystallinity was calculated by taking the weight fraction of PP in the composite into account, according to equation (III-3).

As already observed by Karevan et al. in the case of polyamide 12/expanded graphite nanoplatelets composites, although the filler facilitates nucleation of the polymer crystals (i.e. higher crystallization peak temperature due to nanomodification), the crystal growth process may or may not be affected, and the lower crystallinity can be explained by considering that during crystallization the polymer chains are immobilized at the xGnP surface, resulting in an increase in T_g and a hinder effect on crystallization [62]. The presence of an immobilized amorphous phase at the filler surface is also evidenced in the viscoelastic behavior. In particular, the *tan* δ peak value, evaluated at T_g, decreases and shifts towards higher temperatures upon filler incorporation (Figure IV.2-3). This trend indicates that the filler decreases the viscous and improves the elastic behavior of PP by pinning the polymer chains and forming an immobilized region.

Table IV.2-1. Crystallization and viscoelastic properties of the silica nanocomposites.

Sample	$\chi_{\%}$ (1)	$\tan\delta_{Tg}$ (2)	$C_{\%}$ (3)	$(C-\chi)_{\%}$ (4)
PP	41.8 ± 0.2	0.0789 ± 0.0010	41.8	0.0
PP-A380-0.5	41.4 ± 0.3	0.0762 ± 0.0006	43.4	2.0 ± 0.3
PP-A380-1	40.0 ± 0.2	0.0747 ± 0.0009	44.3	4.3 ± 0.2
PP-A380-3	38.6± 0.3	0.0732 ± 0.0010	45.2	6.6 ± 0.3
PP-A380-5	38.5 ± 0.2	0.0717 ± 0.0008	46.1	7.6 ± 0.2
PP-A380-7	34.8 ± 0.3	0.0657 ± 0.0007	49.8	15.0 ± 0.3
PP-R974-0.5	41.8± 0.2	0.0743 ± 0.0010	44.5	2.7 ± 0.2
PP-R974-1	40.6 ± 0.3	0.0732 ± 0.0009	45.2	4.6 ± 0.3
PP-R974-3	39.2 ± 0.4	0.0715 ± 0.0006	46.2	7.1 ± 0.4
PP-R974-5	37.9 ± 0.2	0.0700± 0.0009	47.2	9.2 ± 0.2
PP-R974-7	34.7 ± 0.4	0.0663 ± 0.0008	49.5	14.8 ± 0.4
PP-PPgMA-5-A380-5	38.0 ± 0.2	0.0654 ± 0.0007	50.0	12.0 ± 0.2
PP-PPgMA-5-R974-5	38.4 ± 0.3	0.0640 ± 0.0009	50.9	12.5 ± 0.3

(1) : Degree of crystallinity based on MDSC measurements. (2) : Loss factor based on DMA analyses.
(3) : Constrained polymer phase [62]. (4) : Amorphous constrained phase.

In order to discern the stiffening effect due to the stiff phase constrained by filler inclusions (elastic behavior observable below T_g) and because of the restriction of polymer chain mobility (elastic behavior observable above T_g), the storage modulus of the silica nanocomposites above and below T_g, normalized with respect to that of neat PP, is represented in Figure IV.2-4 as a function of the filler content.

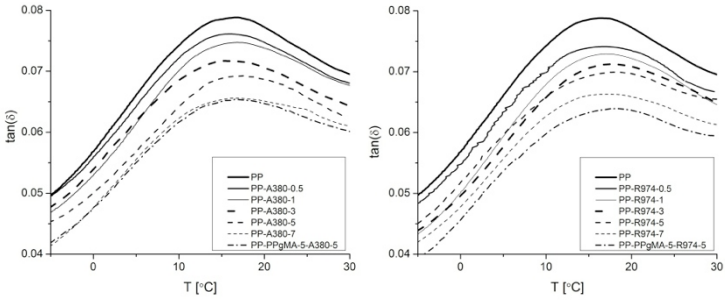

(a) (b)

Figure IV.2-3. *tanδ* of (a) PP-A380 and (b) PP-R974 composites as a function of temperature and filler amount.

The normalized storage modulus (E'_c/E'_m) is higher for both PP-A380 and PP-R974 composites when considered above T_g than when evaluated below T_g. Taking into account that the storage modulus is related to the elastic response of the composites, rather than the viscose behavior, and that the amorphous phase increases (decrease in crystallinity), the increment of E'_c/E'_m above T_g was expected not to be higher than that below T_g, however, this was not the case. Consequently, the observed trend provides further evidence of the presence of immobilized amorphous phase at the filler surface, in concordance with the values reported in Table IV.2-1.

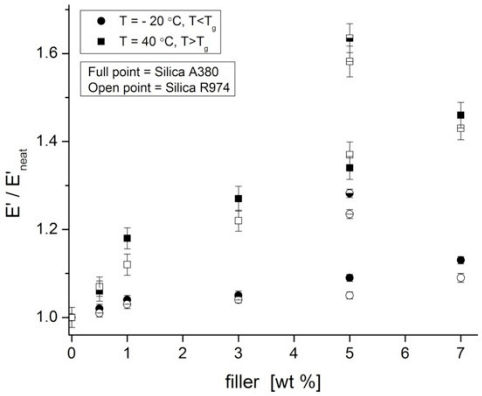

Figure IV.2-4. Normalized storage modulus evaluated below and above the glass transition temperature as a function of filler content. Half full points denote data related to the PP-PPgMA-5-silica-5 samples.

The incorporation of compatibilizer PPgMA induces an increase of storage modulus for the samples added with 5 wt% silica, resulting in a shifting of the normalized moduli towards higher values and showing a slightly greater increase when considering the property above T_g. The better filler dispersion induced by the compatibilizer results in a greater amount of amorphous phase constrained at the filler surface.

The non-isothermal crystallization behavior, as studied by MDSC, showed that incorporation of increasing amounts of filler results in a progressive increase of the onset crystallization temperature (i.e. characterizing the beginning of the crystallization), indicating a nucleation effect [232, 233]. Therefore, the crystallization induction time (Δt_i), defined as the time difference between onset and endset time of the crystallization, was found to increase with the filler content (Figure IV.2-5),

evidencing that the polymer chain have longer time to re-arrange and forming more perfect and / or thicker crystals [192].

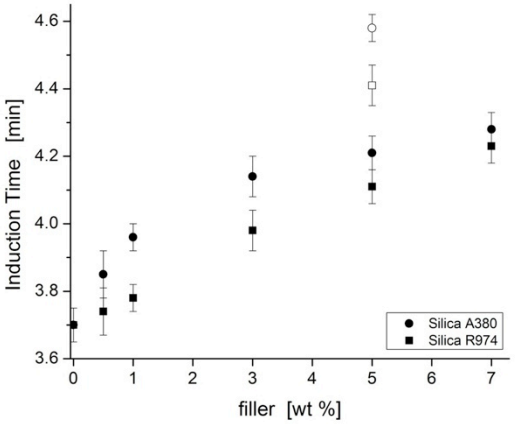

Figure IV.2-5. Crystallization induction time, obtained from the non-isothermal DSC crystallization curves, as a function of the filler content. PP-PPgMA-5-silica-5 samples are represented by open point.

Considering also the nucleation effect produced by silica fillers (i.e. more surfaces are available for nucleation of new crystals), the observed crystallization behavior indicates that a transcrystalline phase forms on the filler surface during crystallization. Moreover, compatibilized samples show even greater values of induction time, revealing an even greater tendency in forming transcrystalline phase at the filler interface. Therefore, the immobilized constrained phase consists of the immobilized amorphous and the immobilized transcrystalline phase

4.2.3 Morphology characterization

AFM not only can provide a direct visualization of 3-dimensional images of the polymer surfaces, but also a concurrent measurement of the mechanical properties and adhesion forces and interactions occurring at the surface. When used to study the interphase characteristics, AFM can provide important insights regarding the factors that are responsible for the peculiar properties exhibited by nanocomposites. In particular, the interphase characteristics were defined in the phase image of the scanned surface as the area where a sharp change in phase occurs, indicating transition between materials with different stiffness (or modulus). The width of this transition area is considered as the interphase width, while the phase gradient can

be related to the interphase stiffness. A representative phase image of the scanned surface of samples filled with 5 wt% of treated silica (R974) is depicted in Figure IV.2-6. The average diameter of the particle agglomerates corresponds to around 200-300 nm.

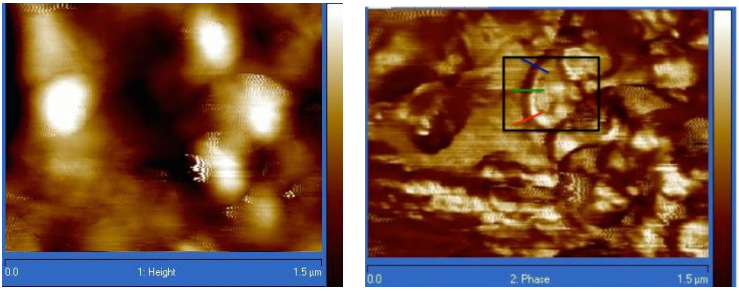

Figure IV.2-6. Representative AFM phase image of the PP-R974-5 nanocomposite: (a) height plot (maximum height = 20 nm), (b) phase lag plot (maximum phase = 40°) indicating the lines used for the height and phase lag measurement across the interphase and (c) profile lines of the phase lag vs. distance across the matrix/filler interphase.

From the analysis of the phase lag vs. distance plots, the interphase width can be estimated as the average of at least three measurements. The average elastic modulus of the interphase was computed by applying the rule of mixtures between polymer matrix and silica particles and assuming a linear trend across the interphase. The elastic modulus of silica particles was assumed as 70 GPa [234]. The interphase average elastic modulus resulted around 35.5 GPa for silica particle agglomerates, while a correspondent average interphase thickness was determined around 15-20 nm. However, because of insufficient available time for this investigation, the AFM characterization remained a preliminary study. With the aim of investigating the dependence of the interphase thickness and properties on the filler

content and morphological properties, a more detailed and systematic study should be carried out.

SEM micrographs of fracture surfaces for PP nanocomposites loaded with 5 wt% silica are shown in Figure IV.2-7(a-b). Isodimensional silica aggregates appear distributed quite homogeneously within the matrix in PP-A380-5 nanocomposite (Figure IV.2-7a). On the other hand, the incorporation of surface-treated silica seems to promote a better dispersion of the filler, as the size of aggregates is markedly lower (Figure IV.2-7b). In particular, the observed aggregates dimension confirms the measurements obtained by AFM. Moreover, the smaller aggregate dimensions observed in PP-R974-5 composites can substantiate the better tensile and viscoelastic mechanical properties when compared to PP-A380-5 sample (Figure IV.2-1). However, the composites filled with 7 wt% silica manifest a rather poorly dispersed silica particles organized in aggregates and agglomeration, with average dimension of around 300-350 and 250-300 nm for PP-A380-7 and PP-R974-7 samples, respectively (Figure IV.2-7(c-d)). The microstructural observations confirm that higher filler contents leads to reduced interfaces, resulting in a lower efficiency in improving the mechanical properties.

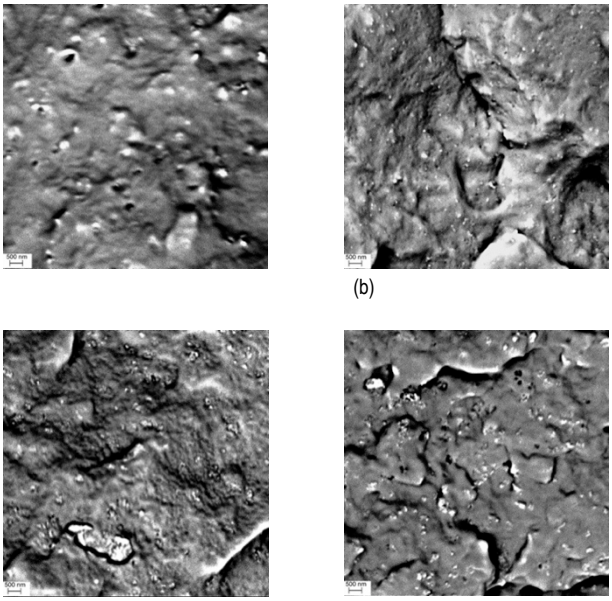

(a) (b)

(c) (d)

Figure IV.2-7. SEM micrographs of fracture surfaces of (a) PP-A380-5, (b) PP-R974-5, (c) PP-A380-7 and (d) PP-R974-7.

This study focused on understanding the interfacial interactions occurring between nanosilica and polypropylene and their effect on the physical and macroscopic properties of PP-silica nanocomposites. A significant correlation between the tensile modulus, glass transition temperature and the amount of constrained phase, as assessed through tensile and DMA analyses, revealed the presence of a secondary reinforcing mechanisms, which, concurrently to the primary stiffening effect of the high modulus filler, contributes to the enhancement of the nanocomposites bulk properties. Crystallization experiments evidenced the existence of a transcrystalline region generating thanks to the nucleating ability of the filler, while DMA experiments were also used to confirm the presence of an immobilized amorphous phase at the filler surface. A complex constrained phase, responsible for providing a secondary reinforcing mechanism, was thus modeled as immobilized amorphous and transcrystalline regions located at the filler surface.

4.3 Viscoelastic behavior of PP nanocomposites and application of superposition principles

Part of this chapter has been published in:

Pedrazzoli D, Pegoretti A,

"Long-term creep behaviour of polypropylene/fumed silica nanocomposites estimated by time-temperature- and time-strain superposition approaches.",
Polymer Bulletin. 71. (2014) 2247-2268.

The creep behavior of PP has been investigated in a series of papers [170, 235-239]. Since the reported stress-strain linearity limit of PP is very low, the creep measurements under this limit remain inaccurate and impractical to be applied in the design of components [175]. A new approach was recently introduced by Kolarik et al. in order to describe how the retardation (or relaxation) times are controlled by the current state of the material in the course of a solicitation [118, 175, 177, 237]. According to this approach, the internal time of a material differs from the experimental time and a shift factor can be considered to convert the experimental time into the internal time. Different quantities are supposed to be controlling the internal time, in particular the free volume, strain and stress. The free volume is usually considered the most suitable parameter, especially because the phenomenological theory of viscoelasticity [240-245] has shown that fractional free volume plays a keyrole in the control the retardation (or relaxation) times in polymeric materials. Applying the free volume approach to the nonlinear tensile creep of PP [118], PP/styrene-acrylonitrile copolymer (SAN) [170], PP/cycloolefin copolymer (COC) [177] and LLDPE/fumed silica [174] the formulae for the shift factors have been derived, which allow us to construct a generalized creep curve over a long time interval by applying the time-strain superposition (TSSP). Generalized creep compliance curves can be conveniently used for predicting the real time-dependent compliance for any selected stress within the region of reversible deformations [175].

Among the accelerated procedures used to characterize the viscoelastic behavior in polymeric systems, the time temperature superposition principle (TTSP) represents one of the most widely applied method for the construction of master curves referred to a constant temperature [246, 247]. Several authors demonstrated that TTSP is valid in the linear viscoelastic region for polymer and polymer composites [248, 249]. On the other hand, the existing literature points to the fact that TTSP is not valid within the nonlinear viscoelastic region due to the change in shape of the creep curve with stress levels [250, 251].

The main objectives of this study are (i) to evaluate the effects of the filler incorporation and of its surface functionalization on the nonlinear tensile creep behavior, (ii) to construct the generalized creep curves by applying the time strain- and time temperature- superposition principles, (iii) to substantiate the equivalence between the two principles by comparing the correspondent superimposed master curves. Noteworthy, PP nanocomposites investigated in this work were prepared by melt compounding and compression molding (section 3.2.1.1).

4.3.1 Filler characterization

The helium pycnometer data obtained on fumed silica nanoparticles are reported in Table IV.3-1. For both samples at least 300 measures were performed in order to reach a constant density value, probably due to the diffused open porosity present on the surface of fumed silica aggregates, among which helium molecules can difficulty penetrate and diffuse. Surface treated nanoparticles show a slightly lower density than untreated nanoparticles, probably because of the presence on the surface of primary nanoparticles of hydrocarbon chains with relatively low density.

Table IV.3-1. Density measurements and surface properties of silica nanoparticles.

Sample	Density [g/cm^3]	BET surface area [m^2/g] (*)	Area of pores (1.7-300 nm) [m^2/g](**)	Average Pore Diameter [nm] (***)
A380	2.359 ± 0.017	320.8 ± 3.4	247.0	11.5
R974	2.298 ± 0.015	124.4 ± 0.6	129.0	12.9

(*) Surface area calculated in according to Brunauer-Emmett-Teller method [252].
(**) Surface area associated to pores of different size according to Barrett-Joiner-Holenda method [253].
(***) Average pore diameter computed in according to Barrett-Joiner-Holenda method [253].

The BET (Brunauer-Emmett-Teller) [252] surface area was calculated from the interpolation of the linear part of the adsorption curve in the plot reporting the adsorbed nitrogen volume versus the relative pressure (Table VI.3-1). Furthermore, following BJH (Barrett-Joiner-Holenda) [253] method it was possible to determine the pore size distribution and the surface area contribution associated to pores of different dimensions. The data referring to Aerosil® A380 were reported from the literature [57]. The samples show significantly different BET surface area and BJH surface area of pores, while the average diameter of pores is similar.

TEM micrographs of silica nanoparticles are represented in Figure IV.3-1, indicating that silica primary nanoparticles have an average diameter around 5-10 nm and 10-15 nm for silica A380 and R974, respectively, according to the producer's datesheet. The primary particles tend to bond together to form aggregates and agglomerates.

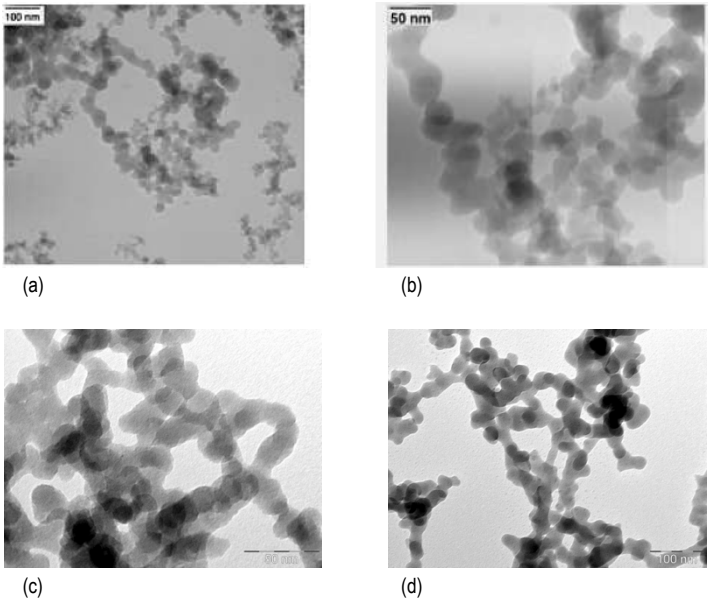

Figure IV.3-1. TEM micrographs of fumed silica nanoparticles at different magnifications: (a-b) A380 – adapted from [254] and (c-d) R974.

4.3.2 Composite characterization

4.3.2.1 Morphology

The ESEM image of the fracture surface of PP-A380-5 and PP-R974-5 samples are represented in Figure IV.3-2a and Figure IV.3-2c, respectively. In the SEM micrographs of PP-silica samples it can be seen that isodimensional aggregates appear distributed quite homogeneously within the matrix in both samples. The ESEM images of the fracture surfaces of PP-PPgMA-5-A380-5 and PP-PPgMA-5-R974-5 samples are shown in Figure IV.3-2b and Figure IV.3-2d, respectively. If compared with the corresponding nanocomposites prepared without the addition of PPgMA, the size of aggregates in ternary nanocomposites is markedly lower. The

reduction of aggregate dimensions can substantiate the enhanced tensile and viscoelastic mechanical properties showed by nanocomposites containing PPgMA (Table IV.3-4 and Table IV.3-5).

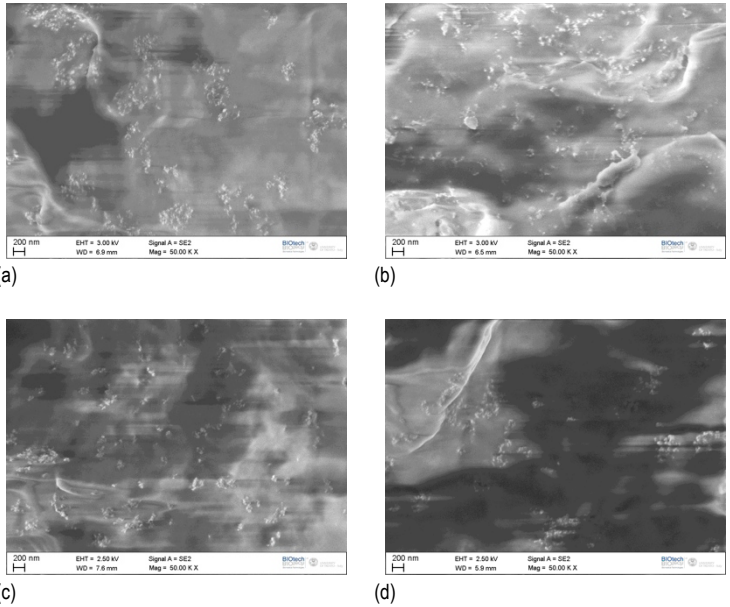

Figure IV.3-2. ESEM images of the fracture surface of (a) PP-A380-5, (b) PP-PPgMA-5-A380-5, (c) PP-R974-5 and (d) PP-PPgMA-5-R974-5.

TEM analyses corroborate the previous observations and allow an estimation of the aggregates dimension. In particular, from TEM micrographs it is possible to clearly discern silica primary particles, spherical in shape and with a diameter between 10 and 20 nm, in according to the produced datasheet (Figure IV.3-3). As a comparison, the mean size of silica aggregates are summarized in Table IV.3-2.

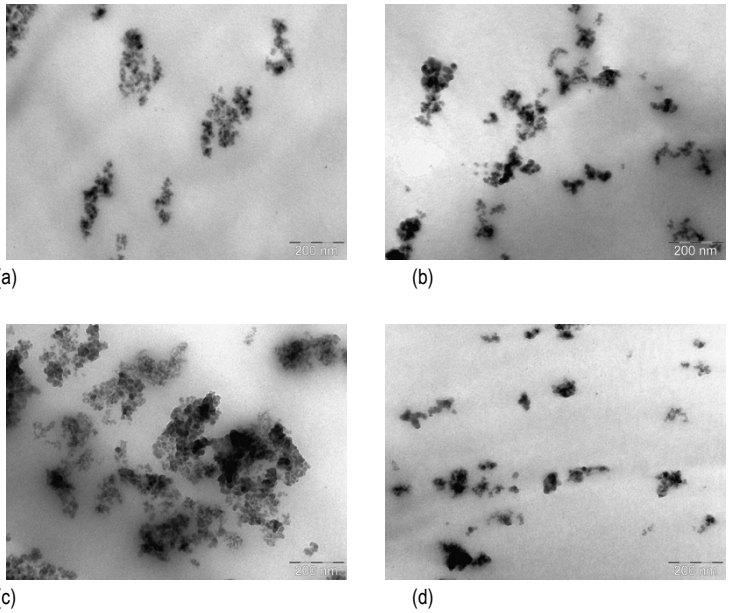

(a) (b)

(c) (d)

Figure IV.3-3. TEM micrographs of cryocut surfaces of (a) PP-A380-5, (b) PP-PPgMA-5-A380-5, (c) PP-R974-5 and (d) PP-PPgMA-5-R974-5.

Table IV.3-2. Mean aggregate size of PP-silica nanocomposites from TEM analyses.

Sample	Mean Aggregate Size [nm]
PP-A380-5	198 ± 15
PP-R974-5	171 ± 23
PP-PPgMA-5-A380-5	106 ± 9
PP-PPgMA-5-R974-5	91 ± 10

4.3.2.2 Thermal analyses

The addition of silica produces a moderate increase of the crystallization temperature, which is further increased by compatibilizer incorporation in the system added with silica A380. However, when the compatibilizer is added to the system containing silica R974 the crystallization temperature is slightly lower. This decrease could be due to the increased interaction between the compatibilized PP and the

silica nanoparticles, which may retard the migration of the PP chains onto the growing crystal nucleus. Concurrently, the melting temperature recorded during the second scan (T_m) is slightly higher for PP nanocomposites, while the crystallinity (χ) does not seem to have a direct correlation with the nanofiller addition (Table IV.3-3).

Table IV.3-3. DSC parameters on unfilled PP and relative nanocomposites.

Sample	T_m [°C] (*)	ΔH [J/g] (**) (χ [%])	Cryst. Peak T [°C] (***)
PP	165.1	102.0 (48.8)	115.6
PP-PPgMA-5	163.1	100.7 (48.2)	117.0
PP-PPgMA-10	162.8	100.3 (48.0)	117.9
PP-A380-5	165.4	98.1 (49.4)	116.8
PP-R974-5	165.5	97.5 (49.1)	116.9
PP-PPgMA-5-A380-5	166.0	98.1 (48.4)	117.5
PP-PPgMA-5-R974-5	166.7	98.4 (49.6)	115.3

(*) Melting temperature recorded during the second scan.
(**) Hentalpy variation recorded during melting and associated crystallinity value.
(***) Crystallization peak temperature.

4.3.2.3 Quasi-static tensile tests

As reported in Table VI.3-4, the addition of silica nanoparticles induces a significant increase of the elastic modulus *(E)* of the PP matrix, which is further enlarged by the incorporation of PPgMA, reaching an overall improvement of 47% for ternary systems, compared to unfilled PP. Noteworthy, the systems produced with the addition of PPgMA showed an increase in elastic modulus comparable with that obtained with the introduction of nanoparticles, at the same weight content. In general, the yield stress *(σ_y)* and the stress at break *(σ_b)* decrease with the addition of the nanofiller for both kinds of silica nanocomposites, probably because of filler aggregation and stronger interaction [255]. For the same reason the elongation at break *(ε_b)* exhibited in nanocomposite is lower than that of unfilled PP.

Table IV.3-4. Elastic modulus and quasi-static tensile properties at yield and at break.

Sample	E [MPa]	σ_y [MPa]	σ_b [MPa]	ε_b [%]
PP	1546 ± 24	37.1 ± 0.1	35.0 ± 0.1	16.8 ± 0.3
PP-PPgMA-5	1729 ± 31	36.7 ± 0.4	34.5 ± 0.6	13.3 ± 0.7
PP-PPgMA-10	1648 ± 12	35.4 ± 0.4	33.6 ± 0.5	12.1 ± 0.6
PP-A380-5	1698 ± 32	37.2 ± 0.5	35.5 ± 0.4	9.0 ± 0.4
PP-R974-5	1865 ± 24	35.6 ± 0.5	33.6 ± 0.5	10.2 ± 0.7
PP-PPgMA-5-A380-5	2015 ± 40	35.7 ± 0.4	34.2 ± 0.3	6.7 ± 0.2
PP-PPgMA-5-R974-5	2281 ± 58	34.2 ± 0.4	31.3 ± 0.9	12.0 ± 1.1

4.3.2.4 Creep behavior and application of superposition principles

In Figure IV.3-4(a-b) the isothermal creep compliance of unfilled PP and PP silica nanocomposites, under a constant load of 3 MPa and at 30 °C, is reported, while in Table IV.3-5 the elastic (D_e) and total components of the creep compliance after 2000 s (D_{t2000}) are summarized. The introduction of silica nanoparticles results in a significant improvement of the creep stability of the material. It is generally believed that nanoparticles can effectively restrict the motion of polymer chains, influencing the stress transfer at a nanoscale, with positive effects on the creep stability of the material [118]. Nevertheless, the creep compliances does not seem to significantly depend on the silica nanoparticle type.

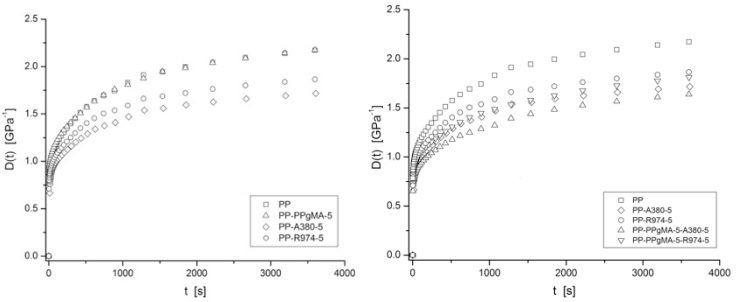

Figure IV.3-4. Creep compliance *(D(t))* of (a) unfilled PP and PP-silica-5 nanocomposites, (b) PP-silica-5 and PP-PPgMA-5-silica-5 (T=30 °C, σ_0 = 3 MPa).

Table IV.3-5. Elastic *(D_e)*, viscoelastic *($D_{ve,2000s}$)* and total creep compliance at 2,000 s *($D_{t,2000s}$)* of PP nanocomposites.

Sample	D_e [GPa^{-1}]	$D_{ve,2000s}$ [GPa^{-1}]	$D_{tot,2000s}$ [GPa^{-1}]	$(D/D_0)_{tot,2000s}$	$E_{a,creep}$ (*) [KJ / mol]
PP	0.85	1.24	2.09	/	209 ± 19
PP-PPgMA-5	0.82	1.22	2.04	0.98	/
PP-PPgMA-10	0.85	1.25	2.10	1.00	/
PP-A380-5	0.68	0.95	1.63	0.78	/
PP-R974-5	0.76	1.00	1.76	0.84	/
PP-PPgMA-5-A380-5	0.65	0.86	1.51	0.72	181 ± 17
PP-PPgMA-5-R974-5	0.72	0.91	1.63	0.78	182 ± 18

(*) Activation energy values obtained from the fitting of the shift factors used when applying the TTSP and according to the Arrhenius equation (Eq. II-20).

Isothermal creep compliance master curves were constructed for the samples PP, PP-PPgMA-5-A380-5 and PP-PPgMA-5-R974-5 applying the TSSP at the reference stress. As proposed by Kolarik et al. [118, 177, 237] with a proper choice of the parameters (Table IV.3-6) it is possible to construct creep compliance master curves taking into account the non-linear viscoelastic behavior of the material when relatively high stresses are applied.

Representative creep compliance curves of unfilled PP at 30 °C are reported in Figure IV.3-5a on double logarithmic scale for different applied stresses and are compared with the theoretical ones, derived from the fitting according to the non linear tensile creep approach (solid lines). The fitting parameters, based on Eq (III-21) and Eq (III.22), are summarized in Table VI.3-7 for PP and all PP nanocomposites. Since *log(C*)* increases with the applied stress and the value of *n**, which should be independent on the applied stress (σ_0), shows very poor dependance on σ_0, the proposed approach is suitable enough in order to study the dependance of the creep behavior on the applied stress for unfilled PP and relative silica nanocomposites. The master curve of PP, constructed according to strain dependent shift factors *log(a_ε),* is depicted in Figure IV.3-5b.

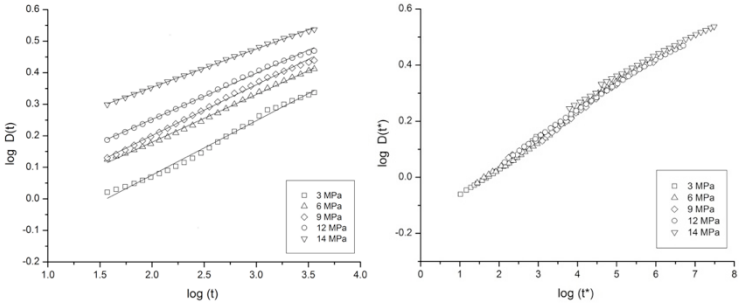

Figure IV.3-5. (a) Representative creep compliance curves *(D(t))* at different creep stresses σ_0 and (b) superimposed creep curves in according to the non-linear tensile creep approach of unfilled PP (T=30 °C).

Table IV.3-6. Parameter used for the evaluation of the non-linear creep behavior of PP nanocomposites (*Appendix A*).

Parameter	Value
f_g	0.025
T_g [°C]	-16.40
T [°C]	30.00
a_{fv} [K^{-1}]	0.000330
Df_{Tc}	0.0153
x_c	0.488
v_2	0.488
v_{2cr}	0.156
q	1.800
M	1.589
n	0.460
B	1.000

Table IV.3-7. Parameters of the fitting of the creep data of PP nanocomposites in according to the model presented in Appendix *A*.

	PP			PP – PPgMA – 5 – A380 - 5			PP – PPgMA – 5 – R974 - 5		
σ_0 [MPa]	log (C*)	n*	R^2	log (C*)	n*	R^2	log (C*)	n*	R^2
3	-0.269±0.008	0.172±0.003	0.990	-0.336±0.008	0.153±0.003	0.999	-0.284±0.008	0.150±0.003	0.999
6	-0.122±0.004	0.151±0.001	0.998	-0.268±0.002	0.163±0.002	0.999	-0.267±0.006	0.152±0.002	0.999
9	-0.121±0.004	0.161±0.002	0.997	-0.220±0.004	0.179±0.002	0.998	-0.264±0.005	0.160±0.002	0.996
12	-0.040±0.004	0.146±0.001	0.997	-0.218±0.003	0.193±0.001	0.997	-0.240±0.003	0.168±0.001	0.994
14	0.110±0.002	0.122±0.001	0.998	-0.098±0.002	0.172±0.001	0.990	-0.184±0.003	0.179±0.001	0.991

Master curves of unfilled PP, PP-PPgMA-5-A380-5 and PP-PPgMA-5-R974-5 are shown in Figure IV.3-6. The comparison highlights the better creep stability for PP nanocomposites with respect to unfilled PP, but not significative differences between PP nanocomposites.

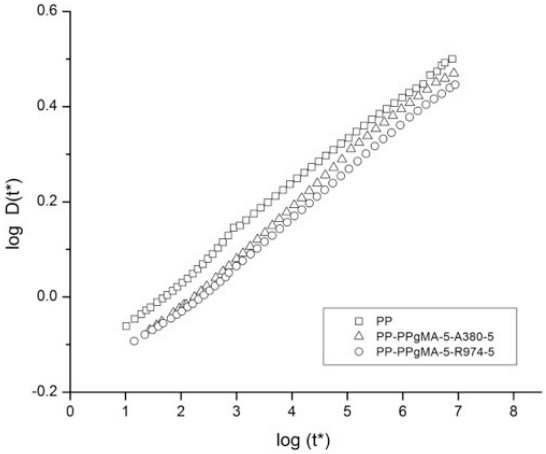

Figure IV.3-6. Master curves of creep compliance *(D(t))*, in according to the non-linear tensile creep superposition principle, of unfilled PP and PP-PPgMA-5-silica-5 nanocomposites (T=30 °C).

Representative creep compliance curves of PP at temperatures ranging from 30 °C to 70 °C, under an applied stress of 3 MPa, are reported in Figure IV.3-7a. Superimposed curves, constructed according to the TTSP and setting the reference temperature to 30 °C, are represented in Figure IV.3-7b for PP and relative nanocomposites. The deformation behavior of the materials is strongly dependent on the temperature, while the introduction of silica nanoparticles leads to a significant decrease of the creep compliance, which is more efficient when long creep times are considered and thus when high temperatures are taken into account.

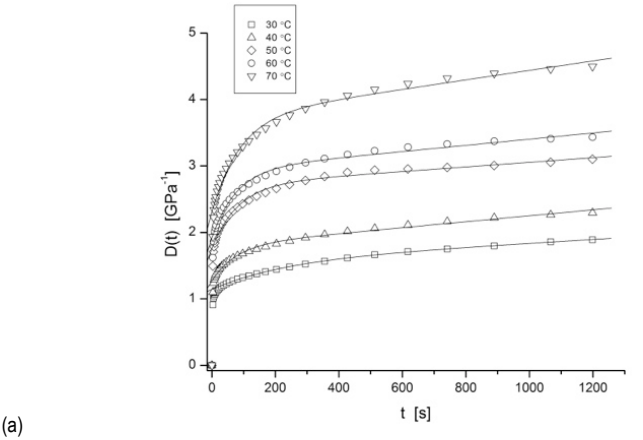

(a)

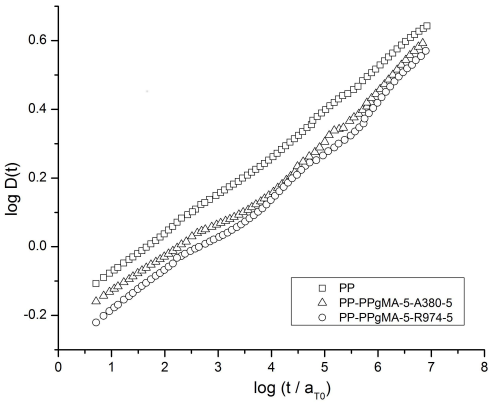

(b)

Figure IV.3-7. (a) Representative creep compliance curves *(D(t))* at different temperatures of PP and (b) master curves of the creep compliance in according to time-temperature superposition principle (σ_0 = 3 MPa, T_0 = 30 °C) of unfilled PP and PP-PPgMA-5-silica-5 nanocomposites.

In order to investigate the correlation between creep properties and polymeric chain dynamics, an analysis of the shift factors derived from the TTSP has been carried out. Activation energy values ($E_{a,creep}$) were obtained by applying the Arrhenius equation (Eq. (III-11)) on a sufficiently linear trend of shift factors with respect to the reciprocal of the absolute temperature [256]. Due to the high uncertainty, activation energy values of the nanocomposites seem quite similar to that of unfilled PP (Table VI.3-5), indicating that the viscous flow of the polymer

macromolecules is not significantly dependent on the presence of the nanoparticles. Nevertheless, further investigations would be essential for a better understanding of the temperature-dependent molecular dynamics of the investigated materials in the solid state, possibly referring to the polymer-filler interaction.

The equivalence between the *time strain-* and *time temperature- superposition principle* can be substantiated by comparing the correspondent superimposed master curves (Figure IV.3-8).

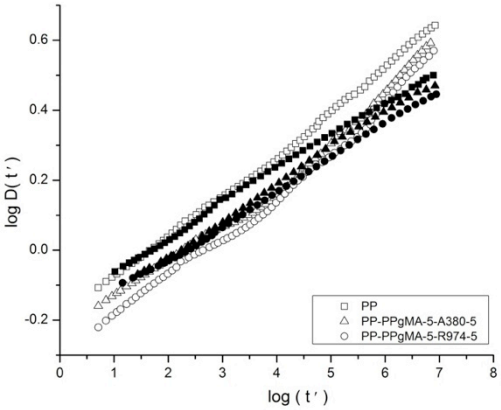

Figure IV.3-8. Comparison of master curves in according to the *time strain-* (full point) and *time temperature-* (open point) *superposition principle* of unfilled PP and PP-PPgMA-5-silica-5 nanocomposites.

Master curves obtained by the two different approaches appear substantially similar for both PP and relative nanocomposites over a wide range of reduced time. However, a slight divergence is manifested at very high reduced times (i.e. elevated temperature or high applied stresses), with the time-temperature data showing a significantly greater compliance compared to the time-strain data. The implication is that temperature and strain affect the creep response in different ways. Moreover, while the TSSP takes into account the underlying viscoelastic response function that is characteristic of the material, the TTSP does not contemplate a full description of the behavior of the material being tested. Further research needs to be done on the TTSP in order to be take into account the characteristic parameters of the material and extend the applicability of the principle in the nonlinear viscoelastic region.

4.3.2.5 Dynamic mechanical behavior

The introduction of the nanofiller produces an enhancement of *E'* both in the glassy region and in the rubbery regions (Figure IV.3-9a). During DMTA experiments two peaks were observed on *tan*δ plot, identified as α and β relaxation, in order of decreasing temperature (Figure IV.3-9b). The T_g of PP nanocomposites, usually referred to the β relaxation, is slightly higher than that of unfilled PP due to the presence of the nanofiller (Table VI.3-8), which decreases the mobility of the macromolecules.

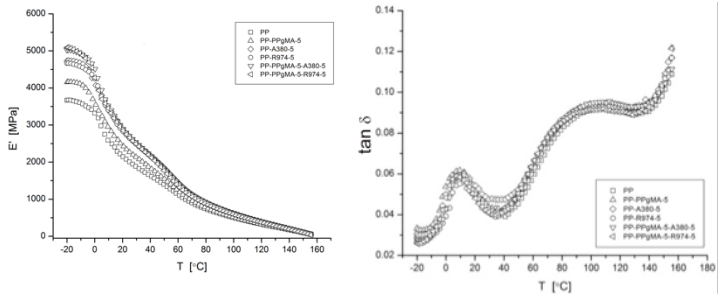

(a) (b)

Figure IV.3-9. Dynamic mechanical properties of unfilled PP and relative nanocomposites (f=1 Hz): (a) Storage modulus *(E')* and (b) Loss tangent (*tan*δ).

Superimposed curves of the storage modulus were constructed from the results of multifrequency tests in according to time-frequency superposition principle, taking as reference temperature T_0=30 °C. The sample PP-PPgMA-5-A380-5 shows an higher enhancement of the storage modulus than PP-PPgMA-5-R974-5, with respect to unfilled PP (Figure IV.3-10a).

Table IV.3-8. Dynamic mechanical properties (f = 1 Hz) and activation energy values of unfilled PP and relative nanocomposites.

Sample	E' (-20 °C) [MPa]	E' (23 °C) [MPa]	E'' (23 °C) [MPa]	$T_{\beta,peak}$[(a)] [°C]	E_a [(b)] [KJ / mol]
PP	3674.4	2063.1	90.3	9.9	231 ± 8 183 ± 4 295 ± 21
PP – PPgMA -5	4155.1	2340.0	115.3	9.1	/
PP – PPgMA -10	3925.2	2268.3	108.7	9.1	/
PP – A380 -5	4733.7	2756.1	141.7	11.8	/
PP – R974 -5	4668.1	2727.5	125.3	11.4	/
PP-PPgMA-5-A380-5	5025.8	2777.1	131.6	11.3	210 ± 9 171 ± 2 286 ± 22
PP-PPgMA-5 R974-5	5092.2	2749.9	123.5	11.2	220 ± 4 167 ± 4 287 ± 22

([a]) Temperature correspondent to the β peak recorded in $tan\delta$ plot.
([b]) Activation energy values E_{a1}, E_{a2} and E_{a3} listed from top to bottom.

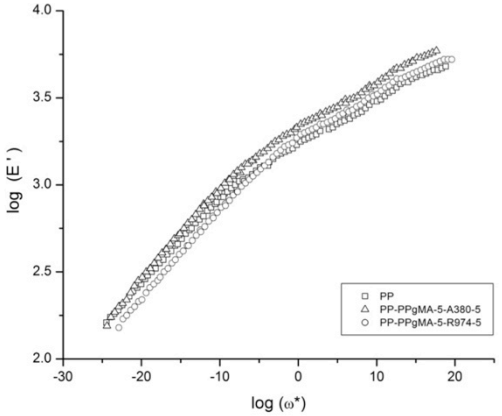

(a)

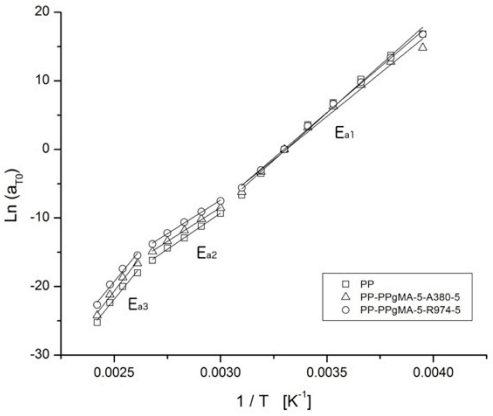

(b)

Figure IV.3-10. (a) Comparison between master curves of *E'* obtained by multi-frequency tests on PP-silica nanocomposites (T_0=30 °C) and (b) shift factors for the construction of the E' master curves with step-wise linear fitting in according to Arrhenius equation (Eq. (III-11)).

The shift factors derived from the construction of the master curves are plotted in Figure IV.3-10b. As already shown for the creep tests conducted at various temperatures, the Arrhenius equation (Eq. (III-11)) was utilized in order to obtain activation energy (E_a) values (Table IV.3-8). However, since the shift factors for the construction of the *E'* master curves did not follow a good linearity over the whole range of the variable *1/T* , the points were properly divided into three regions and a step-wise linear fitting was carried out on each region. In this way three activation energies were computed ($E_{a,1}$, $E_{a,2}$ and $E_{a,3}$), from the fitting of the regions of points going from higher to lower values of *1/T*.

E_a values of PP nanocomposites seem quite similar to those of unfilled PP because affected by high uncertainty, confirming that the viscous flow of PP macromolecules is not significantly affected by the presence of the nanoparticles. The activation energy values computed from multifrequency DMTA tests are quite similar to those found for the creep tests ($E_{a,creep}$) especially when considering $E_{a,1}$ and $E_{a,2}$. Interestingly, activation energy values related to the viscous flow of macromolecules show good concordance when derived from creep and dynamic regime tests.

Therefore, in this study it was shown that the non-linear viscoelastic creep of the composites, successfully studied by the application of the TSSP, showed a considerable enhancement of the creep stability in nanocomposites with respect to

unfilled PP, especially for higher creep stresses, but no significative differences between nanocomposites filled with different nanosilicas.

The study of creep dependance on the temperature showed that the stabilizing effect provided by the nanoparticles was more effective at high temperatures and, considering the TTSP, at long loading times. The equivalence between the time strain- and time temperature- superposition principle was substantiated by comparing the correspondent superimposed master curves. In order to gain some insight on the correlation between creep properties and polymeric chain dynamics, activation energy values were obtained by the analysis of the shift factors derived from the TTSP.

Both storage and loss modulus, measured through DMA tests, were enhanced in all nanocomposites, observing a maximum storage modulus for samples with 5 wt% PPgMA and 5 wt% surface treated silica. Activation energy values obtained from the elaboration of multifrequency tests were in good agreement with those referred to creep tests.

4.4 Evaluation of the fiber/matrix interfacial shear strength in GF reinforced PP nanocomposites

Part of this chapter has been published in:

Pedrazzoli D, Pegoretti A,

"*Silica nanoparticles as coupling agents for polypropylene/glass composites*",
Composites Science and Technology. 76. (2013) 77-83.

Pedrazzoli D, Pegoretti A,

"Expanded graphite nanoplatelets as coupling agents in glass fiber reinforced polypropylene composites",
Composites Part A – Applied Science and Manufacturing. 66. (2014) 25-34.

Over the years, two main strategies have been proposed to improve the fibre/matrix adhesion in PP/glass composites: i) the development of specific fibre sizings/coatings [138-145] and/or ii) the addition of coupling agents to the PP matrix [140, 141]. In particular, some indications emerged on the fact that nanoparticles homogeneously dispersed in a polymer matrix [32, 148, 149] or localized at the interfacial region [150-152] could play a beneficial role on the fibre/matrix interfacial adhesion in several types of structural composites. Moreover, with the addition of nanoparticles a simultaneous enhancement of the mechanical properties of the polymer matrix can be reached [32] or specific functionalities can be added [154].

The main purpose of this study is to investigate the possibility to improve the interfacial shear strength (ISS) between E-GF and PP by dispersing various types and amounts of silica nanoparticles and xGnP_M5 in the polymer matrix. Moreover, with the aim of providing a representative example, the results regarding ISS for the systems GF / PP-xGNP are validated by presenting complementary experimental evidence (based on SEM and TEM, XRD and solid state NMR). Noteworthy, the PP nanocomposite matrices investigated in this work were prepared by melt compounding and compression molding (section 3.2.1.1).

4.4.1 Tensile properties of the glass fibers

In accordance to ASTM standard C 1557-03, the system compliance of the testing configuration on single glass fiber was evaluated by adopting samples of three different gauge lengths. Therefore, an elastic modulus of 63±5 GPa was

estimated. In order to determine the tensile strength, a statistical treatment based on the Weibull distribution was adopted. In particular, following the iterative procedure proposed by Gurvich et al. [257], all experimental data on specimens of different size have been considered together as a statistically representative population. The obtained shape *(m)* and scale *(σ_0)* parameters of a two-parameter cumulative Weibull distribution are reported in Table IV.4-1, along with the mean values of fibre stress and strain at break. The values of strain at break were corrected to take the compliance of the measuring system into account.

Table IV.4-1. Mechanical properties of glass fibre as determined from single fiber tensile tests on samples of different gauge length L_0.

Quantity	L_0 = 5 mm	L_0 = 15 mm	L_0 = 30 mm	Entire population
Number of specimens	18	19	19	56
Diameter (mm)	15.5 ± 1.0	15.7 ± 1.7	14.8 ± 1.6	15.3 ± 1.5
Stress at break (MPa)	2720 ± 748	2614 ± 873	2491 ± 835	2606 ± 820
Strain at break (%)	4.6 ± 1.0	3.6 ± 0.8	3.3 ± 0.5	3.8 ± 0.8
σ_0 (MPa)	3206 ± 31	3710 ± 25	3515 ± 27	3609 ± 19 (*)
m	6.2 ± 0.2	5.8 ± 0.2	4.9 ± 0.2	5.7 ± 0.3
Adjusted R square (R^2)	0.971	0.982	0.978	0.973

(*) referred to a gauge length L_0 = 15 mm

4.4.2 Fiber / matrix interfacial strength

The average saturation length of the fibre fragments as measured by the SFFT is reported in Table IV.4-2 for some selected samples, along with the ISS values estimated according to the Kelly-Tyson *($ISS_{K\text{-}T}$)* or the Cox *(ISS_{COX})* models. It is clear that the addition of PPgMA, nanofiller (i.e. silica nanoparticles or xGnP) or a combination of both additives induces a sharp decrease of the saturation length and, consequently, an enhancement of the ISS values. In particular, ISS values obtained on the basis of the Kelly-Tyson model are plotted in Figure IV.4-1 and Figure IV.4-2 as a function of the percentage of PPgMA or nanofiller for all the investigated samples.

Table IV.4-2. ISS values in according to Kelly-Tyson (ISS_{K-T}) and Cox (ISS_{COX}) models and mechanical parameters (E, σ_{br} and ε_{br}) as measured from tensile tests.

Sample	L_s [mm]	ISS_{K-T} [MPa]	ISS_{COX} [MPa]	G/G_{PP}	E [MPa]	σ_{br} [MPa]	ε_{br} [%]
PP	4.47 ± 0.31	2.7 ± 0.2	3.2 ± 0.6	1.00	1546 ± 24	35.0 ± 0.1	16.8 ± 0.3
PP-PPgMA-5	1.20 ± 0.21	15.2 ± 2.7	8.9 ± 1.5	1.12	1729 ± 31	34.5 ± 0.6	13.3 ± 0.7
PP-PPgMA-10	0.97 ± 0.36	20.2 ± 2.5	13.9 ± 1.1	1.07	1648 ± 12	33.6 ± 0.5	12.1 ± 0.6
PP-A380-5	1.70 ± 0.30	8.4 ± 0.7	6.5 ± 1.0	1.10	1698 ± 32	35.5 ± 0.4	9.0 ± 0.4
PP-R974-1	2.03 ± 0.28	7.6 ± 1.0	4.8 ± 1.0	1.05	1623 ± 57	32.9 ± 0.7	16.7 ± 0.4
PP-R974-3	1.80 ± 0.32	10.9 ± 0.9	7.2 ± 1.2	1.15	1786 ± 57	34.0 ± 0.4	12.9 ± 0.7
PP-R974-5	1.34 ± 0.23	13.1 ± 0.8	8.4 ± 1.5	1.21	1865 ± 24	33.6 ± 0.5	10.2 ± 0.7
PP-R974-7	1.29 ± 0.25	13.9 ± 0.5	9.5 ± 1.8	1.23	1895 ± 23	33.0 ± 0.7	10.1 ± 0.7
PP-xGnP-1	2.24 ± 0.29	6.7 ± 0.9	5.7 ± 1.2	1.15	1786 ± 34	33.3 ± 0.2	13.5 ± 0.4
PP-xGnP-3	1.46 ± 0.23	11.8 ± 1.2	9.9 ± 1.5	1.22	1891 ± 64	31.5 ± 0.1	10.2 ± 0.5
PP-xGnP-5	1.20 ± 0.11	15.3 ± 1.3	12.8 ± 1.7	1.31	2020 ± 77	31.5 ± 0.4	9.4 ± 0.3
PP-xGnP-7	1.14 ± 0.20	16.4 ± 1.8	13.8 ± 2.1	1.44	2222 ± 404	31.3 ± 0.1	8.1 ± 0.3
PP-PPgMA-5-A380-5	0.93 ± 0.19	22.7 ± 2.1	15.2 ± 2.2	1.30	2015 ± 40	34.2 ± 0.3	6.7 ± 0.2
PP-PPgMA-5-R974-5	0.58 ± 0.05	38.8 ± 3.5	25.6 ± 2.4	1.47	2281 ± 58	31.3 ± 0.9	12.0 ± 1.1
PP-PPgMA-5-xGnP-5	0.59 ± 0.09	39.0 ± 5.7	27.9 ± 2.1	1.98	3058 ± 114	33.5 ± 2.3	7.1 ± 1.0

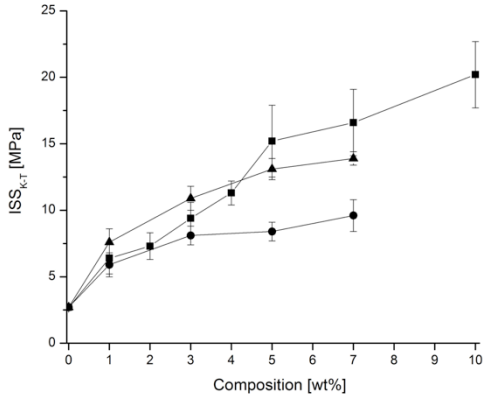

Figure IV.4- 1. ISS values computed according to the Kelly-Tyson model as a function of the content of (■) PP-PPgMA, (●) PP-A380, and (▲) PP-R974.

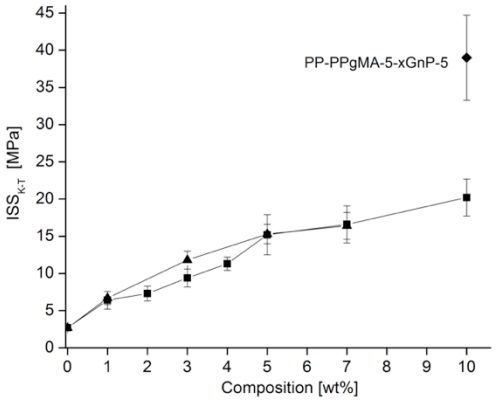

Figure IV.4-2. ISS values computed according to the Kelly-Tyson model as a function of the content of (■) PP-PPgMA,and (▲) PP-xGnP.

As expected, when the PPgMA compatibilizer is added, ISS values considerably increase with respect to the case of neat PP/GF sample. It is interesting to note that comparable improvements can be reached by the addition of silica nanoparticles or xGnP. In fact, when compared to PP-PPgMA systems, PP nanocomposites show similar improvement of ISS values up to a 4-5 wt % content, while for higher percentages PPgMA seems to be more effective than nanoparticles.

In Figure IV.4-3, the effect on the ISS values of adding both PPgMA and silica nanoparticles (ternary composites) is evaluated. It is worthwhile to observe that for any given PPgMA content the addition of silica nanoparticles further enhances the ISS values. This positive effect is particularly strong when surface treated silica nanoparticles (R974) are considered. In fact, the sample PP-PPgMA-10 shows a ISS value similar to the composite PP-PPgMA-5-A380-5 (see Figure IV.4-3a), but remarkably lower than that of PP-PPgMA-5-R974-5 (see Figure IV.4-3b).

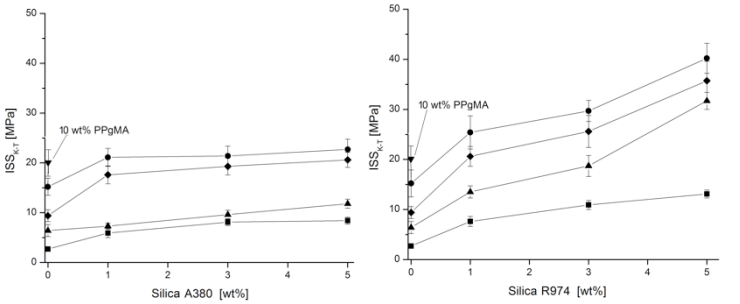

(a) (b)

Figure IV.4-3. ISS values computed according to the Kelly-Tyson model as a function of the content of (a) silica A380 and (b) silica R974, and various PPgMA amounts: (■) 0 wt% PPgMA, (▲) 1 wt% PPgMA, (◆) 3 wt% PPgMA and (●) 5 wt% PPgMA.

The ISS values have been also estimated in accordance to Cox model by assuming a concentric cylindrical geometry. The matrix Poisson's ratio, necessary for the implementation of Cox model, was measured on unfilled PP (ν_m=0.458) by using two extensometers (axial and transversal) mounted on ISO527 1B specimens produced by injection moulding. Relative ISS_{COX} values, i.e. normalized over the value obtained for neat PP, are plotted in Figure IV.4-4 as a function of the relative shear modulus of the matrix. It is interesting to observe that ISS_{COX} exhibits a significant increase with the matrix stiffness for all samples. Therefore, according to the Cox shear lag model, the observed increase in the stress transfer ability of the interface could be explained on the basis of the matrix stiffening effect caused by the additives (both PPgMA and nanofiller). However, a marked discrepancy from the expected trend can be observed for ternary composites. Noteworthy, the samples PP-PPgMA show values of ISS progressively increasing with the PPgMA content even though the mechanical reinforcement of the samples with filler content higher than 5 wt% is decreasing.

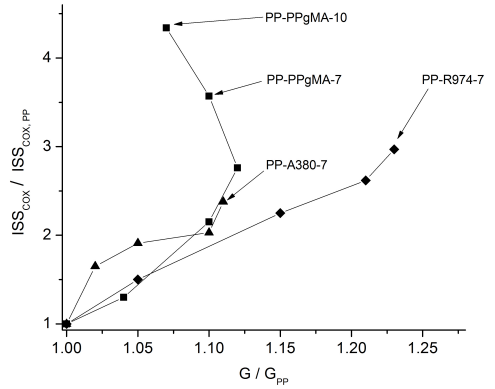

(a)

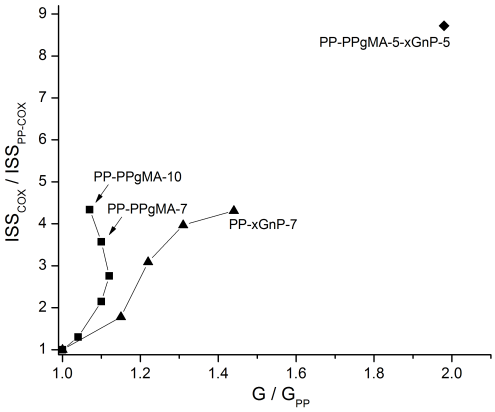

(b)

Figure IV.4-4. Relative ISS values computed according to the Cox model as a function of relative shear modulus of the matrix for (a) PP-silica and (b) PP-xGnP samples. The normalization has been made over the properties of neat PP.

The values of ISS evaluated by applying Cox model need to be interpreted in according to the model hypotheses and the specific operative test conditions. Both the fibre and the matrix are considered as linear elastic bodies, but the actual fragmentation process occurring in model composite samples generally involves plastic deformation regions, thus leading to a significant underestimation of the interfacial toughness. In addition, Cox model is based on the assumption of perfect bonding between matrix and fibre, thus the chemical nature of surfaces and the surface quality are not taken into account.

4.4.3 Surface energetics and roughness

Both the matrix and fibre surface tensions were calculated from measured equilibrium contact angles and from those values the components of thermodynamical work of adhesion *(W_a)* were computed. The polar component of the matrix surface tension *(γ_p)* increased considerably due to the addition of PPgMA, probably due to the presence of hydrophilic maleic anhydride groups [190]. PP-A380 systems show a similar increase in γ_p, likely because silica particles are hydrophilic materials. Less clear is the reason why also for PP-R974 composites an increase of the polar component of the matrix surface tension can be observed, even if of lower intensity. PP-xGnP systems show also a similar increase in γ_p probably because of the surface functionalization of the carbonaceous filler. The dispersive component *(γ_d)* is only slightly higher for all nanocomposites with respect to unfilled PP, in particular for PP-PPgMA-5-R974-5 ternary composites.

As expected, values of work of adhesion *(W_a)* calculated using the geometric mean equation are higher then those calculated from the harmonic mean equation [171]. The quantity W_a represents the adhesion energy between solid phases, the higher the work of adhesion, the better the interfacial bonding between fibre and matrix. W_a values of PP-PPgMA blends and PP nanocomposites are much greater than that of unfilled PP (Table IV.4-3). However, as already stated by Wojuzkij [258] a direct correlation between work of adhesion and the adhesion parameters measured through mechanical tests is not the rule. In fact, micromechanical tests such as the SFFT are characterized by non-equilibrium phenomena (such as the specific viscoelastic properties and the fracture/yield behavior of the matrix). Nevertheless, in the present case a very good correlation exists with the experimentally measured ISS values (Figure IV.4-5). Also for ternary composites a further increment in W_a values can be observed which correlates well with the ISS values. These observation are in good agreement with what previously reported by Ramanathan et al. [259] for an epoxy/carbon system.

Moreover, the roughness of the matrix films used in this work resulted in the range of R_a = 0.2 – 0.4 mm (R_{max} = 2.5 – 3.6 mm) for all samples. The ANOVA analysis carried out on the mean values of R_a and R_{max} showed no statistically significant differences at a significance level of 5 %. Therefore, the contribution of surface roughness to surface properties can be neglected and the differences measured through wettability tests can be mainly attributed to surface chemistry. In addition, IR spectroscopy analyses carried out on the tested PP films confirmed that there was no contamination occurring during the hot pressing of the polymer films within the Mylar® foils.

Table IV.4-3. Surface tension components estimated from the measured equilibrium contact angles and components of the thermodynamic work of adhesion.

Sample	γ^{p} [mN·m^{-1}]	γ^{d} [mN·m^{-1}]	γ [mN·m^{-1}]	W^{h}_{a} [mN·m^{-1}]	W^{g}_{a} [mN·m^{-1}]	$ISS_{K\text{-}T}$ [MPa]
PP	0.1 ± 0.0	30.1 ± 0.4	30.2 ± 0.4	53.0	53.9	2.7 ± 0.2
PP – PPgMA -5	2.7 ± 0.2	31.0 ± 0.5	33.7 ± 0.5	57.8	58.4	15.2 ± 2.7
PP – PPgMA -10	2.8 ± 0.2	34.6 ± 0.4	37.4 ± 0.4	60.4	61.5	20.2 ± 2.5
PP – A380 -5	2.5 ± 0.3	30.6 ± 0.6	33.1 ± 0.7	57.3	57.8	8.4 ± 0.7
PP – R974 -1	1.8 ± 0.1	31.2 ± 0.5	33.0 ± 0.5	57.2	57.8	7.6 ± 1.0
PP – R974 -3	2.3 ± 0.2	31.5 ± 0.7	33.8 ± 0.7	57.8	58.4	10.9 ± 0.9
PP – R974 -5	2.2 ± 0.1	33.0 ± 0.4	35.1 ± 0.4	58.8	59.6	13.1 ± 0.8
PP – R974 -7	2.1 ± 0.2	35.8 ± 0.6	37.9 ± 0.6	60.6	61.9	13.9 ± 0.5
PP – xGnP -1	0.7 ± 0.2	32.4 ± 0.4	33.1 ± 0.4	56.3	57.3	6.7 ± 0.9
PP – xGnP -3	1.6 ± 0.2	35.7 ± 0.5	37.3 ± 0.5	60.0	61.3	11.8 ± 1.2
PP – xGnP -5	2.1 ± 0.1	38.3 ± 0.5	40.4 ± 0.5	62.1	63.9	15.3 ± 1.3
PP – xGnP -7	2.8 ± 0.2	40.3 ± 0.4	43.1 ± 0.4	63.7	66.0	16.4 ± 1.8
PP-PPgMA-5-A380-5	2.4 ± 0.2	35.2 ± 0.5	37.6 ± 0.5	60.4	61.6	22.7 ± 2.1
PP-PPgMA-5-R974-5	1.6 ± 0.3	42.3 ± 0.7	44.0 ± 0.8	63.7	66.4	40.2 ± 3.0
PP-PPgMA-5-xGnP-5	2.2 ± 0.2	39.8 ± 0.5	42.0 ± 0.5	63.9	65.1	39.0 ± 5.7
GF (RO99 P319)	2.0 ± 0.2	23.3 ± 0.5	25.3 ± 0.5	/	/	/

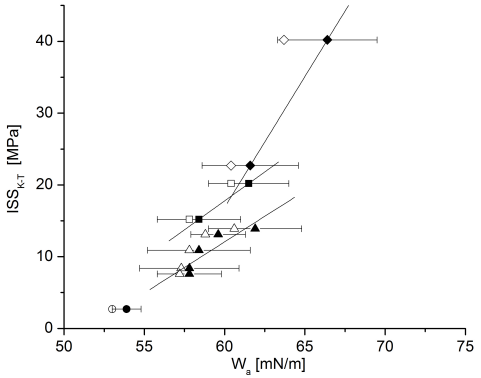

(a)

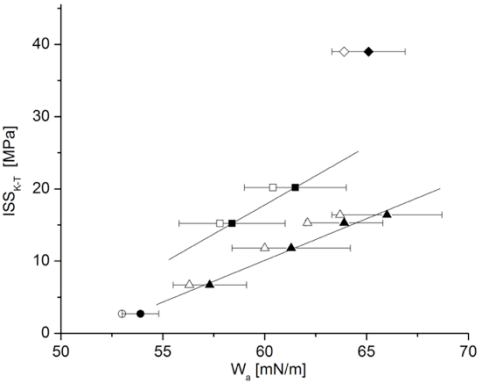

(b)

Figure IV.4-5. ISS values estimated in accordance to Kelly-Tyson model, as function of the thermodynamic work of adhesion W_a calculated using the harmonic (open point) or the geometric (full point) mean equations for (a) PP-silica and (b) PP-xGnP samples. (○,●) PP, (□,■) PP-PPgMA, (△,▲) PP-filler, (◇,◆) PP-PPgMA-5-filler-5. Lines represent a linear fitting operated on each group of data.

In this study, results show that the strength at the interface can be remarkably increased by the addition of dimethyldichlorosilane-functionalized silica nanoparticles or expanded graphite nanoplatelets, and that the improvement is particularly enhanced when the nanofiller are used in combination with PPgMA in ternary composites. The fibre/matrix work of adhesion showed a good correlation with the ISS values. Moreover, in order to corroborate the results about the interfacial adhesion promoted by xGnP incorporation, a comprehensive investigation of the

nanocomposite morphology through FESEM, TEM and NMR is presented in the following section.

4.4.4 Spectroscopic analyses

From the FESEM micrographs of PP-xGnP samples it can be observed that aggregates of graphite nanopateletes appear quite well distributed whithin the matrix (Figure IV.4-6a), while most of the graphite packages do not seem to be intercalated (Figure IV.4-6c). The average length (*L*) and thickness (*t*) of aggregates is 9.5±0.5 mm and 0.5±0.1 mm, respectively, with a correspondent aspect ratio (*L*/*t*) of 19.0±3.9. The effect of the compatibilizer on the filler dispersion can be evidenced in the micrograph of PP-PPgMA-5-xGnP-5 (Figure IV.4-6b) with the intercalation of the matrix within the packages of graphite platelets (Figure IV.4-6d). The graphite nano-layers have been separated to a higher degree with deformed shapes, leading to a significant decrease of the aspect ratio to 6.4±1.7. This can be attributed to the lower melt viscosity of the compatibilized polymer, resulting in a better inter-diffusivity of the matrix onto the structure of the expanded graphite aggregates which then produces an increase in the melt viscosity and therefore higher shearing of the mixture.

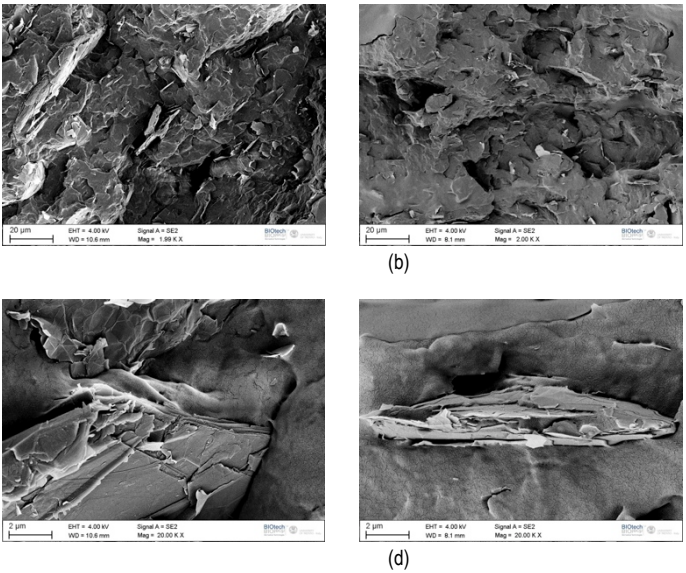

Figure IV.4-6. FESEM image of the fracture surface of (a) PP-xGnP-5 and (b) PP-PPgMA-5-xGnP-5. Higher magnification of graphite packages of (c) PP-xGnP-5 and (d) PP-PPgMA-5-xGnP-5.

TEM images of the sample PP-xGnP-5 and PP-PPgMA-5-xGnP-5 show that graphite sheets are quite homogeneously dispersed throughout the compatibilized matrix (PP-PPgMA-5-xGnP-5) with an average dimension ranging from 100 to 300 nm (Figure IV.4-7b). On the other hand, it can be observed that there are still some graphite sheets existing in micrometer particles in the uncompatibilized matrix (Figure IV.4-7a).

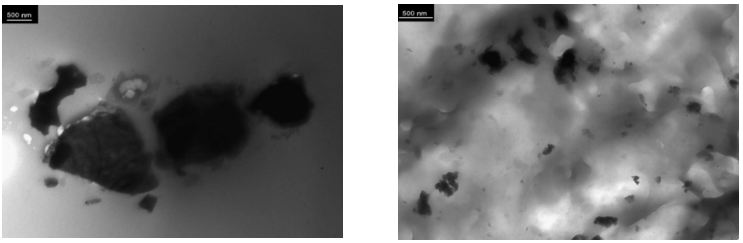

(a) (b)

Figure IV.4-7. TEM images of (a) PP-xGnP-5 and (b) PP-PPgMA-5-xGnP-5 nanocomposites.

The diffractogram of xGnP powder presents a strong peak at 2θ = 26.5° and a smaller peak at 2θ = 54.7° (Figure IV.4-8a), which correspond to the spacing between graphene layers (022) and the (004) crystal orientation, respectively [260]. Furthermore, using Bragg's law and Scherer's equation, the distance between the graphenes that composes the graphite and the size of the crystals formed by them were determined to correspond to 0.334 and 18.91 nm, respectively.

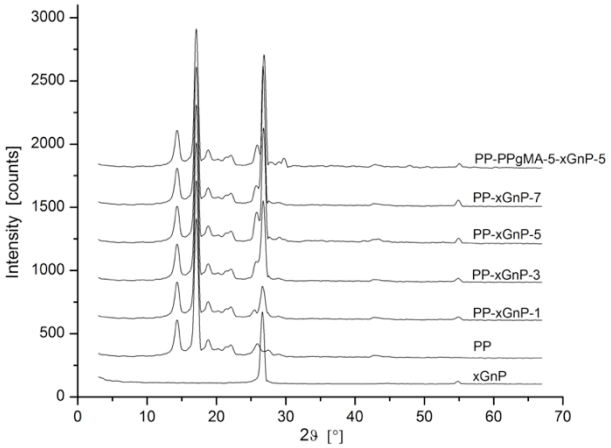

(a)

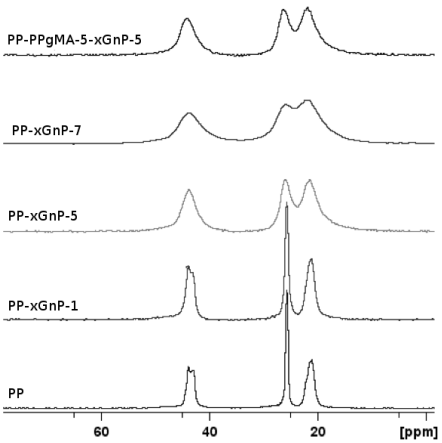

(b)

Figure IV.4-8. (a) XRD diffractrograms and (b) ^{13}C NMR spectrum obtained by CP-MAS-VCT technique for unfilled PP and relative nanocomposites.

In particular, the distance between the graphene sheets is very close to the value reported in the literature (0.335 nm), indicating that the surface treatment did not increase the distance between the graphenes. Unfilled PP shows the typical peaks reported in the literature at 2θ= 14.2°, 17.1°, 18.7° and 21.8°, while PP nanocomposites present additional peaks at around 2θ= 26.5° and 2θ= 54.7° due to the diffraction of the graphene planes. The intensity of the latter peaks is proportional to the graphite amount. Moreover, the interplanar distance between graphene layers *(d_{002})* and the xGnP crystal size *(C)* were calculated for PP-xGnP nanocomposites (Table IV.4-4). While the interplanar distance does not change significatively in PP nanocomposites, the graphite crystal size increases significatively with the graphite content indicating that some sheets are agglomerating during the compounding of the nanocomposites. On the other hand, the sample PP-PPgMA-5-xGnP-5 shows a smaller crystal size than the sample PP-xGnP-5, indicating that xGnP is better dispersed due to the incorporation of compatibilizer PPgMA, thus corroborating the indications coming from FESEM and TEM observations.

The ^{13}C NMR spectrum obtained by VCT-MAS technique is shown in Figure IV.4.8b for unfilled PP and relative composites. Three symmetrical resonance lines, typical of unfilled PP, can be observed with the chemical shifts of 44.2, 26.1 and 22.0 ppm related to CH_2, CH and CH_3 carbons, respectively. Nanocomposite samples show a characteristic broadness of the peaks which increases with the graphite

content due to its high electrical conductivity. On the other hand, no significant change was found in the chemical shifts. Furthermore, the sample PP-PPgMA-5-xGnP-5 produces a spectrum superimposable to that of PP-xGnP-5, probably because the chemical binders related to the maleic anhydride group are lower than the ^{13}C NMR sensitivity. The values of $T^{H}_{1\rho}$ and T_{CH} obtained from the fitting of *variable contact time* experimental decay, in according to Eq (III-1), are summarized in Table IV.4-4 for unfilled PP and its composites.

Table IV.4-4. Results of the CP-MAS–VCT relaxation fit and XRD parameters of unfilled PP and PP nanocomposites.

Sample	$T^{H}_{1\rho}$ (ms) T_{CH} (ms) 44.2 ppm	 26.1 ppm	 22.0 ppm	d_{002} (nm)	C (nm)
PP	8.81±0.62 6.08±0.43	9.23±0.63 5.35±0.38	9.37±0.72 5.70±0.42	/	/
PP – xGnP -1	9.84±0.69 5.81±0.31	10.22±0.96 5.41±0.24	10.98±0.73 4.85±0.12	0.3330	19.62
PP – xGnP -5	10.96±0.88 3.56±0.18	12.84±0.81 3.15±0.19	13.21±0.74 2.98±0.23	0.3324	34.10
PP – xGnP -7 (*)	11.20±0.52 0.97±0.11 2.10±0.23	14.18±0.69 0.80±0.12 1.32±0.21	15.72±0.62 0.68±0.15 0.94±0.22	0.3321	39.72
PP-PPgMA-5-xGnP-5	10.03±0.69 3.94±0.17	11.10±0.81 3.80±0.10	13.20±0.68 3.04±0.17	0.3323	27.21

$T^{H}_{1\rho}$: spin–lattice long relaxation time.
$T^{H}_{2\rho}$: spin–lattice short relaxation time.
d_{002} : spacing between graphene layers.
(*) : $T^{H}_{1\rho}$, $T^{H}_{2\rho}$ and T_{CH} are reported successively in column.
T_{CH} : cross-polarization rate constant.
C : size of graphite crystals.

The relaxation values show that the composites have higher molecular rigidity compared to PP. Furthermore, the good fitting quality obtained for composites containing 1 and 5 wt% graphite indicates that the graphite is quite homogeneously dispersed within the matrix and that the compatibilizer has a positive effect in improving filler dispersibility. Quite on the other hand, since the fitting using Eq (III-1) was not satisfactory in the case of the sample PP-xGnP-7, two spin–lattice relaxation times ($T^{H}_{1\rho}$ and $T^{H}_{2\rho}$) and the cross-polarization rate constant (T_{CH}) were obtained by applying Eq (III-2) reaching a better fitting accuracy. The results of the fitting obtained for the latter sample indicate highly heterogeneous distribution of graphite within the matrix with diffuse segregation phenomena (high density of aggregates and agglomerates).

4.5 Hybridization effect of GF by graphite nanomodification of PP composites

Part of this chapter has been published in:

Pedrazzoli D, Kalaitzidou K, Pegoretti A,

"*Hybridization effect of glass fibers by expanded graphite nanoplatelets in polypropylene composites*",
Journal of Applied Polymer Science. (2014) Under review.

Although polymer nanocomposites exhibit improved thermal and mechanical properties at very low filler contents, loadings of more than 10 wt% usually lead to poor dispersion and processing characteristics [2]. Nevertheless, glass fiber loadings of 30 to 50 wt% are quite common [88, 261]. It is of great interest to explore whether combining two fillers of rather different size scales (i.e. micro- and nano- scale) would give the desired performance at low to intermediate filler loadings. Only few preliminary studies have been reported on the structure and properties of glass fiber reinforced polymer nanocomposites [262, 263].

The aim of this study is to investigate how the morphology, rheology and the specific mechanical properties of short-glass fiber reinforced PP nanocomposites are affected by the combined effect of nanofiller and reinforcing fibers. Moreover, the investigation of the stress-transfer mechanism at the fiber/matrix interface represents another primary aim of this research. Noteworthy, PP composites investigated in this work were prepared by melt compounding and injection molding (section 3.2.1.2).

4.5.1 Rheological behavior

The effect of the GF addition on the isothermal frequency dependence of the dynamic shear storage modulus (*G*') and complex viscosity ($|\eta^*|$) is reported in Figure IV.5-1 for unfilled PP and PP composites. As expected, both *G'* and $|\eta^*|$ significantly increase with the GF loading over the whole frequency range. Moreover, a further increase is recorded upon incorporation of xGnP in the PP composite filled with 10 wt % GF. Incorporation of nanofillers in thermoplastics is generally associated to a marked increase in the $|\eta^*|$ and *G*', mainly because of a pseudo solid-like transition caused by the dispersed nanoparticles [101, 105].

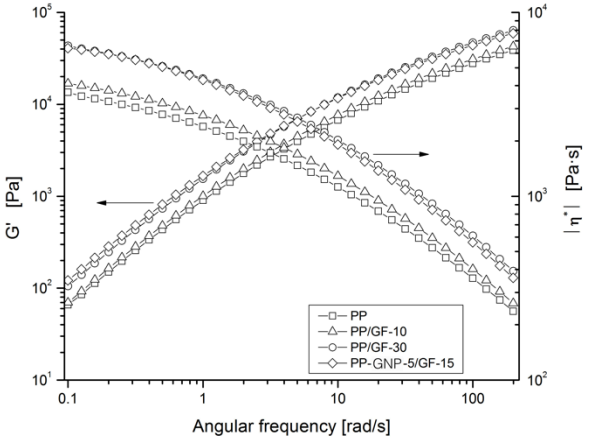

Figure IV.5-1. Complex viscosity $|\eta^*|$ and storage modulus (G') with respect to angular frequency (ω) of PP composites.

Interestingly, the sample PP-xGnP-5/GF-15 exhibits values of viscosity comparable with those of PP/GF-30, indicating that the nanofiller produces a greater increase in viscosity than GF, when considered at the same content. In particular, although the density of the xGnP is significantly lower than that of GF (1.83±0.02 vs. 2.49± 0.01 g/cm^3, respectively, as experimentally measured by helium pycnometry), the nanofiller specific surface area is almost two order of magnitude greater than that of GF (150 vs. 0.3-2 m^2/g, respectively, in according to the supplier information). Therefore, the filler surface area plays the dominant role in altering the rheological properties. Moreover, the higher viscosity exhibited by the hybrid composite might also be attributed to the pinning effect of the nanofiller onto the polymeric chains, as evidenced by the higher glass transition temperature (T_g) with respect to that of the non-hybrid composite PP/GF-30 (17.0±0.1 °C vs. 16.1±0.1 °C, respectively, as reported in Table IV.5-2).

4.5.2 Tensile mechanical behavior

As the amount of xGnP increases both tensile modulus *(E)* and ultimate tensile strength *(σ_b)* increase, as reported in Table IV.5-1, while the elongation at break *(ε_b)* decreases.

Table IV.5-1. Mechanical and morphological properties of the composites.

Sample	E [MPa] E* [MPa/(g/cm³)]	σ_b [MPa] σ_b * [MPa/(g/cm³)]	ε_b [%]	Izod impact strength [J/m]	Weigth av. GF aspect ratio
PP	2059±84 2278	38.5±0.7 42.6	8.9 ± 0.5	15.8 ± 1.4	/
PP/GF-10	3208±76 3323	41.8±0.3 43.3	6.3 ± 0.5	34.2 ± 1.8	23.1
PP/GF-30	4693±77 4199	43.1±0.7 38.6	2.8 ± 0.2	46.2 ± 2.0	19.8
PP-xGnP-1/GF-10	3565±72 3674	43.8±0.4 45.1	4.7 ± 0.2	/	21.3
PP- xGnP -3/GF-10	3660±132 3735	43.8±0.4 44.4	4.4 ± 0.2	/	20.9
PP- xGnP -5/GF-10	4255±135 4299	43.9±0.1 44.4	3.6 ± 0.1	42.2 ± 2.4	20.0
PP- xGnP -7/GF-10	4431±62 4431	43.7±0.3 43.7	3.6 ± 0.1	/	18.7
PP- xGnP -5/GF-15	4670±48 4560	44.8±0.5 43.7	3.6 ± 0.2	46.0 ± 1.6	16.7
PP-PPgMA-5- xGnP -5/GF-10	4287±93 4331	49.1±0.3 49.6	4.1 ± 0.2	50.0 ± 1.6	20.8
PP/GFc-10	3562±26 3689	41.8±0.3 43.3	5.9 ± 0.1	36.3 ± 1.4	22.1
PP- xGnP -5/GFc-10	4472±82 4518	45.4±0.8 45.9	4.1 ± 0.2	45.0 ± 1.9	19.2

This trend is consistent with observations for adding fillers to a relatively brittle matrix. In addition, the higher σ_b exhibited by the hybrid samples with respect to the sample PP/GF-10 reflects the greater interfacial shear strength between fiber and matrix which promotes a better stress transfer between matrix and fiber. The superiority of hybrid composites with respect to just GF composites (i.e. PP/GF-10 and PP/GF-30) is more evident when the specific properties are taken into account (i.e. specific elastic modulus and the specific ultimate tensile strength, *E** and *UTS**, respectively), as presented in Figure IV.5-2.

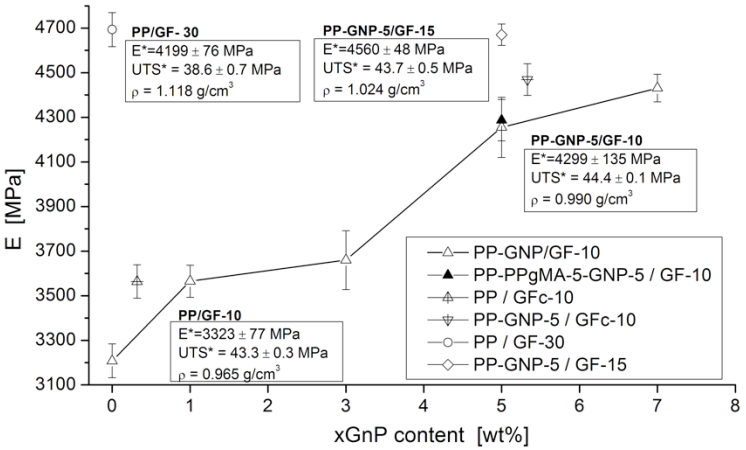

Figure IV.5-2. Elastic modulus of PP composites as a function of the filler amount.

In particular, the values of σ_b* exhibited by hybrid composites greatly overcome those of PP/GF-10 and PP/GF-30. Hybrid composites are thus lighter and stronger than GF composites. Interestingly, the composites incorporating coated GF (i.e. PP/GFc-10 and PP-xGnP-5/GFc-10) exhibit slightly higher *E** and σ_b* compared to PP/GF-10 and PP-xGnP-5/GF-10 composites respectively, where the graphite was added directly in the polymer instead of being introduced at the GF-polymer interface, probably indicating an enhanced adhesion between fiber and matrix. Improved interfacial properties can also be observed when the compatibilizer PPgMA is added to the matrix (i.e. PP-PPgMA-5-xGnP-5), as the σ_b is significantly higher that of the PP-xGnP-5 composite that does not contain compatibilizer.

4.5.3 Elastic modulus prediction in hybrid composites

4.5.3.1 Estimation of fiber length distribution

The measurement of fiber length distribution was carried out by image analysis on the films of composite samples through optical microscopy. From the distribution of glass fiber particle sizes, the weight $\overline{L_w}$ average fiber length was calculated by Eq (IV-7) :

$$\overline{L_w} = \frac{\sum n_i L_i^2}{\sum n_i L_i} \qquad (IV-7)$$

where n_i is the number of glass fibers within a specified range around the length value L_i. The measured average glass fiber length is divided by the mean fiber diameter to compute the weight average aspect ratio of the glass fibers ($i.e. \overline{R_w} = \overline{L_w} / \bar{d}$) which was taken into account for the modulus prediction of the composites. For all composites, there is a substantial decrease in the fiber length as the content of GF increases (Table IV.5-1). Glass fiber attrition is frequently observed due to the high stresses generated during melt processing owing to the high viscosity of the polymer melt. Concurrently, when xGnP is added to systems loaded with 10 wt% GF, the matrix viscosity increases and higher shear stresses are expected. Moreover, as already shown by Yoo et al. in the case of Nylon 6 modified with organoclay particles [135], the nanoparticle impingement on the fiber surfaces occurring during melt processing can be another reason for glass fiber attrition and this has increased importance at high filler concentrations.

4.5.3.2 Predictive models

There have been numerous attempts to model the properties of micro- and nano- composites and to correlate the experimental data with composite models [57, 211]. In particular, Halpin-Tsai and Mori-Tanaka theories have been widely applied to predict the tensile modulus of composites [264, 265]. Both theories are generally used as a model for a single-filler population in a matrix. However, the composites studied in this research consist of both a nanofiller and a microreinforcement (i.e. exfoliated graphite and glass fibers, respectively). These fillers have different effects on the mechanical properties of the composites, and they should be considered separately to more accurately predict the experimental modulus. Recently, Spencer et al. [266] proposed a two-population approach to model the combined effect of exfoliated montmorillonite and intercalated tactoids, while Yoo et al. [135] applied a similar approach to consider the effects of both organoclay and short glass fibers in

Nylon 6 composites. A two-population model can be considered in terms of an additive approach (Eq(IV-8)) :

$$\frac{E_{add}}{E_m} = \frac{E_{GF}}{E_m} + \frac{E_{nc}}{E_m} - 1 \qquad (IV-8)$$

Where E_{GF} and E_{nc} are the moduli of the composites based on the glass fibers and on the nanofiller, respectively, whereas E_m is the modulus of the unfilled matrix. In the additive approach the contributions of each filler are calculated separately and summed together without double counting the matrix contribution. The Halpin-Tsai theory (Eq (IV-9) and (IV-10)) was employed to predict the tensile modulus of the nanocomposites.

$$\frac{E_c}{E_m} = \frac{1 + \xi\eta\varphi}{1 - \eta\varphi} \qquad (IV-9)$$

$$\eta = \frac{\frac{E_f}{E_m} - 1}{\frac{E_f}{E_m} + \xi} \qquad (IV-10)$$

Where E_c corresponds to the modulus of the composites based on the nanofiller (E_{nc}), E_f is the elastic modulus of the filler, ξ is a geometrical correction factor which is a function of fillers' orientation and aspect ratio and φ is the filler volume fraction. In particular, the factor ξ is assumed as $2/3a$, where a is the filler aspect ratio in case of plate fillers such as graphite. Moreover, the filler modulus E_f was assumed as 70 GPa [267]. This model accounts for the mechanical properties of components and fillers' geometry and aspect ratio, but assumes perfect adhesion at the polymer/filler interface, homogeneous dispersion and specific filler orientation [268]. The main limitation of this model is that it does not account for filler agglomeration and the presence of the interphase.

The elastic modulus of the composite based on glass fibers (E_{GF}) was also predicted by applying the Halpin-Tsai model, where the factor ξ is assumed as $2a$, being a is the aspect ratio of the glass fibers. Moreover, on the basis of a previous work of our group, E_f was considered as 63 GPa [129]. The Halpin-Tsai model assumes perfect unidirectional alignment of the filler along the direction of the applied tensile load and seems thus not perfectly appropriate to be applied in the case of short-glass fiber composites. In fact, the glass fibers show an high degree of orientation in the longitudinal direction due to the injection molding, as observed on in-plane images for the PP/GF-30 composite (Figure IV.5-3a). However, when the cross section of the specimen is taken into account, some misalignments in the out-of-plane direction are evident (Figure IV.5-3b). Since a similar morphology was also

observed for the other PP composites, the empirical model proposed by Tsai and Pagano [269] was applied to predict the elastic modulus (E_{GF}) of a composite containing short-fibers randomly oriented in a plane (Eq(IV-11) – Eq(IV-13)).

$$E_{GF} = \frac{3}{8} E_{LL} + \frac{5}{8} E_{TT} \qquad (IV-11)$$

$$\frac{E_{LL}}{E_m} = \frac{1 + \xi_L \eta_L \varphi_f}{1 - \eta_L \varphi_f} \qquad (IV-12.1) \qquad \eta_L = \frac{\frac{E_f}{E_m} - 1}{\frac{E_f}{E_m} + \xi_L} \qquad (IV-12.2)$$

$$\frac{E_{TT}}{E_m} = \frac{1 + \xi_T \eta_T \varphi_f}{1 - \eta_T \varphi_f} \qquad (IV-13.1) \qquad \eta_T = \frac{\frac{E_f}{E_m} - 1}{\frac{E_f}{E_m} + \xi_T} \qquad (IV-13.2)$$

Where ξ_L and ξ_T is assumed as 2*a* and 2, respectively.

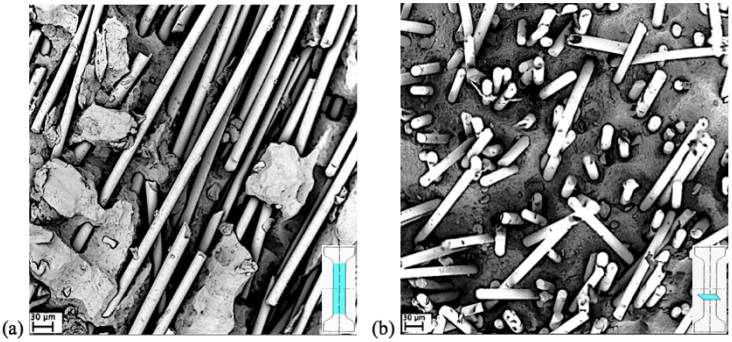

Figure IV.5-3. SEM observations of chemically etched surfaces of PP/30 GF composite considering (a) the in-plane section and (b) the cross section of a dogbone specimen.

4.5.3.3 Results of predictions as compared to the experimental results

The elastic modulus predictions for GF reinforced PP nanocomposites as a function of xGnP content, using the additive two-population method, are presented in Figure IV.5-4. Individual contributes of nanofiller and GF were considered by applying the Halpin-Tsai model *($E_{nc,H\text{-}T}$ & $E_{GF,H\text{-}T}$)* in one case and the Halpin-Tsai and Tsai-Pagano model *($E_{nc,H\text{-}T}$ & $E_{GF,T\text{-}P}$)* in a second case. Moreover, experimental data were compared to theoretical values in two different cases: i) aspect ratio of the nanofiller correspondent to 250 on the basis of the supplier information (*a=250*) and

ii) nanofiller aspect ratio of 80 on the basis of the morphological analysis (*a=80*) which accounts for agglomeration.

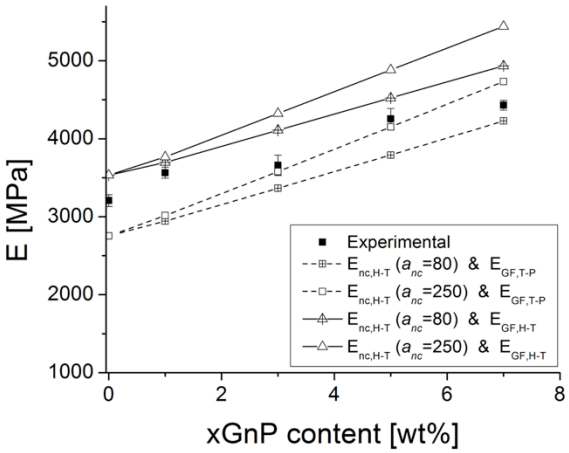

Figure IV.5-4. Comparison of elastic modulus predictions with respect to experimental values. Predictions based on the additive two-population model applying the Halpin-Tsai theory *($E_{nc,H-T}$ & $E_{GF,H-T}$)* and the Halpin-Tsai and Tsai-Pagano models *($E_{nc,H-T}$ & $E_{GF,T-P}$)* for different xGnP aspect ratios.

The Halpin-Tsai model applied for the prediction of the modulus of both nanocomposite and GF composites overpredicts the experimental data when the aspect ratio of 250 is used, indicating that agglomeration occurred and a reduced aspect ratio needs to be considered. On the other hand, when an aspect ratio of 80 is adopted, the model only slightly overpredicts the modulus, accounting for agglomeration but neglecting the presence of the interphase.

When the individual contributes of nanofiller and GF were considered by applying the Halpin-Tsai and Tsai-Pagano model, respectively, the model underpredicts the experimental data when the aspect ratio of 80 is used and also in the case of aspect ratio of 250 for xGnP contents lower than 7 wt%. Therefore, the modulus prediction by applying the two-population model and in according to the Halpin-Tsai and Tsai-Pagano model *($E_{nc,H-T}$ & $E_{GF,H-T}$* and *$E_{nc,H-T}$ & $E_{GF,T-P}$)* can be considered as the upper and lower boundary, respectively. In particular, the first case assumes perfect alignment of the glass fibers, while the second prediction considers the glass fibers randomly distribution in a plane. The actual PP/GF composites exhibits only a partial and inhomogeneous alignment of the glass fibers,

as shown by the in-plane morphological observation, and can thus be considered an intermediate case.

4.5.4 Impact toughness

Significant difference in the impact resistance of the composites can be observed with the addition of only 5 wt% xGnP (Table IV.5-1). The impact toughness has increased by more than 10%. Noteworthy, the increase in toughness obtained in PP-xGnP nanocomposites at low filler loadings can be ascribed to (i) changes in the energy absorbing mechanisms (i.e. higher plastic deformation of the matrix along the filler/matrix interface, crack branching due to hindrance by reinforcements, bridging of the crack, creation of voids etc.) and (ii) different crystalline morphology occurring upon nanomodification. In particular, both spherulite size and polymorphism play a key-role in determining the impact strength of PP [270]. However, the toughening effect given by high modulus filler particles (E~70 GPa for xGnP) is limited by the negative effect due to the formation of filler aggregates within the polymeric matrix.

As expected, the impact resistance increases with the GF loading, while significant improvements can be observed when coated GF have been incorporated in PP with respect to the systems based on uncoated GF. The enhancement in impact toughness corresponds to 6.1% and 6.6% when considering PP/GFc-10 and PP-xGnP-5/GFc-10, respectively. Interestingly, the hybrid sample PP-xGnP-5/GF-15 show almost the same impact toughness as PP/GF-30, evidencing the significant role played by the interfacial shear strength in determining an ultimate property such as the impact strength. Remarkable impact resistance is also exhibited by the sample PP-PPgMA-5-xGnP-5/GF-10, indicating that the increased stiffness and strength overshadow the loss in ductility, resulting in a larger area under the force-deflection curve.

4.5.5 Viscoelastic properties

The dynamic mechanical properties of the composites under investigation were significantly influenced by the fiber weight fraction: as expected, the storage (E') modulus increases with higher GF contents (Table IV.5-2), while the loss tangent decreases. Concurrently, the incorporation of xGnP in composites loaded with 10 wt% GF produces a substantial increase of E' and a slight decrease of the loss tangent with the filler content. Moreover, the glass transition temperature (T_g), as evaluated at the $tan\delta$ peak during DMA experiments, increases with the filler loading. Since changes in T_g are related to the primary relaxation of polymer chains and the extent of the immobilized chains, the alteration of polymer chain mobility promoted

by polymer-xGnP physical interactions might significantly contribute to the reinforcing mechanisms. Therefore xGnP reinforces PP not only because it is stiffer but also because it remarkably alters locally the physical properties of the polymer.

Table IV.5-2. Thermomechanical properties of the composites.

Sample	E' (-20 °C) [MPa]	E' (+23 °C) [MPa]	T_g [°C]	$\tan\delta_{Tg} \cdot 10^{-2}$
PP	2971 ± 14	1479 ± 11	15.1±0.1	7.89±0.11
PP/GF-10	4619 ± 32	2946 ± 14	16.0±0.1	6.15±0.72
PP/GF-30	5988 ± 30	4238 ± 16	16.1±0.1	5.21±0.91
PP-xGnP-1/GF-10	4670 ± 25	3114 ± 35	16.2±0.2	6.03±0.73
PP-xGnP-3/GF-10	4980 ± 41	3238 ± 42	16.2±0.1	5.94±0.71
PP-xGnP-5/GF-10	5128 ± 37	3395 ± 25	16.9±0.2	5.88±0.90
PP-xGnP-7/GF-10	5462 ± 40	3720 ± 33	16.9±0.1	5.75±0.62
PP-xGnP-5/GF-15	5671 ± 42	3849 ± 29	17.0±0.1	5.41±0.43
PP-PPgMA-5-xGnP-5/GF-10	5231 ± 27	3434 ± 21	17.4±0.1	5.73±0.54

In the same way, lower values of $tan\delta$ recorded upon nanofiller addition in hybrid composites can be attributed not only to a stiffening effect and the enhanced fiber-matrix adhesion, but also to polymer-xGnP physical interactions, resulting in lower loss modulus and enhanced elastic modulus of PP. With this regards, the storage modulus of the composites was considered below and above T_g (T=-20 °C and T=+23 °C, respectively) In particular, the elastic behavior observable below T_g better describes the stiffening effect, while the elastic behavior analyzed above T_g takes into account the restriction of polymer chain mobility. Interestingly, the storage modulus of the composite PP-xGnP-7/GF-10, normalized with respect to that of PP/GF-10, corresponds to 1.18 and 1.26 when considered below and above T_g, respectively, confirming the chain blocking mechanism due to xGnP incorporation.

4.5.6 Characterization of the interfacial shear strength

In a recent work of our group, it was shown how the incorporation of both non-functionalized and dimethyldichlorosilane-functionalized silica nanoparticles led to a remarkable increase of the interfacial strength in PP/GF systems [129] (up to a factor of about 5 for a 7 wt% content of surface treated nanoparticles) with respect to the case of neat matrix. Moreover, in another recent research, we reported that the

adhesion measured during SFFT for PP/GF systems modified with the addition of xGnP was found to significantly increase (up to a factor of about 6 for a 7 wt% content of xGnP) with respect to the case of neat PP [153].

The incorporation of xGnP results in a noticeable increase of the shear stress evaluated at the interface *(ISS)*, indicating a substantial enhancement of the load transfer between fiber and matrix (Figure IV.5-5).

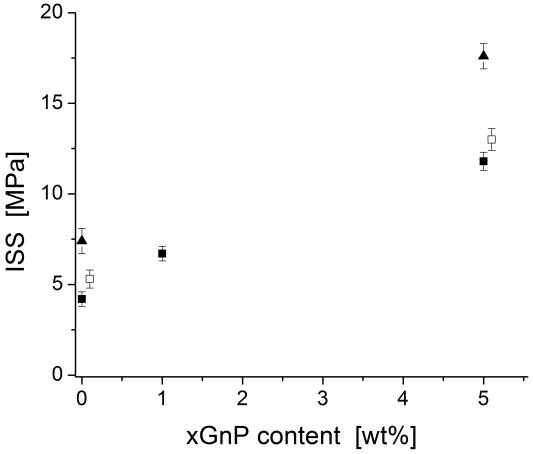

Figure IV.5-5. Interfacial shear strength values of PP/GF composites as a function of the xGnP amount, considering uncoated (full point) and coated (open point) glass fibers, while (▲) indicates the ISS of systems added with or without xGnP and also 5 wt% PPgMA.

Moreover, values of interfacial resistance confirm the superior tensile and viscoelastic properties exhibited by hybrid composites, in particular when considering the ultimate tensile strength. *ISS* values appear quite in concordance with those found by SFFT on model PP/GF composites, as presented in another research of our group [153] (11.8±0.5 vs. 15.3±1.3 MPa, respectively, for a xGnP content of 5 wt%). However, the greatest improvement is reached in the compatibilized system (i.e. PP-PPgMA-5-xGnP-5/GF), indicating the synergistic effect of PPgMA and nanofiller. In particular, PPgMA is supposed not only to improve the nanofiller dispersion, but also to significantly enhance the chemical affinity between PP and xGnP and between PP and GF [129].

Improved *ISS* can also be observed when the using coated glass fibers (i.e. PP/GFc), evidencing the positive effect of the fiber coating on the interfacial interactions. In the same way, when nanomodified PP is combined with coated fibers

(i.e. PP-xGnP-5/GFc) an higher ISS is obtained with respect to the system based on uncoated GF i.e. PP-xGnP-5/GF).

4.5.7 Morphology characterization

SEM micrographs of fracture surfaces for PP composites loaded with 10 wt% GF are shown in Figure IV.5-6a. The glass fibers are generally well dispersed in the PP matrix, and many fibers are pulled out from the matrix. The interfacial debonding appears to be the dominant failure mechanism, indicating low-adhesion condition.

On the other hand, a different failure behavior is observed for hybrid PP composites that contain 5 wt% xGnP and 10 wt% glass fibers (Figure IV.5-6b) and 5 wt% PPgMA, 5 wt% xGnP and 10 wt% glass fibers (Figure IV.5-6c). In this case, a matrix crack occurred, showing a significantly better fiber-matrix adhesion. Furthermore, the substantial chemical affinity between fiber and matrix is evidenced by the presence of matrix residual on the fiber surface after the pull-out.

The effectiveness of the glass fibers coating, when considering the PP-xGnP-5/GFc-10 composite, is evidenced by the presence of some graphite residuals on the fiber surface after the pull-out (Figure IV.5-6d). The fiber coating further enhances the fiber/matrix adhesion, as confirmed by the higher UTS with respect to the composites incorporating uncoated fibers.

Results of this study indicated that hybrid composites can combine the advantages of nano-materials and micro-size reinforcements, resulting in enhanced tensile properties and impact toughness, concurrently with an improved viscoelastic behavior. A two-population model, based on the Halpin-Tsai and Tsai-Pagano composite theories, was used to predict the elastic modulus of the composite samples. Experimental values appear to be reasonably consistent with model predictions when changes in particles aspect ratio and their orientation are accounted for.

Rheological measurements revealed that the processability of hybrid composites is significantly enhanced, because the increase in polymer viscosity reduces with decreasing the GF content. Concurrently, the investigation of the fiber-matrix interfacial adhesion through the single-fiber microdebonding tests and the morphological observations confirmed that the higher UTS obtained in hybrid composites is a result of not only matrix reinforcement through incorporation of rigid fillers, but also of the stronger interfacial interactions between matrix and glass fibers.

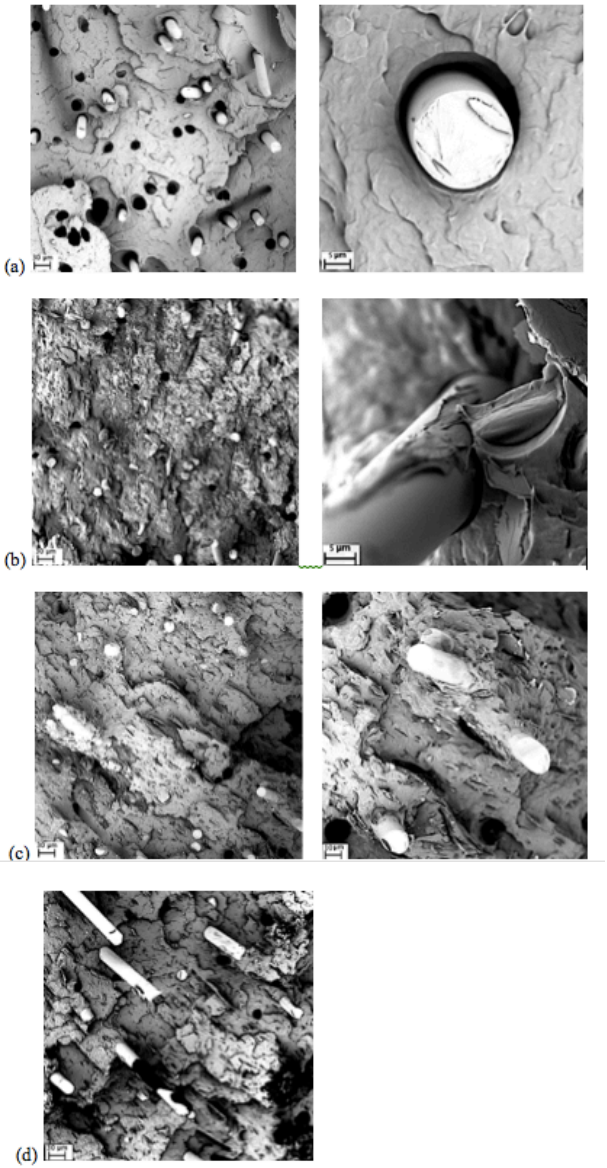

Figure IV.5-6. SEM micrographs of fracture surfaces of (a) PP/GF-10, (b) PP-xGnP-5/GF-10 (c) PP-PPgMA-5-xGnP-5/GF-10 and (d) PP-xGnP-5/GFc-10 composites.

4.6 Hybridization effect of GF by silica nanomodification of PP composites

Part of this chapter has been published in:

Pedrazzoli D, Pegoretti A,

"Hybridization of short glass fiber polypropylene composites with nanosilica and graphite nanoplatelets",
Reinforced Plastics and Composites. (2014) In press.

The effects of various types and amounts of fumed silica on the microstructure and thermo-mechanical properties of PP composites containing 5, 10 and 20 wt% of short GF have been analyzed. Hybrid composites were produced by melt-compounding and compression molding (section 3.2.1.1).

The aspect ratio of the SGF decreased with the fiber loading and the nanofiller amount. The tensile strength and elastic modulus increased, while the elongation at break decreased as the content of both GF and nanofiller increased. Tensile energy to break under impact conditions increased with the GF content but decreased with nanofiller amount. Moreover, storage modulus and creep stability were remarkably enhanced in short GF composites by the presence of nanosilica.

4.6.1 Morphological observations

FESEM micrographs of fracture surfaces for PP nanocomposites loaded with 10 wt% of GF are shown in Figure IV.6-1. The glass fibers are generally well dispersed in the unfilled PP matrix, and several fibers result to be pulled out from the matrix (Figure IV.6-1a) due to poor fiber-matrix adhesion (Figure IV.6-1b). On the other hand, Figure IV.6-1c indicates a quite different failure behavior for composites contaning a compatibilizer (PPgMA), showing that the length of the protruding fibers is significantly lower and the GF seem to be more efficiently wetted by the polymer matrix (Figure IV.6-1d). Composites based on ternary PP matrices (i.e. PP-PPgMA-5-A380-5/GF-10 and PP-PPgMA-5-R974-5/GF-10) showed a qualitatively homogeneous dispersion of GF and a shorter length of the protruding fibers. The above experimental observations are in good agreement with the results obtained for fiber-matrix interfacial shear strength (ISS) from micromechanical tests on microcomposites with the same composition (Table IV.6-1).

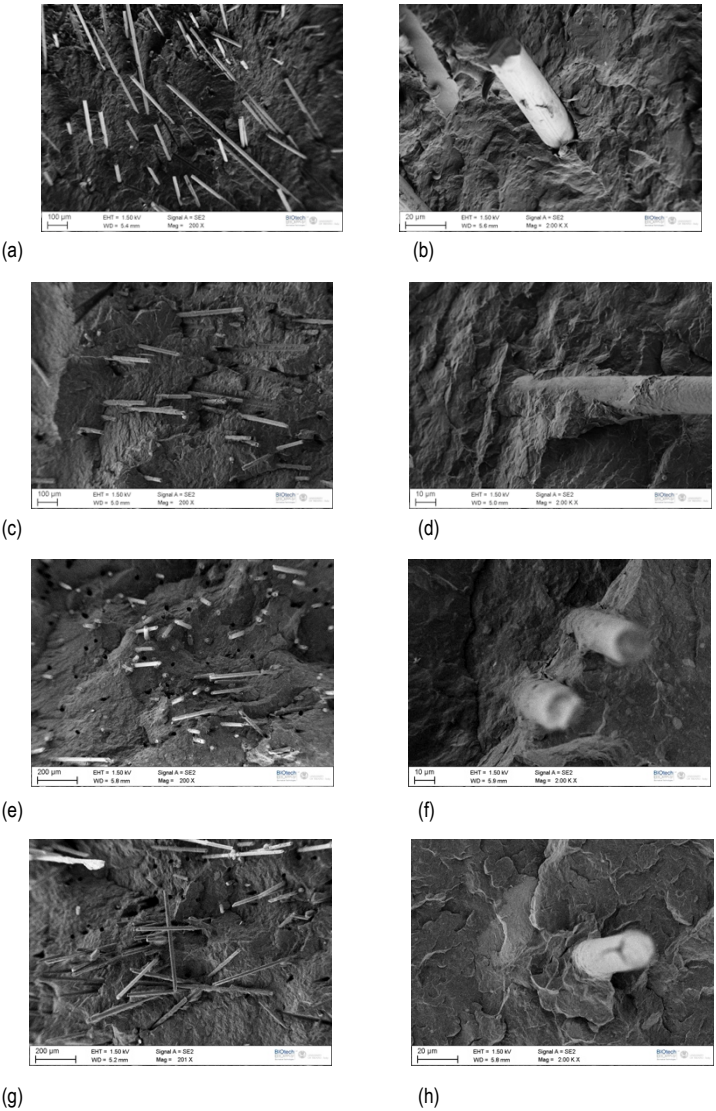

Figure IV.6-1. SEM micrographs of fracture surfaces of (a-b) PP/GF-10, (c-d) PP-PPgMA-5/GF-10 (e-f) PP-PPgMA-5-A380-5/GF-10 and (g-h) PP-PPgMA-5-R974-5/GF-10 composites.

For all composites, there is a substantial decrease in the average aspect ratio of the glass fiber as its content increases (Figure IV.6-2). Noteworthy, this ratio was computed as previously described in section 4.5.3.1. Fiber breakage may result from fiber–polymer interaction, fiber–fiber interaction (due to bending stresses caused by fiber overlap and stress concentrations caused by fiber surface abrasion), and fiber contact with surfaces of the processing equipment. Moreover, as already documented by Yoo et al. for nylon 6 - glass composites modified with organoclay particles, the particle impingement during melt processing can be another reason for an increased attrition with glass fiber and this has increased importance at high filler concentrations .

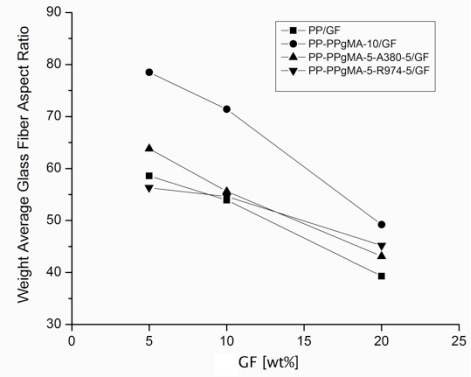

Figure IV.6-2. Weight average glass fiber aspect ratio as a function of GF content for binary and ternary composites.

4.6.2 Mechanical testing

As the amount of GF increases, both tensile modulus *(E)* and strength *(σ_b)* increase, while the elongation at break *(ε_b)* decreases (Table IV.6-1), showing a mechanical behavior which is quite peculiar for short fiber reinforced polymer composites. It is interresting to observe that the presence of the PPgMA compatibilizer does not modify the mechanical properties of the unfilled polymer matrix, but slightly improves those of the GF filled composites. This result can certainly be attributed the the positive effect on the fiber/matrix interface. Similar effects can be observed when 5 wt% of nanofillers A380, R974 are added. The toughness of the composites, evaluated through the critical stress intensity factor (K_{IC}) and strain energy release rate (G_{IC}), improved when GF are incorporated.

Table IV.6-1: Tensile mechanical properties and fracture toughness of the composites.

Sample	E (MPa)	σ_b (MPa)	ε_b (%)	ISS_{K-T}(*) (MPa)	TEB (J·mm^{-2})	K_{Ic} (MPa·m$^{1/2}$) (G_{Ic} (kJ·m^{-2}))
(PP)	1546 ± 24	37.1 ± 0.1	16.8 ± 0.3		0.19±0.05	
PP/GF-5	2086 ± 42	39.3 ± 0.3	6.2 ± 0.5			
PP/GF-10	2896 ± 53	42.1 ± 0.5	3.6 ± 0.4	2.7 ± 0.2	0.43±0.06	3.1±0.1 (2.8 ± 0.1)
PP/GF-20	3697 ± 41	46.6 ± 0.7	2.8 ± 0.6			
(PP-PPgMA-10)	1648 ± 12	37.0 ± 0.5	12.1 ± 0.6		0.25±0.02	
PP-PPgMA-10/GF-5	2595 ± 63	40.6 ± 0.4	5.8 ± 0.5			
PP-PPgMA-10/GF-10	3035 ± 51	43.2 ± 0.6	3.4 ± 0.6	20.2 ± 2.5	0.51±0.06	3.3±0.1 (3.2±0.1)
PP-PPgMA-10/GF-20	3859 ± 66	48.0 ± 0.7	2.5 ± 0.8			
(PP-PPgMA-5-A380-5)	2015 ± 40	35.7 ± 0.4	6.7 ± 0.2		0.24±0.06	
PP-PPgMA-5-A380-5/ GF-5	2614 ± 37	39.4 ± 0.4	5.6 ± 0.5			
PP-PPgMA-5-A380-5/ GF-10	3302 ± 48	43.0 ± 0.6	3.3 ± 0.6	22.7 ± 2.1	0.49±0.09	3.5±0.1 (3.3±0.2)
PP-PPgMA-5-A380-5/ GF-20	4042 ± 44	47.8 ± 0.8	2.4 ± 0.7			
(PP-PPgMA-5-R974-5)	2281 ± 58	34.2 ± 0.4	12.0 ± 1.1		0.28±0.04	
PP-PPgMA-5-R974-5/ GF-5	2862 ± 48	39.2 ± 0.6	5.4 ± 0.6			
PP-PPgMA-5- R974-5/ GF-10	3402 ± 52	43.4 ± 0.5	3.2 ± 0.6	38.8 ± 3.5	0.54±0.04	3.7±0.2 (3.5±0.2)
PP-PPgMA-5- R974-5/ GF-20	4171 ± 40	48.2 ± 0.7	2.2 ± 0.7			

(*) ISS values as reported in the previous section 4.4.2.

Moreover, superior resistance to crack initiation was recorded in the composites based on ternary matrices. Interestingly, tensile energy to break (TEB) values increased with glass fiber incorporation and even more in the systems based on nanocomposite matrices. The observed increased absorbed impact energy reflects the increased stiffness and strength of the composites that overshadows the loss in ductility, resulting in a larger area under the force-deflection curve.

The effect of the incorporation of GF on the creep resistance of PP nanocomposite matrices is represented in Figure IV.6-3a. As the GF content increases, the creep compliance is strongly reduced, showing a remarkable improvement of the creep stability of PP nanocomposites induced by the presence of rigid fibers (Table IV.6-2). Interestingly, the sample PP-PPgMA-10/GF-10 manifested better creep stability than PP/GF-10, probably due to the substantial better interfacial properties rather than the slightly higher stiffness. On the other hand, the best creep

performances are exhibited by the ternary systems, which showed highest stiffness and *ISS*.

The dynamic mechanical properties of the composites under investigation are significantly influenced by the fiber weight fraction: as expected, both storage (*E'*) and loss (*E''*) modulus increase with higher GF contents (Table IV.6-2), while the loss tangent decreases.

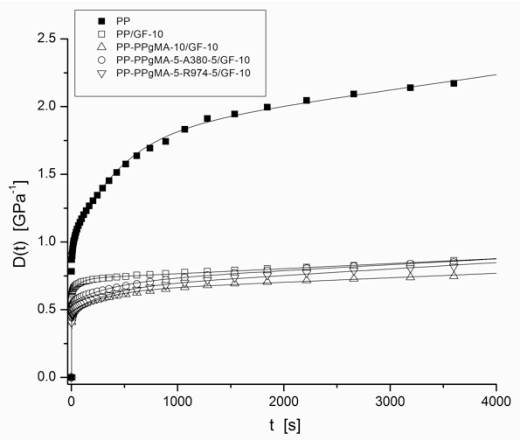

(a)

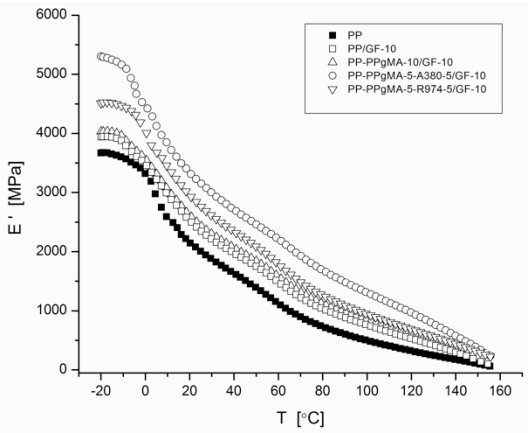

(b)

Figure IV.6-3. (a) Creep compliance (experimental data are fitted by the Burger's model) and (b) storage modulus (*E'*) of composites loaded with 10 wt% of GF.

Table IV.6-2: Visco-elastic properties of GF composites.

Sample	E'_{25C} (MPa)	E''_{25C} (MPa)	$\tan\delta_{25°C}$	D_{3600s} (GPa^{-1})
(PP)	2006.2	88.9	4.43	2.17
PP/GF-5	2244.0	95.4	4.25	1.22
PP/GF-10	2305.1	97.0	4.21	0.86
PP/GF-20	3143.9	116.0	3.69	0.74
(PP-PPgMA-10)	1353.2	70.1	5.18	2.05
PP-PPgMA-10/GF-5	2233.5	97.4	4.36	0.99
PP-PPgMA-10/GF-10	2339.1	100.1	4.28	0.75
PP-PPgMA-10/GF-20	3176.4	132.1	4.16	0.62
(PP-PPgMA-5-A380-5)	2669.4	133.5	5.00	1.64
PP-PPgMA-5-A380-5/ GF-5	3009.5	145.1	4.82	0.90
PP-PPgMA-5-A380-5/ GF-10	3155.9	150.5	4.77	0.85
PP-PPgMA-5-A380-5/ GF-20	3891.7	183.3	4.71	0.64
(PP-PPgMA-5-R974-5)	2646.6	114.7	4.34	1.81
PP-PPgMA-5-R974-5/ GF-5	2691.0	115.4	4.29	1.00
PP-PPgMA-5- R974-5/ GF-10	2959.5	123.7	4.18	0.82
PP-PPgMA-5- R974-5/ GF-20	4176.2	159.1	3.81	0.68

E'_{25C}: Storage modulus at +25 °C. D_{3600s} : Viscoelastic creep compliance at 3600 s.
E''_{25C}: Loss modulus at +25 °C. $\tan\delta_{25°C}$: Loss tangent at +25 °C.

Concurrently, the incorporation of silica in composites loaded with 10 wt% GF produces a substantial increase of *E'* and *E''* and a slight decrease of the loss tangent with the filler content, showing that the elasticity of the composite is improved by the addition of silica nanoparticles.

Therefore, the stronger interfacial strength exhibited in hybrid composites positively affected the tensile viscoelastic behavior of the materials, leading to better tensile properties, higher storage modulus and enhanced creep stability. In conclusion, the results indicates that hybrid composites that combine the advantages of nano-fillers and micro-size reinforcements can be successfully produced in order to obtain lighter and stronger materials, as part of the higher density GF can be replaced with a smaller amount of nanofiller.

Chapter V

Conclusions and future perspectives

In this study, polypropylene (PP) based nanocomposites were prepared by incorporating different kinds and amounts of silica nanoparticles and graphite nanoplatelets (GNP). In order to investigate the effect of the manufacturing process on the material's properties, the samples were produced by two distinct processes: (i) melt compounding and compression molding and (ii) extrusion and injection molding. It was found that injection molding provides significantly greater stiffness and strength compared to compression molding for all types of PP nanocomposites.

Several tools and characterization techniques were used in order to correlate the microstructure to the physical and mechanical properties of the materials:

- The isothermal and non-isothermal crystallization behavior was studied through in-situ crystallization studies using optical microscopy, modulated differential scanning calorimetry (MDSC) and x-ray diffraction analysis.
- The mechanical properties (including tensile elastic modulus and strength and impact tests) and thermo-mechanical properties such as glass transition temperature, storage and loss modulus, were investigated as a function of the filler type and content in order to study the interfacial interactions occurring between filler and matrix. In addition, scanning electron microscopy and atomic force microscopy were carried out to characterize the morphology and properties of the filler/matrix interphase.
- The viscoelastic behavior of the prepared nanocomposites was investigated adopting different techniques. In particular, rheological analyses enabled the characterization of the viscoelastic properties in the molten state (i.e. particle-particle and polymer-particle interactions) under different shearing conditions. Viscoelastic behavior in the solid state was also studied by quasi-static tensile tests, creep tests and dynamic mechanical tensile analyses. Specific attention was placed on the effect of temperature and stress on the creep behavior.
- The fiber/matrix interfacial shear strength was evaluated by the single-fiber fragmentation tests on PP–GF microcomposites containing various types and amounts of nanofillers dispersed in the polymer matrix. Contact angle measurements were performed in order to determine the thermodynamic work of adhesion of PP (and relative nanocomposites) with respect to glass.
- Morphological observations were carried out in order to investigate how the morphology was affected by the presence of the filler and compatibilizer, and

to determine the interphase characteristics (i.e. width and elastic modulus gradient).

It was found that:

- Both silica and GNP were found to be effective nucleating agents, significantly increasing the crystallization rate during isothermal crystallization, with greater changes observed in case of GNP composites. PP crystals nucleate on the GNP surface, as observed in in-situ crystallization studies using optical microscopy. The nucleation of the β-phase, which manifests superior impact strength and toughness compared to the most common α-form crystals, was observed in both silica and graphite composites even at low filler concentration (as low as 0.01 wt%). Because of the overall changes were found generally greater for GNP with respect to silica, the GNP is significantly more efficient in inducing polymorphism and favoring the formation of a transcrystalline phase on the filler surface.
- The interfacial interactions occurring between nanosilica and PP and their effect on the physical and macroscopic properties of PP-silica nanocomposites were investigated. In particular, in order to analyze the relationships between the interfacial interactions in the composites and tensile and viscoelastic properties, different models dealing with the static and dynamic mechanical behavior of the particulate composites were applied. The Pukanszky's model, used to correlate the materials' strength with the interfacial strength, was shown to ascertain the influence of the filler surface functionalization on the intensity of the interfacial interactions. It was found that stronger interfacial interactions exist in the compatibilized silica nanocomposites. The Sumita's model, employed to correlate the normalized loss modulus with the interfacial strength, was found to follow a qualitative similar trend. A significant correlation between the tensile modulus, glass transition temperature and the amount of constrained phase, as assessed through tensile and DMA analyses, revealed the presence of a secondary reinforcing mechanisms, which, concurrently to the primary stiffening effect of the high modulus filler, contributes to the enhancement of the nanocomposites bulk properties. Crystallization experiments evidenced the existence of a transcrystalline region generating thanks to the nucleating ability of the filler, while DMA experiments were also used to confirm the presence of an immobilized amorphous phase at the filler surface. A complex constrained phase, responsible for providing a secondary reinforcing mechanism, was thus

modeled as immobilized amorphous and transcrystalline regions located at the filler surface.

- The role of the silica particles surface area and surface treatment on the viscoelastic properties of the resulting composites was assessed by dynamic mechanical analyses and creep tests. In particular, both untreated and surface treated silica nanoparticles were used to produce binary nanocomposites, while ternary systems were prepared with the incorporation of different percentages of compatibilizer PPgMA into silica nanocomposites. The non-linear viscoelastic creep of the composites, successfully studied by the application of the TSSP, showed a considerable enhancement of the creep stability in nanocomposites with respect to unfilled PP, especially for higher creep stresses, but no significative differences between nanocomposites filled with different nanosilicas. The study of creep dependance on the temperature showed that the stabilizing effect provided by the nanoparticles was more effective at high temperatures and, considering the TTSP, at long loading times. The equivalence between the time strain- and time temperature-superposition principle was substantiated by comparing the correspondent superimposed master curves.
- Interfacial shear strength (ISS) was investigated by means of the single fiber fragmentation test on various PP/GF microcomposites containing various types and amounts of silica nanoparticles. Results show that the strength at the interface can be remarkably increased by the addition of dimethyldichlorosilane-functionalized silica nanoparticles and GNP platelets, and that the improvement is particularly enhanced when the nanoparticles are used in combination with PPgMA in ternary composites. The fiber/matrix work of adhesion showed a good correlation with the ISS values.

Starting from these considerations, hybrid composites reinforced with high amounts of short fibers and GNP were produced and characterized in order to investigate how the morphology and the mechanical properties of the composites were affected by the combined effect of two fillers of rather different size scales (i.e. micro- and nano-scale). In particular, the investigation of the fiber/matrix interfacial adhesion and the morphological observations indicated a remarkable increase of the interfacial interactions between matrix and glass fibers due to the dispersion of GNP in the polymer matrix.

The stronger adhesion combined with the enhancement of the matrix properties resulted in superior tensile properties and impact resistance and improved viscoelastic behavior, determined as a function of the GNP content. A two-population model, based on the Halpin-Tsai and Tsai-Pagano composite theories, was used to

predict the elastic modulus of the hybrid composites. Comparison with the experimental results indicates that the model can satisfactory provide the upper and lower limits of the modulus of the hybrid composites, limits that depend on the aspect ratio (agglomeration) of the nanomaterial and the orientation of the both GNP and GF.

As means of comparison, thermosetting hybrid composites based on epoxy resin were also produced by incorporation of GNP and short GF (see section 6.5).

Chapter VI

Collateral research activities

6.1 Viscoelastic behavior and fracture toughness of linear-low-density polyethylene reinforced with synthetic boehmite alumina nanoparticles

Part of this paragraph has been published in:

Pedrazzoli D, Ceccato R, Karger-Kocsis J, Pegoretti A,

"*Viscoelastic behaviour and fracture toughness of linear-low-density polyethylene reinforced with synthetic boehmite alumina nanoparticles*", *eXPRESS Polymer Letters, 7. (2013) 652-666.*

Aim of the present study is to investigate how synthetic boehmite alumina (BA) nanoparticles modify the viscoelastic and fracture behavior of linear low-density polyethylene (LLDPE). Nanocomposites containing up to 8 wt% of untreated and octyl silane-functionalized BA nanoparticles, were prepared by melt compounding and hot pressing. The BA nanoparticles were finely and uniformly dispersed within the matrix according to scanning electron microscopy (SEM) inspection. The results of quasi-static tensile tests indicated that nanoparticles can provide a remarkable stiffening effect at a rather low filler content. Short-term creep tests showed that creep stability was significantly improved by nanofiller incorporation. Concurrently, both storage and loss moduli were enhanced in all nanocomposites, showing better result for surface treated nanoparticles.

The plane-stress fracture toughness, evaluated by the essential work of fracture (EWF) approach, manifested a dramatic increase (up to 64%) with the BA content, with no significant differences among the various types of BA nanoparticles.

6.1.1 Tensile mechanical properties

The matrix used in this work was a Flexirene® CL10 linear low-density polyethylene (MFI at 190 °C and 2.16 kg = 2.6 g/10min, Mn = 27000 g/mol, density = 0.918 g/cm^3), produced by Versalis S.p.A. (Mantova, Italy) using Ziegler-Natta catalysis and butene as a comonomer (C_4-LLDPE). This type of linear low density polyethylene, containing antioxidants, is suitable for cast extrusion of thin films with high optical properties. Two different grades of untreated BA, namely Disperal® 40 (BA40) and Disperal® 80 (BA80) (supplied by Sasol GmbH, Hamburg, Germany) were used as fillers. Their nominal primary crystallite sizes are 40 and 74 nm, respectively. Moreover, a silane surface treated BA (Disperal® 40 octylsilane treated, BA40 OS), characterized by the same primary crystallite size as Disperal® 40 was also used.
LLDPE chips were used as received while the BA fillers were dried at 80 °C for 12 h prior to use. The samples were prepared by melt compounding in a Brabender® Plasti-Corder internal mixer (T=170 °C, n=50 rpm, t=15 min) followed by compression molding using a Collin® P200E hot press (T=170 °C, P=2 MPa, t=15 min), to shape square plane sheets with a thickness of about 0.5 mm. The filler content was varied between 0 and 8 wt%.
The unfilled matrix was denoted as LLDPE, while the coding of the nanocomposites indicated the matrix, the filler type, and the filler weight amount, as well. For instance, a sample filled with 4 wt% of Disperal® 40 is coded as LLDPE-D40-4.

The addition of BA nanoparticles produces a significant increase of the elastic modulus of the LLDPE matrix, reaching an improvement of 69% for systems filled with 8 wt% of BA D40, compared to unfilled LLDPE (Table VI.1-1). The stiffening effect induced by nanofiller incorporation is most often attributed to the formation of a rigid interphase between the matrix and the particles. Nevertheless, it has also been recently proposed that nanoparticles aggregation can be another mechanism responsible for stiffness increase in polymer nanocomposites [57, 271]. A new approach developed by Dorigato et al. was adopted in order to model the elastic properties of LLDPE-BA nanocomposites taking into account the stiffening effect provided by rigid nanoparticles forming primary aggregates, with the hypothesis that part of the polymer matrix is mechanically constrained within the aggregates [57, 271]. In order to implement the model, the Poisson's ratio of matrix and filler were chosen as 0.44 and 0.23, respectively, while the elastic modulus of BA was considered equal to 385 GPa in according to literature data [272].

Table VI.1-1. Quasi-static tensile properties at yield and at break and tensile energy to break (TEB).

Sample	Tensile modulus [MPa]	Tensile Strength at Yield [MPa]	Elongation at Break [%]	TEB [J/mm²]
LLDPE	200 ± 6	11.7 ± 0.2	1390 ± 91	0.63 ± 0.08
LLDPE-D40-1	218 ± 13	11.8 ± 0.1	1259 ± 40	0.63 ± 0.07
LLDPE-D40-4	262 ± 13	12.2 ± 0.4	1124 ± 69	0.69 ± 0.11
LLDPE-D40-8	337 ± 12	12.3 ± 0.4	964 ± 41	0.70 ± 0.06
LLDPE-D40 OS-1	250 ± 18	11.3 ± 0.2	1330 ± 33	0.73 ± 0.05
LLDPE-D40 OS-4	279 ± 22	12.9 ± 0.2	1249 ± 32	0.84 ± 0.07
LLDPE-D40 OS-8	306 ± 10	13.4 ± 0.2	1040 ± 35	0.87 ± 0.11
LLDPE-D80-1	218 ± 17	12.1 ± 0.3	1336 ± 38	0.63 ± 0.05
LLDPE-D80-4	246 ± 10	12.4 ± 0.2	1135 ± 54	0.93 ± 0.09
LLDPE-D80-8	302 ± 19	13.3 ± 0.1	1043 ± 102	0.90 ± 0.08

The relative elastic modulus of the LLDPE-BA composites is plotted in Figure VI.1-1 as a function of the filler volume fraction, along with the fitting curves generated by the adopted model. It can be noticed that the proposed model can predict quite well the elastic modulus of LLDPE-D40-x and LLDPE-D80-x composites over the whole range of filler concentration. Furthermore, the significative increase of the elastic modulus detected for nanocomposites is associated to enhanced *a* values, which indicates the fraction of matrix constrained by nanoparticles. As already noticed by Dorigato et al. when applying the model tothe case of LLDPE filled with fumed silica nanoparticles, there exists an an apparent correlation between the α parameter and filler surface area [273]. Indeed, the smaller the particle, the higher the surface area and the stronger the propensity to agglomerate, leading to more extensive primary aggregates formed during manufacturing of finer BA filler. On the other hand, the proposed model does not satisfactory fit the case of LLDPE-D40 OS-x systems, probably due to a better polymer–filler interaction which produces superior interface properties especially at low nanofiller contents.

When the ultimate mechanical properties are taken into account, it can be observed that the yield stress increases proportionally to the filler content while the elongation at break decreases for all kinds of BA nanocomposites, probably because of the filler aggregation and stronger interaction [255].

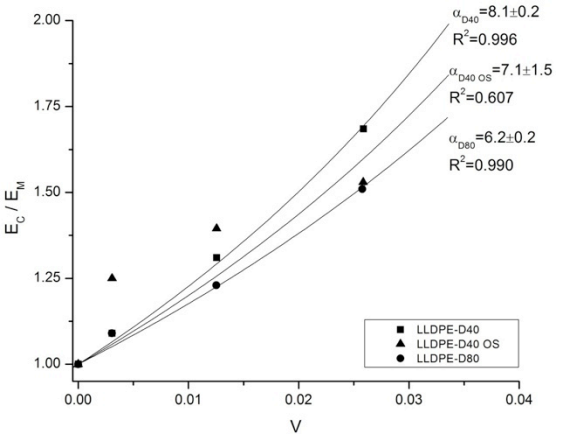

Figure VI.1-1. Relative elastic modulus of LLDPE-BA nanocomposites as a function of the filler volume content, with fitting of experimental data in according to the model proposed by Dorigato et al. [57] (continuous line). Note that the error bars of data are not represented for sake of clarity.

6.1.2 Fracture toughness and impact strength

The EWF method was applied to characterize the plane-stress fracture toughness. At first, the preconditions necessary for the application of the EWF methodology were verified [122]. In particular, the validity criterion verifies that all tests were conducted under plane-stress state. Furthermore, all the specimens exhibited delayed yielding (i.e. the ligament yielding is fully yielded when the crack starts to propagate), with subsequent ductile fracture, showing a large plastic deformation zone surrounding crack tip. Moreover, most specimens manifested evident necking after yielding. Since the force-displacement curves of specimens with different ligament lengths were geometrically similar (self-similarity), the fracture mechanism was probably independent on the ligament length (Figure VI.1-2).

Interestingly, in all samples including nanocomposites, the area under the curve after the maximum force is higher than that prior to maximum force, thus indicating slow crack propagation with high energy absorption, typical of ductile materials [121]. The addition of BA nanoparticles to LLDPE did not modify these general features.

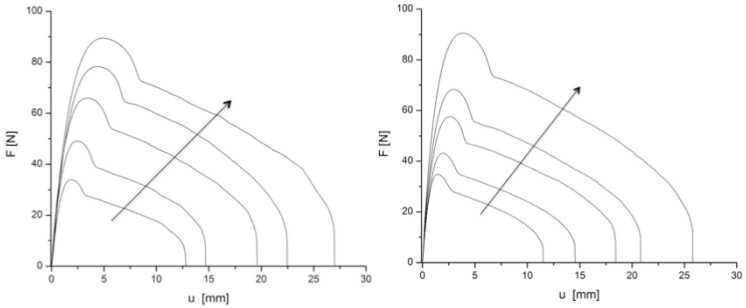

Figure VI.1-2. Load–displacement curves of (a) LLDPE and (b) LLDPE-D40-8 nanocomposites. The arrow indicates increasing ligament length.

The elliptical shape of the stress-whitened zone formed during tensile EWF test performed on LLDPE nanocomposites was similar to that of neat LLDPE with slight variation in the height of the zone. The elliptical shape can be characterized by a shape factor β, estimatedas $\pi h/4L$, where h is the height of whitened zone while L is the ligament length. The total specific essential work of fracture (w_e), the specific essential work of fracture at yielding ($w_{e,y}$) and the specific essential work of fracture for necking ($w_{e,n}$) were obtained by linear fits and summarized in Table VI.1-2. In general, a noticeable improvement of w_e can be observed as the BA content increases for all kinds of BA nanoparticles, whereas βw_p values slightly decrease upon BA addition. These results clearly indicate that BA addition significantly toughens the LLDPE matrix [121].

Moreover, partitioned components of the specific essential work of fracture, such as the yielding-related component ($w_{e,y}$) and EWF for necking-related component ($w_{e,n}$), also show an improvement in all nanocomposites when compared to unfilled LLDPE.

When the load is applied at high speed through tensile impact tests, the introduction of BA nanoparticles leads to an interesting increase of the tensile energy at break (TEB). The toughening effect is more intense as the nanoparticles are surface functionalized, in accordance with the conclusions reached under quasi-static tensile loading (Table VI.1-1). While the presence of anorganic modifier on the surface of the nanoparticles seems to not affect the tensile properties at break under quasi-static conditions, tensile energy at break under impact test is remarkably improved in the case of BA40 OS filled nanocomposites.

Table VI.1-2. Specific EWF properties of LLDPE and relative nanocomposites.

Sample	w_e [kJ / m^2]	β w_p [MJ / m^3]	β	$w_{e,y}$ [kJ / m^2]	β' $w_{p,y}$ [MJ / m^3]	$w_{e,n}$ [kJ / m^2]	β'' $w_{p,n}$ [MJ / m^3]
LLDPE	26.7 ± 3.6	12.7 ± 0.4 (0.983)	0.32 ± 0.04	2.7 ± 0.3	2.78 ± 0.03 (0.997)	24.2 ± 3.6	9.9 ± 0.4 (0.992)
LLDPE-D40-1	26.1 ± 3.3	12.9 ± 0.4 (0.986)	0.27 ± 0.03	3.1 ± 0.5	2.72 ± 0.05 (0.992)	23.1 ± 3.3	10.2 ± 0.2 (0.990)
LLDPE-D40-4	34.1 ± 3.5	11.8 ± 0.4 (0.981)	0.23 ± 0.02	3.5 ± 0.5	2.34 ± 0.06 (0.988)	30.4 ± 3.5	9.5 ± 0.4 (0.993)
LLDPE-D40-8	42.2 ± 3.1	11.0 ± 0.3 (0.983)	0.22 ± 0.02	5.6 ± 0.5	1.92 ± 0.06 (0.985)	36.5 ± 3.1	9.1 ± 0.2 (0.990)
LLDPE-D40 OS-1	29.0 ± 2.0	12.6 ± 0.2 (0.994)	0.28 ± 0.03	2.8 ± 0.5	2.80 ± 0.05 (0.993)	26.1 ± 2.1	9.8 ± 0.4 (0.991)
LLDPE-D40 OS-4	39.1 ± 2.0	11.6 ± 0.2 (0.993)	0.27 ± 0.04	4.3 ± 0.8	2.18 ± 0.09 (0.970)	34.9 ± 2.1	9.4 ± 0.3 (0.995)
LLDPE-D40 OS-8	42.7 ± 2.6	10.5 ± 0.3 (0.986)	0.27 ± 0.03	5.6 ± 0.3	1.96 ± 0.04 (0.993)	37.0 ± 2.6	8.5 ± 0.4 (0.991)
LLDPE-D80-1	28.1 ± 1.3	12.8 ± 0.2 (0.998)	0.27 ± 0.02	2.8 ± 0.3	2.80 ± 0.04 (0.997)	25.2 ± 1.4	10.0 ± 0.3 (0.993)
LLDPE-D80-4	34.0 ± 2.3	11.9 ± 0.3 (0.992)	0.26±0.02	4.4 ± 0.5	2.32 ± 0.06 (0.988)	29.8 ± 2.4	9.6 ± 0.2 (0.993)
LLDPE-D80-8	43.7 ± 1.2	10.8 ± 0.1 (0.997)	0.25±0.02	5.8 ± 0.4	2.15 ± 0.04 (0.992)	37.8 ± 1.3	8.7 ± 0.3 (0.991)

6.1.3 Morphology

SEM pictures taken from the cryogenic surfaces of LLDPE composites with 4 wt% BA are represented in Figure VI.1-3. The nanofiller appears quite homogeneously dispersed in the case of LLDPE-D40-4 composite, although some agglomerates are clearly recognizable. On the other hand, the silane coupling agent present on the surface of BA D40 OS nanoparticles does not seem to affect the filler dispersion in the polymer matrix (Figure VI.1-3b). As already observed by Brostow et al., although the dispersion in not affected by the surface treatment of BA nanoparticles, a better polymer–filler interaction takes place due to replacement of hydroxide surface groups of the nanoparticles with organic ones [274]. The hypothesis of an improved adhesion is consistent with the increment of the mechanical performances. In the case of LLDPE-BA40 OS nanocomposites, wetting of the particles by the polymer matrix is clearly improved by the coupling treatment, making the interface between two phases almost indistinguishable. The enhancement of the interfacial adhesion can be explained by a decrease in surface energy of the filler with silane coupling agents, that leads to a better compatibility with the apolar LLDPE matrix.

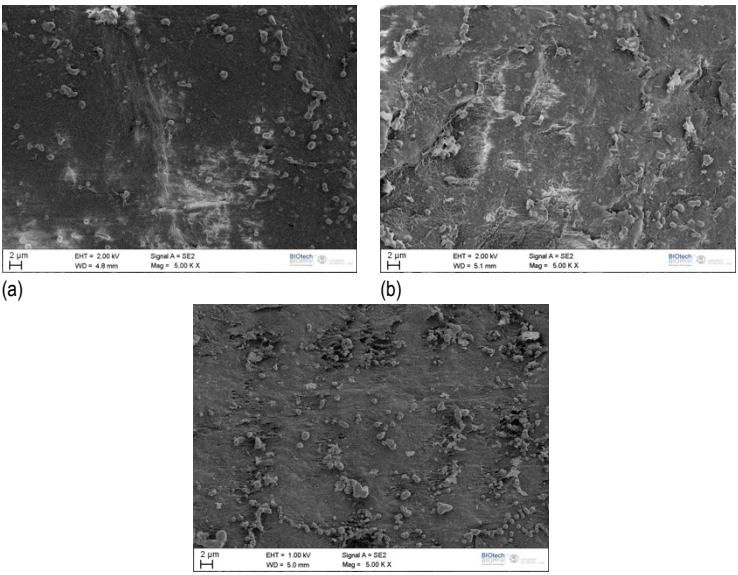

Figure VI.1-3. SEM image of the fracture surface of (a) LLDPE-D40-4, (b) LLDPE-D40 OS-4 and (c) LLDPE-D80-4.

6.2 Toughening linear low density polyethylene with halloysite nanotubes.

Part of this paragraph has been published in:

Pedrazzoli D, Pegoretti A, Thomann R, Kristóf J, Karger-Kocsis J,

"*Toughening linear low density polyethylene with halloysite nanotubes*",
Polymer Composites. (2014) In press.

Linear low density polyethylene (LLDPE) based composites were prepared through melt compounding and hot pressing using both untreated and treated halloysite nanotubes (HNT) up to filler contents of 8 wt% in order to assess the role of the filler exfoliation and surface treatment on the thermal, mechanical and rheological properties of the resulting composites.

The addition of treated nanoparticles resulted in a better dispersion of the filler within the matrix, as confirmed by observations conducted at scanning and transmission electron microscopies. A decrease in both complex viscosity and shear storage modulus was recorded for all LLDPE-HNT nanocomposites in the molten state.

Differential scanning calorimetry analysis evidenced that HNT addition produced an increase of the crystallization peak temperature, while thermogravimetric analysis showed a remarkable improvement of the thermal stability with the nanofiller content.

The addition of treated HNT nanoparticles induced better improvements in elastic modulus and tensile properties at break without significant loss in ductility. The fracture toughness, evaluated by the essential work of fracture (EWF) approach, showed remarkable improvements (up to a factor of 2) with addition of treated HNT. On the other hand, incorporation of untreated HNT produced an adverse effect on the fracture toughness when considering the nanocomposite filled with 8 wt% HNT.

Both creep tests and dynamic mechanical analyses showed an overall enhancement of the viscoelastic properties due to addition of HNT, revealing higher improvements in nanocomposites added with treated HNT.

The matrix used in this work was a Flexirene® CL10 linear low-density polyethylene (MFI at 190 °C and 2.16 kg = 2.6 g/10', Mn = 27000 g/mol[1], density = 0.918 g/cm^3), produced by Polimeri Europa S.p.A., now Versalis (Mantova, Italy) using Ziegler-Natta catalysis and butene as a comonomer (C_4-LLDPE).

Untreated HNT (uHNT) were mined from Turplu/Balikesir (Turkey) and presented an oxide composition as follows (wt/wt%): SiO_2 (46.7%), Al_2O_3 (33.1%), Fe_2O_3 (2.96%), CaO (0.37%), MgO (0.26%), Na_2O (0.12%), K_2O (0.27%), TiO_2 (0.03%). Treated HNT (tHNT) were mined from Szegilon (Hungary) and presented a different morphology and surface properties due to a chemical treatment of the initial kaolinite. The preparation of tHNT can be described as follow: intercalation with K-acetate (CH_3CO_2K) (30:70 wt% K-acetate/wt% kaolinite), drying (T=110 °C, t=24 h), treatment with ethylene glycol ($C_2H_6O_2$) (5:1 mol ethylene glycol/mol kaolinite, T=150 °C, t=4 h) and final treatment with hexamethylenetetramine ($(CH_2)_6N_4$) (5:1 mol hexamethylenetetramine/mol kaolinite, T=20 °C, t=48 h). After each step the degree of intercalation was determined by X-ray diffraction (XRD). Generally, complete delamination was achieved when the last step (treatment with hexamethylenetetramine) was repeated one more time. The excess reagents were removed from the particles' surface after each step with washing with acetone (using a G4-type filter). After the last step, excess reagent was removed by drying at 50 °C for 2 hours.

Table VI.2-1 summarizes the experimental density, Brunauer-Emett-Teller (BET) specific surface area and the diffraction pattern characteristics of the HNTs used in this work.

Table VI.2-1. Physical properties of HNTs utilized in this work.

Filler	Density [a] [g/cm]	BET surface area [b] [m^2/g]	$2\theta_{001}$ [c] [°] d_{001} [nm]	$2\theta_{020}$ [c] [°] d_{020} [nm]	$2\theta_{002}$ [c] [°] d_{002} [nm]
uHNT	2.206 ± 0.001	31.3	13.26 0.667	20.43 0.434	24.71 0.360
tHNT	1.700 ± 0.001	61.8	12.41 0.713	20.29 0.437	24.90 0.357

[a] Measurements were performed by using a Micromeritics Accupyc® 1330 helium pycnometer (T = 23 °C).

[b] Brunauer-Emett-Teller (BET) specific surface area [252].

[c] Reflection ($2\theta_{hkl}$) and basal spacing (d_{hkl}) relative to XRD analyses.

LLDPE was used as received while the fillers were dried at 80 °C for 12 h prior to use. The samples were prepared by melt compounding in a Brabender® Plasti-Corder internal mixer (T=170 °C, n=50 rpm, t=15 min) followed by compression moulding using a Collin® P200E hot press (T=170 °C, p=2 MPa, t=15 min), in order to get plane sheets with thickness of around 0.5 mm. The filler content was varied

between 0 and 8 wt%. The unfilled matrix was denoted as LLDPE, while nanocomposites were designated indicating the matrix, the filler type and the filler weight amount. For instance, a sample filled with 4 wt% of untreated HNT is indicated as LLDPE-uHNT-4.

6.2.1 *Morphology of HNT and LLDPE/HNT nanocomposites*

The morphological characteristics of uHNT and tHNT were obtained from TEM micrographs depicted in Figure VI.2-1a and Figure VI.2-1b, respectively. Firstly, it is worth mentioning that HNT mined from different sources can vary in the level of hydration, morphology (dimension of inner and outer diameter, length and aspect ratio) and colour, depending on the substitutional metals and on mineral origin [275]. uHNT was present in a high proportion of thick unexfoliated stacks, few platy particles and very short tubes. On the other hand, the effect of the exfoliation promoted by chemical treatment is observable in the case of tHNT, mainly represented by platy particles and more and longer tubular elements, with an electron-transparent central lumen. In particular, the tubular particles showed dimensions within the ranges of outer diameter 30-60 nm, inner diameter 6-20 nm and length 150 nm - 2 μm. The thickness of the HNT wall is around 5-25 nm. TEM micrographs indicate that although uHNT and tHNT show different exfoliation and dispersion, their structure and size are comparable, confirming that the two fillers can be used to investigate the solely effect of the surface treatment on the properties of LLDPE. The density values measured through helium pycnometry on the two HNTs are reported in Table VI.2-1. In particular, tHNT presents a density 23% lower with respect to uHNT, clearly indicating an higher degree of exfoliation and dispersion of the tHNT particles due to chemical treatment, as confirmed by TEM observations.

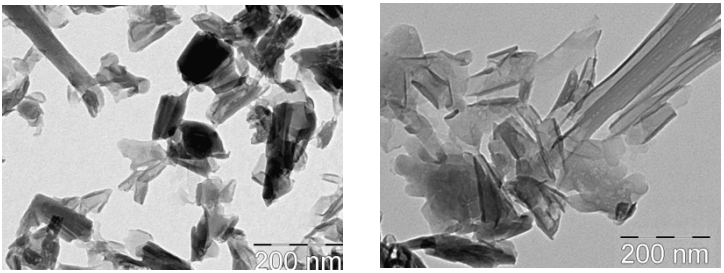

(a) (b)

Figure VI.2-1. TEM micrographs of (a) uHNT and (b) tHNT.

Cryocut surfaces of composites were examined through SEM and TEM analysis. In particular, SEM pictures taken from the cryocut surfaces of LLDPE composites with 4 wt% and 8 wt% tHNT are represented in Figure VI.2-2a-b. It is evident from the SEM microphotographs of LLDPE-tHNT that the nanotubes are finely and homogeneously dispersed within the matrix even at 8 wt % filler loading. The poor dispersion of uHNT in form of numerous and big agglomerates are clearly observable also by naked eye. For this reason, the SEM and TEM micrographs of LLDPE-uHNT composites are not reported.

TEM pictures confirm that the designation nanocomposite is correctly used (Figure VI.2-3a-b) in the case of LLDPE-tHNT composites. Both SEM and TEM morphological analysis confirm that tHNT can be finely dispersed within the LLDPE matrix even at high filler contents and without using polymeric compatibilizer, while uHNT tends to form micrometric aggregates and agglomerates producing negative effects on the mechanical properties.

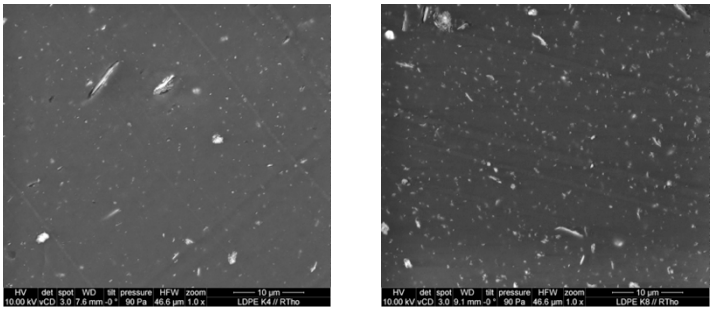

(a) (b)

Figure VI.2-2. SEM images of (a) LLDPE-tHNT-4 and (b) LLDPE-tHNT-8.

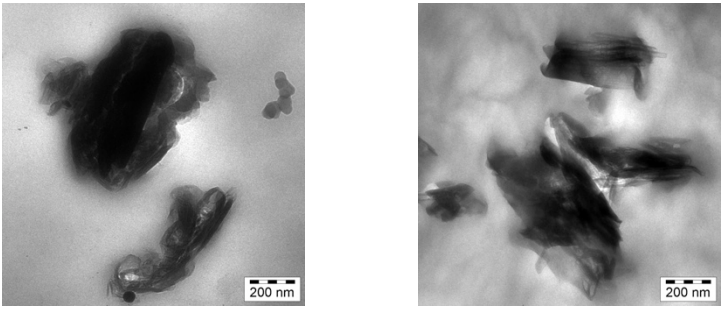

(a) (b)

Figure VI.2-3. TEM micrographs of the cryocut surfaces of (a) LLDPE-tHNT-4 and (b) LLDPE-tHNT-8 nanocomposites.

6.2.2 Thermal degradation behavior

The thermal resistance parameters as detected in TGA measurements are reported in Table VI.2-2. When considering LLDPE-HNT nanocomposites, both $T_{d,onset}$ and $T_{d,max}$ markedly increase with the filler content, showing a slightly higher efficiency in LLDPE-tHNT samples. Improved thermal stability due to the addition of HNT has been already reported for PA6 [276] and PP [277] nanocomposites.
Interestingly, the char content recorded for LLDPE nanocomposites is markedly lower than the added amount of filler, indicating that the filler experienced weight loss during heating. This is probably due to the release of crystal water in the range between 430 and 570 °C [278]. In particular, the lower char content observed in tHNT with respect to uHNT can be attributed to two main causes: the degradation and further loss of the functional groups derived from the chemical treatment of tHNT and the possible higher content of crystal water in tHNT.

Table VI.2-2. TGA parameters of LLDPE and relative nanocomposites.

Sample	$T_{d,\ onset}$ [°C]	$T_{d,\ max}$ [°C]	MMLR [mg / °C]	Char [%]
LLDPE	457.0	477.1	0.195	0.3
LLDPE-uHNT-1	458.9	478.0	0.221	0.6
LLDPE-uHNT-4	461.5	478.2	0.243	2.6
LLDPE-uHNT-8	465.3	480.4	0.293	5.7
LLDPE-tHNT-1	458.5	480.8	0.236	0.4
LLDPE-tHNT-4	461.7	482.2	0.272	1.8
LLDPE-tHNT-8	465.7	484.2	0.308	5.0
uHNT	/	/	/	74.7
tHNT	/	/	/	57.9

$T_{d,\ onset}$: Onset degradation temperature.
$T_{d,max}$: Maximum degradation rate temperature.
MMLR : Maximum mass loss rate.
Char [%] : Residual weight percentage.

Exposing the specimen to elevated temperatures may induce filler aggregates to agglomerate on the surface of the molten polymer, thus creating a barrier that physically protects the rest of the polymer and hinders the volatilization of the oligomers generated during the combustion process [21]. Thus, in general, the

higher the filler amount the lower the maximum mass loss rate (MMLR). However, this is not the case, as an higher content of HNT is associated to a greater MMLR (Table VI.2-2). In fact, the filler weight loss increases with the HNT content and this effect is probably preponderant on the MMLR decrease due to creation of physical barrier by filler aggregates.

6.2.3 Tensile mechanical properties of LLDPE/HNT nanocomposites

The incorporation of HNT nanoparticles produces a significant increase of the elastic modulus of the LLDPE matrix, showing a higher efficiency in the case of tHNT (Figure VI.2-4). In particular, an improvement of 94% is reached for systems filled with 8 wt% of tHNT, compared to unfilled LLDPE.

A recent approach, developed by Dorigato et al. [279], was adopted in order to model the elastic properties of LLDPE-HNT nanocomposites, taking into account the stiffening effect provided by nanoparticles composed of primary aggregates and agglomerates (see Section 10.1.1). In order to implement the model, the Poisson's ratio of matrix and filler were chosen as 0.44 and 0.22, respectively, while the elastic modulus of filler was set to 300 GPa in according to literature data [280, 281]. The relative elastic modulus of the LLDPE-HNT composites is plotted in Figure VI.2-4 as a function of the filler volume fraction, along with the fitting curves obtained with the adopted model.

Table VI.2-3. Quasi-static and impact tensile properties.

Sample	Tensile modulus [MPa]	Tensile Yield Strength [MPa]	Elongation at Break [%]	TEB [a] [J/m³]
LLDPE	200 ± 6	11.7 ± 0.2	1390 ± 91	18.9 ± 2.3
LLDPE-uHNT-1	216 ± 13	11.2 ± 0.8	1085 ± 58	18.0 ± 1.6
LLDPE-uHNT-4	248 ± 17	10.8 ± 0.4	851 ± 74	15.2 ± 3.2
LLDPE-uHNT-8	322 ± 5	11.6 ± 0.4	713 ± 26	14.4 ± 0.5
LLDPE-tHNT-1	220 ± 16	12.8 ± 0.2	1157 ± 66	19.4 ± 2.7
LLDPE-tHNT-4	284 ± 24	13.8 ± 0.3	1001 ± 19	19.3 ± 2.0
LLDPE-tHNT-8	388 ± 46	12.6 ± 0.3	1017 ± 45	18.7 ± 1.3

[a] Tensile energy to break measured during tensile impact test.

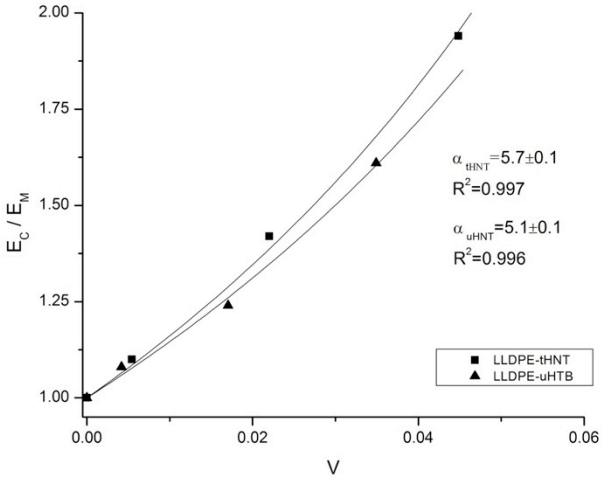

Figure VI.2-4. Relative elastic modulus of LLDPE-HNT nanocomposites as a function of the filler volume content, with fitting of experimental data in according to the model proposed by Dorigato et al. [57] (continuous line). Note that the error bars of data are not represented for sake of clarity.

It can be noticed that the proposed model can model very well the elastic modulus of LLDPE-tHNT-x and LLDPE-uHNT-x composites over the whole range of filler concentration. Furthermore, the significant increase of the elastic modulus detected for nanocomposites is associated to elevated α values, which indicates the fraction of matrix constrained by nanoparticles [279]. As already noticed by Dorigato et al. when applying the model in the case of LLDPE filled with fumed silica nanoparticles, there exists an apparent correlation between the α parameter and filler surface area [273] (Figure VI.2-4 and Table VI.2-1). Specifically, tHNT possesses greater surface area than uHNT due to higher exfoliation, indicating higher capability of being intercalated by polymer matrix during compounding, with a consequent greater fraction of matrix constrained by nanoparticles' agglomerates.

The yield stress decreases with the filler content in the case of LLDPE-uHNT nanocomposites, probably because of extensive filler aggregation [255] (Table VI.2-3). On the other hand, the yield stress appears slightly higher in LLDPE-tHNT composites with respect to LLDPE, while elongation at break moderately decrease, showing a stiffening effect which only slightly reduces the matrix ductility up to a filler content of 8 wt%.

6.2.4 Fracture toughness and impact strength

The EWF method was applied to characterize the fracture behavior. At first, the basic preconditions necessary for the application of the EWF methodology were verified [122]. In particular, the validity criterion verifies that all tests were conducted under plane-stress state. Furthermore, all the specimens exhibited delayed yielding (i.e. ligament yielding is time-dependent and finishes when the crack has already started propagating). However, a relatively brittle behavior is exhibited for the LLDPE-uHNT-8 nanocomposite DEN-T specimen (Figure VI.2-5). The force–displacement curve shows that after yielding, the specimen fails abruptly, showing no stable crack propagation phase. On the other hand, the LLDPE-tHNT-8 nanocomposite DEN-T specimen manifests ductile fracture after yielding. As already observed by Mouzakis et al. when investigating the fracture toughness in both syndiotactic and isotactic PP modified with multiwall carbon nanotubes, the ideal necking-yielding-stable neck tearing sequence, is usually desired for the application of the EWF approach in DEN-T specimens [14].

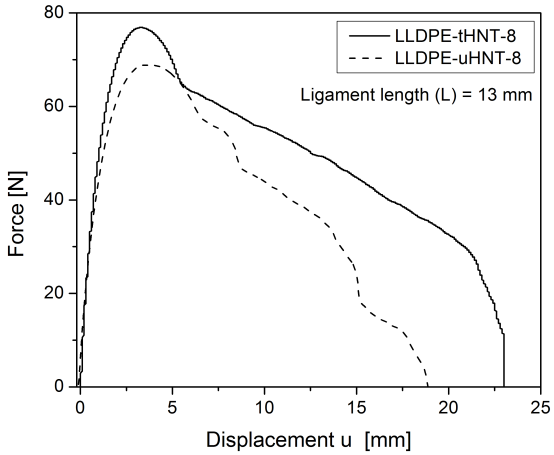

Figure VI.2-5. Typical force-displacement curves recorded for DEN-T specimens of LLDPE-tHNT-8 and LLDPE-uHNT-8 during the EWF tests.

In particular, in all LLDPE-tHNT nanocomposites, the area under the curve after the maximum force was reached is higher than that prior to maximum force, indicating slow crack propagation with high energy absorption, typical of ductile materials [121] (Figure VI.2-6A). This is a clear indication that the addition of tHNT improves the strength of LLDPE without embrittlement of the material.

The elliptical shape of the stress-whitened zone (characterized by the shape factor β) formed during tensile EWF test performed on LLDPE nanocomposites was similar to that of neat LLDPE with slight variation in the height of the zone. The total specific EWF, the specific EWF at yielding and the specific EWF for necking were obtained by linear fits and tabulated in Table VI.2-4. A huge improvement (up to a factor of 2) in w_e is noticed as the tHNT content increases, whereas βw_p values slightly decrease upon filler addition. These results indicate that tHNT addition significantly toughened the matrix [121]. Moreover, partitioned components of total EWF, such as EWF for yielding ($w_{e,y}$) and EWF for necking ($w_{e,n}$), also show an improvement in all nanocomposites when compared to unfilled LLDPE. In particular, the improvement in $w_{e,y}$ is probably due to the higher yield stress recorded for nanocomposites with respect to LLDPE, while the change in $w_{e,n}$ might be because of changes in the crack propagation behavior in the nanocomposites [282].

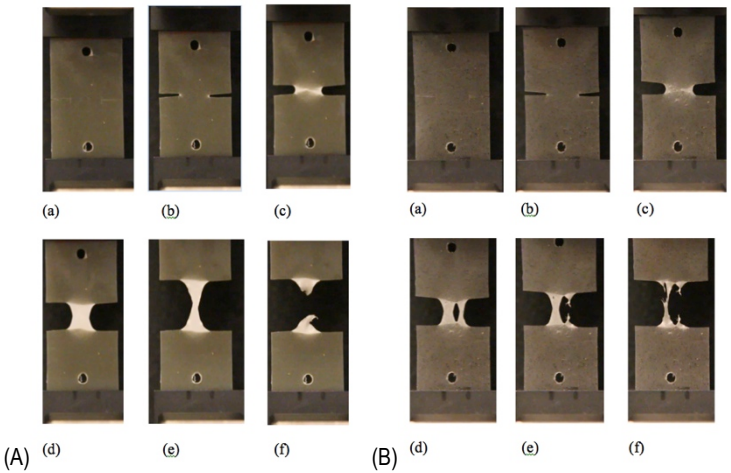

Figure VI.2-6. Serial photographs taken from the DEN-T specimens of the nanocomposites (A) LLDPE-tHNT-8 and (B) LLDPE-uHNT-8 during the EWF tests at different times (L = 13 mm).

On the other hand, LLDPE-uHNT composites show higher w_e only at 1 and 4 wt% concentrations, while the sample LLDPE-uHNT-8 manifests lower toughness properties, showing smaller w_e than unfilled LLDPE. Furthermore, the component $w_{e,y}$ is very high, while $w_{e,n}$ appears quite low compared to other nanocomposites. This indicates that most of the deformation energy is spent for yielding, while very low energy contributes to necking. Moreover, the b factor appears lower than that of the other LLDPE-uHNT samples, indicating a clear reduction in the height of the deformation zone. Although the related specimens exhibit delayed yielding, the

plastic deformation zone, formed by crazing, is highly constrained. The latter yields restricted necking during the subsequent deformation (Figure VI.2-6B). This behavior clearly indicates that the addition of uHNT at 8 wt% is associated with reinforcing effect and parallel to that with a prominent loss in ductility. This feature is in accordance with the results of the quasi-static tensile tests.

Table VI.2-4. Specific EWF properties of LLDPE and relative nanocomposites.

Sample	w_e [kJ / m²]	βw_p [MJ / m³]	β	$w_{e,y}$ [kJ / m²]	$\beta' w_{p,y}$ [MJ / m³]	$w_{e,n}$ [kJ / m²]	$\beta'' w_{p,n}$ [MJ / m³]
LLDPE	26.7 ± 3.6	12.7 ± 0.4 (0.983)	0.32 ± 0.04	2.7 ± 0.3	2.8 ± 0.1 (0.997)	24.2 ± 3.6	9.9 ± 0.4 (0.992)
LLDPE-uHNT-1	29.4 ± 3.4	12.0 ± 0.4 (0.984)	0.31 ± 0.03	3.3 ± 0.5	2.7 ± 0.1 (0.994)	26.1 ± 3.4	9.3 ± 0.4 (0.989)
LLDPE-uHNT-4	38.1 ± 1.9	8.7 ± 0.2 (0.990)	0.30 ± 0.04	6.6 ± 0.5	2.2 ± 0.1 (0.990)	31.5 ± 2.0	6.5 ± 0.2 (0.991)
LLDPE-uHNT-8	21.8 ± 2.3	12.2 ± 0.3 (0.992)	0.26 ± 0.05	8.8 ± 0.5	2.1 ± 0.1 (0.983)	13.0 ± 2.4	10.1 ± 0.3 (0.988)
LLDPE-tHNT-1	29.0 ± 3.0	12.9 ± 0.3 (0.988)	0.29 ± 0.06	3.7 ± 0.5	2.2 ± 0.1 (0.986)	25.3 ± 3.0	10.7 ± 0.3 (0.990)
LLDPE-tHNT-4	40.4 ± 3.0	10.9 ± 0.3 (0.984)	0.25 ± 0.05	6.4 ± 0.7	1.8 ± 0.1 (0.964)	34.0 ± 3.1	9.1 ± 0.3 (0.991)
LLDPE-tHNT-8	55.0 ± 1.3	6.4 ± 0.2 (0.992)	0.26 ± 0.03	6.5 ± 0.4	1.6 ± 0.1 (0.986)	48.5 ± 1.4	4.8 ± 0.2 (0.988)

When the load is applied at high strain rates such as under impact conditions, the introduction of tHNT nanoparticles leads to an increase of the energy adsorbed at break (TEB) (Table VI.2-4). On the other hand, the addition of uHNT produces a slight decrease in TEB, proportional to the filler content. This is most likely due to extensive filler agglomeration and poor matrix/filler interfacial interaction. The enhancement in impact strength, found for LLDPE-tHNT specimens, can be ascribed to the beneficial effects of the well dispersed tHNT nanotubes. The better dispersion tHNT (based on SEM and TEM investigations) and the surface treatment (leading to better interfacial interaction) are further factors, which may be responsible for the observed improvement found for LLDPE-tHNT compared to LLDPE-uHNT nanocomposites.

6.3 Mechanical and rheological response of polypropylene/boehmite nanocomposites

Part of this paragraph has been published in:

Pedrazzoli D, Tuba F, Khumalo V.M, Pegoretti A, Karger-Kocsis J,

"*Mechanical and rheological response of polypropylene/boehmite nanocomposites*",
Journal of reinforced plastics and composites, 33. (2014) 252-265.

In this work the influence of synthetic boehmite alumina (BA) nanoparticles with various surface treatments on the morphology, crystallization behavior and mechanical properties of polypropylene copolymer (PP) nanocomposites was studied. In particular, a series of PP/BA nanocomposites, containing up to 10 wt% of untreated and of octylsilane-functionalized BA nanoparticles, were prepared by melt compounding and film blowing. A third type of composites was produced by incorporation of BA nanoparticles treated with benzene-sulfonic-acid.

Scanning electron microscopy indicated that BA nanoparticles were finely and uniformly dispersed, though agglomerated, in the PP nanocomposites. Surface treated BA nanoparticles were better dispersed in the matrix than untreated ones. BA nanoparticles acted as a weak nucleating agents because they slightly increased the crystallization temperature. The melt viscosity of nanocomposites remained unaltered or decreased by nanofiller incorporation at low contents (2.5 and 5 wt%), while it slightly increased at higher contents contents (10 wt%), indicating a possible percolation limit for the system.

Uniaxial tensile tests indicated that the nanoparticles can induce a remarkable stiffening effect even at a rather low filler content, especially in the case of surface treated particles. Also the tensile creep compliance was significantly reduced by nanofiller incorporation. For all nanocomposites both storage and loss modulus were enhanced in the investigated temperature range, as shown by dynamic-mechanical thermal analysis.

The plane stress fracture toughness of the material, evaluated by the essential work of fracture approach, showed a significative improvement due to BA incorporation, with an optimal effect for a filler concentration of about 2.5 wt%.

A polypropylene impact copolymer (MFI at 230°C and 2.16 kg = 1.5 g/10min, density = 0.905 g/cm^3) with grade CHR 440 was provided by Sasol South Africa (Sasolburg, South Africa). As nanofiller synthetic Disperal®80 boehmite of Sasol GmbH (Hamburg, Germany) has been used. Boehmite was used in pristine (BA80), and in surface treated forms. The latter occurred by octylsilane (BA80-OS) and by C10–C13 alkylbenzene sulphonic acid (BA80-OS2), respectively. BA was incorporated in 2.5, 5 and 10 wt%. BA80 nanoparticles were characterized by a crystallite size of 74.4 nm, mean particle size of 80 μm (as measured on the powder), and BET surface area of 88.0 m^2/g.

Samples were prepared by melt mixing using a Berstorff co-rotating twin-screw extruder (ZE-40, Berstorff, Hannover, Germany) followed by granulation. The barrel temperatures from the hoper to die were 185, 195, 205, 220 °C, the screw rotated at 100 rpm and the melt passed through the extruder in ca. 80 s. The materials were successively blow molded (Scientific laboratory extruder-film blowing machine, 25 mm extruder type, model LE25-30/CV) in order to produce film sheets with a thickness of about 0.05 mm. The barrel temperatures from the hoper to die were 180, 185, 190, 195, 200 °C, the screw rotated at 65 rpm and the pressure was 21 MPa. The die temperatures were 200, 210, 220 °C. The rolling speed of nip rollers and pulling rollers was 3.1 and 3.8 m·min-1, respectively, while the blower pressure was set to 0.4 MPa.

All specimens necessary for the mechanical tests were cut out from the films along the machine direction. Neat matrix was denoted as PP, while nanocomposites were designated indicating the matrix and the amount and type of filler. For instance, a sample filled with 2.5 wt% of BA80-OS nanoparticles was indicated as PP/2.5BA80-OS.

6.3.1 Morphology

SEM micrographs of PP containing the same amount (2.5 wt%) of BA80, BA80-OS and BA80-OS2 nanoparticles, are reported in Figure VI.3-1. Also in absence of a surface treatment, the shear forces developing in the melt compounder seem to be enough to achieve a quite good deagglomeration and a uniform dispersion of BA nanoparticles. In fact, nanofiller appears quite well dispersed in PP/2.5BA80 nanocomposite, although some aggregates and agglomerates are recognizable. The dispersed nanoboehmites are organized in agglomerates with average sizes of 400–500 nm composed of the much smaller crystallites (Figure VI.3-1a). Moreover, some larger humps and cavities are visible on the fracture surface which can be traced to the rubber (ethylene-propylene) phase of the PP copolymer used.

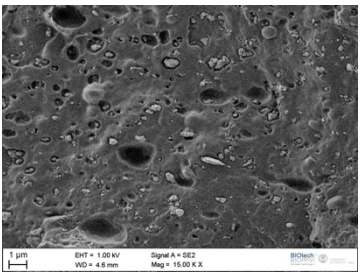

(a)

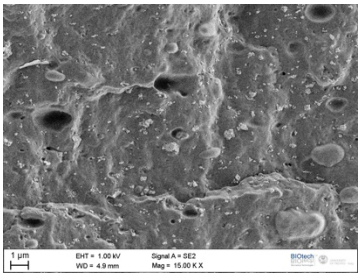

(b)

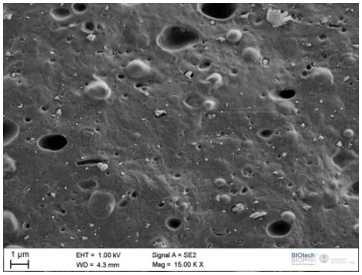

(c)

Figure VI.3-1. ESEM images of the fracture surface of (a) PP/2.5BA80, (b) PP/2.5BA80-OS and (c) PP/2.5BA80-OS2 nanocomposites.

On the other hand, the silane coupling agent present on the surface of BA80-OS nanoparticles slightly improves the filler dispersion in the polymer matrix (Figure VI.3-1b), leading to the presence of smaller and more uniformly distributed BA aggregates. Furthermore, a better polymer–filler adhesion takes place due to replacement of hydroxide groups on the surface of nanoparticles with organic groups [274], showing much less cavities due to detachment of aggregate and agglomerates. A similar filler dispersion is recognizable in the case of BA nanoparticles surface treated with benzene-sulfonic acid (carrying apolar tails), probably because of the higher hydrophobicity of the BA which indicates a lower tendency to filler aggregation (Figure VI.3-1c) [283].

6.3.2 Thermal degradation behavior

The thermal stability parameters as detected by TGA measurements are reported in Table VI.3-1. When considering PP-BA nanocomposites, both $T_{d,onset}$ and $T_{d,max}$ increase with the filler content.

Table VI-3.1. TGA parameters on unfilled PP and relative nanocomposites.

Sample	$T_{d,\ onset}$ [°C]	$T_{d,\ max}$ [°C]	Char [%]
PP	441.2	461.8	0.25
PP/2.5BA80	441.6	462.9	2.86
PP/5BA80	445.2	466.1	4.79
PP/10BA80	449.0	468.8	9.82
PP/2.5BA80-OS	442.5	463.1	2.90
PP/5BA80-OS	446.1	466.3	4.84
PP/10BA80-OS	449.3	468.7	9.93
PP/2.5BA80-OS2	442.4	462.8	2.96

$T_{d,\ onset}$: Onset degradation temperature.
$T_{d,max}$: Maximum degradation rate temperature.
Char [%] : Residual weight percentage.

This could also be mainly attributed to the dehydration process of BA nanofiller which delays the polymer degradation [284]. The char content at 700 °C is also shown in Table VI.3-1 for all the samples. In one of our previous work we observed a remarkable improvement in thermal resistance parameters with the incorporation of BA in LLDPE matrix, noticing a slight dependence on the BA crystallite size [285].

6.3.3 Tensile mechanical properties of PP/BA nanocomposites

The tensile modulus of PP improved with the BA content, showing an improvement of about 46% for systems filled with 10 wt% of BA80-OS (see Table VI.3-2). Moreover, both surface treated BA nanoparticles seem to have a better efficiency in increasing the stiffness of PP with respect to untreated BA. In general, yield stress slightly decreases with the addition of untreated BA, probably due to filler agglomeration [274]. Filler agglomeration is also supposed to be responsible for the decrease in the elongation at break of nanocomposites with respect to the neat matrix, showing the behavior often reported for polymer nanocomposites filled with inorganic fillers. It is worthwhile to note that the stress at yield and strain at break values of PP/BA80-OS nanocomposites are higher than those of PP/BA80 at the same filler weight content. These results suggest that the utilization of surface treated BA is essential to achieve higher strength and stiffness at low nanofiller concentrations.

Table VI.3-2. Quasi-static tensile properties at yield and at break of unfilled PP and relative nanocomposites.

Sample	Tensile modulus [MPa]	Tensile Yield Strength [MPa]	Elongation at break [%]
PP	1426 ± 19	25.2 ± 0.7	711 ± 32
PP/2.5BA80	1614 ± 63	23.9 ± 0.6	601 ± 32
PP/5BA80	1646 ± 39	23.8 ± 0.7	490 ± 81
PP/10BA80	1984 ± 69	17.2 ± 0.5	13 ± 1
PP/2.5BA80-OS	1671 ± 45	28.0 ± 1.4	641 ± 41
PP/5BA80-OS	1712 ± 49	25.2 ± 0.4	600 ± 66
PP/10BA80-OS	2090 ± 23	20.9 ± 0.5	30 ± 2
PP/2.5BA80-OS2	1644 ± 62	22.0 ± 0.3	31 ± 4

Furthermore, the sample PP/2.5BA80-OS2 shows lower ultimate tensile properties with respect to PP/2.5BA80 and PP/2.5BA80-OS samples. Although an increase was expected as a result of smaller agglomerations, which could act as stress concentrators of failure points, however, this was not the case. In particular, the remarkable decrease in the elongation at break might be attributed to the rigidity of the benzene group present on the filler surface and characterizing the polymer-matrix interface.

6.3.4 Fracture toughness

During the facture studies, the correlation coefficients (R^2) of EWF tests varied between 0.96 and 0.99, while the standard deviation values scattered between 3 and 6.5 kJ/m^2, for all samples. Based on previous studies of Williams and Rink [122], and Tuba et al. [286], these results are adequate for an accurate application of the EWF approach. A minimum sample size (N) of 25 ensured the accuracy of the measurements.

The specific essential work of fracture (w_e) of PP increases after the incorporation of boehmite alumina (Figure VI.3-2). This reinforcing effect can be mainly attributed to the nanofiller incorporation. Nevertheless, an increasing filler content induces a reduction of w_e values (Table VI.3-3), which is a general observation for “over-filled” nanocomposites and can be attributed to the agglomeration of nanoparticles.

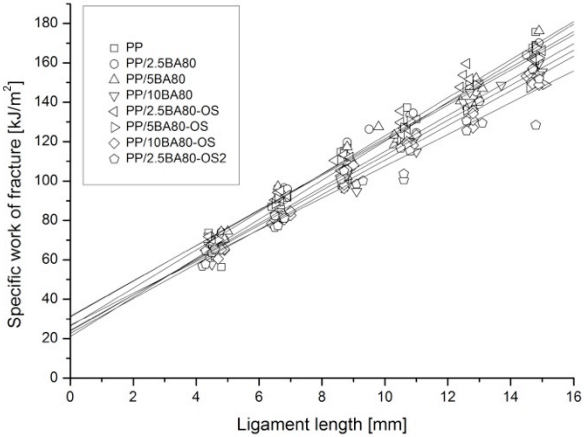

Figure VI.3-2. Specific work of fracture vs. ligament length plots for neat PP and relative nanocomposites.

Although the OS treatment results in increasing yield stress at low filler content, the w_e term does not increase further, and what is even more interesting, it decreases. This observation is in good agreement with the observation of Arkhireyeva and Hashemi [287] regarding the direct proportion between w_e and $e_0 \cdot \sigma_y$, where e_0 is the ordinate intercept of extension at break (DENT specimens) versus ligament length linear regression plots. The nanocomposites have smaller plastic work of fracture, βw_p, compared to the neat PP material. The increasing filler content also results in decreasing βw_p values. However, the w_p terms of the examined nanocomposites, except that of PP/2.5BA80 composite, do not differ significantly (p=0.05), thus the dissipative plastic work was not influenced by the nanofillers.

Table VI.3-3. Specific EWF parameters of PP and relative nanocomposites (for w_e and bw_p the 95% confidence limits are indicated).

Sample	w_e [kJ/m^2]	βw_p [MJ/m^3]	β [-]	w_p [MJ/m^3]	e_0 [mm]	R^2 [-]	N [-]
PP	21.1 ± 7.3	9.9 ± 0.7	0.332 ± 0.047	33.1 ± 5.8	1.48	0.970	27
PP/2.5BA80	31.1 ± 7.8	9.0 ± 0.8	0.275 ± 0.067	44.9 ± 12.3	1.88	0.963	25
PP/5BA80	31.5 ± 6.8	8.9 ± 0.7	0.310 ± 0.034	30.7 ± 4.5	2.25	0.969	25
PP/10BA80	24.4 ± 5.3	8.9 ± 0.5	0.286 ± 0.033	33.3 ± 4.9	1.49	0.981	26
PP/2.5BA80-OS	26.3 ± 5.8	9.7 ± 0.6	0.304 ± 0.044	35.3 ± 6.1	1.78	0.979	26
PP/5BA80-OS	23.8 ± 7.7	9.1 ± 0.7	0.302 ± 0.041	33.3 ± 5.7	1.54	0.966	25
PP/10BA80-OS	22.7 ± 3.9	8.8 ± 0.4	0.304 ± 0.030	30.3 ± 3.6	1.60	0.989	27
PP/2.5BA80-OS2	24.1 ± 6.7	8.5 ± 0.7	0.321 ± 0.060	31.7 ± 7.0	1.60	0.967	24

6.4 Viscoelastic behavior and tear resistance of polypropylene reinforced with synthetic boehmite alumina nanoparticles

Part of this paragraph has been published in:

Pedrazzoli D, Khumalo V. M, Karger-Kocsis J, Pegoretti A,

"Thermal, viscoelastic and mechanical behaviors of polypropylene with synthetic boehmite alumina nanoparticles",
Polymer Testing, 35. (2014) 92-100.

In this paper the effect of nanofiller concentration and surface treatment on the morphology and viscoelastic behavior of polypropylene copolymer (PP)/boehmite alumina (BA) nanocomposites was investigated. Both untreated and BA particles treated with octylsilane (OS) and with sulfonic acid (OS2) were used to produce nanocomposite samples through melt mixing and following film blow molding. The morphology, as analyzed by scanning electron microscopy (SEM), showed that BA nanoparticles can be finely dispersed in PP up to 10 wt%, even when no surface functionalization is applied on the filler.

Differential scanning calorimetry and wide-angle X-ray scattering were adopted to detect changes in the crystalline structure of PP. BA acted as weak nucleation agent in PP matrix. Thermogravimetric analyses put in evidence a substantial enhancement of the degradation properties due to nanomodification.

The mechanical properties, studied through quasi-static tensile tests, dynamic mechanical analyses and creep measurements showed that tensile modulus and yield strength increased in PP/BA composites, together with an enhancement of both storage and loss modulus and creep resistance. On the other hand, PP/BA-OS systems showed lower tensile modulus but greater ductility due to nanofiller addition, while PP/BA-OS2 composites exhibited a noticeable loss in ductility because of greater interaction between matrix and particles.

Elmendorp-type tearing tests highlighted a remarkable improvement in the propagation tear resistance in the case PP/BA-OS composites due to microvoids formation, whereas a slight decrease in tearing capability was recorded for PP/BA and PP/BA-OS2 systems.

A polypropylene impact copolymer (MFI at 230°C and 2.16 kg = 1.5 g/10min, density = 0.905 g/cm^3) with grade CHR 440 was provided by Sasol South Africa (Sasolburg, South Africa). Synthetic boehmite Disperal® 40, provided by Sasol GmbH (Hamburg, Germany), was used as nanofiller in pristine (BA40) and in surface treated forms. Surface functionalization occurred by octylsilane (BA40-OS) and by C10–C13 alkylbenzene sulphonic acid (BA40-OS2), respectively. The nominal primary crystallite size of the pristine form is 40 nm, while the specific surface area is 105 m^2/g^1 [108]. BA was incorporated in 2.5, 5 and 10 wt%.

Samples were prepared by melt mixing using a Berstorff co-rotating twin-screw extruder (ZE-40, Berstorff, Hannover, Germany) followed by granulation. The barrel temperatures from the hoper to die were 185, 185, 195, 195, 205, 205, 220, 220 °C, the screw rotated at 100 rpm and the melt passed through the extruder in ca. 80 s. The granules were successively blow moulded (Scientific laboratory extruder-film blowing machine, 25 mm extruder type, model LE25-30/CV) in order to produce film sheets with thickness of around 0.6 mm. The barrel temperatures from the hoper to die were 180, 185, 190, 195, 200 °C, the screw rotated at 65 rpm and the pressure was 21 MPa. The die temperatures were 200, 210, 220 °C. The rolling speed of nip rollers and pulling rollers was 3.1 and 3.8 m/min, respectively, while the blower pressure was set to 0.4 MPa. The specimens used for the dynamic mechanical thermal analyses were cut out from the blow-molded sheets along the machine direction. On the other hand, the specimens necessary for the Elmendorf tear test were obtained along both machine and transverse direction.

Bulk specimens, necessary for the quasi-static tensile tests, were produced by compression moulding of the granules using a P.H.I hydraulic press (Pasadena Hydraulics Inc, La Puente, USA) in order to produce square sheets with thickness of 4.2 mm. The material was heat up to 190 °C while applying a pressure of 25 MPa for 15 min and then cooled to room temperature by water flow. The unfilled matrix was denoted as PP, while nanocomposites were designated indicating the matrix, the filler weight amount and the filler type. For instance, a sample filled with 5 wt% of pristine BA is indicated as PP/5BA40.

Propagation tear tests were performed using an Elmendorf-type tearing tester ED30 (Ceast®, Torino, Italy) on film specimens (thickness of 0.6 mm) following the standard ASTM D1922. The tests were carried out on at least five specimens for each direction, assuming that the specimens were cut out from the blow molded films along the machine and transverse direction. The propagation tear resistance was measured as the ratio of force (mN) required to propagate tearing across the specimen with respect to the specimen thickness (mm). The force reading was corrected by a multiplication factor of 0.10197 in order to be converted in g/mm^1.

6.4.1 Morphology

The morphology of nanocomposites, as examined by means of SEM analyses, can be observed in Figure VI.4-1(a-b) for PP containing the same amount (5 wt%) of BA40 and BA40-OS nanoparticles. The nanofiller appears quite well dispersed in PP nanocomposite modified with untreated BA particles, although some aggregates and agglomerates with average sizes of 300 – 400 nm are recognizable. The compounding process seems to be effective even in the case of untreated particles, resulting in a good deagglomerating the BA nanoparticles and rather uniform dispersion. Furthermore, some cavities are observable on the fracture surface which can be attributed to the rubber (ethylene-propylene) phase of the PP copolymer (Figure VI.4-1a). On the other hand, the filler dispersion within the polymer matrix is only slightly improved by surface functionalization with silane coupling agent. In fact, nanofiller appear organized in smaller and more uniformly distributed BA aggregates (Figure VI.4-1b). BA nanoparticles remain finely dispersed also when higher amounts are added. In fact, a rather good filler dispersion is recognizable in the case of PP containing 10 wt% of BA40-OS nanoparticles (Figure VI.4-1c), showing particles with submicrometer mean size.

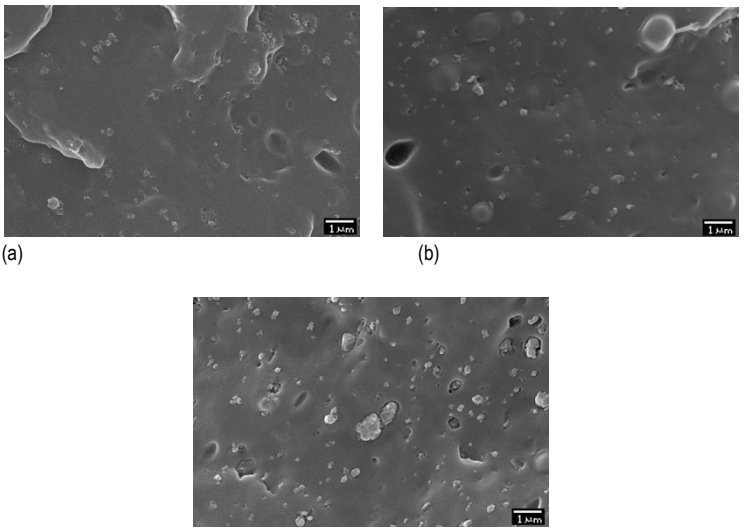

(a) (b)

(c)

Figure VI.4-1. ESEM images of the fracture surface of (a) PP/5BA40, (b) PP/5BA40-OS and (c) PP/10BA40-OS nanocomposites.

6.4.2 Thermal degradation behavior

The thermal resistance parameters, as detected by TGA measurements, are reported in Table VI.4-1. Both $T_{2wt\%\ loss}$ and $T_{10wt\%\ loss}$ noticeably increase with the filler content in all PP/BA nanocomposites, showing a slightly higher efficiency in PP/BA40-OS2 samples. This effect could also be mainly attributed to the dehydration process of BA nanofiller which delays the polymer degradation. Indeed, TGA analyses conducted on the fillers BA40 and BA40-OS alone show a comparable residue value slightly above 80%, probably indicating the loss of crystal water. On the other hand, the residue value recorded for the filler BA40-OS2 appears relatively lower (i.e. 63.7%), likely due to the loss of part of the organic surface treatment. Representative TGA traces are depicted in Figure VI.4-2 for PP and PP/BA40 nanocomposites. Improved thermal and thermo-oxidative stability due to the addition of BA has been already reported for polyethylenes (PEs) [108], polypropylene (PP) [288, 289] and linear low density polyethylene [290]. Nevertheless, further research is required in order to clarify the mechanism of improvement of thermal and thermo-oxidative stability in thermoplastics by BA incorporation.

Table VI.4-1. TGA parameters on PP and relative nanocomposites.

Sample	$T_{2wt\%\ loss}$ [°C]	$T_{10wt\%\ loss}$ [°C]	Residue [%]
PP	382.6	430.0	0.25
PP/2.5BA40	383.5	431.7	2.91
PP/5BA40	388.7	437.2	4.36
PP/10BA40	393.4	442.6	9.51
PP/2.5BA40-OS	384.6	432.8	2.74
PP/5BA40-OS	388.5	437.6	4.58
PP/10BA40-OS	395.1	445.7	9.84
PP/2.5BA40-OS2	383.6	431.9	2.82
PP/5BA40-OS2	388.1	438.0	4.32
PP/10BA40-OS2	394.0	443.2	9.87
BA40 (*)	/	/	81.32
BA40-OS (*)	/	/	83.45
BA40-OS2 (*)	/	/	63.68

$T_{2wt\%\ loss}$: Temperature associated with a weight loss of 2 %.

$T_{10wt\%\ loss}$: Temperature associated with a weight loss of 10 %.

(*) Sample in form of nanopowder.

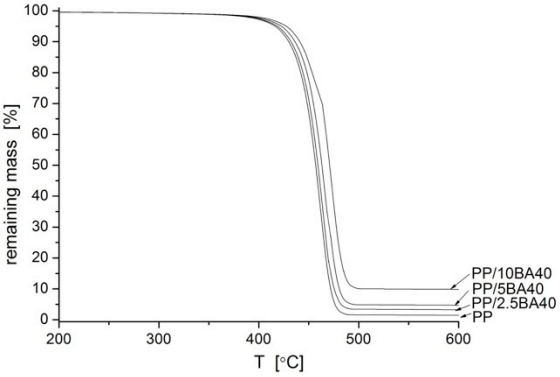

Figure VI.4-2. Remaining mass with respect to the temperature during TGA analysis performed on PP and PP/BA40 nanocomposites with different filler contents.

6.4.3 Tensile mechanical behavior

The addition of BA40 nanoparticles produces a significant increase of the elastic modulus *(E)* of the PP matrix, reaching an improvement of 15 % for systems filled with 10 wt% of nanofiller, compared to unfilled PP (Table VI.4-2).

Table VI.4-2. Quasi-static tensile properties and tear resistance of PP nanocomposites.

Sample	E [MPa]	σ_y [MPa]	ε_b [%]	Tear [g/mm]	
				M.D.(*)	T.D. (**)
PP	901 ± 9	28.5 ± 0.4	127 ± 11	21.5 ± 0.9	24.1 ± 0.8
PP/2.5BA40	987 ± 15	30.2 ± 0.2	168 ± 18	16.5 ± 0.5	27.6 ± 3.5
PP/5BA40	1020 ± 32	30.4 ± 0.5	153 ± 18	15.8 ± 0.7	17.6 ± 0.4
PP/10BA40	1034 ± 25	30.2 ± 0.2	149 ± 28	10.0 ± 1.0	15.2 ± 1.4
PP/2.5BA40-OS	962 ± 34	28.9 ± 0.4	253 ± 103	22.5 ± 1.1	42.9 ± 2.0
PP/5BA40-OS	930 ± 5	29.0 ± 0.2	334 ± 87	14.6 ± 0.8	45.9 ± 6.0
PP/10BA40-OS	(***)	(***)	(***)	14.3 ± 0.9	34.0 ± 10.2
PP/2.5BA40-OS2	920 ± 18	31.4 ± 0.5	136 ± 26	11.0 ± 1.5	12.9 ± 2.0
PP/5BA40-OS2	933 ± 19	30.8 ± 0.6	116 ± 13	/	/
PP/10BA40-OS2	919 ± 3	29.6 ± 0.3	105 ± 41	/	/

(*) Machine direction. (**) Transverse direction.

(***) No possibility of obtaining specimens for tensile mechanical testing.

When the properties at yield and at break of PP/BA40 composites are considered with respect to the unfilled matrix, it can be observed that the yield strength (σ_y) slightly increases, while the elongation at break (ε_b) is also enhanced, reaching a maximum for a filler content of 2.5 wt%.

The addition of BA40-OS nanoparticles results in a remarkable enhancement of the material ductility, producing an increase in strain at break of 163% for the system PP/5BA40-OS, while elastic modulus and yield strength only slightly increase. The increased ductility shown in PP/BA40-OS composite can be attributed to either a reduction in the molecular weight of PP by the octylsilane compound, the improved adhesion between PP and BA40–OS, or both processes took place. Composites added with BA40-OS2 show the highest enhancement in yield strength with respect to the other systems. On the other hand, nanofiller addition produce a noticeable decrease in strain at break, probably because of strong interaction between filler and matrix [255]. Although an increase was expected as a result of smaller agglomerations, however, this was not the case. It seems that, the sulfonic acid surface treatment of BA promotes a greater interaction between matrix and particles. As a result, the BA nanoparticles, inhibit the elongation of the nanocomposite, making it less ductile [291].

6.4.4 Creep behavior

Figure VI.4-3 reports the isothermal creep compliance of PP and PP/BA40 nanocomposites, under a constant load of 4 MPa and at 30 °C.

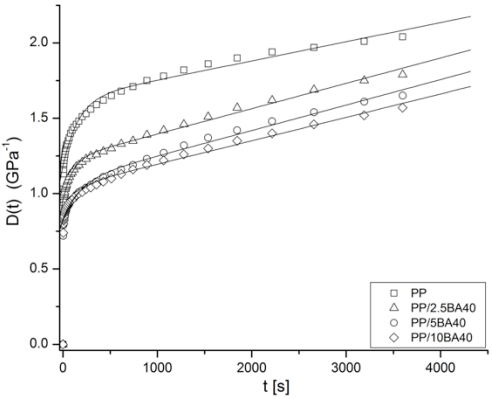

Figure VI.4-3. Creep compliance (D(t)) of PP/BA40 nanocomposites (T=30 °C, σ_0 = 4 MPa).

The introduction of BA nanoparticles results in a significant improvement of the creep stability of the material in the case of PP/BA40 systems. It is generally believed that nanoparticles can effectively restrict the motion of polymer chains, influencing the stress transfer at a nanoscale, with positive effects on the creep stability of the material. On the other hand, the addition of BA40-OS nanoparticles leads to lower creep compliance with respect to unfilled PP only at filler contents as high as 10 wt%. Moreover, incorporation of BA40-OS2 filler results in a slightly higher creep compliance when compared to unfilled PP. Since the creep compliance can be factorized into the elastic and visco-elastic components, creep results are generally in good agreement with the modulus trend observed in quasi-static tensile tests

6.4.5 Propagation tear resistance

Due to orientation during their manufacture, plastic films and sheeting frequently show marked anisotropy in their resistance to tearing. This is further complicated by the fact that some films elongate greatly during tearing. The degree of this elongation is dependent on film orientation and the inherent mechanical properties of the polymer from which it is made [292]. The Elmendorf tearing energy (Figure VI.4-4) of the PP nanocomposites decreased with the BA content for PP/BA40 and PP/BA40-OS2 samples, whereas it was noticeably increased at low BA contents and gradually decreased for higher filler loadings in PP/BA40-OS composites.

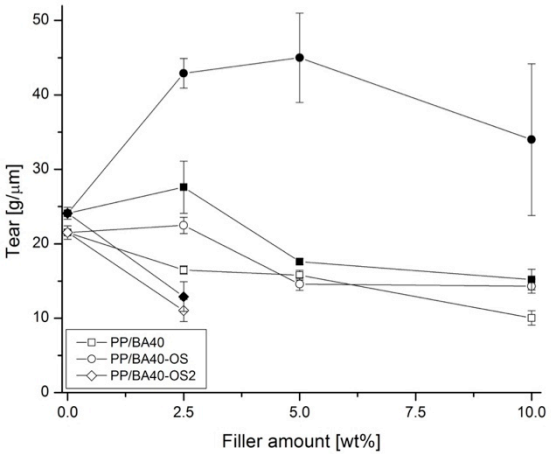

Figure VI.4-4. Propagation tear resistance of PP nanocomposites as a function of the filler content along the machine (open point) and transverse (full point) direction.

Moreover, a marked anisotropy is observable in PP nanocomposites with respect to unfilled PP (Table VI.4-2). This effect could happen because of variations in molecular weight distribution due to nanomodification, which produces a change in molecular orientation and in turn affects many physical properties included tear strength [293]. However, as already seen in the case of tensile properties, this is not the case. A more probable reason is represented by an higher macro orientation occurring in nanocomposites during manufacturing. Nevertheless, in order to obtain a deeper understanding of this phenomenon, rheology measurements would be required. Noteworthy, results of tear resistance are in good agreement with values of strain at break obtained in tensile tests.

The microvoids formation might be responsible for the increment in toughness in PP/BA40-OS samples. As already observed by Soundararajan in the case of poly(vinyl alcohol) nanomodified with montmorillonite, these microvoids release the plastic constraint in the matrix, triggering large-scale plastic deformation with consequent tearing of matrix ligaments between microvoids. Moreover, the higher the filler content, the larger the aggregates and agglomerates, resulting in brittle fracture and limiting the microvoid formation. On the other hand, only crazing contributes to energy absorption in neat PP, which is much lower in comparison [294]. Interestingly, the incorporation of BA40-OS2 particles results in a significative decrease in tear resistance, probably due to the greater interaction established between matrix and particles which strongly inhibits the deformation and tearing capabilities of the nanocomposite. Unfortunately, none result was reported regarding the PP/5BA40-OS2 and PP/10BA40-OS2 samples, as the formation of a great amount of bubbles during the film processing strongly limited the possibility of obtaining wide specimens for tearing testing.

6.5 Synergistic effect of expanded graphite nanoplatelets and short glass fiber on the mechanical and interfacial properties of epoxy resin

Part of this paragraph has been published in:

Pedrazzoli D, Kalaitzidou K, Pegoretti A,

"*Synergistic effect of expanded graphite nanoplatelets and short glass fiber on the mechanical and interfacial properties of epoxy composites*",
Composites Science and Technology, 98. (2014) 15-21.

In this study, epoxy composites reinforced with short glass fibers (GF) and exfoliated graphite nanoplatelets (GNP) were prepared and investigated varying the GF loading. Quasi-static tensile tests and impact tests were performed in order to explore how the combined effect of the two fillers of rather different size scales (i.e. micro- and nano- scale) affected the macroscopic mechanical properties under low and high strain rates.

The improved tensile modulus, ultimate tensile strength and impact resistance observed in hybrid composites revealed that it is possible to introduce the nano-materials at the fiber/matrix interface and significantly improve the interfacial properties, leading to lighter and stronger composites. Concurrently, the storage modulus and the viscoelastic behavior were remarkably enhanced in hybrid composites, evidencing the chain-pinning mechanism promoted by GNP-polymer physical interactions. The introduction of GNP, either within the matrix or at the fiber surface, promoted the formation of a stronger fiber/matrix interface, as evaluated by the single-fiber microdebonding test, resulting in an increase of the interfacial shear strength of 59% in the system incorporating 5 wt% GNP and coated GF.

As part of the higher density GF can be replaced with a small amount of the nano-materials, in addition to a reduced weight, the decreased viscosity leads to better processability, as confirmed by rheological measurements. In conclusion, the combined effect of nano-materials and micro-size reinforcements can be exploited to produce light-weight hybrid composites with enhanced mechanical properties.

A bicomponent epoxy resin, supplied by US Composites (West Palm Beach, FL), was used as matrix. In particular, an epoxy resin constituted by a mixture of 635 thin epoxy (viscosity = 600 mPa·s) was added to a 556 slow amminic hardener at a weight ratio of 2:1.

Exfoliated graphite nanoplatelets xGnP®-M5 have been supplied from XG SCIENCE Inc. (East Lansing, USA). E-glass fibers, designed as RO99 P319, were supplied by Saint-GobainVetrotex (Chambèry Cedex, France) and were used as-received. These GF are indicated as treated with a silane based coupling agent. Chopped strand glass fibers (single fiber diameter = 15.3±1.5 μm, average length = 6.50±0.44 mm) were obtained by chopping long glass fibers using a chopper gun CDA-08 provided by GlasCraft (Graco®, Bury, England).

GNP-coated glass fibers were prepared by sonication of xGnP-M5 in isopropanol with a filler concentration of 5 mg/ml. Sonication was carried out using a Misonix S-4000-010 (Farmingdale, NY) for 1 h (30% amplitude, 8 W power) equipped with a probe of 12.5 mm diameter. After adding the glass fibers to the solution, a second sonication was performed for ½ h. Coated glass fibers were finally rinsed in isopropanol and left under hood overnight to let the solvent completely evaporate. The GNP content added onto the fibers' surfaces through sonication was measured around 0.10-0.15 wt% as considered with respect to the composite weight.

In order to breakdown the filler agglomerates, GNP were mixed for 30 min at room temperature with isopropyl alcohol (IPA) by sonication. A Misonix S-4000-010 sonicator (Farmingdale, NY), equipped with a probe of 12.5 mm diameter was set at 30% amplitude (8 W power). The GNP powder was collected after filtering the IPA solution and mixed with the epoxy at 800 rpm and T=60 °C for 40 min using a magnetic stirring plate. The GF were then added to the solution and further mixing was continued for 20 min. After adding the curing agent to the solution, stirring was carried on at 800 rpm for 30 min at room temperature. The mixture was degassed in a vacuum oven and casted in a mold. Curing cycle was performed at T=80 °C for 1h, followed by post-curing at T=100 °C for 4h.

Composites were designated indicating the kind of filler with its amount, the GF amount and the matrix. For instance, the composite based on unfilled matrix loaded with 10 wt% GF was denoted as 10GF/Epoxy. On the other hand, a sample filled with 5 wt% of xGnP-M5 and 10 wt% GF was indicated as 5GNP/10GF/Epoxy. Coated glass fibers were indicated as GFc.

6.5.1 Solid-state rheology

The effect of the GF addition on the isothermal frequency dependence of the dynamic shear storage modulus (*G'*) and complex viscosity ($|\eta^*|$) is reported in Figure VI.5-1a-b for unfilled epoxy and epoxy composites. As expected, both *G'* and $|\eta^*|$ significantly increase with the GF loading over the whole frequency range. Moreover, a further increase is recorded upon incorporation of GNP in the epoxy composite filled with 15 wt % GF, mainly because of a pseudo solid-like transition caused by the dispersed fillers [102, 106]. Furthermore, the viscosity of the neat resin decreases sharply with the increase of the frequency due to shear thinning (viscosity decreases with an increase of shear rate/frequency), while the viscosity of composite samples exhibits a plateau behavior at high frequencies. This frequency independent fluid properties (i.e., Newtonian-type flow) are usually observed in nanocomposites at low filler contents [295].

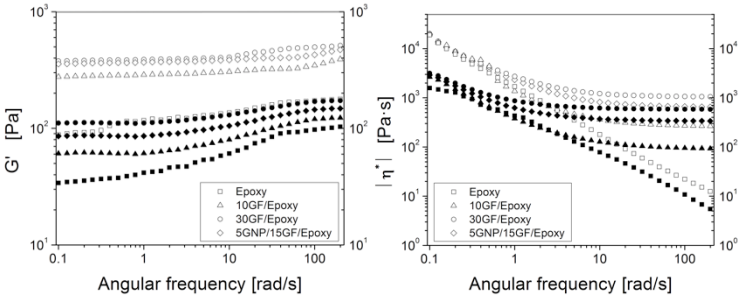

Figure VI.5-1. Viscosity measurements on neat epoxy and relative GNP nanocomposites: (a) Storage modulus (*G'*) and (b) Complex viscosity $|\eta^*|$ of Epoxy composites evaluated below (open point) and above T_g (full point) with respect to angular frequency.

Because of the peculiar viscoelastic rheological behavior of the epoxy matrix, shear storage modulus and viscosity were evaluated below and above T_g (Figure VI.5-1a and Figure VI.5-1b, respectively). Temperature is observed to have a significant effect on the *G'* and viscosity. As the temperature increases, both quantities decrease owing to the polymer chain relaxation at high temperatures [296]. In particular, the decrease in G' observed when increasing the temperature above T_g can be ascribed to a transition from elastic-solid to viscous-liquid behavior.

Interestingly, the sample 5GNP/15GF/Epoxy exhibits values of G' comparable with those of 30GF/Epoxy, while when the viscosity is taken into account, the hybrid system shows slightly lower values, reflecting the greater efficiency of GNP in

increasing G' and the viscosity when compared to GF, probably due to the higher specific surface area (0.3-2 vs. 150 m^2/g, for GF and GNP, respectively, in according to the supplier information). In addition, the pinning effect of the nanofiller onto the polymeric chains [225, 297] might also play a key role in increasing the viscosity in hybrid composites, as evidenced by the higher T_g with respect to that of the non-hybrid composite 30GF/Epoxy (67.7±0.3 °C vs. 66.8±0.4 °C, respectively, as reported in Table VI-5-2).

6.5.2 Quasi-static and impact tensile mechanical properties

The tensile elastic modulus (*E*) and ultimate tensile strength (*UTS*) increase significantly in GNP nanocomposites and even more in GF composites, while the elongation at ultimate tensile strength (ε_{UTS}) decreases (Table VI.5-1). This trend is consistent with observations for adding fillers to a relatively brittle matrix.

Table VI.5-1. Absolute and specific mechanical properties of Epoxy composites.

Sample	E [MPa] E*[MPa/(g/cm³)]	UTS [MPa] UTS*[MPa/(g/cm³)]	ε_{UTS} [%]	Impact strength [J/m]
Epoxy	2917 ± 37 (2537)	59.6 ± 0.7 51.8	4.1 ± 0.1	26.5 ± 2.1
5GNP/Epoxy	3543 ± 76 (3023)	62.4 ± 0.2 (53.2)	3.5 ± 0.1	28.6 ± 1.4
10GF/Epoxy	3793 ± 40 (3122)	63.7 ± 0.3 (52.4)	3.1 ± 0.2	80.5 ± 2.3
30GF/Epoxy	4266 ± 80 (3111)	67.8 ± 0.2 (49.5)	2.0 ± 0.2	116.2 ± 2.4
5GNP/10GF/Epoxy	3907 ± 74 (3156)	67.0 ± 0.6 (54.2)	3.0 ± 0.2	92.4 ± 1.9
5GNP/15GF/Epoxy	4178 ± 91 (3282)	70.4 ± 0.7 (55.3)	2.2 ± 0.2	107.5 ± 1.9
10GFc/Epoxy	3818 ± 65 (3140)	64.7 ± 0.2 (53.2)	3.0 ± 0.2	86.4 ± 1.4
5GNP/10GFc/Epoxy	3949 ± 47 (3189)	67.9 ± 0.2 (54.8)	2.8 ± 0.2	101.4 ± 1.1

Interestingly, although the highest value in elastic modulus is obtained in composite at 30 wt% GF (+ 46%), the greatest UTS is shown by hybrid composites 5GNP/15GF/Epoxy, while maintaining a comparable elastic modulus to that of 30GF/Epoxy (+ 43%). The higher UTS exhibited by the hybrid composites with

respect to the UTS of 10GF/Epoxy and 30GF/Epoxy, reflects the greater interfacial shear strength between fiber and matrix which promotes a better stress transfer across the interface, as investigated in the section 10.5.4. The superiority of hybrid composites with respect to non-hybrid composites (i.e. 10GF/Epoxy and 30GF/Epoxy) is even more evident when the specific properties are taken into account (specific elastic modulus and specific ultimate tensile strength, E* and UTS*, respectively). In particular, the UTS* exhibited by hybrid composites remarkably overcomes that of 10GF/Epoxy and 30GF/Epoxy. Moreover, the hybrid sample 5GNP/10GF/Epoxy shows an improvement in UTS* of around 4.6%, which is greater than that represented by the sum of contributions obtained in 5GNP/Epoxy and 10GF/Epoxy (+3.9%), possibly indicating a synergistic effect due to the co-existence of the micro- and nano- fillers. Hybrid composites are thus lighter and stronger than GF reinforced epoxy composites.

Improved mechanical properties can also be observed when coated GF are incorporated, (i.e. 10GFc/Epoxy and 5GNP/10GFc/Epoxy), resulting in enhanced modulus and ultimate properties with respect to composites added with uncoated fibers (10GF/Epoxy and 5GNP/10GF/Epoxy). In particular, the enhancement in UTS* obtained by using coated GF corresponds to 1.5 and 1.1% for 10GFc/Epoxy and 5GNP/10GFc/Epoxy with respect to the correspondent composites prepared with uncoated glass fibers, reflecting the superior fiber/matrix adhesion promoted by the coating.

The impact resistance exhibited by 5GNP/Epoxy nanocomposites and GF/Epoxy composites is reported in Table VI.5-1 as a function of the GF loading. Moreover, the effect of filler synergy on the impact toughness is also reported for hybrid composites. Results show that incorporation of GNP slightly improves the impact resistance by around 8% when added at 5 wt%, indicating the beneficial effect of the filler on the matrix impact toughness. As observed by Moloney et al., the crack growth in thermosetting matrices is generally dominated by matrix failure and particle breakage. Therefore, interface debonding is irrelevant and the nanofiller interfacial adhesion is not effective to increase the toughness [298, 299]. The maintenance of the impact toughness with GNP is a benefit for GNP/Epoxy nanocomposites, that induces a noticeable increase of the elastic modulus without sacrificing the impact strength. Moreover, impact energy values in the investigated nanocomposites also evidenced the relatively good filler dispersion and distribution within the matrix. On the other hand, the matrix toughness noticeably increased with the glass fiber content in GF/Epoxy composites, showing a significant dependence on the interfacial properties determined by the glass fibers surface coating. Owing to the GF modified surface and the beneficial presence of the nanofiller within the matrix, hybrid composites exhibit a considerable improvement in impact resistance when compared

to non-hybrid composites at the same GF loading. In particular, being the impact resistance an ultimate mechanical property, it is supposed to be positively affected by the higher interfacial shear strength (see section 10.5.4). Composites incorporating coated GF (i.e. 10GFc/Epoxy and 5GNP/10GFc/Epoxy) show an improvement of around 7% and 10% when compared to the composites reinforced with uncoated GF.

6.5.3 Viscoelastic properties

The dynamic mechanical properties of the composites under investigation were significantly influenced by the fiber weight fraction: as expected, the storage modulus (*E'*) increases with higher GF contents (Table VI.5-2), while the loss tangent ($tan\delta$) decreases. In addition, the incorporation of GNP in the epoxy matrix produces a considerable increase of *E'* and a concurrent decrease of the loss tangent (Figure VI.5-2). Moreover, the glass transition temperature (T_g), as evaluated at the tanδ peak during DMA experiments, significantly increases in both GNP nanocomposites and GF composites. In particular, the increase in T_g observed in the nanocomposite can be attributed to a chain-pinning mechanism promoted by polymer-GNP physical interactions. Therefore GNP reinforces the epoxy matrix not only because it is stiffer but also because it remarkably alters locally the physical properties of the polymer.

Table VI.5-2. Thermal and viscoelastic properties of Epoxy composites.

Sample	E' (25 °C) [MPa]	E' (80 °C) [MPa]	T_g [°C]	tanδ $_{Tg}$
Epoxy	786 ± 16	6 ± 2	64.8 ± 0.2	1.17 ± 0.06
5GNP/Epoxy	862 ± 21	15 ± 3	65.2 ± 0.3	1.07 ± 0.04
10GF/Epoxy	1032 ± 29	84 ± 6	66.2 ± 0.2	0.78 ± 0.04
30GF/Epoxy	1581 ± 32	161 ±11	66.8 ± 0.4	0.48 ± 0.08
5GNP/10GF/Epoxy	1221 ± 24	119 ± 8	67.7 ± 0.3	0.53 ± 0.06
5GNP/15GF/Epoxy	1311 ± 35	138 ± 12	67.7 ± 0.3	0.45 ± 0.04
10GFc/Epoxy	1062 ± 20	89 ± 9	66.3 ± 0.2	0.75 ± 0.03
5GNP/10GFc/Epoxy	1240 ± 14	122 ± 8	67.9 ± 0.3	0.49 ± 0.04

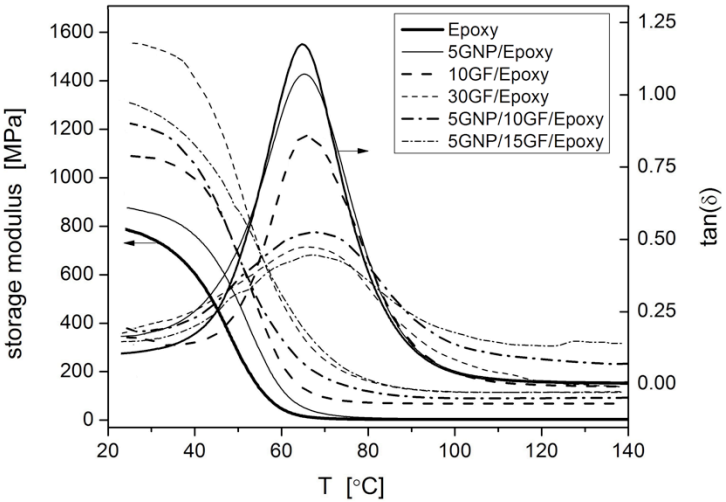

Figure VI.5-2. Dynamic mechanical properties of Epoxy composites.

As GNP and GF are filled in the epoxy matrix, the synergistic effect of both fillers could further reduce and restrict molecular motions, and thus enhance the restriction on the rate of relaxation, leading to higher T_g. Lower values of tanδ recorded upon nanofiller addition in hybrid composites (Table VI.5-2) can be attributed not only to the stiffening effect and enhanced fiber-matrix adhesion, but also to greater physical interactions occurring between polymer and GNP, resulting in lower viscous modulus and improved elastic modulus. With this regard, the storage modulus of the composites was considered below and above T_g (T=25 °C and T=80 °C, respectively) In particular, the elastic behavior observable below T_g better describes the stiffening effect, while the elastic behavior investigated above T_g takes into account the restriction of polymer chain mobility. As a representative example, the storage modulus of the composite 5GNP/10GF/Epoxy, normalized with respect to that of 10GF/Epoxy, corresponds to 1.18 and 1.42 when considered below and above T_g, respectively, confirming the chain blocking mechanism due to GNP incorporation.

6.5.4 Characterization of the interfacial shear strength

A micrograph of a microdebonding single fiber specimen is reported in Figure VI.5-3a, evidencing that the neat epoxy microdrop with a diameter of around 570 μm appears symmetrically centered with respect to the fiber axis. Magnifications of the microdrop interface were taken before and after the microdebonding test, as reported in Figure VI.5-3b and Figure VI.5-3c, respectively, in order to investigate the interfacial fracture mechanism occurring during debonding. Noteworthy, the droplet surface shows evident local deformation marks, ascribed to the contact with the shearing plate during testing. Moreover, the matrix appears detached from the fiber surface in correspondence to the interfacial region, confirming that debonding occurred.

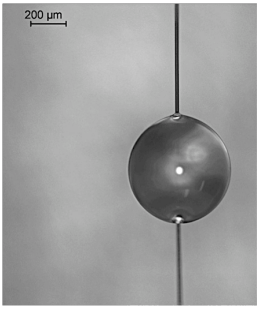

(a)

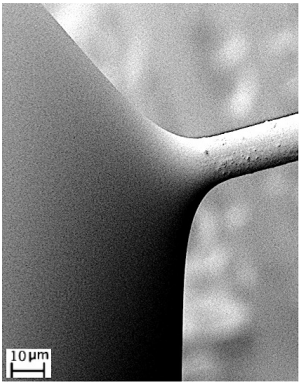

(b)

(c)

Figure VI.5-3. SEM images of (a) neat epoxy drop deposited on a glass fiber for the microdebonding tests, (b) magnification at the fiber/drop interface before microdebonding, and (c) detail of the interface after debonding.

The incorporation of GNP results in a remarkable increase of the interfacial shear stress evaluated at the interface (ISS), indicating a beneficial enhancement in the load transfer across the fiber/matrix interface (Figure VI.5-4). Values of interfacial resistance confirm the superior tensile and viscoelastic properties exhibited by hybrid composites, in particular when considering the ultimate tensile strength and toughness.

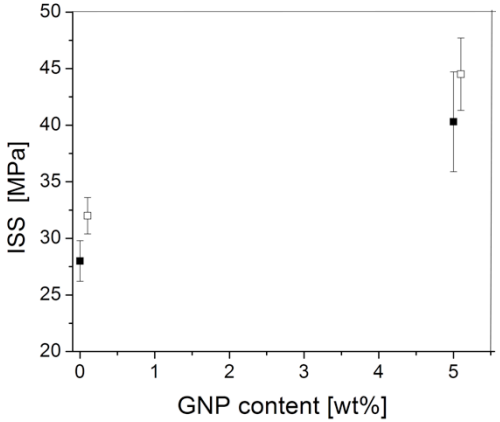

Figure VI.5-4. Interfacial shear strength values of GF/Epoxy composites, as a function of the GNP amount, considering uncoated (full point) and coated (open point) glass fibers. An average GNP content of around 0.10 wt% was measured as deposited onto the glass fibers.

Interestingly, improved interfacial strengths are also observed when the microdebonding test is performed on the system GFc/Epoxy, evidencing the beneficial effect of the fiber coating on the interfacial interactions. However, the best ISS values are obtained when combining nanomodified epoxy with coated fibers (i.e. 5GNP/GFc), showing an improvement of 58.9% which is slightly greater than that represented by the sum of contributions obtained in the systems GFc/Epoxy and 5GNP/GFc/Epoxy (+58.2%), indicating a possible synergistic effect occurring between the micro- and nano- fillers. In particular, the higher ISS can be ascribed to (i) better mechanical and viscoelastic properties of the host matrix and (ii) greater chemical affinity between matrix and fiber, which is further promoted by the coexistence of GNP in the matrix and on the fiber surfaces. Therefore, the fiber coating effectively enhances the fiber/matrix adhesion, as confirmed by the higher UTS with respect to the composites incorporating uncoated fibers.

6.5.5 Morphology characterization

Fracture surfaces of epoxy nanocomposites and composites were analyzed and compared to that of neat epoxy (Figure VI.5-5a). In the SEM micrographs of 5GNP/Epoxy sample it can be seen that aggregates of graphite nanoplatelets with dimension of around 5-10 μm are quite well distributed within the matrix, while most of the graphite aggregates do not seem to be intercalated (Figure VI.5-5b).

Morphological analyses conducted on GF composites revealed that the glass fibers are generally well dispersed in the unfilled Epoxy matrix, and many fibers are pulled out from the matrix (Figure VI.5-5c). The interfacial debonding appears to be the dominant failure mechanism, indicating low-adhesion condition. On the other hand, a different failure behavior is observed for composites based on epoxy matrix additivated with GNP (Figure VI.5-5d), where fewer fibers are pulled out from the matrix and the matrix crack becomes a concurrent failure mechanism, showing a significantly better fiber-matrix adhesion.

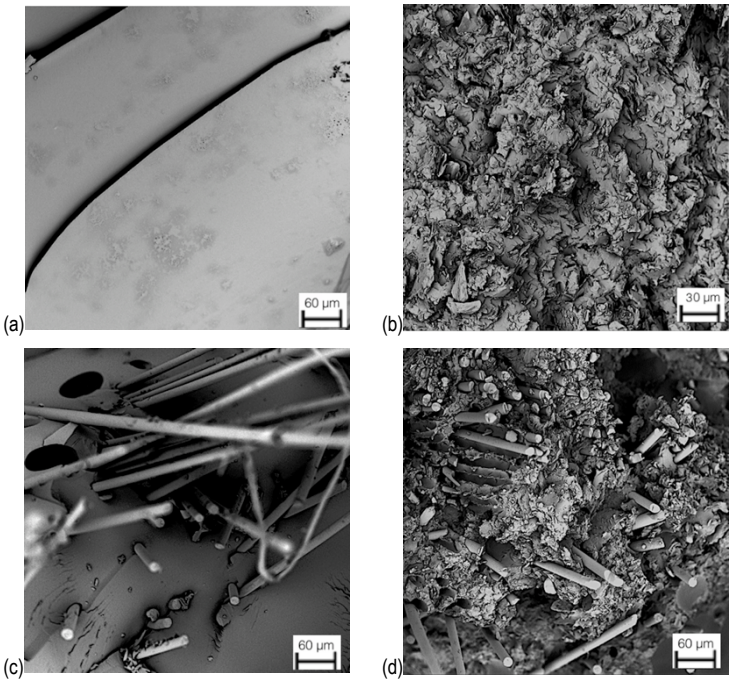

Figure VI.5-5. SEM micrographs of fracture surfaces of (a) neat Epoxy, (b) 5GNP/Epoxy, (c) 10GF/Epoxy and (d) 5GNP/10GF/Epoxy composites.

6.6 Effect of nanofiller geometry on the polymer physical structure and mechanical properties of nanocrystalline Fe-Ni alloy/Polyamide 6 nanocomposites.

Part of this paragraph has been published in:

Mohamed M, Pedrazzoli D, Nady N, Kalaitzidou K,

"*Effect of nanofiller geometry on the polymer physical structure and mechanical properties of nanocrystalline Fe-Ni alloy/Polyamide 6 nanocomposites*",
In 'Proceedings of ECCM16', June 22-27th 2014, Seville (Spain).

This study reports the preparation and structural characterization of polyamide 6 nanocomposites (PA6 PNCs) based on nanocrystalline (nc) $Fe_{20}Ni_{80}$ alloy with two different geometries, spherical-sea urchin particles (UMB2-SU) and necklace chains UMB2NL.

The tensile properties and physical structure of the PNCs were characterized. The results reveal that the addition of nc Fe_{20} Ni_{80} particles to PA6 remarkably enhances the elastic modulus and strength at the expense of toughness and UMB2-SU PNC exhibits synergistic tensile properties when compared to UMB2-NL PNC. Such synergism observed in nanocomposites based on spherical-sea urchin particles, as compared to those incorporating necklace particles was attributed to (i) the higher dispersibility and surface area of the particles and (ii) the greater crystallinity and lower ratio of γ - form to α - form crystals of PA6 phase.

Nanocrystalline (nc) Fe-Ni alloy is considered of great importance for numerous technological applications, including high-density magnetic storage devices, bimetallic temperature sensors, electromagnetic shielding and microelectromechanical systems (MEMS). The attention to this alloy is attributed to its unique mechanical and magnetic properties, low thermal expansion and high electrical conductivity. Previous studies have been conducted on Fe-Ni alloy/polyamide 6 (PA6) nanocomposites produced by ultrasound assisted master batch (UMB) technique. The characterization of the mechanical and thermomechanical properties of such nanocomposites indicated a great potential of improvement when compared to the more investigated PA6 nanocomposites based

on clay, silica and carbon nanotubes. This evidenced that the novel Fe-Ni/PA6 nanocomposite can be a good candidate material for current and future engineering applications.

In particular, the shape and aspect ratio of the nanofiller represents one of the most important parameters affecting various properties of polymer nanocomposites (PNCs). Therefore, the main aim of this study is to synthesize nc Fe-Ni alloy with different geometries and investigate the effect of the filler geometry on the structural properties and mechanical performances of PA6 PNCs.

The synthesis of the nc $Fe_{20}Ni_{80}$ particles with two different geometries was carried ouyt following the procedure described in [300]. The PNCs samples were prepared in a two-step process: first the nc $Fe_{20}Ni_{80}$ particles were compounded with half of the PA6 amount via ultrasound-assisted solution mixing (USM) to prepare concentrated USM PNCs containing 4 wt% nc $Fe_{20}Ni_{80}$. The USM PNCs were then compounded (diluted) with the rest of PA6 pellets via melt mixing to prepare UMB PNCs with 2 wt% nc $Fe_{20}Ni_{80}$. A final injection molding was carried out to prepare standard dog bone samples (ASTM D638, Type V) and standard Izod bars (ASTM D256). A DSM Micro 15 cc extruder, (vertical, co-rotating twin-screw micro extruder) and 10 cm^3 injection molding machine were used for compounding USM PNCs with the rest of PA6 pellets and fabrication of the UMB PNCs, respectively. The conditions used were: 240 ˚C as T_{barrel} in the compounder and injection molding machine, screw speed of 150 rpm, residence time of 4 min, T_{mold} of 70 ˚C and injection pressure of 0.8 MPa. The detailed samples' codes are listed in Table VI.6-1.

Table VI.6-1. Samples' codes.

Sample	Code
Control PA6	UMB0
2 wt% spherical-sea urchine $Fe_{20}Ni_{80}$/PA6 PNC	UMB2-SU
2 wt% necklace $Fe_{20}Ni_{80}$/PA6 PNC	UMB2-NL

X-ray diffraction (XRD) was used to identify the synthesized black particles and characterize their crystallographic texture and crystal size. The measurements were performed on a Shimadzu XRD-7000 diffractometer (30 kV, 30 mA; Cu Kα + Ni-filtered radiation, λ = 0.15406 nm). The 2θ range was 30-110°, at a scanning rate of 4°/min and a scanning step of 0.018°. The chemical composition was estimated by an area analysis using energy dispersive X-ray spectroscopy (EDS) equipped with the scanning electron microscope (SEM, JEOL, Model JSM 6360 LA). The morphology was investigated by scanning electron microscopy (SEM, JEOL, Model JSM 6360 LA, Japan) operating at 20 kV.

Tensile test was performed using an electro-mechanical testing machine (Instron 33R 4466) equipped with a 10 KN load cell, according to ASTM-D638. The tests were carried out at ambient temperature at a crosshead speed of 1 mm/min. The results were computed as the average of three measurements.

Modulated differential scanning calorimeter (MDSC Q200, TA instruments) was used to determine the degree of crystallinity and analyze the melting and crystallization behaviors of neat PA6 and PA6 phase in the nanocomposites. Slices had a net weight of about 8 mg were cut from the injection molded bars. The sliced samples were heated from ambient temperature to 270 °C, held at this temperature for 3 min to erase the thermal history and then cooled to 25 °C. All MDSC runs were conducted under nitrogen atmosphere with heating/cooling rates of 5 °C/min. The degree of crystallinity was calculated from the enthalpy evolved during melting based on the heating scans, taking into account the filler weight fraction. In particular, the melting of 100% crystalline pure PA6 was considered as 190 J/g.

XRD was used to determine the relative fraction of α and γ crystalline phases in neat PA6 and PA6 phase within the PNCs. XRD patterns were obtained using X'Pert PRO Alfa-1 diffractometer in reflection mode (45 kV, 40 mA; Cu Kα + Ni-filtered radiation, λ = 0.154 nm). The analysis was performed at ambient temperature with a 2θ range between 8 and 80°, at a scanning rate of about 4°/min and a scanning step of 0.016°. XRD traces were de-convolved to diffraction peaks corresponding to amorphous phase and crystalline phase (composed of α and γ crystal forms) using xPert Pro software. The percentage of γ-phase, with respect to the total crystalline phase, was computed as:

$$\gamma(\%) = \frac{A_\gamma}{A_\alpha + A_\gamma} \times 100 \qquad (VI-1)$$

Where A_α and A_γ is the total area under the α and γ diffraction peaks, respectively.

6.6.1 Characterization of the nc Fe_{20}/Ni_{80} particles

The XRD pattern of the synthesized particles is shown in Figure VI.6-1. The five characteristic peaks for the disordered FCC γ-Fe-Ni taenite phase can be observed (2θ = 44.4°, 51.6°, 76.3°, 92.7° and 98.2), marked by the Miller indices ((111), (200), (220), (311) and (222)) respectively, considering as a reference the database of International Centre of Diffraction Data (ICDD).

According to EDS quantitative analysis, the atomic percentage of Ni is 79%, excluding the other elements like carbon in the supporting film and oxygen in the oxide layer formed on the particle surface. Moreover, the atomic percentage of

oxygen is only 4%, indicating that the oxide layer formed on particle surface is very thin. These results reveal the formation of $Fe_{20}Ni_{80}$ alloy with high purity. The average crystallite sizes of the $Fe_{20}Ni_{80}$ alloys were calculated based on the full width at half maximum of the (111) peak in the corresponding XRD patterns, adopting the Scherrer formula [12]. The data range from 14.5-16 nm, indicating that both alloys are nanocrystalline structured, regardless of the synthesis conditions.

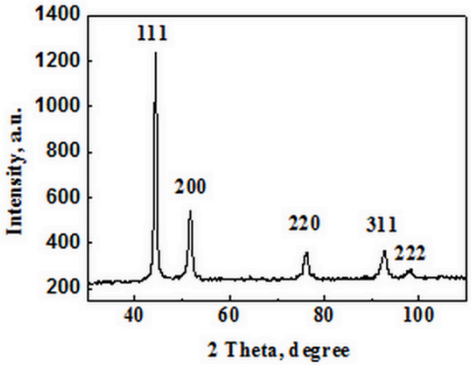

Figure VI.6-1. XRD pattern of the chemically synthesized black particles.

SEM micrographs of the nc $Fe_{20}Ni_{80}$ alloys are presented in Figure VI.6-2. The alloy exhibiting sea urchin-like particles presents spherical morphology of average diameter of about 230 nm (Figure VI.6-2a), while the sea urchin-like architecture is composed of several dendrites with average diameter of about 122 nm. On the other hand, necklace-like chains with average diameter of about 225 nm seem predominant (Figure VI.6-2b) in the other case. In particular, the necklace-like chains appear quite smooth and little bit branched, few dendritic branches can be hardly seen at high magnification.

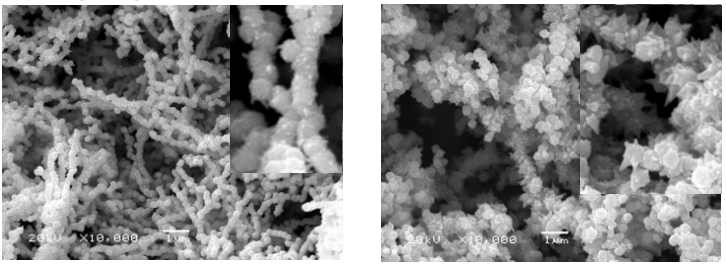

(a) (b)

Figure VI.6-2. SEM micrographs of nc $Fe_{20}Ni_{80}$ alloy synthesized at (a) 0.6 M and (b) 0.2 M.

6.6.2 Characterization of PA6 nanocomposites

The typical stress-strain curves of neat PA6, UMB2-SU and UMB2-NL indicates that PA6 nanocomposites exhibit a significantly higher strength at break but lower ductility (Figure VI.6-3).

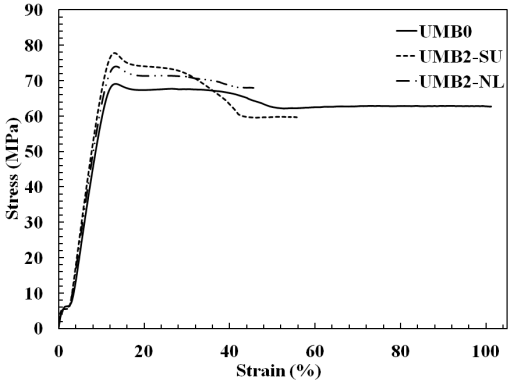

Figure VI.6-3. Representative stress-strain curves of PA6 and $Fe_{20}Ni_{80}$/PA6 PNCs.

A summary of the relative tensile properties of UMB2-SU PNC and UMB2-NL PNC with respect those of neat PA6, is shown in Table VI.6-2. The data reveal that the addition of nc $Fe_{20}Ni_{80}$ particles to PA6 produces a significant increase in modulus and strength at the expense of toughness. Furthermore, UMB2-SU PNC shows synergistic tensile properties as compared to UMB2-NL one, probably due to the better dispersion of spherical-sea urchin particles.

Table VI.6-2. Relative tensile properties of $Fe_{20}Ni_{80}$/PA6 PNCs.

Sample	Relative Modulus	Relative yield strength	Relative strain at yield (%)	Relative Strain at break (%)
UMB0	1.00 ± 0.04	1.00 ± 0.02	1.00 ± 0.07	1.00 ± 0.15
UMB2-SU	1.13 ± 0.02	1.12 ± 0.007	1.00± 0.02	0.54 ± 0.1
UMB2-NL	1.08 ± 0.01	1.07 ± 0.025	1.02 ± 0.03	0.41 ± 0.1

The DSC melting and crystallization thermograms have been used to characterize the degree of crystallinity *(X_C)*, melting temperature *(T_m)* and crystallization peak temperature *(T_c)* of neat PA6 and relative nanocomposites (Table VI.6-3). Upon analyzing the DSC data, it is noticed that UMB2-SU and UMB2-NL PNCs have significantly higher X_C and slightly higher T_c of PA6 phase when compared to the neat PA6, indicating that the nc $Fe_{20}Ni_{80}$ particles act as effective nucleating agent,

allowing the PA6 crystallization to start earlier and inducing the rate of crystallization leading eventually to increased degree of crystallinity.

Table VI.6-3. DSC data for PA6 and $Fe_{20}Ni_{80}$/PA6 PNCs.

Sample	X_c (%)	T_m (°C)	T_c (°C)
UMB0	32.5	224.0	198.5
UMB2-SU	38.5	223.0	199.5
UMB2-NL	37.0	222.5	199.0

XRD patterns for neat PA6 and relative nanocomposites are presented in Figure VI.6-4. The peaks around $2\theta \approx 20°$ and 23° are assigned to α_1 and α_2 crystal planes of PA6, respectively, while the peaks around $2\theta \approx 10°$ and 21° are assigned to γ_1 and γ_2 crystal planes of PA6, respectively. The observed peaks around (2θ = 44°, 51°, 75°) are attributed to the disordered FCC γ-Fe-Ni taenite phase.

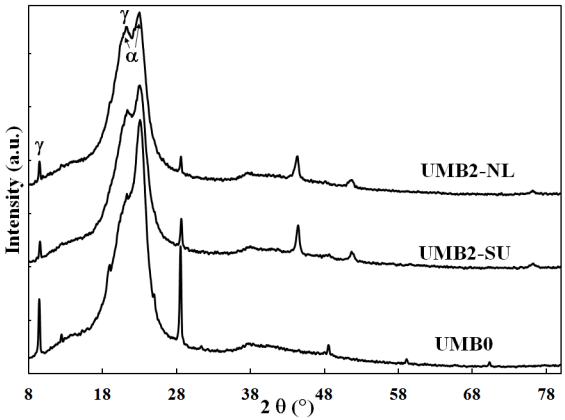

Figure VI.6-4. XRD pattern for PA6 and $Fe_{20}Ni_{80}$/PA6 PNCs.

Interestingly, the nanocomposites exhibit increased relative fraction of γ-form to α-form PA6 crystals when compared to the neat PA6. Specifically, the PA6 γ phase (%) measures 20%, 26% and 41% for neat PA6, UMB2-SU and UMB2-NL PNCs, respectively. The lower T_m of PA6 phase, out from the DSC analyses, is in agreement with the increased PA6 γ phase (%), out from XRD analyses, within the nanocomposites as compared to neat PA6, indicating that less ordered PA6 crystals are favored in the presence of nc $Fe_{20}Ni_{80}$ particles. It is speculated that the nc $Fe_{20}Ni_{80}$ particles disturb the PA6 crystals while being formed during the crystallization process, leading to the profusion of less ordered γ-phase crystals in the PNCs as compared to neat PA6.

References

[1] Schadler LS, Brinson LC, Sawyer WG. *Polymer Nanocomposites: A Small Part of the Story.* Nanocomposite Materials. 2007:53-60.

[2] Kalaitzidou K, Fukushima H, Drzal LT. *Multifunctional polypropylene composites produced by incorporation of exfoliated graphite nanoplatelets.* Carbon. 2007;**45**(7):1446-1452.

[3] Qian H, Greenhalgh ES, Shaffer MSP, Bismarck A. *Carbon nanotube-based hierarchical composites: a review.* Journal of Materials Chemistry. 2010;**20**(23):4751.

[4] Evans AG, Zok FW. Review. *The physics and mechanics of fibre-reinforced brittle matrix composites.* Journal of Materials Science. 1994;**29**:3857-3896.

[5] Ashby MF. Materials election in mechanical design. Oxford: Elsevier; 2005.

[6] Amateau MF. *Engineering composite materials*; The Pennsylvania State University (University Park); 2003.

[7] Mai Y, Yu Z.Z. *Polymer Nanocomposites.* Cambridge: CNR press; 2006.

[8] Hussain F. *Review article: Polymer-matrix Nanocomposites, Processing, Manufacturing, and Application: An Overview.* Journal of Composite Materials, 2006;**40**(17):1511-1575.

[9] Koo JH. *Polymer nanocomposite: process, characterization and applications*, The McGraw-Hill Companies; 2006.

[10] Kalaitzidou K, Fukushima H, Drzal LT. *A new compounding method for exfoliated graphite–polypropylene nanocomposites with enhanced flexural properties and lower percolation threshold.* Composites Science and Technology. 2007;**67**(10):2045-2051.

[11] Ganguli S, Roy AK, Anderson DP. *Improved thermal conductivity for chemically functionalized exfoliated graphite/epoxy composites.* Carbon. 2008;**46**(5):806-817.

[12] Xanthos Me. Functional fillers for plastics. Weinheim: Wiley; 2010.

[13] Chung DDL. *Composite Materials: Science and Applications.* New York: Springer; 2010.

[14] Mouzakis DE, Papanicolaou GC, Giannadakis K, Zuburtikudis I. *On the Toughness Response of iPP and sPP/MWNT Nanocomposites.* Strain. 2013;**49**(4):348-353.

[15] Mittal Ve. *Optimization of polymer nanocomposite properties.* Weinheim: Wiley-VCH.; 2010.

[16] Jancar J. *Review of the role of the interphase in the control of composite performance on micro- and nano-length scales.* Journal of Materials Science. 2008;**43**(20):6747-6757.

[17] Shenoy AV. *Rheology of filled polymer systems.* Dordrecht: Kluwer Academic Publishers; 1999.

[18] Pedrazzoli D, Ceccato R, Karger-Kocsis J, Pegoretti A. *Viscoelastic behaviour and fracture toughness of linear-low-density polyethylene reinforced with synthetic boehmite alumina nanoparticles.* eXPRESS Polymer Letters. 2013;**7**(8):652-666.

[19] Móczó J, Pukánszky B. *Polymer micro and nanocomposites: Structure, interactions, properties.* Journal of Industrial and Engineering Chemistry. 2008;**14**(5):535-563.
[20] Isitman NA, Gunduz HO, Kaynak C. *Nanoclay synergy in flame retarded/glass fibre reinforced polyamide 6.* Polymer Degradation and Stability. 2009;**94**(12):2241-2250.
[21] Dorigato A, Pegoretti A, Frache A. *Thermal stability of high density polyethylene–fumed silica nanocomposites.* Journal of Thermal Analysy and Calorimetry. 2012;**109**(2):863-873.
[22] Fina A, Abbenhuis HCL, Tabuani D, Frache A, Camino G. *Polypropylene metal functionalised POSS nanocomposites: A study by thermogravimetric analysis.* Polymer Degradation and Stability. 2006;**91**(5):1064-1070.
[23] Wang D-Y, Das A, Leuteritz A, Boldt R, Häußler L, Wagenknecht U, et al. *Thermal degradation behaviors of a novel nanocomposite based on polypropylene and Co–Al layered double hydroxide.* Polymer Degradation and Stability. 2011;**96**(3):285-290.
[24] Rao YQ, Blanton TN. *Polymer Nanocomposites with a Low Thermal Expansion Coefficient.* Macromolecules. 2008;**41**:935-941.
[25] Cai D, Song M. *Recent advance in functionalized graphene/polymer nanocomposites.* Journal of Material Chemistry. 2010;**20**(37):7906.
[26] Drzal LT, Fukushima H. *Exfoliated Graphite Nanoplatelets (xGnP): A Carbon Nanotube Alternative.* NSTI-Nanotech, 2006.
[27] Kyprianidou-Leodidou T, Caseri W, Suter U. *Size variation of PbS particles in high refractive index nanocomposites.* The Journal of Physical Chemistry. 1994;**98**(8992-8997).
[28] Lecouvet B, Gutierrez JG, Sclavons M, Bailly C. *Structure–property relationships in polyamide 12/halloysite nanotube nanocomposites.* Polymer Degradation and Stability. 2011;**96**(2):226-235.
[29] Avella M, Errico E, Martuscelli E. *Novel PMMA/$CaCO_3$ Nanocomposites Abrasion Resistant Prepared by an in Situ Polymerization Process.* Nano Letters 2001;**1**(213-217).
[30] Alberts M, Kalaitzidou K, Melkote S. *An investigation of graphite nanoplatelets as lubricant in grinding. International Journal of Machine Tools and Manufacture*. 2009;**49**(12-13):966-970.
[31] Scott MA, Carrado, K.A. and Dutta, P.K. (eds). *Handbook of Layered Materials*. Taylor & Francis; 2004.
[32] Dorigato A, Morandi S, Pegoretti A. *Effect of nanoclay addition on the fiber/matrix adhesion in epoxy/glass composites.* Journal of Composite Materials. 2011;**46**(12):1439-1451.
[33] Chaudhary AK, Jayaraman K. *Extrusion of linear polypropylene-clay nanocomposite foams.* Polymer Engineering & Science. 2011;**51**(9):1749-1756.
[34] Choi D, Kader MA, Cho B-H, Huh Y-i, Nah C. *Vulcanization kinetics of nitrile rubber/layered clay nanocomposites.* Journal of Applied Polymer Science. 2005;**98**(4):1688-1696.

[35] Roy S, Hussain F, Lu H, Narasimhan K. *Characterization and modeling of strength enhancement mechanism in polymer clay nanocomposites,* In: AIAA Conference Proceedings, Texas, 2005.
[36] Findeissen B, Thomasius M. East Germany Patent DD. 1981.
[37] Fukushima H, Drazal LT. *Graphite Nanocomposites: Structural & Electrical Properties.* Proceedings of the 14th International Conference on Composite Materials (ICCM-14), San Diego, CA.2003.
[38] Iijima S. *Helical microtubules of graphitic carbon.* Nature. 1991;**354**:56-58.
[39] Shaffer MSP, Sandler JKW. *Carbon Nanotube/Nanofibre Polymer Composites*. In: London IC, editor.; 2008.
[40] Bethune DS, Kiang CH, de Vries CH, Gorman G, Savoy R, Vazquez J, et al. *Cobalt-catalysed growth of carbon nanotubes with single-atomic-layer walls.* Nature. 1993;**363**(6430):605–607.
[41] Cheng HM, Li F, Su G, Pan HY, He LL, Sun X, et al. *Large- scale and low-cost synthesis of single-walled carbon nanotubes by the catalytic pyrolysis of hydrocarbons.* Applied Physic Letters. 1998;**72**(25):3282–3284.
[42] Carneiro OS, Covas JA, Bernado CA, Caldeira G, Van Hattum FWJ, Ting JM, et al. *Production and assessment of polycarbonate composites reinforced with vapour-grown carbon fibres.* Composites Science and Technology. 1998;**58**(3-4):401–407.
[43] Kalaitzidou K, Fukushima H, Askeland P, Drzal LT. *The nucleating effect of exfoliated graphite nanoplatelets and their influence on the crystal structure and electrical conductivity of polypropylene nanocomposites.* Journal of Materials Science. 2007;**43**(8):2895-2907.
[44] Assouline E, Lustiger A, Barber AH, Cooper CA, Klein E, Wachtel E, et al. *Nucleation ability of multiwall carbon nanotubes in polypropylene composites.* Journal of Polymer Science, Part B: Polymer Physics. 2003;**41**(5):520–527.
[45] Grady BP, Pompeo F, Shambaugh RL, Resasco DE. *Nucleation of polypropylene crystallization by single-walled carbon nanotubes*. Journal of Physics Chemistry Part B. 2002;**106**(23):5852–5858.
[46] Stephan C, Nguyen TP, Lahr B, Blau WJ, Lefrant S, Chauvet O. *Raman spectroscopy and conductivity measurements on polymer-multiwalled carbon nanotubes composites.* Journal of Materials Resources. 2002;**17**(2):396– 400.
[47] Kilbride BE, Coleman JN, Fraysse J, Fournet P, Cadek M, Drury A, et al. *Experimental observation of scaling laws for alternating and direct current conductivity in polymer-carbon nanotube composite thin films.* Journal of Applied Physics. 2002;**92**(7):4024-4030.
[48] Werner P, Altstädt V, Jaskulka R, Jacobs O, Sandler JKW, Shaffer MSP, et al. *Tribological behaviour of carbon-nanofibre-reinforced poly(ether-ether ketone)*. Wear. 2004;**257**((9-10)):1006-1014.
[49] Tenne R, Zettl AK. *Carbon Nanotubes: Synthesis, structure, properties and applications.* New York: Springer; 2000.
[50] Du M, Guo B, Jia D. *Newly emerging applications of halloysite nanotubes: a review.* Polymer International. 2010;**59**:574-582.
[51] Ajayan PM, Schadler LS, Braun PVe. *Nanocomposite Science and Technology.* Weinheim: Wiley-VCH.; 2003.

[52] Peters S. Te. *Handbook of composites.* London: Chapman and Hall; 1998.
[53] Pedrazzoli D, Dorigato A, Pegoretti A. *Monitoring the mechanical behaviour under ramp and creep conditions of electrically conductive polymer composites.* Composites Part A: Applied Science and Manufacturing. 2012;**43**:1285-1292.
[54] Pedrazzoli D, Dorigato A, Pegoretti A. *Monitoring the mechanical behaviour of electrically conductive polymer nanocomposites under ramp and creep conditions.* Journal of Nanoscience and Nanotechnology. 2012;**12**:4093-4102.
[55] Friedlander SK. *R&D Status and Trends*, ed. R.W. Siegel, E. Hu, and M.C. Roco. Dordrecht (Netherlands);1998.
[56] Zhou R-J, Burkhart T. *Polypropylene/SiO_2 nanocomposites filled with different nanosilicas: thermal and mechanical properties, morphology and interphase characterization.* Journal of Materials Science. 2011;**46**(5):1228-1238.
[57] Dorigato A, Dzenis Y, Pegoretti A. *Nanofiller aggregation as reinforcing mechanism in nanocomposites.* Procedia Engineering. 2011;**10**:894-899.
[58] Dorigato A, Dzenis Y, Pegoretti A. *Filler aggregation as a reinforcement mechanism in polymer nanocomposites.* Mechanics of Materials. 2013;**61**:79-90.
[59] Fina A, Abbenhuis HCL, Tabuani D, Camino G. *Metal functionalized POSS as fire retardants in polypropylene.* Polymer Degradation and Stability. 2006;**91**(10):2275-2281.
[60] Scott DW. Thermal *Rearrangement of Branched-Chain Methylpolysiloxanes.* Journal of American Chemical Society. 1946;**68**:356-368.
[61] Phillips SH, Haddad TS, Tomczak SJ. *Developments in nanoscience: polyhedral oligomeric silsesquioxane (POSS)-polymers.* Current Opinion Solid State Material Science. 2004;**8**:21-29.
[62] Karevan M, Kalaitzidou K. *Formation of a complex constrained region at the graphite nanoplatelets-polyamide 12 interface.* Polymer. 2013;**54**(14):3691-3698.
[63] Wu S. *Polymer interface and adhesion.* New York: Marcel Dekker, Inc; 1982.
[64] Karger-Kocsis J, Varga J, Ehrenstein GW. *Comparison of the fracture and failure behavior of injection-molded α- and β-polypropylene in high-speed three-point bending tests.* Journal of Applied Polymer Science. 1997;**64**:2057-2066.
[65] Huy TA, Adhikari R, Lupke T, Henning S, Michler GH. *Molecular deformation mechanisms of isotactic polypropylene in α- and β-crystal forms by FTIR spectroscopy.* Journal of Polymer Science Part B: Polymer Physics. 2004;**42**(24):4478-4488.
[66] Yuan Q, Misra RDK. *Polymer nanocomposites: current understanding and issues.* Material Science and Technology. 2006;**22**(7):742-755.
[67] Karger-Kocsis J. *Polypropylene: an A-Z reference.* Dordrecht, The Netherlands: Kluwer Publishers; 1999.
[68] Karger-Kocsis J. *How Does "Phase Transformation Toughening" Work in Semicrystalline Polymers?* Polymer Engineering and Science. 1996;**36**(2):203-210.
[69] Tordjeman P, Robert C, Marin G, Gerard P. *The effect of α, β crystalline structure on the mechanical properties of polypropylene.* The European Physical Journal E. 2001;**4**:459-465.
[70] Janeschitz-Kriegl H. *Crystallization modalities in Polymer Melt Processing.* Wien: Springer, NewYork; 2010.

[71] Garbarczyk J, Paukszta D, Borysiak S. *Polymorphism of Isotactic Polypropylene in Presence of Additives, in Blends and in Composites.* Journal of Macromolecular Science, Part B. 2002;**41**(4):1267-1278.
[72] Menyhárd A, Varga J. *The effect of compatibilizers on the crystallisation, melting and polymorphic composition of β-nucleated isotactic polypropylene and polyamide 6 blends.* European Polymer Journal. 2006;**42**(12):3257-3268.
[73] Cao Y, Feng J, Wu P. *DSC and morphological studies on the crystallization behavior of β-nucleated isotactic polypropylene composites filled with Kevlar fibers.* Journal of Thermal Analysis and Calorimetry. 2010;**103**(1):339-345.
[74] Romankiewicz A, Sterzynski T, Brostow W. *Structural characterization of α- and β-nucleated isotactic polypropylene.* Polymer International. 2004;**53**(12):2086-2091.
[75] Zhang Z, Tao Y, Yang Z, Mai K. *Preparation and characteristics of nano-CaCO3 supported β-nucleating agent of polypropylene.* European Polymer Journal. 2008;**44**(7):1955-1961.
[76] Park S-Y, Cho Y-H, Vaia RA. *Three-Dimensional Structure of the Zone-Drawn Film of the Nylon-6/ Layered Silicate Nanocomposites.* Macromolecules. 2005;**38**:1729-1735.
[77] Karger-Kocsis J, Varga J. *Effects of β-α Transformation on the Static and Dynamic Tensile Behavior of Isotactic Polypropylene.* Journal of Applied Polymer Science. 1996;**62**:291-300.
[78] Leelapornpisit W, Ton-That M-T, Perrin-Sarazin F, Cole KC, Denault J, Simard B. *Effect of carbon nanotubes on the crystallization and properties of polypropylene.* Journal of Polymer Science Part B: Polymer Physics. 2005;**43**(18):2445-2453.
[79] Grady BP, Pompeo F, Shambaugh RL, Resasco DE. *Nucleation of Polypropylene Crystallization by Single-Walled Carbon Nanotubes.* Journal of Physical Chemistry B. 2002;**106**:5852-5858.
[80] King JA, Via MD, Morrison FA, Wiese KR, Beach EA, Cieslinski MJ, et al. *Characterization of exfoliated graphite nanoplatelets/polycarbonate composites: electrical and thermal conductivity, and tensile, flexural, and rheological properties.* Journal of Composite Materials. 2011;**46**(9):1029-1039.
[81] Kim S, Do I, Drzal LT. *Multifunctional xGnP/LLDPE Nanocomposites Prepared by Solution Compounding Using Various Screw Rotating Systems.* Macromolecular Materials and Engineering. 2009;**294**(3):196-205.
[82] Tait M, Pegoretti A, Dorigato A, Kalaitzidou K. *The effect of filler type and content and the manufacturing process on the performance of multifunctional carbon/poly-lactide composites.* Carbon. 2011;**49**(13):4280-4290.
[83] Thridandapani RR, Mudaliar A, Yuan Q, Misra RDK. *Near surface deformation associated with the scratch in polypropylene–clay nanocomposite: A microscopic study.* Materials Science and Engineering: A. 2006;**418**(1-2):292-302.
[84] Di Marzio EA, Guttman CM, Hoffman JD. *Study of amorphous-crystal interfaces in polymers using the wicket model: estimates of bounds on degree of adjacent reentry.* Polymer. 1980;**21**:1379-1384.
[85] Jancar J, Dibenedetto AT, Hadziinikolau Y, Goldberg AJ, Dianselmo A. *Measurement of the elastic modulus of fibre-reinforced composites used as*

orthodontic wires. Journals of materials science: materials in medicine. 1994;**5**:214-218.
[86] Vollenberg PHT, Heikens D. *Particle size dependence of the Young's modulus of filled polymers: 1. Preliminary experiments.* Polymer. 1989;**30**:1656-1662.
[87] Karevan M, Kalaitzidou K. *Understanding the property enhancement mechanism in exfoliated graphite nanoplatelets reinforced polymer nanocomposites.* Composite Interfaces. 2013;**20**(4):255-268.
[88] Chamis CC. Polymer *Composite Mechanics Review 1965 to 2006.* Journal of Reinforced Plastics and Composites. 2007;**26**(10):987-1019.
[89] Barber AH, Cohen SR, Wagner HD. *Measurement of carbon nanotube–polymer interfacial strength.* Applied Physics Letters. 2003;**82**(23):4140-4142.
[90] Aït Hocine N, Médéric P, Aubry T. *Mechanical properties of polyamide-12 layered silicate nanocomposites and their relations with structure.* Polymer Testing. 2008;**27**(3):330-339.
[91] Pukanszky B, Turcsanyi B, Tudos F. *Effect of interfacial interaction on the tensile yield stress of polymer composites in Interfaces in Polymer, Ceramic and Metal Matrix Composites*, ed by Ishida H, Elsevier, pp 467–477. New York; 1988.
[92] Sumita M, Tsukihi KM, Ishikawa K. *Dynamic Mechanical Properties of Polypropylene Composites Filled with Ultrafine Particles.* Journal of Applied Polymer Science. 1984;**29**:1523-1530.
[93] Shang SW, Williams JW, Soderholm K-JM. *How the work of adhesion affects the mechanical properties of silica-filled polymer composites.* Journal of Materials Science. 1994;**29**:2406-2416.
[94] Ellison CJ, Torkelson JM. *The distribution of glass-transition temperatures in nanoscopically confined glass formers.* Nature Materials. 2003;**2**(10):695-700.
[95] Ash BJ, Schadler LS, Siegel RW. *Glass transition behavior of alumina/polymethylmethacrylate nanocomposites.* Materials Letters. 2002;**55**(1):83-87.
[96] Sternstein SS, Zhu A-J. *Reinforcement mechanism of nanofilled polymer melts as elucidated by nonlinear viscoelastic behavior.* Macromolecules. 2002;**35**(19):7262-7273.
[97] Barnes HA. *Handbook of elementary rheology.* Llanbadarn Road, Aberystwyth: Howard A. Barnes; 2000.
[98] Carreau PJ, De Kee DCR, Chhabra RP. *Rheology of Polymeric Liquids*. Munich-Vienna-New York: Hanser; 1997.
[99] Yudin VE. *Effects of nanofiller morphology and aspect ratio on the rheo-mechanical properties of polyimide nanocomposites.* eXPRESS Polymer Letters. 2008;**2**(7):485-493.
[100] Trunec M, Hrazdera J. *Effect of ceramic nanopowders on rheology of thermoplastic suspensions.* Ceramics International. 2005;**31**(6):845-849.
[101] Abdel-Goad M, Pötschke P. *Rheological characterization of melt processed polycarbonate-multiwalled carbon nanotube composites.* Journal of Non-Newtonian Fluid Mechanics. 2005;**128**(1):2-6.
[102] Cassagnau P. *Melt rheology of organoclay and fumed silica nanocomposites.* Polymer. 2008;**49**(9):2183-2196.

[103] Ganß M, Satapathy BK, Thunga M, Weidisch R, Pötschke P, Jehnichen D. *Structural interpretations of deformation and fracture behavior of polypropylene/multi-walled carbon nanotube composites.* Acta Materialia. 2008;**56**(10):2247-2261.
[104] Renger C, Kuschel P, Kristoffersson A, Clauss B, Oppermann W, Sigmund W. *Rheology studies on highly filled nano-zirconia suspensions.* Journal of the European Ceramic Society. 2007;**27**(6):2361-2367.
[105] Sarvestani AS. *Modeling the solid-like behavior of entangled polymer nanocomposites at low frequency regimes.* European Polymer Journal. 2008;**44**(2):263-269.
[106] Sepehr M, Utracki LA, Zheng X, Wilkie CA. Polystyrenes with macro-intercalated organoclay. Part II. *Rheology and mechanical performance.* Polymer. 2005;**46**(25):11569-11581.
[107] Wu D, Wu L, Wu L, Zhang M. *Rheology and thermal stability of polylactide/clay nanocomposites.* Polymer Degradation and Stability. 2006;91(12):3149-3155.
[108] Khumalo VM, Karger-Kocsis J, Thomann R. *Polyethylene/synthetic boehmite alumina nanocomposites: Structure, thermal and rheological properties.* eXPRESS Polymer Letters. 2010;**4**(5):264-274.
[109] Blaszczak P, Brostow W, Datashvili T, Lobland HEH. *Rheology of low-density polyethylene + Boehmite composites.* Polymer Composites. 2010;31(11):1909-1913.
[110] Jeffrey DJ, Acrivos A. *The rheological properties of suspensions of rigid particles.* AlChE Journal. 1976;**22**(3):417-432.
[111] Utracki LA. *The Shear and Elongational Flow of Polymer Melts Containing Anisometric Filler Particles; Part I.* Rubber Chemistry Technology. 1984;**57**(3):507-522.
[112] McKeen LW. *The effect of creep and other time related factors on plastics and elastomers.* Burlington (USA): Elsevier; 2009.
[113] Brinson HF, Brinson LC. *Polymer Engineering Science and Viscoelasticity An Introduction.* New York: Springer; 2008.
[114] Yeow Y. *The time-temperature behavior of graphite epoxy laminate.* Virginia Polytechnic Institute and State University, 1978.
[115] Gramoll K, Dillard D, Brinson H. *Thermo viscoelastic characterization and prediction of kevlar epoxy composite laminate.* Composite Material Testing and Design. 1990;**9**:477-493.
[116] Dillard D, Morris D, Brinson H. *Creep and creep rupture of laminates graphite/epoxy composites.* In: A report prepared for NASA V, ed. Blacksburg (USA) 1981.
[117] Montgomery TS, MacKnight WJ. *Introduction to polymer viscoelasticity*. Hoboken (New Jersey): Wiley Interscience; 2005.
[118] Kolarik J, Pegoretti A. *Non-linear tensile creep of polypropylene: Time-strain superposition and creep prediction.* Polymer. 2006;**47**(1):346-356.
[119] Menczel JD, Prime RB. *Thermal analysis of polymers - Fundamentals and Applications.* Hoboken (New Jersey): Wiley; 2009.
[120] Kaufmann EN. *Characterization of Materials*. John Wiley & Sons; 2012.

[121] Bárány T, Czigány T, Karger-Kocsis J. *Application of the essential work of fracture (EWF) concept for polymers, related blends and composites: A review.* Progress in Polymer Science. 2010;**35**(10):1257-1287.
[122] Williams JG, Rink M. *The standardisation of the EWF test.* Engineering Fracture Mechanics. 2007;**74**(7):1009-1017.
[123] Mai YW, Cotterell B. *On the essential work of ductile fracture in polymers.* International Journal of Fracture. 1986;**32**:105-125.
[124] Hill R. *On discontinuous plastic states, with special reference to localized necking in thin sheets.* Journal of the Mechanics and Physics of Solids. 1952;**1**(1):19-30.
[125] Kaw AK. *Mechanics of composite materials.* Boca Raton (Florida): CRC Taylor and Francis; 2006.
[126] Hull D, Clyne TW. *An introduction to composite materials.* Cambridge: Cambridge Unversity Press; 1996.
[127] Piggot M. *Load bearing fibre composites*. Oxford: Pergamon Press; 1980.
[128] Malchev PG. *Short fiber reinforced thermoplastic blends.* Technische Universiteit Delft, 2008.
[129] Pedrazzoli D, Pegoretti A. *Silica nanoparticles as coupling agents for polypropylene/glass composites.* Composites Science and Technology. 2013;**76**:77-83.
[130] Fu S-Y, Lauke B, Mai Y-W. *Science and engineering of short fibre reinforced polymer composites.* Oxford, Cambridge, New Delhi: CRC Press; 2009.
[131] Cox H. *The elasticity and strength of paper and other fibrous materials.* British Journal of Applied Physics. 1952;**3**:72-79.
[132] Kim J-K, Mai Y-M. *Engineered interfaces in fiber reinforced composites.* Amsterdam, The Netherlands: Elsevier; 1998.
[133] Vlasveld DPN. *Fibre reinforced polymer nanocomposites.* Technische Universiteit Delft, 2005.
[134] Akkapeddi MK. *Glass fiber reinforced polyamide-6 nanocomposites.* Polymer Composites. 2000;**21**(4):576-585.
[135] Yoo Y, Spencer MW, Paul DR. *Morphology and mechanical properties of glass fiber reinforced Nylon 6 nanocomposites.* Polymer. 2011;**52**(1):180-190.
[136] Kim J-K, Hu C, Woo RSC, Sham M-L. *Moisture barrier characteristics of organoclay–epoxy nanocomposites.* Composites Science and Technology. 2005;**65**(5):805-813.
[137] Mukhopadhyay S, Deopura BL, Alagiruswamy R. *Interface Behavior in Polypropylene Composites.* Journal of Thermoplastic Composite Materials. 2003;**16**(6):479-495.
[138] Etcheverry M, Ferreira ML, Capiati NJ, Pegoretti A, Barbosa SE. *Strengthening of polypropylene-glass fiber interface by direct metallocenic polymerization of propylene onto the fibers.* Composites Part A - Applied Science and Manufacturing. 2008;**39**(12):1915-1923.
[139] Feller JF, Grohens Y. *Coupling ability of silane grafted poly(propene) at glass fibers/poly(propene) interface.* Composites Part A - Applied Science and Manufacturing. 2004;**35**(1):1-10.

[140] Mader E, Freitag KH. *Interface properties and their influence on short fiber composites.* Composites. 1990;**21**(5):397-402.
[141] Mader E, Jacobasch HJ, Grundke K, Gietzelt T. *Influence of an optimized interphase on the properties of polypropylene/glass fibre composites.* Composites Part A - Applied Science and Manufacturing. 1996;**27**(9):907-912.
[142] Nygard P, Redford K, Gustafson C-G. *Interfacial strength in glass fibre-polypropylene composites: in fluence of chemical bonding and physical entanglement.* Compos Interfaces. 2002;**9**(4):365-388.
[143] Thomason JL, Schoolenberg GE. *An investigation of glass-fiber polypropylene interface strength and its effect on composite properties.* Composites. 1994;**25**(3):197-203.
[144] Yue CY, Cheung WL. *Interfacial properties of fiber-reinforced composites.* Journal of Materials Science. 1992;**27**(14):3843-3855.
[145] Mader E, Moos E, Karger-Kocsis J. *Role of film formers in glass fibre reinforced polypropylene - new insights and relation to mechanical properties.* Composites Part A - Applied Science and Manufacturing. 2001;**32**(5):631-639.
[146] Barber AH, Zhao Q, Wagner HD, Baillie CA. *Characterization of E-glass–polypropylene interfaces using carbon nanotubes as strain sensors.* Composites Science and Technology. 2004;**64**(13-14):1915-1919.
[147] DiBenedetto AT. *Tailoring of interfaces in glass fiber reinforced polymer composites: a review.* Materials Science and Engineering A-Structural Materials Properties Microstructure and Processing. 2001;**302**:74-82.
[148] Zhamu A, Zhong WH, Stone JJ. *Experimental study on adhesion property of UHMWPE fiber/nano-epoxy by fiber bundle pull-out tests.* Composites Science and Technology. 2006;**66**(15):2736-2742.
[149] Vlasveld DPN, Parlevliet PP, Bersee HEN, Picken SJ. *Fibre-matrix adhesion in glass-fibre reinforced polyamide-6 silicate nanocomposites.* Composites Part A - Applied Science and Manufacturing. 2005;**36**(1):1-11.
[150] Gao X, Jensen RE, McKnight SH, Gillespie JW. *Effect of colloidal silica on the strength and energy absorption of glass fiber/epoxy interphases.* Composites Part A - Applied Science and Manufacturing. 2011;**42**(11):1738-1747.
[151] Gao SL, Mader E, Plonka R. *Nanocomposite coatings for healing surface defects of glass fibers and improving interfacial adhesion.* Composites Science and Technology. 2008;**68**(14):2892-2901.
[152] Rausch J, Zhuang RC, Mader E. *Application of nanomaterials in sizings for glass fibre/polypropylene hybrid yarn spinning.* Materials Technology. 2009;**24**(1):29-35.
[153] Pedrazzoli D, Pegoretti A. *Expanded graphite nanoplatelets as coupling agents in glass fiber reinforced polypropylene composites.* Composite Week @ Leuven, Leuven; 2013.
[154] Pedrazzoli D, Dorigato A, Pegoretti A. *Monitoring the mechanical behaviour under ramp and creep conditions of electrically conductive polymer composites.* Composites Part A - Applied Science and Manufacturing. 2012;**43**(8):1285-1292.
[155] Leng J, Du S. *Shape-memory polymers and multifunctional composites.* Boca Raton: CRC Press; 2010.

[156] James E. *Polymer data handbook.* New York: Oxford University Press; 1999.
[157] Stickel JM, Nagarajan M. *Glass Fiber-Reinforced Composites: From Formulation to Application.* International Journal of Applied Glass Science. 2012;**3**(2):122-136.
[158] Dorigato A, Pegoretti A, Penati A. *Linear low-density polyethylene – silica micro- and nanocomposites: dynamic rheological measurements and modeling.* eXPRESS Polymer Letters. 2010;**4**(2):115-129.
[159] Fukushima H. *Graphite nanoreinforcements in polymer nanocomposites.* PhD tehsis at Michigan State University, 2003.
[160] Bernasconi A, Davoli P, Basile A, Filippi A. *Effect of fibre orientation on the fatigue behaviour of a short glass fibre reinforced polyamide-6.* International Journal of Fatigue. 2007;**29**(2):199-208.
[161] XG Sciences; 2014 *(www.xgsciences.com)*.
[162] Downing TD, Kumar R, Cross WM, Kjerengtroen L, Kellar JJ. *Determining the interphase thickness and properties in polymer matrix composites using phase imaging atomic force microscopy and nanoindentation.* Journal of Adhesion Science and Technology. 2000;**14**(14):1801-1812.
[163] Schroeder PA, Pruett RJ. *Fe ordering in kaolinite: Insights from ^{29}Si and ^{27}Al MAS NMR spectroscopy.* American Mineralogist. 1996;**81**:26-38.
[164] Reading M, Hourston DJ. *Modulated-temperature differential scanning calorimetry.* Dordrecht: Springer; 2006.
[165] Pedrazzoli D, Tuba F, Khumalo VM, Pegoretti A, Karger-Kocsis J. *Mechanical and rheological response of polypropylene/boehmite nanocomposites.* Journal of Reinforced Plastics and Composites. 2014; In press.
[166] Pegoretti A, Fidanza M, Migliaresi C, DiBenedetto AT. *Toughness of the fiber/matrix interface in nylon-6/glass fiber composites.* Composites Part A - Applied Science and Manufacturing. 1998;**29**(3):283-291.
[167] Pegoretti A, Fambri L, Migliaresi C. *Interfacial stress transfer in nylon-6/E-glass microcomposites: effect of temperature and strain rate.* Polymer Composites. 2000;**21**(3):466-475.
[168] Tyson WR, Kelly A. *Tensile properties of fibre-reinforced metals: Copper/tungsten and copper/molybdenum.* Journal of the Mechanics and Physics of Solids. 1965;**13**(6):329-338.
[169] Thomason JL, Yang L. *Temperature dependence of the interfacial shear strength in glass reinforced polypropylene and epoxy composites.* The 19th International conference on composite materials; 2013.
[170] Kolarik J, Fambri L, Pegoretti A, Penati A, Goberti P. *Prediction of the creep of heterogeneous polymer blends: rubber-toughened polypropylene / poly(styrene-co-acrylonitrile).* Polymer Engineering and Science. 2002;**42**(1):161-169.
[171] Wu S. *Polymer interface and adhesion.* New York: Marcel Dekker, Inc; 1892.
[172] Fridman A. Plasma Chemistry. New York; 2008.
[173] Della Volpe C, Siboni S. *A 'conveyor belt' model for the dynamic contact angle.* European Journal of Physics. 2011;**32**(4):1019-1032.

[174] Dorigato A, Pegoretti A, Kolařík J. *Nonlinear tensile creep of linear low density polyethylene/fumed silica nanocomposites: Time-strain superposition and creep prediction.* Polymer Composites. 2010;**31**(11):1947-1955.
[175] Kolarik J. *Tensile creep of thermoplastics: time-strain superposition of non-iso free-volume data.* journal of Polymer Science B: Polymer Physics. 2003;**41**:736-748.
[176] Kolarik J, Fambri L, Pegoretti A, Penati A, Goberti P. *Prediction of the Creep of Heterogeneous Polymer Blends: Rubber-Toughened Polypropylenepoly(Styrene-co-Acrylonitrile).* Polymer Engineering & Science. 2002;**42**(1):161-169.
[177] Kolarik J, Pegoretti A, Fambri L, Penati A. *Non-Linear Long-Term Tensile Creep of Poly(propylene)/Cycloolefin Copolymer Blends with Fibrous Structure.* Macromolecular Materials and Engineering. 2003;**288**(8):629-641.
[178] Sax J, Ottino JM. *Modeling of transport of small molecules in polymer blends: application of effective medium theory.* Polymer Engineering & Science. 1983;**23**(3):165-176.
[179] Hsu WY, Wu S. *Percolation behavior in morphology and modulus of polymer blends.* Polymer Engineering & Science. 1993;**33**(5):293-302.
[180] Mendels D. *Analysis of the single-fibre fragmentation test.* Teddington, UK: National Physical Laboratory; 2001.
[181] Nairn JA, Liu YC. *On the use of energy methods for interpretation of results of single-fiber fragmentation experiments.* Composite Interfaces. 1996;**4**:241-267.
[182] Zhou XF, Nairn JA, Wagner HD. *Fiber-matrix adhesion from the single-fiber composite test: nucleation of interfacial debonding.* Composites A. 1999;**30**(12):1387-1400.
[183] Kelly A, Tyson W. *Tensile properties of fibre-reinforced metals.* Journal of Mechanical Physics Solids. 1965;**13**:329-350.
[184] Okabe T, Takeda N, Kamoshida Y, Shimizu M, Curtin WA. *A 3D shear-lag model considering micro-damage and statistical strength prediction of unidirectional fiber-reinforced composites.* Composites Science and Technology. 2001;**61**:1773-1787.
[185] Ogihara S, Nakatani H. *Stress analysis of single fiber composites using an elastoplastic shear- lag approach.* Science Engineering Composite Materials. 2012;**19**:61-65.
[186] Yasuda H. *Vapor deposition and interface engineering.* New York: Marcel Dekker; 2005.
[187] Whang HS, Gupta BS. *Surface wetting characteristics of cellulosic fibers.* Textile Research Journal. 2000;**70**(4):351-358.
[188] Drelich J, Miller JD. *A critical review of wetting and adhesion phenomena in the preparation of polymer-filler composites.* Mineral and Metallurgical Processing. 1995;**12**(4):197-204.
[189] Pegoretti A, Dorigato A, Brugnara M, Penati A. *Contact angle measurements as a tool to investigate the filler–matrix interactions in polyurethane–clay nanocomposites from blocked prepolymer.* European Polymer Journal. 2008;**44**(6):1662-1672.
[190] Garbassi F, Morra M, Occhiello E. *Polymer surfaces: from physics to technology.* New York: John Wiley & Sons Ltd; 1998.

[191] Sun Y, Zhang Z, Wong C. *Study on mono-dispersed nano-size silica by surface modification for underfill applications.* Journal of Colloid Interface Science. 2005;**292**(2): 436-444.
[192] Yusoff WAY, Dotchev KD, Pham DT. *Deterioration of polyamide powder properties in the laser sintering process.* Proceedings of the Institution of Mechanical Engineers, Part C: Journal of Mechanical Engineering Science. 2008;**222**(11):2163-2176.
[193] Zheng W, Lu X, Ling Toh C, Hua Zheng T, He C. *Effects of clay on polymorphism of polypropylene in polypropylene/clay nanocomposites.* Journal of Polymer Science Part B: Polymer Physics. 2004;**42**(10):1810-1816.
[194] Chen J-H, Tsai F-C, Nien Y-H, Yeh P-H. *Isothermal crystallization of isotactic polypropylene blended with low molecular weight atactic polypropylene.* Part I. Thermal properties and morphology development. Polymer. 2005;**46**(15):5680-5688.
[195] Zheng Q, Shangguan Y, Yan S, Song Y, Peng M, Zhang Q. *Structure, morphology and non-isothermal crystallization behavior of polypropylene catalloys.* Polymer. 2005;**46**(9):3163-3174.
[196] Supaphol P, Spruiell JE. *Crystalline Memory Effects in Isothermal Crystallization of Syndiotactic Polypropylene.* Journal of Applied Polymer Science. 2000;**75**:337-346.
[197] Turner Jones A, Alizlewood JM, Beckett DR. *Crystalline Forms of Isotactic Polypropylene.* Macromolecular Chemistry and Physics. 1964;**75**(1):134-158.
[198] Nuffield EW. *X-ray diffraction methods.* New York: Wiley; 1966.
[199] Chung DDL. *Review Graphite*. Journal of Materials Science. 2002;**37**:1475-1489.
[200] Mirzazadeh H, Katbab AA, Hrymak AN. *The role of interfacial compatibilization upon the microstructure and electrical conductivity threshold in polypropylene/expanded graphite nanocomposites.* Polymer Advanced Technologies. 2011;**22**(6):863-869.
[201] Planes E, Duchet J, Maazouz A, Gerard J-F. *Characterization of new formulations for the rotational molding based on ethylene–propylene copolymer/graphite nanocomposites.* Polymer Engineering & Science. 2008;**48**(4):723-731.
[202] Gopakumar TG, Pagè DJYS. *Polypropylene/graphite nanocomposites by thermo-kinetic mixing.* Polymer Engineering and Science. 2004;**44**(6):1162-1169.
[203] Kalaitzidou K. *Exfoliated graphite nanoplatelets as reinforcement for multifunctional polypropylene nanocomposites.* PhD thesis, Michigan State University, 2006.
[204] Petraccone V, Guerra G, De Rosa C, Tuzi A. *Extrapolation to the Equilibrium Melting Temperature for Isotactic Polypropylene.* Macromolecules. 1984;**18**:813-814.
[205] Marco C, Gomez MA, Ellis G, Arribas JM. *Activity of a β-nucleating agent for isotactic polypropylene and its influence on polymorphic transitions.* Journal of Applied Polymer Science. 2002;**86**(3):531-539.
[206] Varga J. *Melting memory effect of the β modification of polypropylene.* Journal of Thermal Analysis. 1986;**31**:165-172.

[207] Varga J, Garzò G, Ille A. *Kristallisation, Umkristallisation und Schmelzen der β-Modifikation des Polypropylens.* Die Angewandte Makromolekulare Chemie. 1986;**142**:171-181.
[208] Varga J, Karger-Kocsis J. *Rules of Supermolecular Structure Formation in Sheared Isotactic Polypropylene Melts.* Journal of Polymer Science Part B: Polymer Physics. 1996;**34**:657-670.
[209] Passingham C, Hendra PJ, Cudby MEA, Zichy V, Weller M. *The re-evaluation of multiple peaks in the DSC melting endotherm of isotactic polypropylene.* European Polymer Journal. 1990;**26**(6):631-638.
[210] Fillon B, Thierry A, Wittmann JC, Lotz B. *Self-Nucleation and Recrystallization of Polymers. Isotactic Polypropylene, β Phase: β-α Conversion and β-α Growth Transitions.* Journal of Polymer Science Part B: Polymer Physics. 1993;**31**:1407-1424.
[211] Zeng QH, Yu AB, Lu GQ. *Multiscale modeling and simulation of polymer nanocomposites.* Progress in Polymer Science. 2008;**33**(2):191-269.
[212] Gibson RF. *A review of recent research on mechanics of multifunctional composite materials and structures.* Composites Structures. 2010;**92**(12):2793-2810.
[213] Duncan RK, Chen XG, Bult JB, Brinson LC, Schadler LS. *Measurement of the critical aspect ratio and interfacial shear strength in MWNT/polymer composites.* Composites Science and Technology. 2010;**70**(4):599-605.
[214] Bhuiyan MA, Pucha RV, Worthy J, Karevan M, Kalaitzidou K. Defining the lower and upper limit of the effective modulus of CNT/polypropylene composites through integration of modeling and experiments. Composites Structures. 2013;**95**:80-87.
[215] Evans W, Prasher R, Fish J, Meakin P, Phelan P, Keblinski P. *Effect of aggregation and interfacial thermal resistance on thermal conductivity of nanocomposites and colloidal nanofluids.* International Journal of Heat Mass Transfer. 2008;**51**(5-6):1431-1438.
[216] Qiao R, Catherine Brinson L. *Simulation of interphase percolation and gradients in polymer nanocomposites.* Composites Science and Technology. 2009;**69**(3-4):491-499.
[217] Ning N, Fu S, Zhang W, Chen F, Wang K, Deng H, et al. *Realizing the enhancement of interfacial interaction in semicrystalline polymer/filler composites via interfacial crystallization.* Progress in Polymer Science. 2012;**37**(10):1425-1455.
[218] Gutowski WS. *Interface/Interphase engineering of polymers for adhesion enhancement: Part I. Review of micromechanical aspects of polymer interface reinforcement through surface grafted molecular brushes.* The Journal of Adhesion. 2003;**79**(5):445-482.
[219] Bhuiyan MA, Pucha RV, Karevan M, Kalaitzidou K. *Tensile modulus of carbon nanotube/polypropylene composites – A computational study based on experimental characterization.* Computational Materials Science. 2011;**50**(8):2347-2353.
[220] Ciprari D, Jacob K, Tannenbaum R. *Characterization of Polymer Nanocomposite Interphase and Its Impact on Mechanical Properties.* Macromolecules. 2006;**39**:6565-6573.

[221] Deng F, Van Vliet KJ. *Prediction of elastic properties for polymer-particle nanocomposites exhibiting an interphase.* Nanotechnology. 2011;22(16):165703.
[222] Liu H, Brinson LC. *Reinforcing efficiency of nanoparticles: A simple comparison for polymer nanocomposites.* Composites Science and Technology. 2008;**68**(6):1502-1512.
[223] Pukánszky B. *Interfaces and interphases in multicomponent materials: past, present, future.* European Polymer Journal. 2005;**41**(4):645-662.
[224] Winey KI, Vaia RA. *Polymer Nanocomposites.* MRS Bulletin. 2007;32:314-322.
[225] Fu S, Feng X, Lauke B, Mai Y. *Effects of particle size, particle/matrix interface adhesion and particle loading on mechanical properties of particulate–polymer composites.* Composites Part B: Engineering. 2008;**39**(6):933-961.
[226] Dorigato A, Dzenis Y, Pegoretti A. *On the Reinforcement Mechanism in Particulate Nanocomposites.* Mechanics of Materials. 2011.
[227] Zhang X, Loo LS. *Study of Glass Transition and Reinforcement Mechanism in Polymer/Layered Silicate Nanocomposites.* Macromolecules. 2009;**42**(14):5196-5207.
[228] Qiao R, Deng H, Putz KW, Brinson LC. *Effect of particle agglomeration and interphase on the glass transition temperature of polymer nanocomposites.* Journal of Polymer Science Part B: Polymer Physics. 2011;**49**(10):740-748.
[229] Prado L.A.S.A, Kwiatkowska M, Funari SS, Roslaniec Z, Broza G, Schulte K. *Studies on morphology and interphase of poly(butylene terephthalate)/carbon nanotubes nanocomposites.* Polymer Engineering & Science. 2010;**50**(8):1571-1576.
[230] Putz KW, Palmeri MJ, Cohn RB, Andrews R, Brinson LC. *Effect of Cross-Link Density on Interphase Creation in Polymer Nanocomposites.* Macromolecules. 2008;**41**:6752-6756.
[231] Rong MZ, Zhang MQ, Pan SL, Lehmann B, Friedrich K. *Analysis of the interfacial interactions in polypropylene/silica nanocomposites.* Polymer International. 2004;**53**(2):176-183.
[232] Garcia M, Van Vliet G, Jain S, Schrauwen BAG, Sarkissov A, Van Zyl WE, et al. *Polypropylene/SiO_2 nanocomposites with improved mechanical properties.* Reviews on Advanced Materials Science. 2004;**6**:169-175.
[233] Zou H, Wu S, Shen J. *Polymer/Silica Nanocomposites: Preparation, Characterization, Properties, and Applications. Chemical Review.* 2008;**108**:3893-3957.
[234] Klocek P. *Handbook of Infrared Optical Materials.* New York: Marcel Dekker; 1991.
[235] Banik K, Karger-Kocsis J, Abraham T. *Flexural creep of all-polypropylene composites: Model analysis.* Polymer Engineering & Science. 2008;**48**(5):941-948.
[236] Andrew W. *The effect of creep and other time related factors on plastics and elastomers.* New York, 1991.
[237] Kolarik J, Pegoretti A, Fambri L, Penati A. *Prediction of non-linear long-term tensile creep of heterogeneous blends: Rubber-toughened polypropylene-poly(styrene-co-acrylonitrile).* Journal of Applied Polymer Science. 2003;**88**(3):641-651.

[238] Read BE, Dean GD, Tomlins PE. *Effects of physical ageing on creep in polypropylene.* Polymer. 1988;**29**(12):2159-2169.
[239] Tomlins PE, Read BE. *Creep and physical ageing of polypropylene: a comparison of models.* Polymer. 1997;**39**(2):355-367.
[240] Ferry JD. *Viscoelastic properties of Polymers*. New York, 1980.
[241] Lakes RS. *Viscoelastic Solids.* London, 1999.
[242] Moore DR, Turner S. *Mechanical Evaluation Strategies for Plastics*, Cambridge, 2001.
[243] Nielsen LE, Landel RF. *Mechanical Properties of Polymers and Composites.* New York, 1994.
[244] Rodriguez F. *Principles of Polymer Systems.* Washington DS, 1996.
[245] Ward IM, Hadley DW. *An Introduction to the Mechanical Properties of Solid Polymers.* Chichester, 1993.
[246] McKeen LW. *The effect of creep and other related factors on plastics and elastomers.* Oxford, 2009.
[247] Betten J. *Creep mechanics.* Aachen, 2005.
[248] Matsumoto DS. *Time-temperature superposition and physical aging in amorphous polymers.* Polymer Engineering & Science. 2004;**28**(20):1913-1317.
[249] Tajvidi M, Falk RH, Hermanson JC. *Time-temperature superposition principle applied to a kenaf-fiber/high-density polyethylene composite.* Journal of Applied Polymer Science. 2005;**97**(5):1995-2004.
[250] Yeow YT. *The time-temperature behavior of graphite epoxy laminates.* PhD thesis at Virginia Polytechnic institute and state university, 1978.
[251] Struik LCE. *Mechanical behaviour and physical ageing of semi-crystalline polymers: 3. Prediction of long term creep from short time tests.* Polymer. 1989;**30**(5):799-814.
[252] Brunauer S, Emmett PH, E T. *Adsorption of gases in multimolecular layers.* Bureau of Chemistry and Soils and George Washington University. 1938;**60**:309-319.
[253] Barrett E, Leslie G, Halenda P. *The Determination of Pore Volume and Area Distributions in Porous Substances. I. Computations from Nitrogen Isotherms.* Journal of American Chemical Society. 1951;**73**:373:380.
[254] Dorigato A. *Viscoelastic and fracture behaviour of polyolefin based nanocomposites.* PhD thesis at University of Trento (Italy), 2009.
[255] Bikiaris DN, Vassiliou A, Pavlidou E, Karayannidis GP. *Compatibilisation effect of PP-g-MA copolymer on iPP/SiO_2 nanocomposites prepared by melt mixing.* European Polymer Journal. 2005;**41**(9):1965-1978.
[256] Turi A. *Thermal characterization of polymeric materials, Vol 1 and 2 (2nd ed).* New York: Academic Press; 1997.
[257] Gurvich MR, Di Benedetto AT, Pegoretti A. *Evaluation of the statistical parameters of a Weibull distribution.* Journal of Materials Science. 1997;**32**:3711-3716.
[258] Wojuzkij SS. *Uber das Fehlen einer Korrelation zwisehen der AdMision und Benetzung yon Substraten dureh das Polymere Adhaisiv.* Polymere. 1966;**214**(2):97-100.

[259] Ramanathan T, Bismarck A, Schulz E, Subramanian K. *Investigation of the influence of acidic and basic surface groups on carbon fibres on the interfacial shear strength in an epoxy matrix by means of single-fibre pull-out test.* Composites Science and Technology. 2001;**61**:599-605.
[260] Shang S. A *High-Luminescence Fringelike Field Emission from Screen-Printed Carbon Nanotube and Zinc Oxide Composite Film.* Journal of Electromagnetic Analysis and Applications. 2010;**2**(12):649-653.
[261] Dorigato A, Pegoretti A. *Fatigue resistance of basalt fibers-reinforced laminates.* Journal of Composite Materials. 2012;**46**(15):1773-1785.
[262] Jacob S, Suma KK, Mendez JM, George KE. *Reinforcing effect of nanosilica on polypropylene–nylon fibre composite.* Materials Science and Engineering: B. 2010;**168**(1-3):245-249.
[263] Vlasveld DPN, Parlevliet PP, Bersee HEN, Picken SJ. *Fibre–matrix adhesion in glass-fibre reinforced polyamide-6 silicate nanocomposites.* Composites Part A: Applied Science and Manufacturing. 2005;**36**(1):1-11.
[264] Fu S-Y, Lauke B. *The elastic modulus of misaligned short-fiber-reinforced polymers.* Composites Science and Technology. 1998;**58**:389-400.
[265] Halpin JC, Kardos JL. *The Halpin-Tsai Equations: a Review.* Polymer Engineering & Science. 1976;**16**(5).
[266] Spencer MW, Cui L, Yoo Y, Paul DR. *Morphology and properties of nanocomposites based on HDPE/HDPE-g-MA blends.* Polymer. 2010;**51**(5):1056-1070.
[267] Karevan M, Pucha RV, Bhuiyan MA, Kalaitzidou K. *Effect of interphase modulus and nanofiller agglomeration on the tensile modulus of graphite nanoplatelets and carbon nanotube reinforced polypropylene nanocomposites.* Carbon Letters. 2011;**11**(4):325-331.
[268] Mallick PK. *Fiber-reinforced composites: materials, manufacturing, and design.* New York: Marce Dekker, Inc.; 1993.
[269] Tsai SW, Pagano NJ. *Composite materials workshop.* In: Technomic, editor., Stamford (CT); 1968.
[270] Kalaitzidou K, Fukushima H, Drzal LT. *Mechanical properties and morphological characterization of exfoliated graphite–polypropylene nanocomposites.* Composites Part A: Applied Science and Manufacturing. 2007;**38**(7):1675-1682.
[271] Dorigato A, Dzenis Y, Pegoretti A. *On the Reinforcement Mechanism in Particulate Nanocomposites.* Mechanics of Materials. In press.
[272] Bansal NP. *Handbook of Ceramic Composites.* New Yourk: Kluwer Academic Publishers; 2005.
[273] Dzenis Y. *Effect of aggregation of a dispersed rigid fillller on the elastic characteristics of a polymer composite.* Mechanics of Composite Materials 1986;**22**:14-22.
[274] Brostow W, Datashvili T, Huang B, Too J. *Tensile properties of LDPE + Boehmite composites.* Polymer Composites. 2009;**30**(6):760-767.

[275] Murariu M, Dechief A-L, Paint Y, Peeterbroeck S, Bonnaud L, Dubois P. *Polylactide (PLA)—Halloysite Nanocomposites: Production, Morphology and Key-Properties.* Journal of Polymers and the Environment. 2012;**20**(4):932-943.
[276] Marney DCO, Russell LJ, Wu DY, Nguyen T, Cramm D, Rigopoulos N, et al. *The suitability of halloysite nanotubes as a fire retardant for nylon 6.* Polymer Degradation and Stability. 2008;**93**(10):1971-1978.
[277] Du M, Guo B, Jia D. *Thermal stability and flame retardant effects of halloysite nanotubes on poly(propylene).* European Polymer Journal. 2006;**42**(6):1362-1369.
[278] Jia Z, Luo Y, Guo B, Yang B, Du M, Jia D. *Reinforcing and Flame-Retardant Effects of Halloysite Nanotubes on LLDPE.* Polymer-Plastics Technology and Engineering. 2009;**48**(6):607-613.
[279] Dorigato A, Pegoretti A, Dzenis Y. *Filler aggregation as a reinforcement mechanism in polymer nanocomposites.* Mechanics of Materials. 2013;**61**:79-90.
[280] Lourenço MP, de Oliveira C, Oliveira AF, Guimarães L, Duarte HA. *Structural, Electronic, and Mechanical Properties of Single-Walled Chrysotile Nanotube Models.* The Journal of Physical Chemistry C. 2012;**116**(17):9405-9411.
[281] Guimarães L, Enyashin AN, Seifert G, Duarte HIA. *Structural, Electronic, and Mechanical Properties of Single-Walled Halloysite Nanotube Models.* The Journal of Physical Chemistry C. 2010;**114**(26):11358-11363.
[282] Yang W, Xie B-H, Shi W, Li Z-M, Liu Z-Y, Chen J, et al. *Essential work of fracture evaluation of fracture behavior of glass bead filled linear low-density polyethylene.* Journal of Applied Polymer Science. 2006;**99**(4):1781-1787.
[283] Adhikari R, Brostow W, Datashvili T, Henning S, Menard B, Menard KP, et al. *Effect of surfactant treated boehmite nanoparticles on properties of block copolymers.* Materials Research Innovations. 2012;**16**(1):19-24.
[284] Zhang J, Ji Q, Zhang P, Xia Y, Kong Q. *Thermal stability and flame-retardancy mechanism of poly(ethylene terephthalate)/boehmite nanocomposites.* Polymer Degradation and Stability. 2010;**95**(7):1211-1218.
[285] Pedrazzoli D, Ceccato R, Karger-Kocsis J, Pegoretti A. *Viscoelastic behaviour and fracture toughness of linear-low-density polyethylene reinforced with synthetic boehmite alumina nanoparticles.* Express Polymer Letters. 2013;**7**(8):652-666.
[286] Tuba F, Oláh L, Nagy P. *Essential work of fracture study of polymers: a novel criterion for the validation of tested ligament range.* Journal of Materials Science. 2011;**46**(24):7901-7904.
[287] Arkhireyeva A, Hashemi S. *Combined effect of temperature and thickness on work of fracture parameters of unplasticized PVC film.* Polymer Engineering & Science. 2002;**42**(3):504-518.
[288] Streller RC, Thomann R, Torno O, Mülhaupt R. *Isotactic Poly(propylene) Nanocomposites Based upon Boehmite Nanofillers*. Macromolecular Materials and Engineering. 2008;**293**(3):218-227.
[289] Bocchini S, Morlat-Thérias S, Gardette J-L, Camino G. *Influence of nanodispersed boehmite on polypropylene photooxidation.* Polymer Degradation and Stability. 2007;**92**(10):1847-1856.

[290] Pedrazzoli D, Ceccato R, Karger-Kocsis J, Pegoretti A. *Viscoelastic behaviour and fracture toughness of linear-low-density polyethylene reinforced with synthetic boehmite alumina nanoparticles.* Express Polymer Letters. 2013;**7**(8):652-666.
[291] Pedrazzoli D, Tuba F, Khumalo VM, Pegoretti A, Karger-Kocsis J. *Mechanical and rheological response of polypropylene/boehmite nanocomposites.* Journal of Reinforced Plastics and Composites. 2014;**33**(3):252-265.
[292] D1922-09 A. *Standard test method for propagation tear resistance of plastic film and thin dheeting by pendulum method.* 2009.
[293] Peacock AJ, Calhoun A. *Polymer chemistry: properties and applications.* Munich, 2006.
[294] Soundararajah QY, Karunaratne BSB, Rajapakse RMG. *Mechanical Properties of Poly(vinyl alcohol) Montmorillonite Nanocomposites.* Journal of Composite Materials. 2009;**44**(3):303-311.
[295] Kaully T, Siegmann A, Shacham D. *Rheology of highly filled natural CaCO3 composites. II. Effects of solid loading and particle size distribution on rotational rheometry.* Polymer Composites. 2007;**28**(4):524-533.
[296] Osman MA, Atallah A. *Interparticle and particle–matrix interactions in polyethylene reinforcement and viscoelasticity.* Polymer. 2005;**46**(22):9476-9488.
[297] Wan T, Liao S, Wang K, Yan P, Clifford M. *Multi-scale hybrid polyamide 6 composites reinforced with nano-scale clay and micro-scale short glass fibre.* Composites Part A: Applied Science and Manufacturing. 2013;**50**:31-38.
[298] Moloney AC, Kausch HH, Kaiser T, Beer HR. *Review: Parameters determining the strength and toughness of particulate filled epoxide resins.* Journal of Materials Science. 1987;**22**:381-393.
[299] Moloney AC, Kausch HH, Stieger HR. *The fracture of particulate-filled epoxide resins.* Journal of Materials Science. 1984;**19**:1125-1130.
[300] Mohamed M.A.A. *Morphology-Controlled Facial Synthesis and Magnetism of Nanocrystalline Fe-Ni alloy.* Materials Science and Engineering: B.Submitted in March 2014.

Publications on peer reviewed journals

[1] Pedrazzoli D, A. Dorigato and A. Pegoretti, *Monitoring the mechanical behaviour of electrically conductive polymer nanocomposites under ramp and creep conditions*. Journal of Nanoscience and Nanotechnology, **2012**. 12: p. 4093-4102.

[2] Pedrazzoli D, A. Dorigato and A. Pegoretti, *Monitoring the mechanical behaviour under ramp and creep conditions of electrically conductive polymer composites.* Composites Part A: Applied Science and Manufacturing, **2012**. 43: p. 1285-1292.

[3] Pedrazzoli D, A. Pegoretti and K. Kalaitzidou, *Understanding the effect of silica nanoparticles and expanded graphite nanoplatelets on the crystallization behavior of polypropylene.* Polymer Engineering and Science, **2014**. In press.

[4] Pedrazzoli D and A. Pegoretti, *Long-term creep behaviour of polypropylene/fumed silica nanocomposites estimated by time- temperature- and time-strain superposition approaches.* Polymer Bulletin, **2014**. 71: p. 2247-2268.

[5] Pedrazzoli D, A. Pegoretti and K. Kalaitzidou, *Understanding the interfacial interactions in silica reinforced polypropylene nanocomposites and their impact on the mechanical properties*, Polymer Composites, **2014**. Under review.

[6] Pedrazzoli D and A. Pegoretti, *Silica nanoparticles as coupling agents for polypropylene/glass composites.* Composites Science and Technology, **2013**. 76: p. 77-83.

[7] Pedrazzoli D and A. Pegoretti, *Expanded graphite nanoplatelets as coupling agents in glass fiber reinforced polypropylene composites*. Composites Part A: Applied Science and Manufacturing, **2014**. 66: p. 25-34.

[8] Pedrazzoli D and A. Pegoretti, *Hybridization of short glass fiber polypropylene composites with nanosilica and graphite nanoplatelets*. Journal of Reinforced Plastics and Composites, **2014**. 33: p. 1682-1695.

[9] Pedrazzoli D, A. Pegoretti and K. Kalaitzidou, *Hybridization effect of glass fibers by expanded graphite nanoplatelets in polypropylene composites,* Journal of Applied Polymer Science, **2014**. In press.

[10] Pedrazzoli D, R. Ceccato, J. Karger-Kocsis and A. Pegoretti, *Viscoelastic behaviour and fracture toughness of linear-low-density polyethylene reinforced with synthetic boehmite alumina nanoparticles,* eXPRESS Polymer Letters, **2013**. 7(8): p. 652-666.

[11] Pedrazzoli D, A. Pegoretti, R. Thomann, J. Kristóf, J. Karger-Kocsis, *Toughening linear low density polyethylene with halloysite nanotubes.* Polymer Composites, **2014.** In press.

[12] Pedrazzoli D, F. Tuba, V.M. Khumalo, A. Pegoretti and J. Karger-Kocsi, *Mechanical and rheological response of polypropylene/boehmite nanocomposites.* Journal of Reinforced Plastics and Composites, **2014.** 33(3): p. 252-265.

[13] Pedrazzoli D, V.M. Khumalo, J. Karger-Kocsis and A. Pegoretti, *Thermal, viscoelastic and mechanical behaviors of polypropylene with synthetic boehmite alumina nanoparticles.* Polymer Testing, **2014**. 35: p. 92-100.

[14] Pedrazzoli D, A. Pegoretti and K. Kalaitzidou, *Synergistic effect of exfoliated graphite nanoplatelets and short glass fiber on the mechanical and interfacial properties of epoxy composites.* Composites Science and Technology, **2014**. 98: p. 15-21.

[15] Pedrazzoli D., A. Dorigato, T. Conti, L. Vanzetti, M. Bersani and A. Pegoretti, *Liquid crystalline polymer nanocomposites reinforced with in-situ reduced graphene oxide,* **2014**. Carbon. Submitted.

[16] Mohamed M, D. Pedrazzoli, N. Nady and K. Kalaitzidou, *Effect of nanofiller geometry on the polymer physical structure and mechanical properties of nanocrystalline Fe-Ni alloy/Polyamide 6 nanocomposites.* Journal of Polymer Research, **2014**. In preparation.

Participation to congresses, schools and workshops

[1] Pedrazzoli D and A. Pegoretti, *Adesione fibra-matrice in compositi polipropilene/vetro nanomodificati.* in 2° convegno nazionale Assocompositi, May 29-31st **2012**, Torino (Italy).

[2] Pedrazzoli D and A. Pegoretti, *Monitoraggio del comportamento a creep di compositi strutturali epossidica/vetro mediante misure di conducibilità elettrica.* in 2° convegno nazionale Assocompositi, May 29-31st **2012**, Torino (Italy).

[3] Pedrazzoli D and A. Pegoretti, *Interfacial stress transfer in nanomodified PP/E-Glass composites. in* Interface 21 (The International Conference on Composite Interfaces), August 6-8th **2012**, Kyoto (Japan).

[4] Pedrazzoli D and A. Pegoretti, *Expanded graphite nanoplatelets as coupling agent in glass fiber reinforced polypropylene composites. in* Composite Week @ Leuven, September 16-20th **2013**, Leuven (Belgium).

[5] Pedrazzoli D, K. Kalaitzidou and A. Pegoretti, *Effect of the manufacturing process on the interphase properties of nanomodified polypropylene / E-glass composites. in* ASME 2013, November 15-21st **2013**, San Diego (California, USA).

[6] Pedrazzoli D, Kalaitzidou K, Pegoretti A. *Light hybrid composites for automotive applications. in* A Collaborative Approach to Meeting the Materials Genome Initiative – poster presentation, February 21st **2014**, Atlanta (Georgia, USA).

[7] Pedrazzoli D, K. Kalaitzidou and A. Pegoretti, *Light weight multifunctional composites with enhanced mechanical properties. in* ANTEC 2014 – oral presentation, April 28-30th **2014**, Las Vegas (Nevada, USA).

[8] Pedrazzoli D, K. Kalaitzidou and A. Pegoretti, *Light weight multifunctional epoxy composites with enhanced mechanical properties. in* ANTEC 2014 – poster presentation, April 28-30th **2014**, Las Vegas (Nevada, USA).

[9] Pedrazzoli D, A. Pegoretti and K. Kalaitzidou, *Multi-scale hybrid micro-nanocomposites based on graphite nanoplatelets and glass fibers. in* COMPO 2014, April 28th-May 1st **2014**, Rehovot (Israel).

[10] Pedrazzoli D, K. Kalaitzidou and A. Pegoretti, *Understanding the interfacial interactions in silica reinforced polypropylene nanocomposites. in* ECCM16, June 22-26th **2014**, Seville (Spain).

[11] Mohamed M, D. Pedrazzoli, N. Nady and K. Kalaitzidou, *Effect of nanofiller geometry on the polymer physical structure and mechanical properties of nanocrystalline Fe-Ni alloy/Polyamide 6 nanocomposites. in* ECCM16, June 22-26th **2014**, Seville (Spain).

[12] Pedrazzoli D, K. Kalaitzidou and A. Pegoretti, *Hybrid polymeric composites based on expanded graphite and glass fibers. in* 2014 ASC 29/US-Japan 16/ASTM D30, September 8-10th **2014**, San Diego (California-USA).

[13] Pedrazzoli D, A. Pegoretti and K. Kalaitzidou, *Multi-scale hybrid composites based on graphite nanoplatelets and glass fibers. in* ASME-IMECE 2014, November 14-20th **2014**, Montreal (Canada).

[14] Pegoretti A, D. Pedrazzoli and K. Kalaitzidou, *Multiscale polymer composites based on graphite nanoplatelets and glass fibers. in* ICSS MEETING, December 8-11th **2014**, Hong Kong (China).

[15] Pegoretti A, D. Pedrazzoli and K. Kalaitzidou, *Multiscale hybrid polymer composites based on graphite nanoplatelets and glass fibers. in* ICCM20, July 19-24th **2015**, Copenhagen (Denmark).

Other activities

Internships abroad

- 09/2012 – 10/2012 at Budapest University of Technology and Economics (Hungary) – Department of Polymer Engineering. **Internship under the supervision of Prof. J. Karger-Kocsis**

- 07/2013 – 05/2014 at Georgia Institute of Technology (USA) – Woodruff School of Mechanical Engineering. **Internship under the supervision of Prof. K. Kalaitzidou.**

Journal reviewing

- Nanotechnology (IF=3.67)
- Journal of Physics D: Applied Physics (IF=2.52)
- Polymer Composites (IF=1.46)
- Journal of Applied Polymer Science (IF=1.64)
- Journal of Reinforced Plastics and Composites (IF=1.19)

Teaching activities and student tutoring

- Assistant teacher of the course **'Mechanics of Materials'**
  (Master program, University of Trento, 2012)

- Research advisor of a graduate students in Materials Science and Engineering (University of Trento, 2012-2013) regarding the '**Study of in-situ reduction of graphene oxide in Vectran nanocomposites'**

Acknowledgements

I am gratefully thankful to my tutors who followed me throughout this period, Prof. Alessandro Pegoretti (Department of Industrial Engineering – University of Trento, Italy), Prof. Kyriaki Kalaitzidou (G. W. Woodruff School of Mechanical Engineering – Georgia Institute of Technology – Atlanta, USA) and Prof. Joseph Karger-Kocsis (Department of Polymer Engineering – Budapest University of Technology and Economics – Budapest, Hungary).

I kindly thank all professors and technicians working at the department of Industrial Engineering (University of Trento) for their support on some experimental analyses, especially Prof. Riccardo Ceccato, Prof. Claudio Della Volpe, Prof. Luca Fambri, Dr. Emanuela Callone, Dr. Gloria Ischia, Dr. Matteo Traina and Mr. Lorenzo Moschini. Special acknowledgents are also due to the technician Alfredo Casagranda and Claudia Gavazza working with me at the Polymers and Composites Laboratory.

Other acknowledgements are due to Dr. Mehdi Karevan and Dr. Md Bhuiyan (Woodruff School of Mechanical Engineering – Georgia Institute of Technology) and Mr. Matthew Smith (School of Materials Science and Engineering – Georgia Institute of Technology) for their kind assistance during the training for the use of machines and instruments.

I would like to kindly thank all colleagues working with me at the 'Polymers and Composites Laboratory' (Department of Industrial Engineering – University of Trento) and those who supported me while working at the Woodruff School of Mechanical Engineering – Georgia Institute of Technology.

Finally, I gratefully thank my family for their devoted support throughout these years; my parents Fabio and M.Grazia and my brother Alfredo.

Trento, September 29th 2014